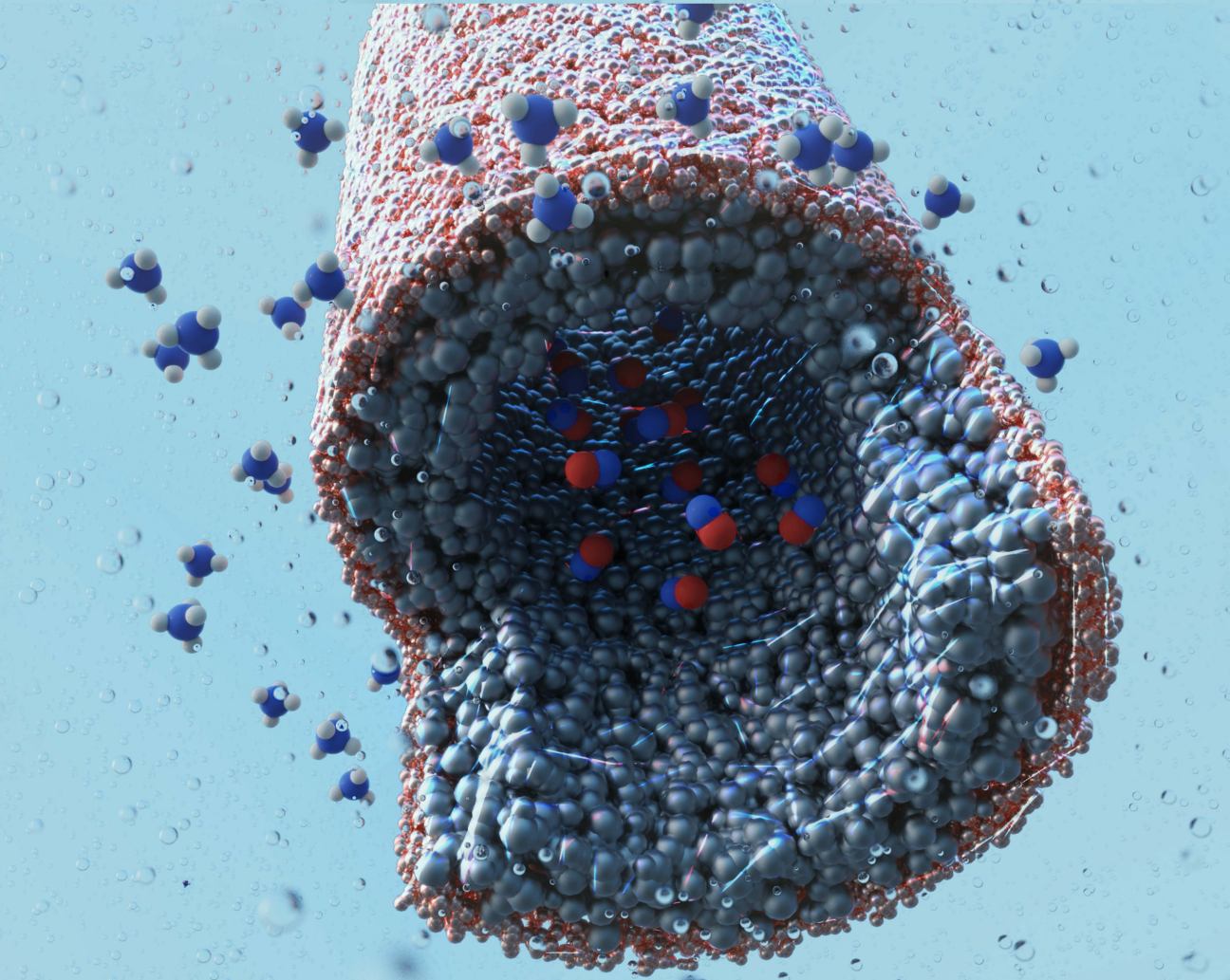

APPLICATION OF HOLLOW FIBER ELECTRODES FOR GREEN AMMONIA FORMATION

PIOTR KRZYWDA

APPLICATION OF HOLLOW FIBER ELECTRODES FOR GREEN AMMONIA FORMATION

Piotr Marek Krzywda

APPLICATION OF HOLLOW FIBER ELECTRODES FOR GREEN AMMONIA FORMATION

DISSERTATION

to obtain
the degree of doctor at the University of Twente,
on the authority of the rector magnificus,
prof. dr. ir. A. Veldkamp,
on account of the decision of the Doctorate Board,
to be publicly defended
on Friday the 13th of May 2022 at 16:45 hours

by

Piotr Marek Krzywda

born on the 28th of September 1992
in Tarnów, Poland

This dissertation has been approved by:

Supervisors

prof. dr. G. Mul

prof. dr. ir. N. E. Benes

The research described in this thesis was performed in a collaboration of the PhotoCatalytic Synthesis and Films in Fluids group, both part of the MESA+ Institute for Nanotechnology at the University of Twente. This work took place within the framework of the Institute of Sustainable Process Technology, co-funded with subsidy from the Topsector Energy by the Ministry of Economic Affairs and Climate Policy, The Netherlands.

Cover design: Representation of a hollow fiber electrode, based on P.M. Krzywda et al. "Cover Feature: Effect of Electrolyte and Electrode Configuration on Cu-Catalyzed Nitric Oxide Reduction to Ammonia (ChemElectroChem 5/2022)" with permission of John Wiley and Sons.
Printed by: Gildeprint
ISBN: 978-90-365-5377-3
DOI: 10.3990/1.9789036553773

Graduation Committee

Chairman/secretary

prof. dr. J. L. Herek	University of Twente

Supervisors

prof. dr. G. Mul	University of Twente
prof. dr. ir. N. E. Benes	University of Twente

Committee Members:

prof. dr. D. R. MacFarlane	Monash University
prof. dr. F. M. Mulder	Delft University of Technology
prof. dr. ir. A. Nijmeijer	University of Twente
prof. dr. S. R. A. Kersten	University of Twente
prof. dr. ir. L. Lefferts	University of Twente

Table of Contents

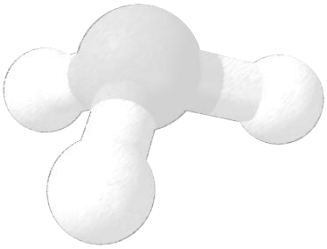

Chapter 1

General introduction

This chapter is partially based on:

K. H. R. Rouwenhorst, **P. M. Krzywda**, N. E. Benes, G. Mul, L. Lefferts, "Ammonia Production Technologies" in *Techno-Economic Challenges of Green Ammonia as an Energy Vector*, 41-83, **2021**.

K. H. R. Rouwenhorst, **P. M. Krzywda**, N. E. Benes, G. Mul, L. Lefferts "Ammonia, 4. Green ammonia production", *Ullmann's Encyclopedia of Industrial Chemistry*, **2020**.

Sustainability and climate change

What does sustainability mean? The human population should be in balance with everything that Earth gives, such as air, flora, fauna, and all other resources we use for making our life more comfortable in order to call the world sustainable. Therefore, sustainability means balance. Currently, we do not have that balance, which leads to many problems we have to face now and in the future.[1]

Due to the population growth and intensive industrial development, mainly powered by fossil fuels, a significant increase in greenhouse gases emission has occurred in the last century. It was estimated that ~10 % of the total world energy consumption is used by the chemical sector, which makes it the largest energy consumer among all industrial sectors. This has an enormous effect on our planet, continuously contributing to climate change.[2] Since the problem has become rather serious, especially in recent years, an agreement between the majority of the countries was made in which targets for limiting temperature rise were set.[3] As a result, these countries should aim to reduce emissions of greenhouse gases as soon as possible.

In order to make a change, the fossil fuel-based industry needs to transition towards renewable energy and abundant/recycled feedstocks. Electrochemistry is an emerging route that can enable that transition to happen, *via* various electrocatalytic approaches. Examples include water splitting to green hydrogen and oxygen, CO_2 reduction to fuels, CH_4 oxidation to methanol, N_2 reduction to ammonia and oxidation to nitrate. Such electrochemistry can be integrated in one system, combining for example C-N coupling on the cathode with H_2O_2 synthesis on the anode. Many other cathode/anode combinations can be the core of this transition.[2] Among all possibilities, the electrosynthesis of ammonia can play a significant role to mitigate CO_2 emissions, which will be discussed and addressed further in this thesis.

Ammonia

The nitrogen cycle is within the most important biogeochemical cycles on Earth due to nitrogen being the key element for all forms of life in the form of nucleic acids, amino acids, vitamins, and hormones. Although N_2 is widely available in the atmosphere, it cannot be easily used due to its high stability. Therefore nitrogen needs to be activated to become more accessible to consecutive chemical processes, and usually, nitrogen is activated to form ammonia. In nature, microorganisms containing enzyme nitrogenase can do that, which results in 120 million tons of fixed nitrogen becoming available to the biosphere.[4] However, natural fixation does not meet the demand for nitrogen in our developing world.

Therefore, artificial fixation via the Haber-Bosch process is necessary to produce enough ammonia to sustain the needs of humanity.[5] That makes ammonia one of the most important inorganic chemicals worldwide, being the starting material of all the N-based chemical compounds in the world.

Ammonia application

Many possible applications of ammonia exist. On a relatively small scale, ammonia is used as a feedstock for explosives, pharmaceuticals, refrigerants, dyes, cleaning agents, textiles, polyamides, polyimides, and other industrial chemicals.[6] However, the biggest market is the fertilizer industry where ~80 % out of 175 million tons of ammonia produced globally, is used (Figure 1.1).[7] In 2008 nitrogen fertilizers were responsible for feeding ~ 48% of the human population[8] and it is only expected to grow further.[7]

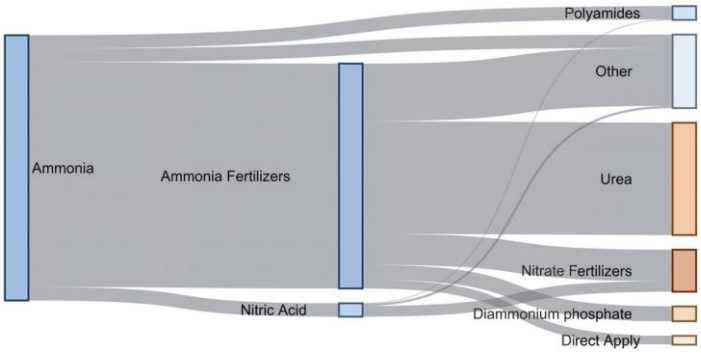

Figure 1.1. Schematic representation of ammonia mass flow to different applications. Adapted with modification from [7].

Two main types of nitrogen-based fertilizers exist, urea and nitrates with the first one being the most important due to its high nitrogen content (Figure 1.1). Urea needs to be decomposed into ammonium before it can be used by plants. Urea is produced thermally from NH_3 and CO_2 with ~155 million tons per year.[9] The production plants are usually combined with the Haber-Bosch process for ammonia synthesis, which results in a relatively low cost of urea. Recently, there is interest in electrochemical urea synthesis by simultaneous reduction of CO_2 and NO_x using renewable energy, in order to decrease carbon footprint.[10] However not much is known about this approach so far.

Nitrates, usually in the form of ammonium nitrate are the second most used nitrogen fertilizers. Their preparation is based on the Ostwald process where ammonia is oxidized over Pt-Ru based catalyst at almost 1000 °C producing NO, which is further converted to nitric acid. Since nitrates are soluble in soil water, they are transported together with water

into the plant root, making it rapidly available, unlike ammonium which is fixed onto clay minerals, and thus immobile.[11] Since ammonium nitrate is a carbon-free fertilizer, it is considered to play a bigger role in the future than carbon-based urea.

Recently, ammonia is also considered as a possible energy carrier.[12] It contains 17.6 wt.% hydrogen which in combination with easier storage compared to H_2, can work as carbon-free hydrogen storage.[13] Additionally, it was proposed to use NH_3 as fuel in combustion engines where only water and nitrogen can be formed as end products.[14] Also, the use of ammonia in fuel cells for electricity generation was proposed.[15]

Ammonia production on an industrial scale

Currently, industrial ammonia synthesis is based on the Haber-Bosch process. The possibility of ammonia formation from N_2 and H_2 was demonstrated by Fritsch Haber in 1908 and the idea was transformed into an industrial process by Carl Bosch. In 1913, the first plant was launched by BASF in Germany with a capacity of 30 ton/day of NH_3.[16]

$$3H_2 + N_2 \leftrightharpoons 2NH_3 \quad \Delta H^0 = -92.4\ kJ\ mol^{-1} \qquad (1.1)$$

The reaction (1.1) requires relatively harsh conditions to achieve sufficient performance. A high temperature is required to break the very stable N≡N bond which allows for nitrogen dissociation. This step is considered the rate-determining step in ammonia synthesis. However, since the reaction is exothermic, a high temperature favors ammonia decomposition (based on Le Chatelier's principle). For this reason, high pressure is applied which allows to shift the reaction equilibrium towards ammonia. The operational temperature and pressure depend on the catalyst used but typically are in the range of 350 to 550 °C and 100 to 300 bar.[17]

The energy of binding nitrogen to the catalyst surface determines its activity for ammonia synthesis. A high binding strength/energy will promote nitrogen dissociation but will limit ammonia desorption after the reaction. On the other hand, when the metal binds nitrogen too weakly, limitations in N_2 dissociation can occur which will result in low activity. Based on the volcano plot, metals with intermediate binding strength can be found.[18] The most common catalyst commercially used in the Haber-Bosch process is an iron-based catalyst with the addition of multiple promoters in the form of Al_2O_3, MgO, and SiO_2, which act as structural promoters as well as CaO and K_2O as electronic promoters.[19] Other, less common but still used on the industrial scale, is the ruthenium-based catalyst on a carbon support. Although Ru shows high activity, lower stability due to methanation of the carbon support with H_2 and the high price of Ru, limit the application of this catalyst.[17]

Hydrogen used for ammonia synthesis is produced mainly via the steam methane reforming process where CH_4 reacts with water to produce CO and H_2. The formed CO is oxidized further to CO_2 by air, which is also the source of N_2. Next, a water-gas shift reactor is used to maximize the conversion. After careful purification, H_2 and N_2 can be compressed and reacted into ammonia in a high-pressure reactor.[16]

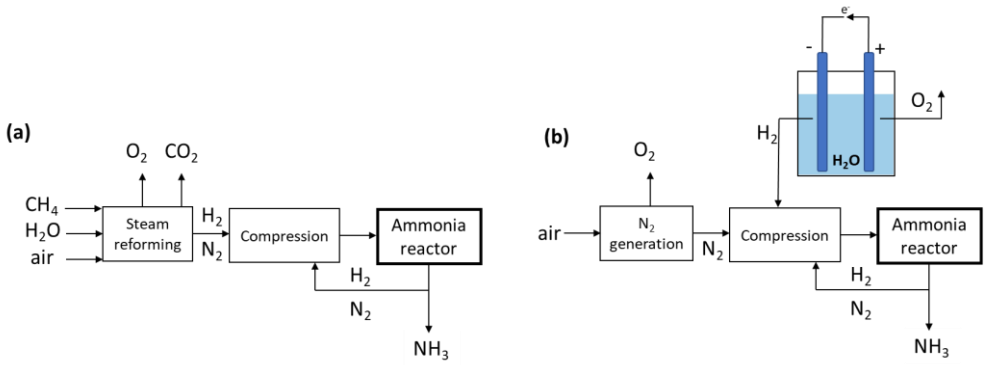

Figure 1.2. Simplified scheme of Haber-Bosch process with hydrogen form (a) steam methane reforming and (b) electrolysis.

Despite the amazing technology which enabled the growth of the human population,[8] the Haber-Bosch process is recently considered as one of the significant factors contributing to environmental pollution due to a large amount of CO_2 being released into the atmosphere (1.2 % of anthropogenic CO_2 emissions[20]) which does not go in line with current decarbonization goals.[21] However, this opinion is not fully deserved as the "heart" of the process (ammonia synthesis reactor, usually referred to as the Haber-Bosch process) can in principle operate with no carbon footprint.[20] The H_2 feedstock preparation is mainly responsible for CO_2 release. If the source of hydrogen could be changed, the entire process would become more environmentally friendly by decreasing the amount of CO_2 formed, and green ammonia could be produced. Hydrogen can come either from biomass or electrolysis. A comparison of methane- and electrolysis-based hydrogen production combined with the Haber-Bosch process is shown in Figure 1.2. Surprisingly, electrolysis-based hydrogen was used in ammonia synthesis up till the 1950s-1960, after which the low-cost natural gas became a game changer.[22] Currently, the cost of electrolysis-based hydrogen is still higher than fossil fuel-based, which hinders the transition in the industry. However, since renewable energy is becoming more available as well as continuous development in water electrolysis is observed, the future for electrolysis-based Haber-Bosch process exists.[20]

Nonconventional technologies for ammonia synthesis [23]

Even though green ammonia synthesis based on the Haber-Bosch process with H_2 provided from alternative sources is feasible, nonconventional alternatives are being investigated with a focus on enhancing the catalytic activity at relatively mild reaction conditions. The nonconventional technologies can potentially allow for scale-down operation in remote areas where the economic risks of the innovations are smaller as compared to conventional plants, and a faster pace of innovation may occur. Various nonconventional technologies are studied such as heterogeneous, homogeneous, and bio-catalysis, absorbent- and adsorbent-enhancement, non-thermal plasma, electro-, and photo-chemical synthesis as well as chemical looping.[24]

Heterogeneous catalysis aims to the development of new catalysts based on computational calculations. Most of the research focuses on improving ruthenium-based catalysts and replacing the carbon support with metal oxide[17]. Moreover, single metal atom catalysts are of interest which can allow for ammonia formation via an associative mechanism rather than dissociative, thus decreasing the amount of energy needed.[25] On the other hand, homogeneous catalysis is mainly used for understanding the ammonia synthesis by nitrogenase.[26] Absorbent- and adsorbent-enhanced Haber-Bosch is based on the traditional way of ammonia synthesis, however, the use of ammonia absorbents or adsorbents ensures significantly lower pressure for ammonia separation which can match the pressure of the hydrogen and nitrogen production units thus decreasing the energy consumption.[27]

The non-thermal plasma approach is based on ionized gas where hot electrons can activate the strong N≡N bond while the other species present in plasma are near ambient conditions. N_2 adsorption or NH_3 desorption can inhibit activity at low temperatures which can be overcome by a combination of plasma with a catalyst. Plasma can activate the nitrogen molecule via vibrational or electronic excitation[28] and further hydrogenation over the catalytic surface is relatively fast. That can allow for ammonia synthesis over late-transition metals where N_2 adsorption limitation under ambient conditions occurs. Another electron-driven approach is electrochemical synthesis where water can act as a proton source for hydrogenation of N_2 in ambient conditions. A more elaborate description of electrochemical ammonia synthesis is provided in the next chapter. Photochemical synthesis is based on a similar principle, with semiconductor instead of electrocatalyst. Absorbed light by the semiconductor produces charge carriers in form of electrons and holes which then migrate to the surface of the semiconductor, where redox reactions can take place. Water can be oxidized to O_2 and H^+ by surface holes, while N_2 can be reduced by electrons from the conduction band and hydrogenated by water-liberated H^+.[29]

Lastly, chemical looping approaches are studied. The main advantage is the possibility of independent control of nitrogen activation and ammonia formation which allows for optimizing the operating conditions of each step separately. Different variations exist such as hydrogen chemical looping, water chemical looping, and alkali or alkaline earth metal hydride chemical looping, as well as their combination with electrocatalysis.[30,31] The general idea is based on metal nitridation, subsequent reduction to ammonia, and metal regeneration. An interesting example of an electrochemically assisted chemical cycle is lithium-mediated ammonia synthesis. Electrodeposited metallic Li is exposed to an N_2 atmosphere at room temperature and atmospheric pressure to form Li_3N which is then treated with a proton source forming ammonia and Li^+, thereby closing the loop.[32] A continuous process was also reported where ethanol is used as a proton source. Due to the difference in reaction rates between Li-nitridation and ethanol reduction on Li ammonia formation is possible.[33]

All approaches presented above are attractive alternatives for green ammonia synthesis for different reasons, however, no commercial application exists yet. For now, research should focus on a better understanding of reaction mechanisms and materials development for the fundamental improvement of each approach. Research in this thesis focuses on electrochemical ammonia synthesis thus only this approach will be discussed further.

Electrochemical ammonia synthesis [23]

Due to the emergence of low-cost, renewable electricity, electrochemical conversions have recently gained considerable interest.[34] Electrochemical ammonia synthesis is widely researched,[35] inspired by biological nitrogen fixation, where proton-coupled electron transfer occurs under mild conditions in the enzyme nitrogenase.[36] Electrochemical ammonia synthesis has several potential advantages over the Haber-Bosch process,[37] such as the compact design of the reactor, due to the integration of hydrogen production from water and nitrogen reduction in a single process unit. Furthermore, the formation of gaseous hydrogen can be totally bypassed by using water oxidation as a counter reaction in an electrochemical cell, which delivers protons for the nitrogen reduction reaction (NRR). Most importantly, the electricity required to drive the reaction can be obtained from renewable sources, which creates pathways to fully CO_2-free NH_3 synthesis.

The general idea of NH_3 electrosynthesis via the nitrogen reduction reaction (NRR) involves oxidation of H_2 (Reaction 1.2) or H_2O (Reaction 1.3) on the anode, transport of protons through liquid or solid electrolytes, and electrons through the external circuit to the cathode, where they combine with N_2 forming NH_3 (Reaction 1.4).

$$3H_2 \rightarrow 6H^+ + 6e^- \quad (1.2)$$

$$3H_2O \rightarrow 6H^+ + 6e^- + \frac{3}{2}O_2 \quad (1.3)$$

$$N_2 + 6H^+ + 6e^- \rightarrow NH_3 \quad (1.4)$$

Various approaches can be distinguished based on the temperature of operation, namely high-temperature solid-state electrolyte reactors (400-750 °C), molten salt reactors, composite membrane reactors (100-500 °C), and liquid electrolyte reactors at low temperature (<100 °C).[38]

Research in this thesis focuses on electrochemical ammonia synthesis at ambient conditions in aqueous electrolytes, thus only this approach will be discussed further.

Electrochemical reduction of N_2 to NH_3 in ambient conditions [23]

Studies at room temperatures are performed with liquid electrolytes, which are usually aqueous-based,[37] while the use of ionic liquids [39] has also been reported. An advantage of aqueous-based electrolytes is that water can be used directly as the proton source.[37] Electrochemical ammonia synthesis in ambient conditions is very challenging. First of all, the inert nature of N_2 with high dissociation energy of 941 kJ mol^{-1} makes activation difficult. Another issue is the low nitrogen solubility in water, which results in the limited availability of N_2 near the electrode surface. Due to the significant overpotential required, the competing hydrogen evolution reaction is usually dominant over the mass transport limited N_2 reduction.[40]

The reaction mechanism for the electrochemical nitrogen reduction reaction is currently under investigation. Various alternatives have been proposed.[36] Due to the high activation barrier for breaking the triple N≡N bond, the dissociative pathway is not considered to play a role in ambient conditions. Thus, associative pathways with partial hydrogenation to N_2H_X species are more likely to occur at low temperatures, similar to that of nitrogenase [36]. Additionally, a Mars-van Krevelen (MvK) mechanism may occur in the case of metal nitride catalysts, in which N from the catalyst lattice is hydrogenated to ammonia, leaving an N vacancy on the surface, which can be regenerated with a nitrogen atom.[41] However, little experimental data is currently available to explain the mechanism in detail.

A wide variety of catalysts was tested experimentally, starting from noble metals such as Ag, Ag, Pd, Pt, Rh, and Ru, after which metal oxides based on Ce, Co, Fe, Mo, Mn, Nb, Ta, Ti and V, metal sulfides based on Co, Fe, and Mo, and metal carbides based on Mo were also studied. Another group of catalysts consists of transition metal nitride materials such as CrON, Mo_2N, and VN, for which the possibility of a Mars-Van Krevelen

mechanism is considered. The activity of organometallic complexes based on Al and Ti, and metal-free catalysts such as B, BN, P, and polymeric carbon nitride were also evaluated. Various reviews provide a more detailed description of low-temperature electrochemical ammonia synthesis systems.[37,42–45]

Despite many recent reports, low ammonia production rates of 10^{-12}-10^{-9} mol s^{-1} cm^{-2} with faradaic efficiencies below 10 % are generally reported at room temperature. Although various publications reported higher faradaic efficiencies, even up to 67.8 %,[46] the presented faradaic efficiencies are usually measured at low current densities (below -0.1 mA cm^{-2}) and low ammonia concentrations (<1 ppm). Thus, any ammonia contamination in the system used for catalyst evaluation causes a large error.[47]

Ammonia is a common impurity in the air,[48] it can easily dissolve in water and adsorb at a wide variety of surfaces, which makes it very difficult to eliminate from any set-up used for evaluation of the reduction of nitrogen to ammonia. This implies that researchers working on the nitrogen reduction reaction should pay extra attention to those contaminations. Ammonia can be found in gas tubes, glassware, gloves, nitrogen streams, and even human breath. Trace contaminations can appear at certain stages of the experiment, such as membrane pre-treatment, improper reactor cleaning, sample post-treatment, storage, and ammonia detection. Moreover, nitrogen-containing compounds present as contaminations in nitrogen streams, such as nitrates, nitrites (in the electrolyte), amines, and nitrogen oxides, can be converted electrochemically to ammonia.[47,49] Special attention should also be paid to catalyst and electrode preparation. Various catalyst precursors consist of nitrate salts, contain additives necessary to form a certain morphology, or alternatively HNO_3 is used for pH adjustments. Lastly, ammonia is sometimes used during catalyst preparation. All of those situations should be avoided as much as possible. For all those reasons, special attention should be paid to proper control experiments, to prove the origin of detected ammonia during an electrochemical experiment, and to avoid false-positive results.[47,50–52]

The problems with reliability in the evaluation of nitrogen electroreduction, including experimental data and additional discussion, are further elaborated on in more detail in the Supporting Information 1 at the end of this chapter.

Electrochemical reduction of NO_x to NH_3 in ambient conditions

Since the reduction of N_2 to NH_3 is not feasible presently and requires extensive, highly accurate screening of catalytic materials, NO_x can be considered as an alternative feed for the formation of green ammonia, which might be attractive from an economic and environmental point of view.[53,54] Electroreduction of NO_x is more facile and it can occur at significantly less negative potentials than the reduction of N_2, which can potentially increase the energy efficiency (Figure 1.3).[51] NO_x electroreduction has been studied for a long time, however, since NO_x is a contaminant,[55] the focus was mainly on improving selectivity towards nitrogen as the most environmentally friendly product of NO_x reduction.[56] Nevertheless, since energy input is required to form nitrogen from NO_x, which is then 'lost' into the atmosphere, changing the selectivity toward a useful product seems reasonable. Therefore, there is recent interest in selective ammonia formation from NO_x.[57]

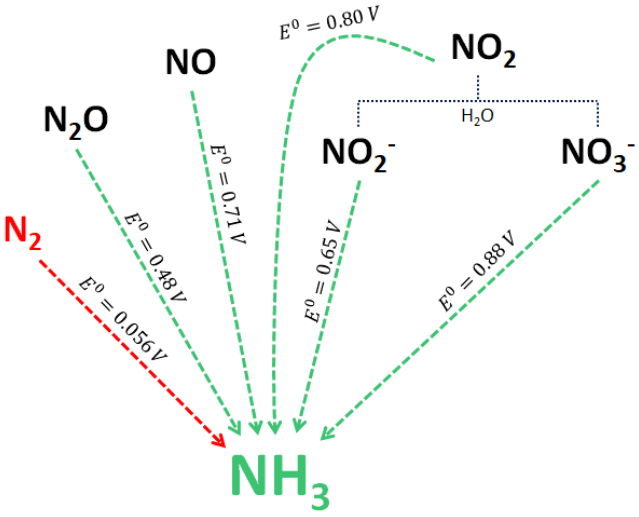

Figure 1.3. Different NOx as feedstock for ammonia electrosynthesis. Indicated standard reduction potentials are V vs RHE.

Several different NO_x representatives exist (Figure 1.3). Based on the abundancy and stability, nitrate is the most common source in the liquid phase (the highest oxidation state of nitrogen in NO_x) and nitric oxide is the most common representative form in the gas phase. Therefore, most studies are using either of those. Nitrate reduction is a complex reaction involving many proton and electron transfer steps which can lead to many possible products such as NO_2, NO_2^-, NO, N_2O, N_2, NH_2OH, N_2H_4, and NH_3 (Figure 1.4).[58] To

date, not much is known about materials and conditions for selective and efficient ammonia formation.

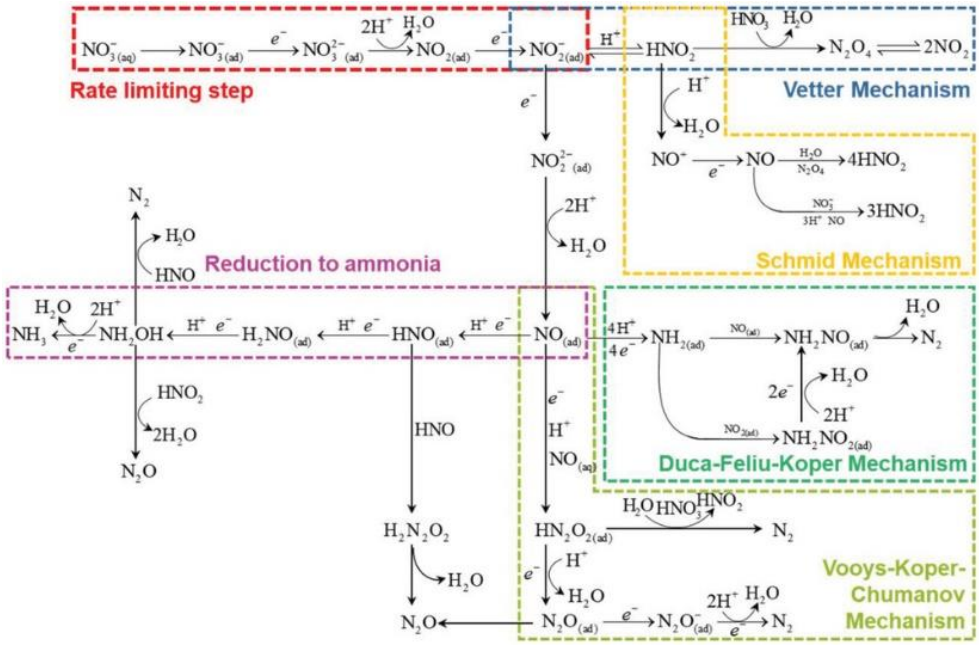

Figure 1.4. Suggested nitrate electroreduction mechanism with highlighted different pathways with possible chemical steps leading to different products.[59]

Different metals were studied as possible electrocatalysts in aqueous reduction of NO_3^-. Noble metals such as Ru[60], Ag[61], and Pd[62,63] were reported to produce ammonia, however, their high price can limit their practical application. Ni[64] and Cu[65] based catalysts as well as bimetallic surfaces[66–68] were also reported. Fe[69,70] and Ti[54,71] based catalysts are especially interesting due to their abundancy, which can facilitate industrial applications.[72] Not much is known about gaseous NO electroreduction to ammonia. Studies on Bi, Au/C[49], NiO[73], Ag[74] and Cu[75] exist, out of which the latter is the most promising metal, as confirmed by both theoretical and experimental investigations.

One of the major problems in NO_x electroreduction is mass transport limitations. Insufficient availability of the reactant close to the reactive site results in preferential hydrogen evolution, and thus the overall activity decreases. The concentration of NO_3^- as well as the overall convection in the cell, will have a significant effect on the conversion rates. This can be an issue especially when gaseous NO_x resources are targeted, due to the low solubility in aqueous electrolytes (especially nitric oxide). For these reasons, new approaches for minimizing mass transport limitations in an electrochemical cell are desired.

Hollow fiber electrodes

Planar electrodes, commonly used in electrochemical reactors (Figure 1.5a) often suffer from poor mass transport due to low solubility of gases in aqueous electrolytes and limited reactant supply.[76] Gas diffusion electrodes (GDEs) are an interesting alternative when gas reactants are used. It allows for an improved supply of gas by diffusion through the porous layer of the electrode towards the active site, where a three-phase boundary layer exists and high current densities can be achieved (Figure 1.5b).[77] However, one of the biggest drawbacks of GDEs is the low long-term stability due to salt precipitation in the pores and loss of hydrophobicity, causing flooding which results in preferential hydrogen formation.[78]

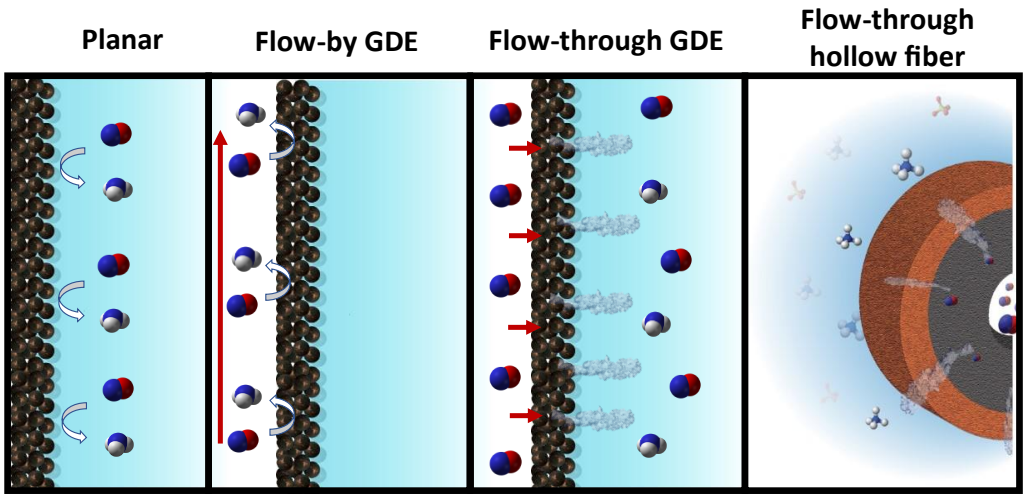

Figure 1.5. Comparison of gas supply methods to the electrode surface on the example of NO conversion to NH_3.

A new approach of GDEs operation is emerging in which flow-through is applied (Figure 1.5c). The field is rather unexplored but the concept was presented. Gas is forced to flow through the electrode not allowing electrolyte to penetrate too deep into the electrode pores, and thus flooding can be prevented.[79,80] However, drawbacks of GDEs are the fact that carbon is used as a substrate, as well as the necessity of a binder to anchor the catalyst. This limits the number of available active sites and can influence catalytic activity.[81] GDEs made entirely from metal could improve the performance but flat, porous metal sheets were not reported as flow-through electrodes so far. The low mechanical strength of thin metal foams can limit practical applications and induce problems with scalability. Alternatively, a tubular geometry in the form of a hollow fiber can help to solve these problems (Figure 1.5d). Hollow fiber technology is widely known in membrane science and

thus their fabrication methods are well established.[82] Although polymeric hollow fibers are mostly produced, which are typically non-conductive and not of interest for electrochemical applications, inorganic fibers based on Al_2O_3, SiC, stainless steel, Ni or Ti have been also developed,[83,84] with the primary goal to induce membrane separations in harsh conditions.

Recently, the use of metallic hollow fibers was proposed for electrochemical applications.[85] Reports on hollow fiber electrodes focus almost exclusively on CO_2 electroreduction. The concept was first demonstrated for Cu-oxide-derived Cu hollow fibers, showing efficient conversion of CO_2 to CO, which results in a big improvement in the CO formation rate in comparison to state-of-the-art nanocrystalline copper electrodes.[85] The preparation method of Cu fibers can affect their performance leaving a lot of room for improvement.[86,87] The formation of CO was further investigated on Au and Ni coated Cu,[88] SnO_2 coated carbon,[89] and Bi-based zeolite coated Ni[90] hollow fibers.

It was suggested that the pore structure of the hollow fiber can play a crucial role in the reaction selectivity, and the formation of formate with a high current density was achieved.[91] The presence of Cu(100) and Cu(110) was also shown to provide good selectivity toward formate on Cu hollow fibers.[92] Further modification of Cu hollow fibers with an optimized ratio of SnO_x[93–95] or addition of Bi,[96] promotes the effective formation of formate. C-C coupling into acetone and acetaldehyde on SnO_2 coated Cu,[97] as well as electrosynthesis of CH_4 on Ni hollow fiber[98] were also reported. One exception from CO_2 electroreduction on hollow fiber electrodes is nitrogen reduction. A Ru coated carbon nanotube-based hollow fiber was used for electrochemical conversion of nitrogen to ammonia in order to facilitate the transport of N_2 to the electrode surface, however, low performance was achieved.[99] Despite that, the applicability of hollow fiber electrode geometry for other reactions than described above is not reported in the literature. Since many systems suffer from poor mass transport conditions, the great potential of this type of electrode geometry exists and can open up new possibilities to improve commonly known electrochemical reactions.

In summary, hollow fiber electrodes provide a promising geometry that can help to facilitate mass transport in an electrochemical cell. Lack of flooding in contrast to GDEs can increase the stability. Moreover, the possibility of fiber preparation entirely from the desired metal or their coating with catalyst, without the need of a binder, can provide an increase in the amount of the active sites. Lastly, the production of hollow fibers can be compatible with existing large-scale manufacturing facilities, which makes it promising for possible scale-up when desired.

Decentralized fertilizer production concept

Industrial ammonia synthesis plants are operating efficiently on a big scale. Small possible improvements are being investigated, however, bigger changes are causing difficulties because of the lack of flexibility in big-scale plants.[100] Small scale plants (3-60 t_{NH3}/day compared to 3300 t_{NH3}/day in the traditional plant)[22] would be more flexible for changes thus innovation can become possible faster. That kind of plants can be coupled with renewable energy systems. Produced ammonia can be used by local farmers which eliminates the need for transport and large storage. To make this idea feasible, the process needs to run at milder temperatures and pressures compared to Haber-Bosch to compensate for the capital costs which will be higher per ammonia produced. Therefore, non-conventional technologies should be considered for small-scale production plants.

In this thesis, the focus is on electrochemical ammonia synthesis for fertilizer applications. Although N_2 as a feed for decentralized ammonia synthesis plants is the most attractive due to its abundancy, its direct reduction using non-conventional technologies is an unsolved scientific challenge at the current stage, as discussed in previous sections. Electroreduction of NO_x is more facile and it can occur at significantly less negative potentials than the reduction of N_2 which can potentially increase energy efficiency.[51] The disadvantage is that NO_x are not an abundant source. Currently, NO_3^- is produced on an industrial scale in the form of nitric acid via the Ostwald process by oxidation of NH_3.[7] Therefore, other sources of NO_x need to be available to make this process valuable.

Currently, oxidation of molecular nitrogen to NO_x is becoming a topic of interest which could become the required source of NO_x. Electrochemical N_2 oxidation is investigated by numerical as well as experimental methods. Although promising results were achieved on Ru/TiO_2,[101] Pd,[102] or ZnFeCo-based spinel oxides,[103] oxygen evolution reaction is highly competing limiting the performance toward nitrate. More fundamental understanding, as well as new materials, are needed to overcome this issue and run this process efficiently.[104] Another approach, more feasible in the coming future is the oxidation of nitrogen with plasma technology. A number of promising experimental systems were developed.[105–109] Recently, it was reported that plasma is potentially viable for electricity-based HNO_3 production.[110] Even preliminary systems where N_2 oxidation with subsequent reduction to ammonia in one process occurs were reported.[111,112] Therefore, plasma oxidation of N_2 is a promising method for NO_3^- feed preparation.

Nitrates are commonly present in waste streams from the nuclear or metal finishing industry[54] which after purification, could act as an additional source for ammonia formation, minimizing overall waste. Besides nitrate, gaseous nitrogen oxides could also be

used as a feed for ammonia electrosynthesis. Gaseous nitrogen oxides are formed in many combustion processes at high temperatures in presence of nitrogen and oxygen.[55] After careful purification, an additional source of nitrogen can be available and conversion of waste to useful products can be possible.

As prepared feed can be used in an electrochemical reactor with an aqueous-based electrolyte. With the use of renewable electricity, partial conversion of NO_x to ammonia can take place. This will result in ammonium nitrate formation which is one of the most important N-based fertilizers. The schematic representation of the small-scale ammonia synthesis plant based on NO_x conversion to ammonia fertilizers is shown in Figure 1.6.

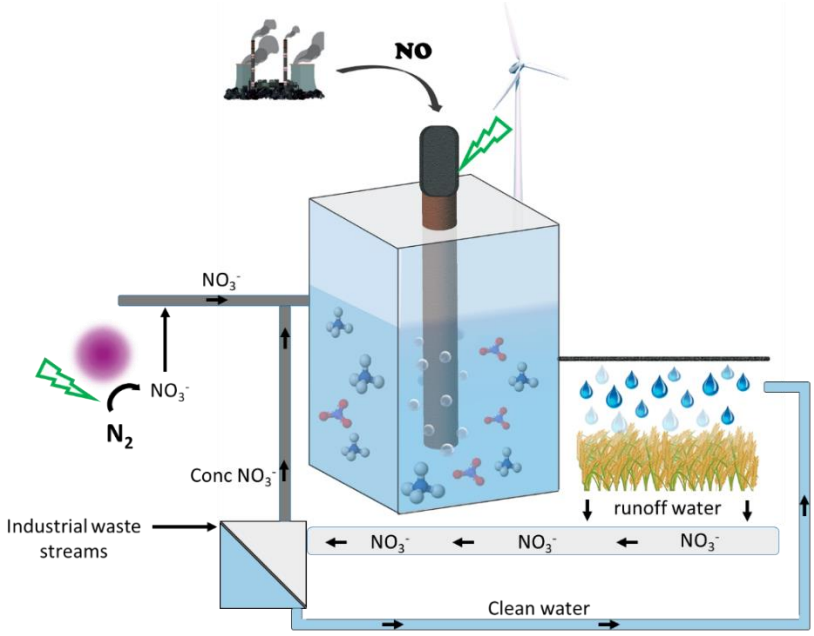

Figure 1.6. The concept of a decentralized, small-scale green ammonia production plant for fertilizer application. Adapted with modification from [113].

Nitrate-based fertilizers are known to leach into the groundwater.[114,115] Once NO_3^- moves below the root zone of the plants, is considered lost and cannot be the N-source for the crops anymore. In combination with overfertilization, it results in a significant loss of N-nutrients thus extremely low nitrogen-use efficiency.[8] For example, in 1960 the global N-use efficiency of cereals was ~80 % which decreased to ~30 % in 2000 as a result of increased demand for food.[8] Collected and possibly concentrated runoff water from the fields could be recycled back to the electrolyzer where further conversion to ammonia would be possible. Therefore, a fertilizer loop [54,116,117] with the support of NO_x from waste streams and produced from oxidized N_2 is possible.

Scope and outline of this thesis

The research described in this thesis focuses on the electrochemical formation of green ammonia in ambient conditions. Since N_2 reduction suffers from the extremely low activity and reliability, NO_x are proposed as an alternative feed. Instead of removing NO_x to harmless N_2, a useful product can be made. Since NO_x electroreduction in aqueous electrolytes suffers from mass transport limitations, a new type of electrode geometry was developed and tested for reduction of NO_3^- from liquid-, and NO from gas-phase to ammonia which can be applied as green fertilizer. Additionally, the possibility of electrochemical urea formation was investigated which could be used together with ammonium nitrate as green fertilizer.

The general introduction to the thesis is given in **Chapter 1**. The importance of ammonia, its typical applications, and the industrial synthesis method are highlighted. Then, non-conventional approaches of ammonia production with a focus on electrochemical methods using N_2 or NO_x as feedstock are discussed. Finally, the concept of decentralized, small-scale green ammonia synthesis plants for fertilizer applications is presented.

In **Chapter 2** the preparation of Ti-based hollow fibers via dry-wet spinning has been investigated. Titanium was chosen as desired material due to its high stability, low cost, and high overpotential for hydrogen evolution reaction which is desirable in cathodic reactions. Carefully designed, two-step thermal decomposition of the polymer involved in the spinning process, leads to the formation of entirely metallic titanium hollow fiber. Moreover, the possibility of composites formation in the form of Ti/TiC and Ti/TiN by altering the thermal treatment conditions is shown. Detailed characterization of prepared hollow fibers reveals their porous structure and low resistivity making them suitable for electrochemical applications.

In **Chapter 3** the activity of previously synthesized Ti hollow fibers has been tested for electroreduction of nitrate to ammonia. Efficient mixing of the electrolyte was observed by inert gas bubbles coming from the inside of the porous electrode wall which results in significantly improved mass transport of the reactants from the bulk electrolyte to the electrode surface. The target application is a partial transformation of nitrate to ammonium which results in ammonium nitrate formation in an aqueous electrolyte and can be applied as green fertilizer.

In **Chapter 4**, Ti hollow fibers were modified with a Cu layer in order to enhance the ammonia formation from NO_x. This time, nitric oxide (NO) as a gaseous representative of NO_x with low solubility in aqueous solutions was chosen as a feed for ammonia synthesis. The reactant was supplied from the inside of the porous wall of the hollow fiber electrode

which results in the creation of a three-phase boundary with an effective supply of NO greatly enhancing its conversion to green ammonia.

In **Chapter 5**, the possibility of urea formation in the simultaneous electroreduction of CO_2 and NO_3^- on polycrystalline, rough Cu surfaces was studied. Surface-Enhanced Raman Spectroscopy and Electrochemical Mass Spectrometry were used in order to determine adsorbed species that could potentially lead to urea formation. Insight into this complex system provides information about carbon-nitrogen coupling reactions, and the impact on possible routes for urea electrosynthesis is discussed.

Finally, **Chapter 6** summarizes the research in this thesis and provides a perspective on the future of this subject.

References

[1] P. J. A. Kenis, *Electrochem. Soc. Interface* **2020**, *29*, 41–42.

[2] C. Tang, Y. Zheng, M. Jaroniec, S. Z. Qiao, *Angew. Chemie - Int. Ed.* **2021**, 2–21.

[3] J. Foran, *Nation* **2016**, *302*.

[4] N. Lehnert, H. T. Dong, J. B. Harland, A. P. Hunt, C. J. White, *Nat. Rev. Chem.* **2018**, *2*, 278–289.

[5] M. Nazemi, M. A. El-Sayed, *Acc. Chem. Res.* **2021**, DOI 10.1021/acs.accounts.1c00446.

[6] S. Ghavam, M. Vahdati, I. A. G. Wilson, P. Styring, *Front. Energy Res.* **2021**, *9*, 1–19.

[7] J. Lim, C. A. Fernández, S. W. Lee, M. C. Hatzell, *ACS Energy Lett.* **2021**, 3676–3685.

[8] J. W. Erisman, M. A. Sutton, J. Galloway, Z. Klimont, W. Winiwarter, *Nat. Geosci.* **2008**, *1*, 636–639.

[9] M. Aresta, A. Dibenedetto, A. Angelini, *Chem. Rev.* **2014**, *114*, 1709–1742.

[10] C. Lv, L. Zhong, H. Liu, Z. Fang, C. Yan, M. Chen, Y. Kong, C. Lee, D. Liu, S. Li, J. Liu, L. Song, G. Chen, Q. Yan, G. Yu, *Nat. Sustain.* **2021**, DOI 10.1038/s41893-021-00741-3.

[11] Yara, *Yara Fertil. Ind. Handb.* **2018**.

[12] J. Guo, P. Chen, *Chem* **2017**, *3*, 709–712.

[13] A. Valera-Medina, H. Xiao, M. Owen-Jones, W. I. F. David, P. J. Bowen, *Prog. Energy Combust. Sci.* **2018**, *69*, 63–102.

[14] O. Elishav, B. Mosevitzky Lis, E. M. Miller, D. J. Arent, A. Valera-Medina, A. Grinberg Dana, G. E. Shter, G. S. Grader, *Chem. Rev.* **2020**, *120*, 5352–5436.

[15] M. Zhang, P. Zou, G. Jeerh, S. Chen, J. Shields, H. Wang, S. Tao, *ACS Sustain. Chem. Eng.* **2020**, *8*, 12817–12824.

[16] M. Appl, *Ullmann's Emcyclopedia Ind. Chem.* **2012**, DOI 10.1002/14356007.o02.

[17] H. Liu, *Chinese J. Catal.* **2014**, *35*, 1619–1640.

[18] C. J. H. Jacobsen, S. Dahl, B. G. S. Clausen, S. Bahn, A. Logadottir, J. K. Nørskov, *J. Am. Chem. Soc.* **2001**, *123*, 8404–8405.

[19] H. Liu, W. Han, *Catal. Today* **2017**, *297*, 276–291.

[20] C. Smith, A. K. Hill, L. Torrente-Murciano, *Energy Environ. Sci.* **2020**, *13*, 331–344.

[21] E. Papadis, G. Tsatsaronis, *Energy* **2020**, *205*, 118025.

[22] K. H. R. Rouwenhorst, Y. Engelmann, K. Van 'T Veer, R. S. Postma, A. Bogaerts, L. Lefferts, *Green Chem.* **2020**, *22*, 6258–6287.

[23] K. H. R. Rouwenhorst, P. M. Krzywda, N. E. Benes, G. Mul, L. Lefferts, in *Techno-Economic Challenges Green Ammon. as an Energy Vector*, **2020**, pp. 41–83.

[24] J. G. Chen, R. M. Crooks, L. C. Seefeldt, K. L. Bren, R. Morris Bullock, M. Y. Darensbourg, P. L. Holland, B. Hoffman, M. J. Janik, A. K. Jones, M. G. Kanatzidis, P. King, K. M. Lancaster, S. V. Lymar, P. Pfromm, W. F. Schneider, R. R. Schrock, *Science (80-.).* **2018**, *360*, DOI 10.1126/science.aar6611.

[25] E. Skúlason, T. Bligaard, S. Gudmundsdóttir, F. Studt, J. Rossmeisl, F. Abild-Pedersen, T. Vegge, H. Jónsson, J. K. Nørskov, *Phys. Chem. Chem. Phys.* **2012**, *14*, 1235–1245.

[26] I. Dance, *Dalt. Trans.* **2010**, *39*, 2972–2983.

[27] K. H. R. Rouwenhorst, A. G. J. Van der Ham, G. Mul, S. R. A. Kersten, *Renew. Sustain. Energy Rev.* **2019**, *114*, DOI 10.1016/j.rser.2019.109339.

[28] P. Mehta, P. Barboun, F. A. Herrera, J. Kim, P. Rumbach, D. B. Go, J. C. Hicks, W. F. Schneider, *Nat. Catal.* **2018**, *1*, 269–275.

[29] S. Zhang, Y. Zhao, R. Shi, G. I. N. Waterhouse, T. Zhang, *EnergyChem* **2019**, *1*, 100013.

[30] W. Gao, J. Guo, P. Wang, Q. Wang, F. Chang, Q. Pei, W. Zhang, L. Liu, P. Chen, *Nat. Energy* **2018**, *3*, 1067–1075.

[31] J. M. McEnaney, A. R. Singh, J. A. Schwalbe, J. Kibsgaard, J. C. Lin, M. Cargnello, T. F. Jaramillo, J. K. Nørskov, *Energy Environ. Sci.* **2017**, *10*, 1621–1630.

[32] K. Kim, Y. Chen, J.-I. Han, H. C. Yoon, W. Li, *Green Chem.* **2019**, *21*, 3839–3845.

[33] N. Lazouski, Z. J. Schiffer, K. Williams, K. Manthiram, *Joule* **2019**, *3*, 1127–1139.

[34] Z. J. Schiffer, K. Manthiram, *Joule* **2017**, *1*, 10–14.

[35] V. Kyriakou, I. Garagounis, E. Vasileiou, A. Vourros, M. Stoukides, *Catal. Today* **2017**, *286*, 2–13.

[36] C. J. M. van der Ham, M. T. M. Koper, D. G. H. Hetterscheid, *Chem. Soc. Rev.* **2014**, *43*, 5183–5191.

[37] X. Cui, C. Tang, Q. Zhang, *Adv. Energy Mater.* **2018**, *8*, 1800369.

[38] S. Giddey, S. P. S. Badwal, A. Kulkarni, *Int. J. Hydrogen Energy* **2013**, *38*, 14576–14594.

[39] F. Zhou, L. M. Azofra, M. Al-Agele, M. Kar, A. N. Simonov, C. J. McDonnell-Worth, C. Sun, xinyi zhang, D. MacFarlane, *Energy Environ. Sci.* **2017**, *10*, 2516–2520.

[40] J. H. Montoya, C. Tsai, A. Vojvodic, J. K. Nørskov, *ChemSusChem* **2015**, *8*, 2180–2186.

[41] Y. Abghoui, A. L. Garden, J. G. Howalt, T. Vegge, E. Skúlason, *ACS Catal.* **2016**, *6*, 635–646.

[42] I. J. McPherson, T. Sudmeier, J. Fellowes, S. C. E. Tsang, *Dalt. Trans.* **2019**, *48*, 1562–1568.

[43] C. Guo, J. Ran, A. Vasileff, S. Qiao, *Energy Environ. Sci.* **2017**, 45–56.

[44] G. Chen, S. Ren, L. Zhang, H. Cheng, Y. Luo, K. Zhu, L. Ding, H. Wang, *Small Methods* **2019**, *3*, 1800337.

[45] S. Zhao, X. Lu, L. Wang, J. Gale, R. Amal, *Adv. Mater.* **2019**, *31*, 1–9.

[46] Z.-H. Xue, S.-N. Zhang, Y.-X. Lin, H. Su, G.-Y. Zhai, J.-T. Han, Q.-Y. Yu, X.-H. Li, M. Antonietti, J.-S. Chen, *J. Am. Chem. Soc.* **2019**, *0*, null-null.

[47] S. Z. Andersen, V. Čolić, S. Yang, J. A. Schwalbe, A. C. Nielander, J. M. McEnaney, K. Enemark-Rasmussen, J. G. Baker, A. R. Singh, B. A. Rohr, M. J. Statt, S. J. Blair, S. Mezzavilla, J. Kibsgaard, P. C. K. Vesborg, M. Cargnello, S. F. Bent, T. F. Jaramillo, I. E. L. Stephens, J. K. Nørskov, I. Chorkendorff, *Nature* **2019**, *570*, 504–508.

[48] T. Butler, F. Vermeylen, C. M. Lehmann, G. E. Likens, M. Puchalski, *Atmos. Environ.* **2016**, *146*, 132–140.

[49] J. Choi, J. Choi, H. L. Du, H. L. Du, C. K. Nguyen, C. K. Nguyen, B. H. R. Suryanto, A. N. Simonov, A. N. Simonov, D. R. MacFarlane, D. R. MacFarlane, *ACS Energy Lett.* **2020**, *5*, 2095–2097.

[50] L. Li, C. Tang, D. Yao, Y. Zheng, S.-Z. Qiao, *ACS Energy Lett.* **2019**, *4*, 2111–2116.

[51] J. Choi, B. H. R. Suryanto, D. Wang, H. Du, R. Y. Hodgetts, F. M. F. Vallana, D. R. Macfarlane, A. N. Simonov, *Nat. Commun.* **2020**, *11*, 1–10.

[52] B. H. R. Suryanto, H. L. Du, D. Wang, J. Chen, A. N. Simonov, D. R. MacFarlane, *Nat. Catal.* **2019**, *2*, 290–296.

[53] R. Daiyan, T. Tran-Phu, P. Kumar, K. Iputera, Z. Tong, J. Leverett, M. H. A. Khan, A. A. Esmailpour, A. Jalili, M. Lim, A. Tricoli, R.-S. Liu, X. Lu, E. Lovell, R. Amal, *Energy Environ. Sci.* **2021**, *14*, 3588–3598.

[54] J. M. McEnaney, S. J. Blair, A. C. Nielander, J. A. Schwalbe, D. M. Koshy, M. Cargnello, T. F. Jaramillo, *ACS Sustain. Chem. Eng.* **2020**, *8*, 2672–2681.

[55] S. Roy, M. S. Hegde, G. Madras, *Appl. Energy* **2009**, *86*, 2283–2297.

[56] I. Katsounaros, D. Ipsakis, C. Polatides, G. Kyriacou, *Electrochim. Acta* **2006**, *52*, 1329–1338.

[57] X. Lu, H. Song, J. Cai, S. Lu, *Electrochem. commun.* **2021**, *129*, 107094.

[58] Y. Wang, C. Wang, M. Li, Y. Yu, B. Zhang, *Chem. Soc. Rev.* **2021**, *50*, 6720–6733.

[59] Y. Zeng, C. Priest, G. Wang, G. Wu, *Small Methods* **2020**, *4*, 1–28.

[60] J. Li, G. Zhan, J. Yang, F. Quan, C. Mao, Y. Liu, B. Wang, F. Lei, L. Li, A. W. M. Chan, L. Xu, Y. Shi, Y. Du, W. Hao, P. K. Wong, J. Wang, S. X. Dou, L. Zhang, J. C. Yu, *J. Am. Chem. Soc.* **2020**, *142*, 7036–7046.

[61] H. Liu, J. Park, Y. Chen, Y. Qiu, Y. Cheng, K. Srivastava, S. Gu, B. H. Shanks, L. T. Roling, W. Li, *ACS Catal.* **2021**, *11*, 8431–8442.

[62] J. Lim, C. Y. Liu, J. Park, Y. H. Liu, T. P. Senftle, S. W. Lee, M. C. Hatzell, *ACS Catal.* **2021**, *11*, 7568–7577.

[63] Y. Han, X. Zhang, W. Cai, H. Zhao, Y. Zhang, Y. Sun, Z. Hu, S. Li, J. Lai, L. Wang, *J. Colloid Interface Sci.* **2021**, *600*, 620–628.

[64] P. Gao, Z. H. Xue, S. N. Zhang, D. Xu, G. Y. Zhai, Q. Y. Li, J. S. Chen, X. H. Li, *Angew. Chemie - Int. Ed.* **2021**, *60*, 20711–20716.

[65] X. Fu, X. Zhao, X. Hu, K. He, Y. Yu, T. Li, Q. Tu, X. Qian, Q. Yue, M. R. Wasielewski, Y. Kang, *Appl. Mater. Today* **2020**, *19*, 100620.

[66] Y. Wang, A. Xu, Z. Wang, L. Huang, J. Li, F. Li, J. Wicks, M. Luo, D. H. Nam, C. S. Tan, Y. Ding, J. Wu, Y. Lum, C. T. Dinh, D. Sinton, G. Zheng, E. H. Sargent, *J. Am. Chem. Soc.* **2020**, *142*, 5702–5708.

[67] T. Gu, W. Teng, N. Bai, Z. Chen, J. Fan, W. X. Zhang, D. Zhao, *J. Mater. Chem. A* **2020**, *8*, 9545–9553.

[68] C. Wang, Z. Liu, T. Hu, J. Li, L. Dong, F. Du, C. Li, C. Guo, *ChemSusChem* **2021**, *14*, 1825–1829.

[69] P. Li, Z. Jin, Z. Fang, G. Yu, *Energy Environ. Sci.* **2021**, DOI 10.1039/d1ee00545f.

[70] Z. Y. Wu, M. Karamad, X. Yong, Q. Huang, D. A. Cullen, P. Zhu, C. Xia, Q. Xiao, M. Shakouri, F. Y. Chen, J. Y. (Timothy) Kim, Y. Xia, K. Heck, Y. Hu, M. S. Wong, Q. Li, I. Gates, S. Siahrostami, H. Wang, *Nat. Commun.* **2021**, *12*, 1–10.

[71] R. Jia, Y. Wang, C. Wang, Y. Ling, Y. Yu, B. Zhang, *ACS Catal.* **2020**, *10*, 3533–3540.

[72] A. S. Fajardo, P. Westerhoff, C. M. Sanchez-Sanchez, S. Garcia-Segura, *Appl. Catal. B Environ.* **2021**, *281*, 119465.

[73] P. Liu, J. Liang, J. Wang, L. Zhang, J. Li, **2021**, 2–5.

[74] D. Y. Kim, D. Shin, J. Heo, H. Lim, J. A. Lim, H. M. Jeong, B. S. Kim, I. Heo, I. Oh, B. Lee, M. Sharma, H. Lim, H. Kim, Y. Kwon, *ACS Energy Lett.* **2020**, *5*, 3647–3656.

[75] J. Long, S. Chen, Y. Zhang, C. Guo, X. Fu, D. Deng, J. Xiao, *Angew. Chemie Int. Ed.* **2020**, *59*, 9711–9718.

[76] K. J. P. Schouten, *Nat. Energy* **2021**, *6*, 335–336.

[77] H. Rabiee, L. Ge, X. Zhang, S. Hu, M. Li, Z. Yuan, *Energy Environ. Sci.* **2021**, *14*, 1959–2008.

[78] K. Yang, R. Kas, W. A. Smith, T. Burdyny, *ACS Energy Lett.* **2021**, *6*, 33–40.

[79] M. Li, M. N. Idros, Y. Wu, T. Burdyny, S. Garg, X. S. Zhao, G. Wang, T. E. Rufford, *J. Mater. Chem. A* **2021**, *9*, 19369–19409.

[80] M. Duarte, B. De Mot, J. Hereijgers, T. Breugelmans, *ChemElectroChem* **2019**, *6*, 5596–5602.

[81] L. de Sousa, C. Harmoko, N. Benes, G. Mul, *ACS ES&T Eng.* **2021**, DOI 10.1021/acsestengg.1c00228.

[82] M. Ayub, M. H. D. Othman, S. H. S. A. Kadir, A. Ali, I. U. Khan, M. Z. M. Yusop, T. Matsuura, A. F. Ismail, M. A. Rahman, J. Jaafar, *Membranes (Basel).* **2021**, *11*, DOI 10.3390/membranes11080600.

[83] M. W. J. Luiten-Olieman, M. J. T. Raaijmakers, L. Winnubst, T. C. Bor, M. Wessling, A. Nijmeijer, N. E. Benes, *J. Memb. Sci.* **2012**, *407–408*, 155–163.

[84] O. David, Y. Gendel, M. Wessling, *J. Memb. Sci.* **2014**, *461*, 139–145.

[85] R. Kas, K. K. Hummadi, R. Kortlever, P. De Wit, A. Milbrat, M. W. J. Luiten-Olieman, N. E. Benes, M. T. M. Koper, G. Mul, *Nat. Commun.* **2016**, *7*, 1–7.

[86] K. K. Hummadi, A. Sustronk, R. Kas, N. Benes, G. Mul, *Catalysts* **2021**, *11*, DOI 10.3390/catal11050571.

[87] D. Bell, D. Rall, M. Großeheide, L. Marx, L. Hülsdünker, M. Wessling, *Electrochem. commun.* **2020**, *111*, 106645.

[88] I. Merino-Garcia, J. Albo, P. Krzywda, G. Mul, A. Irabien, *Catal. Today* **2020**, *346*, 34–39.

[89] M. Y. Lee, S. Han, H. Lim, Y. Kwon, S. Kang, *ACS Sustain. Chem. Eng.* **2020**, *8*, 2117–2121.

[90] X. Zhao, Y. Song, S. Yang, W. Chen, T. Li, G. Wu, S. Li, G. Li, X. Dong, Z. Jiang, W. Wei, Y. Sun, *ACS Appl. Energy Mater.* **2021**, DOI 10.1021/acsaem.1c01195.

[91] C. Zhu, G. Shen, W. Chen, X. Dong, G. Li, Y. Song, W. Wei, Y. Sun, *J. Power Sources* **2021**, *495*, 229814.

[92] D. Liu, Y. Hu, E. Shoko, H. Yu, T. T. Isimjan, X. Yang, *Electrochim. Acta* **2021**, *365*, 137343.

[93] B. Chen, J. Xu, J. Zou, D. Liu, Y. Situ, H. Huang, *ChemSusChem* **2020**, *13*, 6594–6601.

[94] H. Rabiee, L. Ge, X. Zhang, S. Hu, M. Li, S. Smart, Z. Zhu, H. Wang, Z. Yuan, *Appl. Catal. B Environ.* **2021**, *298*, 120538.

[95] H. Rabiee, X. Zhang, L. Ge, S. Hu, M. Li, S. Smart, Z. Zhu, Z. Yuan, *ACS Appl. Mater. Interfaces* **2020**, *12*, 21670–21681.

[96] H. Rabiee, L. Ge, X. Zhang, S. Hu, M. Li, S. Smart, Z. Zhu, Z. Yuan, *Appl. Catal. B Environ.* **2021**, *286*, 119945.

[97] X. Dong, G. Li, W. Chen, C. Zhu, T. Li, Y. Song, N. Sun, W. Wei, *Mater. Adv.* **2021**, *2*, 241–247.

[98] M. F. Alqahtani, K. P. Katuri, S. Bajracharya, Y. Yu, Z. Lai, P. E. Saikaly, *Adv. Funct. Mater.* **2018**, *28*, DOI 10.1002/adfm.201804860.

[99] X. Wei, D. Vogel, L. Keller, S. Kriescher, M. Wessling, *ChemElectroChem* **2020**, *7*, 4679–4684.

[100] K. H. R. Rouwenhorst, P. M. Krzywda, N. E. Benes, G. Mul, L. Lefferts, *Ullmann's Encycl. Ind. Chem.* **2020**, 1–20.

[101] M. Kuang, Y. Wang, W. Fang, H. Tan, M. Chen, J. Yao, C. Liu, J. Xu, K. Zhou, Q. Yan, *Adv. Mater.* **2020**, *32*, 1–7.

[102] S. Han, C. Wang, Y. Wang, Y. Yu, B. Zhang, *Angew. Chemie* **2021**, *133*, 4524–4528.

[103] C. Dai, Y. Sun, G. Chen, A. C. Fisher, Z. J. Xu, *Angew. Chemie - Int. Ed.* **2020**, *59*,

9418–9422.

[104] M. Anand, C. S. Abraham, J. K. Nørskov, *Chem. Sci.* **2021**, *12*, 6442–6448.

[105] B. S. Patil, N. Cherkasov, J. Lang, A. O. Ibhadon, V. Hessel, Q. Wang, *Appl. Catal. B Environ.* **2016**, *194*, 123–133.

[106] F. Jardali, S. Van Alphen, J. Creel, H. Ahmadi Eshtehardi, M. Axelsson, R. Ingels, R. Snyders, A. Bogaerts, *Green Chem.* **2021**, *23*, 1748–1757.

[107] Y. Yu, C. Wang, Y. Yu, Y. Huang, C. Liu, S. Lu, B. Zhang, *J. Mater. Chem. A* **2020**, *8*, 19623–19630.

[108] E. Vervloessem, M. Aghaei, F. Jardali, N. Hafezkhiabani, A. Bogaerts, *ACS Sustain. Chem. Eng.* **2020**, *8*, 9711–9720.

[109] H. Patel, R. K. Sharma, V. Kyriakou, A. Pandiyan, S. Welzel, M. C. M. Van De Sanden, M. N. Tsampas, *ACS Energy Lett.* **2019**, *4*, 2091–2095.

[110] K. H. R. Rouwenhorst, F. Jardali, A. Bogaerts, L. Lefferts, *Energy Environ. Sci.* **2021**, *14*, 2520–2534.

[111] L. Li, C. Tang, X. Cui, Y. Zheng, X. Wang, H. Xu, S. Zhang, T. Shao, K. Davey, S. Z. Qiao, *Angew. Chemie - Int. Ed.* **2021**, *60*, 14131–14137.

[112] L. Hollevoet, F. Jardali, Y. Gorbanev, J. Creel, A. Bogaerts, J. A. Martens, *Angew. Chemie - Int. Ed.* **2020**, *59*, 23825–23829.

[113] P. M. Krzywda, A. Paradelo, B. T. Mei, N. E. Benes, G. Mul, *ChemElectroChem* **2022**, DOI doi.org/10.1002/celc.202101273.

[114] Y. Zhang, F. Li, Q. Zhang, J. Li, Q. Liu, *Sci. Total Environ.* **2014**, *490*, 213–222.

[115] K. Köhler, W. H. M. Duynisveld, J. Böttcher, *J. Plant Nutr. Soil Sci.* **2006**, *169*, 185–195.

[116] L. F. Greenlee, *Nat. Energy* **2020**, 1–2.

[117] P. H. van Langevelde, I. Katsounaros, M. T. M. Koper, *Joule* **2021**, *5*, 290–294.

Supplementary information 1

Electrochemical reduction of N_2 to NH_3

How not to make ammonia

Introduction

In order to reduce the CO_2 footprint of the chemical industry, novel solutions for the production of chemicals are urgently needed. Recently, green ammonia attracts a lot of attention. One of the promising approaches is electrochemical N_2 reduction in ambient conditions and aqueous electrolyte, applicable in small-scale ammonia production plants for fertilizer applications.[1] Despite many systems proposed in the literature for the nitrogen reduction reaction (NRR), very low activity is always reported,[2] which can lead to false-positive results due to adventitious ammonia contaminations.[3] One of the big challenges in NRR is the mass transport of nitrogen to the electrode surface. Due to the very low solubility of N_2 in aqueous electrolytes, the amount of available reactant is low, which will result in H_2 formation rather than NH_3. Different reactor designs for the improvement of mass transport, mainly based on gas diffusion electrodes, were reported however, little success was achieved.[4–9]

Herein, we propose the use of hollow fiber electrode geometry where flow-through supply of N_2 to the electrode surface is expected to improve mass transport limitations and thus selectivity and production rate of ammonia. We evaluate the performance of Ru-Ti and TiN hollow fiber electrodes for the NRR, provide a critical assessment of the results with elaboration on contaminations, and provide a perspective on the subject.

Experimental

Electrodes preparation

Ti hollow fibers were prepared by dry-wet spinning according to the previously reported method.[10] In brief, Ti powder was mixed with PES and NMP to form a homogeneous suspension. The spinning mixture was pressed through a spinneret with water as a bore liquid. Fibers were thermally treated in order to remove the polymer and form the metallic hollow fiber. Ti fibers sintered at 800 °C were used in this work.

Ruthenium coated Ti hollow fibers (Ru-Ti) were prepared via electrodeposition. 5 mM $RuCl_3$ in 1 M HCl electrolyte was prepared 3 days before the deposition, to stabilize Ru complexes formed in the solution. Ag/AgCl and Pt mesh were used as reference and counter electrode respectively. -0.5 V vs Ag/AgCl was applied for 20 min after which the electrode was rinsed thoroughly with water.

TiN electrodes were prepared by modification of previously prepared Ti fibers by thermal treatment at 800 °C in N_2 atmosphere for 2 h, which results in surface TiN formation.[10]

Hollow fiber electrode assemblies were prepared using silver epoxy glue to ensure electrical contact to the Swagelok connected stainless steel tube. The assembly was covered with two-compartment adhesive glue to prevent either silver or the stainless steel tube to get in contact with the electrolyte. To ensure a homogeneous distribution of gas through the fibers, the open end of the fiber was also covered with adhesive.

Electrochemical measurements

All electrochemical measurements were carried out at room temperature using a BioLogic VSP potentiostat. A gas-tight, H-type cell (a Nafion 117 membrane for compartment separation) was used for linear scan voltammetry and chronoamperometry experiments. A Pt mesh and Ag/AgCl (3 M NaCl, BASi) were used as counter and reference electrode, respectively. 30 ml of electrolyte was purged with Ar or N_2 before the measurement to remove dissolved O_2. Chronoamperometry was performed for 3 h unless indicated otherwise. The measured potentials were corrected for solution resistance (iR drop) and were converted to potentials vs RHE using:

$$E_{RHE} = E_{Ag/AgCl} + 0.059\,pH + E^0_{Ag/AgCl}$$

Ammonia quantification

The concentration of ammonia was determined by an indophenol blue method described elsewhere.[11] Calibration was performed using standard NH_4Cl solutions with known concentration. Generally, 2 ml of the electrolyte solution was mixed with 2 ml of 1 M NaOH containing 5 wt.% salicylic acid and 5 wt.% sodium citrate; 1 ml of 0.05 M NaClO and 0.2 ml of 1 wt.% of sodium nitroferricyanide. The reaction mixture was left in the dark for 2 h and absorption spectra were recorded by UV-Vis spectrometry between 550 and 750 nm. The absorption value at 655 nm was used for quantification.

Results and discussion

Electrodes characterization

SEM images of the cross section of the hollow fiber electrode (Figure S1.1a) reveal the porous structure of the electrode wall. Gas supplied from the inside of the tube escapes through the pores which in the outer part are filled with electrolyte. That causes formation of bubbles over the length of the fiber (Figure S1.1a) and results in gas supply very close to the electrode surface, which can improve mass transport limitations caused by the very low concentration of N_2 in aqueous electrolyte. Moreover, bubbles can cause mixing close to the electrode surface which can enhance mass transport from and towards the bulk.

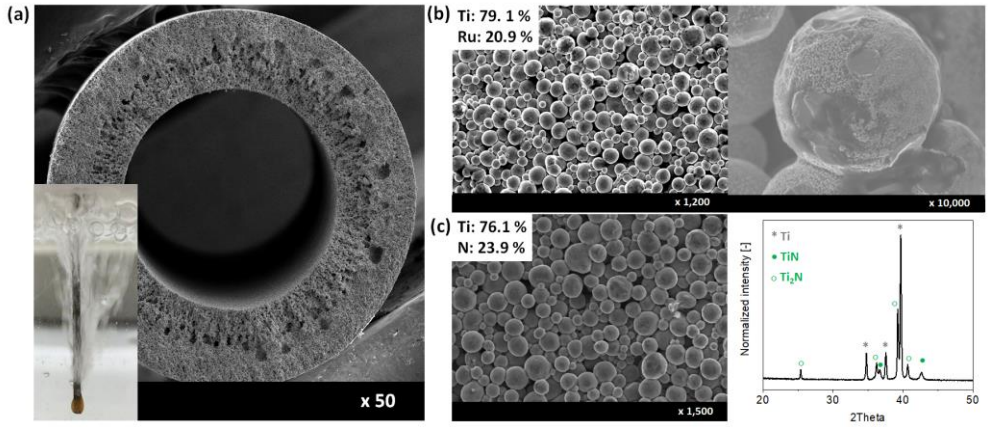

Figure S1.1. Characterization of hollow fiber electrodes used in NRR experiments. (a) SEM of hollow fiber electrode cross section with a photograph of gas purged through the fiber in an aqueous electrolyte. (b) SEM of Ru-Ti hollow fiber surface with EDS analysis and magnification into a single Ti particle covered with Ru. (c) SEM image of a TiN hollow fiber surface with EDS and XRD analysis.

First, the Ru-Ti electrode was prepared and evaluated as an example of a system without nitrogen-containing components. Based on numerical calculations, titanium was suggested as a metal on which electrochemical N_2 reduction might occur via a dissociative mechanism. Ti can bind N-adatoms stronger than H-adatoms, thus protons from the electrolyte are more likely to react directly with adsorbed nitrogen rather than combine to form the H_2 molecule. Therefore, a good selectivity to NH_3 is predicted, although at relatively high over-potentials.[12]

On the other hand, ruthenium was proposed as one of the most active metals on top of volcano diagrams for the NRR.[12] Moreover, stepped Ru surfaces should facilitate N_2

dissociation more than flat surfaces.[13,14] However, at negative potentials, the surface will be mostly covered by H-adatoms which can shift the selectivity to H_2. Several studies have been published using different variations of Ru, while high partial current densities towards ammonia have not yet been achieved.[15,16] Successful modification of Ti hollow fiber surface with Ru nanoparticles was confirmed by SEM and EDS analysis (Figure S1.1b).

Next, the TiN hollow fiber electrode was prepared as an example of the system with nitrogen-containing components in the form of metal nitride (metal oxynitride). Several metal nitrides were reported to produce ammonia via the Mars van Krevelen mechanism[17–19] however no TiN was tested. Successful preparation of TiN hollow fiber was confirmed by EDS and XRD analysis (Figure S1.1c).

Ru-Ti for NRR

The activity of Ru-Ti hollow fiber under N_2 and Ar atmosphere is shown in Figure S1.2. A neutral pH electrolyte was chosen to suppress the competing HER.[20]

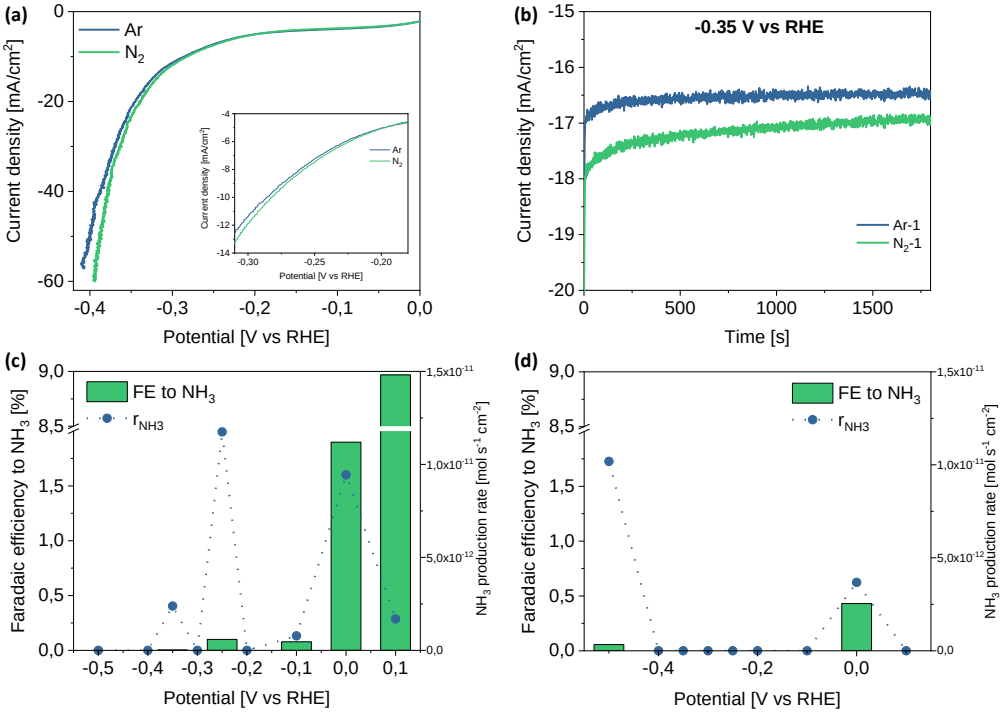

Figure S1.2. The activity of Ru-Ti electrodes for NRR in 0.1 M PBS electrolyte. (a) LSV with Ar and N_2 flow, (b) current density during chronoamperometry at -0.35 V vs RHE, (c) faradaic efficiency and NH_3 production rate at different potentials (d) with subsequent repetition.

Small current density difference was observed with an onset at ~-0.2 V vs RHE between Ar and N_2 atmosphere, suggesting N_2 reduction. Although H_2 formation from water becomes dominant below -0.3 V vs RHE, the current density difference is still observed and it even increases at more negative potentials. It suggests that NRR can still occur along with HER, despite many publications reporting otherwise. Similar current density was observed in chronoamperometry at -0.35 V vs RHE. Assuming that the difference is due to NRR, ~4 ppm of NH_3 is expected, which would be a remarkable amount if confirmed. However, no NH_3 was detected after this experiment, suggesting other, unknown reactions contribute to the observed difference in current density.

In order to further verify ammonia formation on Ru-Ti electrode, chronoamperometry at different potentials was performed for extended time (3h) to accumulate possible product. Very low faradaic efficiencies and ammonia production rates were measured (Figure S1.2c). The highest FE to NH_3 was measured in the potential region where no current differences in the LSV were observed and the overall current density was very small (~ 5μA/cm^2 at 0.1 V vs RHE), which results in ammonia concentration <0.1 ppm). Repeated series of measurements (Figure S1.2d) show the irreproducible behavior of Ru-Ti hollow fibers in N_2 reduction.

Although at first glance the current density difference suggests N_2 reduction to ammonia, various factors could contribute to it. For example, contamination of the N_2 stream with O_2 could result in very common oxygen reduction on Ru,[21] or the presence of NO_x and its conversion to NO, N_2O, or N_2 might also contribute to it. On the other hand, ammonia detected in chronoamperometry experiments must come from external sources as contamination, rather than being produced electrochemically, since the results are highly irreproducible. The origin of ammonia will be discussed in more detail in the general discussion section of this chapter.

TiN for NRR

Another catalytic system tested for NRR was based on TiN hollow fiber electrode. A MvK mechanism is expected to play a role, thus efficient supply of N_2 will be crucial for filling empty N-vacancies and closing the catalytic cycle. The electrochemical activity of TiN hollow fiber for N_2 electroreduction is shown in Figure S1.3. Note, that titanium nitride mostly exists as titanium oxynitride when exposed to an air atmosphere.

Relatively low current densities were recorded but still higher activity between -0.2 V and -0.4 V vs RHE was observed when N_2 was supplied. At more negative potentials the current density was not stable over CV cycles indicating possible corrosion while interacting with

in-situ produced hydrogen. TiN is a relatively new material in the electrochemical field, mostly studied in oxidation reactions, [22,23] therefore not much is known about its corrosion behavior under reductive potentials. To further verify the current density difference, stable potential experiments with gas switching between Ar and N_2 were performed (Figure S1.3b). The presence of N_2 causes an increase in current density which is in line with the LSV and suggests the activity of the electrode for NRR.

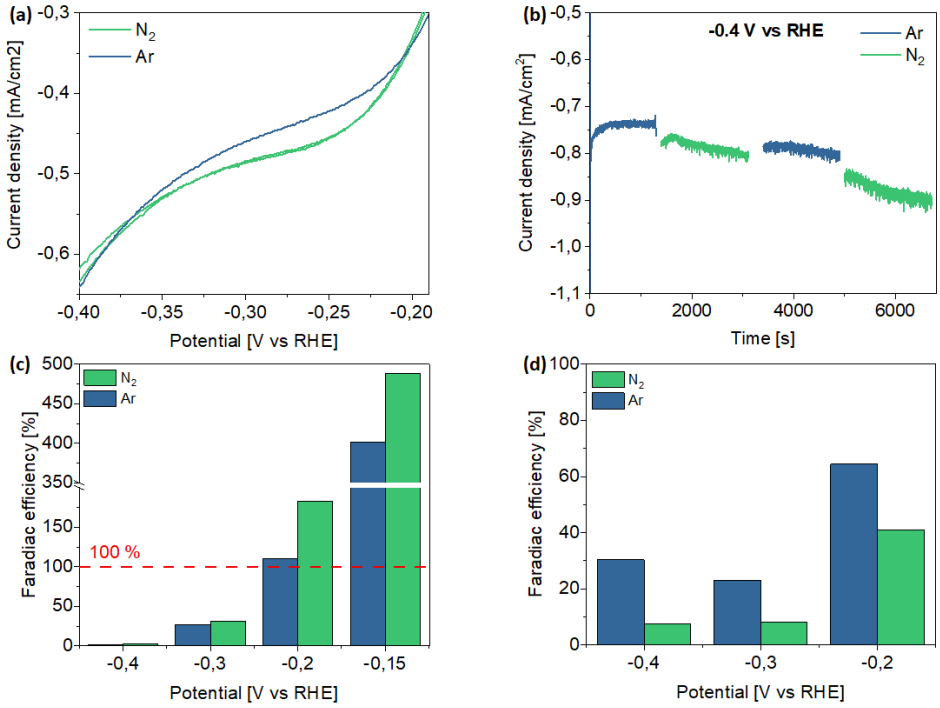

Figure S1.3. The activity of TiN hollow fiber in 0.05 M H_2SO_4 electrolyte. (a) LSV with Ar and N_2 flow, (b) current density during chronoamperometry at -0.4 V vs RHE, with a switch between Ar and N_2, (c) faradaic efficiency to NH_3 at different potentials with N_2 and Ar flow (d) with subsequent repetition and changed the order of measurements (Ar first, N_2 second).

In order to determine the selectivity to ammonia, chronoamperometry at different potentials was performed. Since a MvK mechanism was expected, ammonia formation under N_2 and Ar was verified using the same electrode. The concentration of NH_3 after each electrolysis was higher when N_2 was used which could suggest MvK mechanism however, FE reached almost 500 % at -0.15 V vs RHE (Figure S1.3c). Moreover, when the order of the measurement was changed and Ar was used first on the same fiber, FE also changed being higher for Ar measurements while the exact FE value was irreproducible

compared to the first set of measurements (Figure S1.3d). It is highly doubtful if any ammonia measured comes from the reduction of N_2. It could hypothesize that N from TiN-lattice is converted to ammonia but empty vacancy cannot be re-filled therefore no catalytic cycle is occurring. That could also explain why the current density is not stable at more negative potentials. Consumption of N from TiN can increase surface roughness thus electrode instability and increased current density. However, no changes on XRD and SEM were observed after electrolysis which could be related to very small current densities thus overall changes on the electrode are relatively small.

In order to verify if electrochemistry plays a role in ammonia formation in the system studied, the spontaneous release of ammonia from TiN lattice was verified. A piece of TiN hollow fiber was immersed in the electrolyte and samples were taken over time (Figure S1.4a). Already after 1 min of immersion, ammonia could be detected proving spontaneous formation of NH_3 from TiN. Interestingly, not much change in ammonia release is observed in the first 2 h after which a significant increase occurs.

Generally known corrosion of TiN in acid is based on anodic oxidation to ionic Ti species and NO_2/NO or N_2.[24] No ammonia was reported as a corrosion product so far but considering that the oxidation state of nitrogen in nitride and ammonia is the same, it is not unlikely to happen. Note that titanium nitride is known to interact with oxygen when exposed to air thus layer of titanium oxynitride (TiO_xN_y) is always present. This layer can be attacked and gradually removed by acid at a rate depending on acid concentration.[24] It suggests that TiN rather than TiO_xN_y is responsible for ammonia release assuming that TiO_xN_y layer is removed after >2 h of acid treatment. Low accessibility of TiN in initial phases causes low ammonia release. Interestingly, differences in ammonia release between samples are observed with one barely showing ammonia even after 120 min. Although the corrosion rate of titanium nitride was shown to be dependent on surface defect rather than crystal orientation,[25] the latter cannot be excluded in corrosion to ammonia. Nevertheless, full corrosion resistance in aqueous solutions can be only obtained in fully dense coatings.[26] TiN hollow fiber surface is rather defect-rich which originates from the electrode preparation method. A series of thermal treatment steps were needed to prepare the electrode which can influence surface defects due to possible local temperature differences or gas flow distribution in the oven depending on fiber position. This can cause slightly different surface defects or crystal structures which can be responsible for differences in ammonia release.

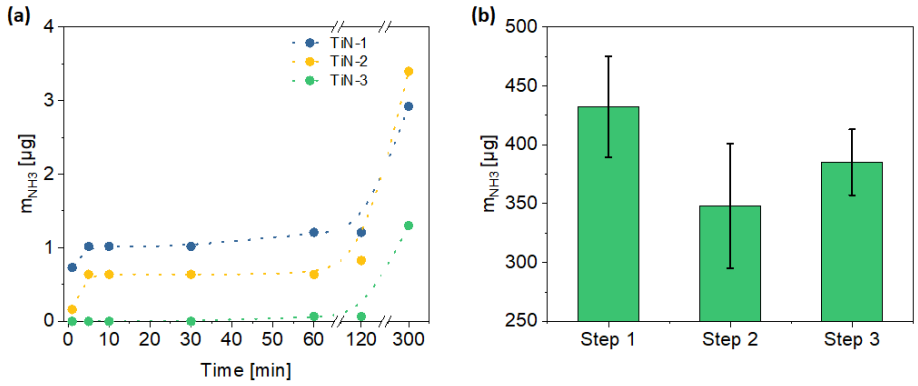

Figure S1.4. Spontaneous NH_4^+ release from TiN hollow fiber in 0.05 M H_2SO_4. Mass of NH_4^+ released (a) over time in 3 different samples and (b) in 3 steps on the same fiber: 1- after 24 h immersion; 2- after subsequent 24 h immersion in the fresh electrolyte; 3- after 24 h immersion of fiber with additional thermal treatment.

Additional experiment proving the effect of oven treatment is shown in Figure S1.4b. A piece of the electrode was exposed to 2 subsequent 24 h acid wash (steps 1 and 2) and lower ammonia content after the 2nd step was detected indicating fewer sites releasing NH_3. After 2 h thermal treatment in N_2 atmosphere at 800 °C, which corresponds to conditions used for the preparation of TiN coating on Ti hollow fiber, NH_3 release increased confirming the specific site being created during oven treatment. This system can be seen as a thermochemical approach of NH_3 synthesis[1] however, conditions required to restore active TiN and the amount of NH_3 released make this approach very inefficient.

Although more insight into the surface structure, TiN layer depth, and content of titanium oxynitride would be needed to explain the corrosion mechanism, spontaneous release of ammonia in an acidic solution can be responsible for highly irreproducible results observed in Figure S1.3b and c. Nevertheless, the MvK mechanism in TiN hollow fiber for N_2 reduction cannot be excluded, but due to the electrode instability, it also can not be confirmed. In any case, spontaneous reaction of TiN with electrolyte appears to dominate the formation of ammonia, and the effect of the electrochemical potential and the presence of N_2 seems minor.

General discussion

Both systems described above, although different, raise similar problems in assessing nitrogen conversion efficiency. The low quantity of ammonia and lack of reproducibility suggest a problem with contaminations. Ru-Ti catalyst is an example where no N-based components are used at any stage. On the other hand, TiN hollow fiber contains N in form of metal nitride thus another N-source than N_2 is present. No special precautions were applied in the experimental part of this study due to limited awareness at the time. Note that the literature cited in this section is just an example since it is impossible to cite all literature relevant to every statement, but the effect of artifacts has now been widely accepted by the community.

In most literature reports, the highest faradaic efficiencies are achieved at rather more positive potentials[27–30] as also observed here. On one hand, this is reasonable because HER is not competing with NRR, but on the other hand, current densities at those potentials are usually very low (in the order of μA) making accurate ammonia quantification challenging. At such low concentrations, it is very easy to get false-positive results.[3] Faradaic efficiency and ammonia production rate are usually shown and concentration data are not included, except for the measurement at the most optimal conditions. Although no reproducible (stable) contamination was observed in our study, imagine a situation where the same amount of contamination is present in every measurement. It will result in the same concentration of NH_3 detected but FE will be different due to different current densities at each potential, and thus a trend in FE can be found. Multiple studies report trends in FE with the highest value at the least negative potential where the current density will be the lowest.

However, different trends in FE than described above are not enough to prove successful NRR. NO_x are common contaminants (also in N_2 gas) of which reduction to ammonia is more facile than the reduction of N_2.[31] If gas is not purified, the activity of NO_x reduction to ammonia will also depend on reaction conditions and optimum FE at certain potential can be observed, and thus the trend will look different than previously discussed. Therefore careful N_2 purification to remove NO_x is also necessary to avoid false-positive results.

In order to confirm the electrochemical synthesis of ammonia, isotope experiments with $^{15}N_2$ in combination with ^1H NMR which allows for distinction between $^{14}NH_3$ and $^{15}NH_3$ became common, while the field was progressing. Commercially available $^{15}N_2$ is contaminated with $^{15}NO_x$ and $^{15}NH_3$ thus purification is also needed. Lack of purification in combination with qualitative, rather than quantitative NMR measurements will "confirm" successful NRR.[32]

Another important aspect is careful catalyst preparation. Plenty of "successful" NRR systems use N-containing precursors in catalyst preparation steps, such as nitrate salts [33–38], urea [18,39], thiourea [40,41], polyvinylpyrrolidone [35–37], DMF [37,42], hydroxylamine[34] or an imidazole-type molecule,[38] which can spontaneously or electrochemically convert to ammonia. Even ammonium salts[32,37,41] and thermal treatment in NH_3 atmosphere[43] were reported. Moreover, it was shown that some commercially available catalysts can be contaminated with traces of NO_x[44]. All of this and more can introduce contamination.

Extreme care should be taken when working with systems containing nitrogen atoms such as metal nitride catalysts or very commonly used N-doped catalyst supports (mostly N-doped carbon).[45–49] As demonstrated in this study as well as in literature,[50,51] that kind of systems can spontaneously form ammonia rather than produce it catalytically, either with or without an electrochemical potential.

More and more surprising ammonia sources can be found than those described above.[3] It is commonly present in the atmosphere and easily adsorbs on a variety of surfaces. Thus it can be found in glassware, tubing, analytical tools, or electrolyte solutions exposed to air. Moreover, it can leach from nitrile gloves, ionic membranes, or even can be exhaled due to the presence in human breath. Some of those reasons are likely responsible for false-positive results obtained in this study – as well as others.

Reliable experiments

Several reports have already proposed how to tackle the contamination problem and which protocols should be followed. Here, the most important points based on literature and own data are summarized. For a more detailed description, see example literature.[3,52–57]

Care should be taken from the very beginning of catalyst preparation where N-containing precursors/additives should be avoided as much as possible at any stage. If possible, catalyst, electrode, and other reactor components should be pretreated with acid/base wash while keeping in mind that pretreatment can also be the source of contamination as ammonia from the air can dissolve in aqueous solutions [3]. Catalysts on N-doped supports or metal nitride-based should be treated with extreme caution. A Series of blank measurements in an inert atmosphere at variable conditions should be performed to ensure a lack of system contaminations or catalyst/support decomposition to ammonia and the background NH_3 levels should be established. N_2 feeds should be carefully prepared to remove NO_x, O_2, and other possible components. Despite purification, NO_x should be quantified after gas bubbling at open circuit potential. Establishing current density differences between N_2/Ar is not enough to claim catalytic activity for NRR. Different

electrochemical techniques (CV, LSV, chronoamperometry with gas switch) should be used to verify ammonia formation. Electrolysis conditions such as applied potential, time, catalyst loading, and N_2 concentration should be varied and trends in faradaic efficiency and ammonia production rates should be visible. Experiments with the same electrode over different conditions as well as fresh electrodes should be performed. Most relevant process conditions should be evaluated also in the presence of Ar instead of N_2. Different methods should be used for ammonia quantification (UV-Vis, IC, NMR) since some of them might not be suitable in certain conditions. The most important part is reproducibility! Although the exact value is not as important, the order of magnitude should be reproducible to claim successful NRR. Finally, control experiments with extensively purified $^{15}N_2$ and subsequent $^{15}NH_3$ detection by ^1H NMR have to be shown, ideally in varied experimental conditions. The ammonia quantity and efficiency should be similar to $^{14}N_2$ experiments.

Overall, great care and common sense while performing experiments are highly advised. All of those precautions are strictly necessary to provide reliable data which can contribute to pushing the field in a good direction.

Final thoughts

All of the described problems associated with NRR need to be addressed only because the amount of detected ammonia is very low. Relatively small contaminations or traces of NO_x in most of the systems as well as strict protocols could be ignored if synthesized NH_3 would reach levels where such small contaminations don't matter for the final result thus no doubts are present about the origin of measured ammonia. Despite the small volume of the electrolytic cell, the high electrode surface area, or long electrolysis time, the amount of NH_3 detected is typically <1 ppm, often even <0.1 ppm which easily falls in the contamination range. If we have to go through all that trouble to prove that the system works, we should think deeply about if we can even say that it actually works.

Only if experiments will be performed in accordance with strict protocol and results will be reported with honesty taking into account contamination problems as much as possible, we can move the NRR field forward. When no awareness of such common NH_3 contaminations existed, all "positive results" while needing to treat them with extreme caution, at the time might have appeared credible. However, while the field was developing and such awareness increased, some researchers still attempt to publish data without discussing the accuracy.

In order to stop the field from growing even more into the wrong direction, authors claiming activity of their catalysts/systems towards NRR should revise their work including

knowledge that we possess now. One might even suggest to authors to revisit their earlier work, and write addenda to their publications if necessary.

The biggest question now is if electrochemical N_2 reduction in an aqueous electrolyte in ambient conditions was ever achieved to date? Despite many publications claiming success, there is very little proof to actually believe the reliability of the data. Electrochemical nitrogen reduction is a very interesting and promising approach that is worth further studying, but in the current stage, the (electro)catalytic performance of a variety of formulations is still too small.

We should stop the race for getting as many publications as possible and focus on reliable results reported with honesty, even if it makes the story look less attractive. At that point, I address this message not only to the NRR community but to scientists in every field. This is the only way to contribute to real scientific developments which our world can make use of.

References

[1] K. H. R. Rouwenhorst, P. M. Krzywda, N. E. Benes, G. Mul, L. Lefferts, in *Techno-Economic Challenges Green Ammon. as an Energy Vector*, **2020**, pp. 41–83.

[2] G. Qing, R. Ghazfar, S. T. Jackowski, F. Habibzadeh, M. M. Ashtiani, C. P. Chen, M. R. Smith, T. W. Hamann, *Chem. Rev.* **2020**, *120*, 5437–5516.

[3] S. Z. Andersen, V. Čolić, S. Yang, J. A. Schwalbe, A. C. Nielander, J. M. McEnaney, K. Enemark-Rasmussen, J. G. Baker, A. R. Singh, B. A. Rohr, M. J. Statt, S. J. Blair, S. Mezzavilla, J. Kibsgaard, P. C. K. Vesborg, M. Cargnello, S. F. Bent, T. F. Jaramillo, I. E. L. Stephens, J. K. Nørskov, I. Chorkendorff, *Nature* **2019**, *570*, 504–508.

[4] H. Wei, Q. Jiang, C. Ampelli, S. Chen, S. Perathoner, Y. Liu, G. Centi, *ChemSusChem* **2020**, *13*, DOI 10.1002/cssc.202001719.

[5] B. L. Sheets, G. G. Botte, *Chem. Commun.* **2018**, *54*, 4250–4253.

[6] S. Chen, S. Perathoner, C. Ampelli, C. Mebrahtu, D. Su, G. Centi, *Angew. Chemie - Int. Ed.* **2017**, *56*, 2699–2703.

[7] K. Kugler, B. Ohs, M. Scholz, M. Wessling, *Phys. Chem. Chem. Phys.* **2014**, *16*, 6129–6138.

[8] N. Lazouski, M. Chung, K. Williams, M. L. Gala, K. Manthiram, *Nat. Catal.* **2020**, *3*, 463–469.

[9] L. Hu, Z. Xing, X. Feng, *ACS Energy Lett.* **2020**, 430–436.

[10] R. P. H. Jong, P. M. Krzywda, N. E. Benes, G. Mul, *RSC Adv.* **2020**, *10*, 31901–31908.

[11] L. Xia, X. Wu, Y. Wang, Z. Niu, Q. Liu, T. Li, X. Shi, A. M. Asiri, X. Sun, *Small Methods* **2018**, *1800251*, 1803111.

[12] E. Skúlason, T. Bligaard, S. Gudmundsdóttir, F. Studt, J. Rossmeisl, F. Abild-Pedersen, T. Vegge, H. Jónsson, J. K. Nørskov, *Phys. Chem. Chem. Phys.* **2012**, *14*, 1235–1245.

[13] S. Back, Y. Jung, *Phys. Chem. Chem. Phys.* **2016**, *18*, 9161–9166.

[14] R. Manjunatha, A. Schechter, *Electrochem. commun.* **2018**, *90*, 96–100.

[15] H. Tao, C. Choi, L. X. Ding, Z. Jiang, Z. Han, M. Jia, Q. Fan, Y. Gao, H. Wang, A. W. Robertson, S. Hong, Y. Jung, S. Liu, Z. Sun, *Chem* **2019**, *5*, 204–214.

[16] J. Zeng, Z. Geng, J. Du, Z. Liu, R. Si, P. Li, M. Shu, K. Li, X. Kong, Y. Liu, *Adv. Mater.* **2018**, *30*, 1803498.

[17] Y. Abghoui, E. Skúlason, *Catal. Today* **2017**, *286*, 69–77.

[18] X.-Z. Yuan, S. Zhu, M. Gu, M. Shao, H. Wang, Y. Wang, J. Li, Q. Feng, Y. Yao, Y. Yao, Q. Wang, H. Li, *Small Methods* **2018**, *1800324*, 1800324.

[19] X. Yang, J. Nash, X. Chang, Y. Yan, B. Xu, S. Kattel, J. H. Lee, J. G. Chen, *Angew. Chemie - Int. Ed.* **2019**, 1–6.

[20] J. Wang, L. Yu, L. Hu, G. Chen, H. Xin, X. Feng, *Nat. Commun.* **2018**, *9*, DOI 10.1038/s41467-018-04213-9.

[21] J. W. Lee, B. N. Popov, *J. Solid State Electrochem.* **2007**, *11*, 1355–1364.

[22] N. R. Mucha, J. Som, J. Choi, S. Shaji, R. K. Gupta, H. M. Meyer, C. L. Cramer, A. M. Elliott, D. Kumar, *ACS Appl. Energy Mater.* **2020**, *3*, 8366–8374.

[23] M. Bele, P. Jovanovič, Ž. Marinko, S. Drev, V. S. Šelih, J. Kovač, M. Gaberščček, G. Koderman Podboršek, G. Dražić, N. Hodnik, A. Kokalj, L. Suhadolnik, *ACS Catal.* **2020**, *10*, 13688–13700.

[24] S. D. Chyou, H. C. Shih, T. T. Chen, *Corros. Sci.* **1993**, *35*, 337–347.

[25] A. D. Bauer, M. Herranen, H. Ljungcrantz, J.-O. Carlsson, J.-E. Sundgren, *Surf. Coatings Technol.* **1997**, *91*, 208–214.

[26] A. C. Agudelo, J. R. Gancedo, J. F. Marco, D. Hanžel, *J. Vac. Sci. Technol. A* **1997**, *15*, 3163–3169.

[27] C. Zhang, D. Wang, Y. Wan, R. Lv, S. Li, B. Li, X. Zou, S. Yang, *Mater. Today* **2020**, *40*, 18–25.

[28] H. Zhao, D. Zhang, H. Li, W. Qi, X. Wu, Y. Han, W. Cai, Z. Wang, J. Lai, L. Wang,

Adv. Energy Mater. **2020**, *10*, 1–6.

[29] P. Huang, Z. Cheng, L. Zeng, J. Yu, L. Tan, P. Mohapatra, L. S. Fan, Y. Zhu, *ACS Catal.* **2020**, 14928–14935.

[30] P. Li, Z. Jin, Z. Fang, G. Yu, *Angew. Chemie - Int. Ed.* **2020**, *59*, 22610–22616.

[31] J. Choi, J. Choi, H. L. Du, H. L. Du, C. K. Nguyen, C. K. Nguyen, B. H. R. Suryanto, A. N. Simonov, A. N. Simonov, D. R. MacFarlane, D. R. MacFarlane, *ACS Energy Lett.* **2020**, *5*, 2095–2097.

[32] M. Wang, S. Liu, T. Qian, J. Liu, J. Zhou, H. Ji, J. Xiong, J. Zhong, C. Yan, *Nat. Commun.* **2019**, *10*, 1–8.

[33] Y. C. Hao, Y. Guo, L. W. Chen, M. Shu, X. Y. Wang, T. A. Bu, W. Y. Gao, N. Zhang, X. Su, X. Feng, J. W. Zhou, B. Wang, C. W. Hu, A. X. Yin, R. Si, Y. W. Zhang, C. H. Yan, *Nat. Catal.* **2019**, DOI 10.1038/s41929-019-0241-7.

[34] L. Han, M. Hou, P. Ou, H. Cheng, Z. Ren, Z. Liang, J. A. Boscoboinik, A. Hunt, I. Waluyo, S. Zhang, L. Zhuo, J. Song, X. Liu, J. Luo, H. L. Xin, *ACS Catal.* **2021**, *11*, 509–516.

[35] M. Nazemi, S. R. Panikkanvalappil, M. A. El-Sayed, *Nano Energy* **2018**, *49*, 316–323.

[36] M. Nazemi, M. A. El-Sayed, *J. Phys. Chem. Lett.* **2018**, *9*, 5160–5166.

[37] C. Lv, C. Yan, G. Chen, Y. Ding, J. Sun, Y. Zhou, G. Yu, *Angew. Chemie - Int. Ed.* **2018**, *57*, 6073–6076.

[38] S. Mukherjee, D. A. Cullen, S. Karakalos, K. Liu, H. Zhang, S. Zhao, H. Xu, K. L. More, G. Wang, G. Wu, *Nano Energy* **2018**, *48*, 217–226.

[39] Y. Li, Y. Kong, Y. Hou, B. Yang, Z. Li, L. Lei, Z. Wen, *ACS Sustain. Chem. Eng.* **2019**, *7*, 8853–8859.

[40] L. Zhang, X. Ji, X. Ren, Y. Ma, X. Shi, Z. Tian, A. M. Asiri, L. Chen, B. Tang, X. Sun, *Adv. Mater.* **2018**, *1800191*, 2–7.

[41] Z. Zhao, S. Luo, P. Ma, Y. Luo, W. Wu, Y. Long, J. Ma, *ACS Sustain. Chem. Eng.* **2020**, *8*, 8814–8822.

[42] Z. Wang, J. Niu, Y. Xu, L. Wang, H. Wang, H. Liu, *ACS Sustain. Chem. Eng.* **2020**, DOI 10.1021/acssuschemeng.0c03970.

[43] X. Zhang, R.-M. Kong, H. Du, L. Xia, F. Qu, *Chem. Commun.* **2018**, *54*, 5323–5325.

[44] Y. Chen, H. Liu, N. Ha, S. Licht, S. Gu, W. Li, *Nat. Catal.* **2020**, *3*, DOI 10.1038/s41929-020-00527-4.

[45] T. He, S. K. Matta, A. Du, *Phys. Chem. Chem. Phys.* **2019**, *21*, 1546–1551.

[46] K. Peramaiah, V. Ramalingam, H. Fu, M. M. Alsabban, R. Ahmad, L. Cavallo, V.

Tung, K. Huang, J. He, **2021**, *2100812*, 1–12.

[47] Y. Liu, Y. Su, X. Quan, X. Fan, S. Chen, H. Yu, H. Zhao, Y. Zhang, J. Zhao, *ACS Catal.* **2018**, acscatal.7b02165.

[48] X. Wang, Q. Zhang, X. Zhang, C. Wang, Z. Xie, Z. Zhou, *Small Methods* **2019**, *3*, 1800334.

[49] Y. Liu, Y. Su, X. Quan, X. Fan, S. Chen, H. Yu, H. Zhao, Y. Zhang, J. Zhao, *ACS Catal.* **2018**, *8*, 1186–1191.

[50] H. L. Du, T. R. Gengenbach, R. Hodgetts, D. R. Macfarlane, A. N. Simonov, *ACS Sustain. Chem. Eng.* **2019**, *7*, 6839–6850.

[51] B. Hu, M. Hu, L. Seefeldt, T. L. Liu, *ACS Energy Lett.* **2019**, *4*, 1053–1054.

[52] J. Choi, B. H. R. Suryanto, D. Wang, H. Du, R. Y. Hodgetts, F. M. F. Vallana, D. R. Macfarlane, A. N. Simonov, *Nat. Commun.* **2020**, *11*, 1–10.

[53] L. F. Greenlee, J. N. Renner, S. L. Foster, *ACS Catal.* **2018**, *8*, 7820–7827.

[54] G. Y. Duan, Y. Ren, Y. Tang, Y. Z. Sun, Y. M. Chen, P. Y. Wan, X. J. Yang, *ChemSusChem* **2020**, *13*, 88–96.

[55] H. Liu, Y. Zhang, J. Luo, *J. Energy Chem.* **2020**, *49*, 51–58.

[56] L. Shi, Y. Yin, S. Wang, X. Xu, H. Wu, J. Zhang, S. Wang, H. Sun, *Appl. Catal. B Environ.* **2020**, *278*, 119325.

[57] H. Liu, N. Guijarro, J. Luo, *J. Energy Chem.* **2021**, *61*, 149–154.

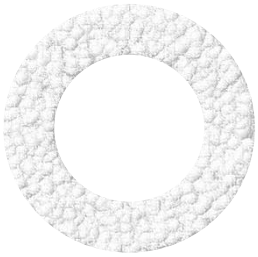

Chapter 2

Preparation of Ti, Ti/TiC or Ti/TiN based hollow fibers with extremely low electrical resistivity

This chapter is based on:

R. P. H. Jong, **P. M. Krzywda**, N. E. Benes, G. Mul, "Preparation of Ti, Ti/TiC or Ti/TiN based hollow fibres with extremely low electrical resistivity", *RSC Advances*, 10, 31901, **2020**.

Abstract

Porous Ti based hollow fibers with low electrical resistivity (4.1-9.6 μΩ·m), orders of magnitude smaller than reported for Ti-fibres in the literature, were produced by dry-wet spinning of a mixture of Ti-particles, Polyethersulfone (PES), and N-methylpyrrolidone (NMP). Utilizing a two-step thermal decomposition of PES, consisting of treatment in air at 475 °C, followed by treatment in Argon at 800 °C, hollow fibers of entirely metallic Ti are obtained, as confirmed by XRD, SEM-EDS, and TGA-MS analyses. Only a thin native oxide layer is formed due to ambient surface oxidation, as identified by XPS analysis. Carbonization of the polymer under an inert atmosphere can be used to produce a Ti/TiC-composite. To obtain a Ti/TiN composite, the porous Ti-tubes can be treated in nitrogen atmosphere at 800 °C. The porosity, pore size distribution, and bending strength of the fibers were determined for a low (800 °C) and high (1100 °C) degree of sintering, and it was found that these are largely independent of the chemical surface composition. The presence of TiC or TiN, likely in an outer, but crystalline shell, results in lower resistivity than of the pure Ti fibers, which can be attributed to the insulating layer of TiC or TiN preventing capacitive effects at the Ti/air interface. The developed preparation methodology results in porous metallic and composite Ti based fibers, which are very suitable for electrochemical applications.

Introduction

Inorganic membranes in tubular form (also called hollow fibers) can be produced using a scalable dry-wet spinning method. Ceramic fibers, based on e.g. Al_2O_3, as well as metallic fibers made of stainless steel, Cu, Ni or Ti have been previously prepared using this method [1–4]. Inorganic hollow fibers have been investigated as electrode materials and a recent study of electrochemical reduction of CO_2, using Cu-based fibers, indicates significant application potential.[3,5,6] Ti is also an attractive metal for electrochemical applications due to various properties such as high conductivity, favorable mechanical strength, and high corrosion resistance.[7] Ti furthermore is utilized in structural and biomedical applications [8]. The same application window exists for TiN or TiC, while the coating of Ti with a layer of TiN or TiC further improves the corrosion resistance and the mechanical strength.[8] While the effect of the temperature of sintering, ranging from 1100 to 1500 °C, on the properties of Ti-hollow fibers has been previously addressed,[4] to the best of our knowledge, methods to control the chemical composition of porous Ti hollow fibers have not been developed. Ti readily oxidizes at elevated temperatures, resulting in fibers with a high electrical resistivity. Furthermore, Ti becomes highly reactive towards many substrates, e.g. used as crucibles, above 800 °C,[9] and any reductive H_2 treatment at elevated temperatures could cause embrittlement.[10]

In this work the synthesis of Ti hollow fibers is reported with a focus on the process conditions during the thermal treatment steps, to control the decomposition chemistry of the polymer and the resulting composition of the sintered Ti-particles. We demonstrate that metallic Ti can be obtained without any reductive H_2 treatment if Ti oxidation is limited to a semi-stable oxide layer by applying relatively low temperatures in air.[11–15] This TiO_x-layer can be reduced to Ti, under the appropriate conditions, by reaction with carbon residues of the decomposed polymer. This is possible due to the two-step decomposition behavior of polyethersulfone (PES), used in the preparation of the fibers.[16,17] It is furthermore shown that carbonization of the polymer under an inert atmosphere can be used to produce a Ti/TiC-composite. The resulting TiC content has been analyzed by XRD and XPS. To further evaluate the effect of a poor conducting shell on the properties of Ti hollow fibers, the porous metallic Ti hollow fiber was treated in a nitrogen atmosphere to create a Ti/TiN composite.[18–20] Properties of the resulting fibers (Ti, Ti/TiC, and Ti/TiN), including porosity, pore size distribution, bending strength, and resistivity, are reported for a low (800 °C) and high (1100 °C) degree of sintering.

Experimental section

Dry-wet spinning

The porous tube electrodes were produced by a dry-wet spinning method.[1–4] The homogenous spinning mixture is introduced to a non-solvent. Solvent exchange occurs between the solvent and non-solvent resulting in a phase inversion, and solidification of the previously dissolved polymer. The spinning mixture consisted of 69.8 wt.% Ti, 22.7 wt.% NMP, and 7.5 wt.% PES for a total weight of 150 g. Ti powder was added to the NMP while stirring; this suspension underwent 30 minutes of sonication. PES (kept at 120 °C before addition) was added in four equivalent portions with an interval of 2 hours between each addition. The resulting mixture was stirred for 1.5 days. Hereafter, the mixture was transferred to the spinning vessel and kept under a vacuum prior to use (overnight). The spinneret had an outer diameter of 2.0 mm and an inner diameter of 0.8 mm. For the bore liquid and coagulation bath demineralized water was used. The air gap was set to 20 mm. The bore liquid flow rate was set to 7 ml/min and 3 bar of N_2 pressure was used to extrude the mixture. After spinning, the green fibers were kept in a demineralized water bath for 2 days, followed by drying for another 2 days under ambient conditions.

Thermal treatment

Three types of Ti-based porous tube electrodes are discussed in this work; Ti, Ti/TiC, and Ti/TiN. For each of these three types two sets were made; one without severe sintering (thermal treatment up to 800 °C) and one after thermal treatment up to 1100 °C. Each type and set requires its own specific treatment, which are schematically shown in Figure 2.1 with specific parameters described in Table 2.1.

Note that the incorporation of nitrogen, to obtain the Ti/TiN samples, is an additional step of the material obtained after steps Ti-2 and Ti-3. It was found that Ti can reduce Al_2O_3 at 800 °C, therefore a quartz (SiO_2) substrate which does not exhibit any reaction with Ti at 800 °C was applied instead. However, at temperatures above 800 °C, an exchange between Ti and SiO_2 was noticed; to prevent this a Mo-foil substrate was used when preparing samples at 1100 °C.[9] The substrates used in steps Ti-1 and Ti-2 needed to be cleaned after use to remove any organic residue. The removal of Ti dust from the Ti-2 substrate is also necessary as the Ti/TiO_x/C sample is very brittle. Keeping the substrate clean is much more feasible when using Al_2O_3 (cleaning by thermal oxidation) or quartz (acid cleaning), rather than Mo. The Mo substrate was therefore only used for the treatment of samples at 1100 °C, after initial sintering in quartz at 800 °C.

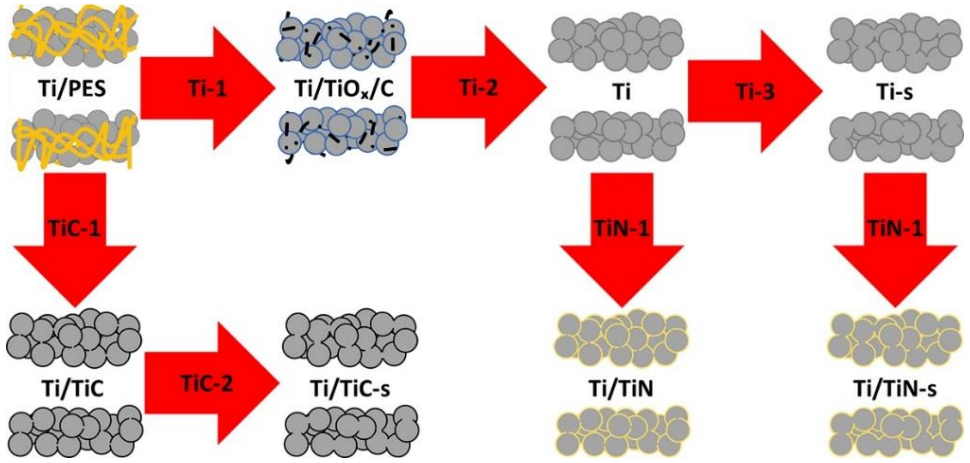

Figure 2.1. Processing scheme of green fiber (Ti+PES) after spinning to obtain, Ti, Ti/TiC, and Ti/TiN porous tubes.

The obtained samples are denoted Ti, Ti-s, Ti/TiC, Ti/TiC-s, Ti/TiN, and Ti/TiN-s in the remainder of the text. These notations indicate the respective material; Ti metal, Ti/TiC composite, and Ti/TiN composite, accompanied by "-s" to indicate the additional sintering step at 1100 °C.

Table 2.1. Thermal treatment parameters for the production of Ti, Ti/TiC and Ti/TiN materials.

Step	Substrate	Heating rate ($°C \cdot min^{-1}$)	Temperature (°C)	Time (min)	Atmosphere
Ti-1	Al_2O_3	3	475	480	Air
Ti-2	Quartz	10	800	480	Ar
Ti-3	Mo	10	1100	75	Ar
TiC-1	Quartz	10	800	480	Ar
TiC-2	Mo	10	1100	75	Ar
TiN-1*	Quartz	10	800	120	N_2

*thermal treatment starting from either step Ti-2 or Ti-3.

Results and discussion

Analysis of the composition and morphology

Photographs of the prepared samples are presented in Figure 2.2. The oxidation step at low temperature yields sample (A), which appears blue. The blue color indicates the presence of a mixed-valence state (III, IV) in Ti-oxide, while residual carbon is likely also

present, as will be discussed later. The Ti and Ti-s samples (B, C) show a shiny grey color, which is expected for metallic Ti tubes. The Ti/TiC and Ti/TiC-s samples (D, E) are observed to be darker grey, indicating the presence of TiC. The Ti/TiN and Ti/TiN-s samples (F, G) have a distinct yellow color, resulting from the formed TiN after nitridation. After treatment at 1100 °C the samples appear slightly paler than before.

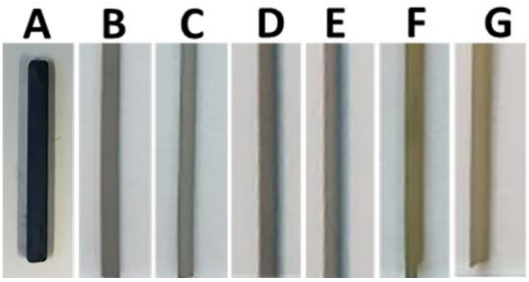

Figure 2.2. Photographs of (A) Ti/TiOx/C, (B) Ti, (C) Ti-s, (D) Ti/TiC, (E) Ti/TiC-s, (F) Ti/TiN and (G) Ti/TiN-s.

The XRD patterns of prepared tubes are shown in Figure 2.3a (see Figure S2.1 for XRD of tubes sintered at 1100 °C). The XRD pattern of the intermediate composition formed after calcination in air at 475 °C ($Ti/TiO_x/C$), confirms the presence of an oxidized form of Ti. The (crystalline) oxide layer is likely covering a metallic Ti-core, as can be judged from the very clear metallic Ti signal. After the next treatment step (Ti-2), a pure metallic Ti phase is observed. The absence of crystalline TiO_x species after the treatment in Ar, suggests a polymer-associated carbon residue is present in $Ti/TiO_x/C$ sample, which enables the reduction of TiO_x during the Ar-treatment at 800 °C. More important is that crystalline TiC is not formed during this step, indicating that the polymer was effectively converted into CO_2, as will be further discussed based on MS data. The XRD patterns of Ti/TiC and Ti/TiN, show the successful formation of TiC and TiN with the remaining Ti core. Furthermore, for the TiN samples, a mix of TiN and Ti_2N phases is present which is the result of the relatively low temperature used for nitridation.[18–20]

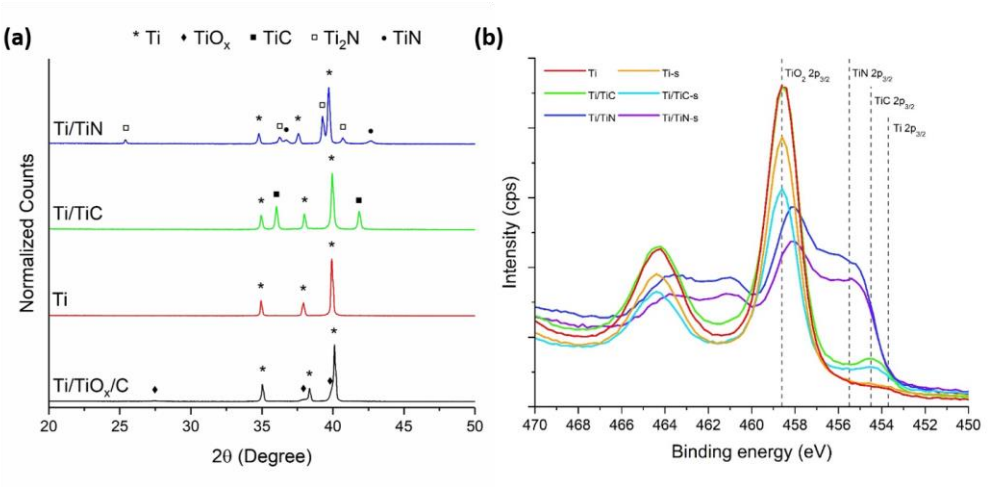

Figure 2.3. (a) XRD patterns of Ti/TiN, Ti/TiC, Ti, and Ti/TiOx/C. (b) XPS spectra in the Ti 2p region for prepared hollow fibers.

XPS spectra of prepared tubes are shown in Figure 2.3b. Note no big changes after additional sintering step are observed. Significant TiO_2 signal in all samples is observed, which can be assigned to the presence of a native oxide layer formed by oxidation in ambient conditions. In agreement with an increased oxidation resistance in the order of Ti < TiC < TiN, the relative contribution of the TiO_2 peak decreases in the series. Surface TiC can be identified at 454.5 eV with additional confirmation of C 1s spectra (Figure S2.2). Due to the overwhelming presence of adventitious carbon, TiC is difficult to quantify. TiN can be identified by the overall spectral signature containing multiple peaks, including the broad feature between 455 and 457 eV. Depth profiling (~10nm) is shown in Figure S2.2. By removal of the native oxide layer, the oxide contribution decreased while nitride and carbide signals were still observed after sputtering. However, the formation of TiC by the sputtering-induced reaction of Ti with adventitious carbon led to TiC signals in the Ti and Ti/TiN samples and resulted in an over-estimation of the quantity of TiC in the Ti/TiC samples.

In Figure 2.4, SEM images of the cross section and wall of Ti (top) and Ti-s (bottom) are shown. The porous structure of the metallic tubes originates from the dry-wet spinning process. By varying spinning conditions e.g. bore liquid flow, applied pressure, spinning mixture, or coagulation bath composition, the morphology can be varied. The spinning conditions used here, result in a structure that consists of macro voids starting from the inside, towards a more dense sponge-like structure on the outside of the sample. The clear boundary between these two types of structures can be seen at approximately the middle of the tube wall in both Ti and Ti-s samples. The overall structure of the porous tubes is

thus retained after treatment at 1100 °C. Similar wall structures are found for the Ti/TiC, Ti/TiC-s, Ti/TiN and Ti/TiN-s samples (Figures S2.3 and S2.4).

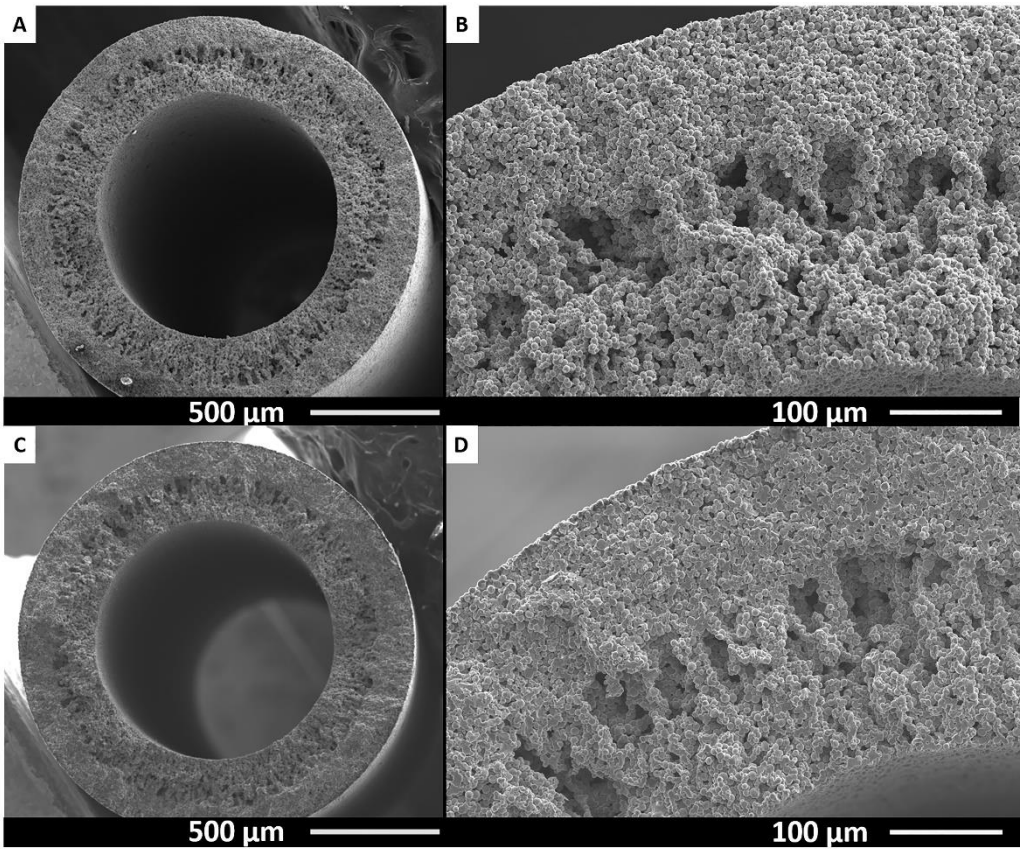

Figure 2.4. Cross section SEM images of Ti (A, B) and Ti-s (C, D).

Although the macrostructure appears similar after treatment at 1100 °C, an increased degree of particle sintering is observed using a higher magnification, as is displayed in Figure 2.5. Ti particles are more intimately connected after treatment at 1100 °C. In panel A the spheres are connected to less extent, as indicated by the breaking points. However, in panel B these breaking points constitute the particles themselves and a larger contact area can be seen. The SEM picture of the Ti/TiC sample (Figure 2.5c) shows particles connected in different ways from those in the Ti-type samples. The surface after breaking is significantly rougher, suggesting a multiple phase contact between the particles. This is likely due to the layer of TiC around the Ti particles, which is higher in hardness compared to Ti metal. Increased connectivity of the particles due to sintering is also visible for Ti/TiC-s (Figure 2.5d). The result appears less pronounced however when compared to

the Ti samples (Figure 2. 5a and b) likely due to almost twice as high melting point for TiC compared to Ti. The Ti/TiN and Ti/TiN-s materials (Figures 2.5e and f) show similar behavior to Ti and Ti-s. Since those samples were prepared via modification of the previously synthesized Ti and Ti-s structures, the connection between particles was already established prior to the nitridation step.

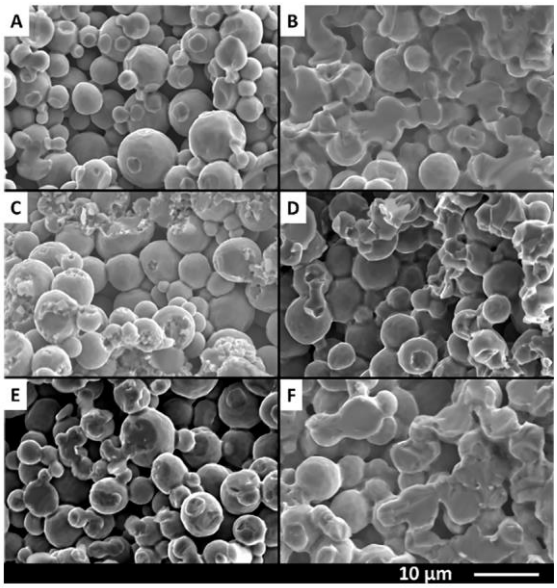

Figure 2.5. Cross section SEM images of (A) Ti, (B) Ti-s, (C) Ti/TiC, (D) Ti/TiC-s, (E) Ti/TiN and (F) Ti/TiN-s indicating the degree of sintering.

While EDS spectroscopy should be treated with care for quantitative analysis of light elements ($Z<11$) such as O, N and C, an indication of the elemental composition of the porous tubes, is presented in Table 2.2. The EDS data confirm the suggested composition for all types of the porous tubes, in agreement with XRD. Although adventitious carbon is present in all samples, notably more carbon is found for the Ti/TiO_x/C and Ti/TiC samples. Moreover, a significant amount of oxygen was found in Ti/TiO_x/C, what confirms the presence of TiO_x after treatment Ti-1. Additionally, the C-content of 11.6 % suggests that organic residue from the polymer might still be present in the sample. In Ti sample, oxygen is no longer detected, thus the heat treatment in Ar seems to reduce the previously present TiO_x by reaction with the C-residue. This is supported by the absence of a TiC peak in the XRD pattern of the Ti sample (Figure 2.3a). The Ti/TiC sample contains a significantly higher amount of C and no oxygen. The presence of sulfur suggests that the source of this carbon is the pyrolyzed polymer.

Table 2.2. EDS data of all types of porous tubes.

Element (%)	Ti/TiO_x/C	Ti	Ti-s	Ti/TiC	Ti/TiC-s	Ti/TiN	Ti/TiN-s
Ti	63.8	93.5	93	75.4	73	74.1	74.5
C	11.6	6.5	7	23.6	25.8	4	6
S	-	-	-	1	1.2	-	-
N	-	-	-	-	-	21.9	19.5
O	24.6	-	-	-	-	-	-

Formation mechanism of the variable Ti surface compositions

In order to clarify the chemistry during thermal treatments that led to Ti and TiC, several TGA-MS measurements were performed. TiN formation from Ti and N_2 by thermal treatment is a method often reported in the literature and will not be discussed in detail [18–20]. In order to obtain metallic Ti porous tubes from dry-wet spinning, the polymer needs to be removed. PES has a distinct two-step decomposition in air; the oxygen bonds (ether and sulfone groups) are released below 600 °C, whereas the decomposition of the aromatic ring structures is only achieved at temperatures above 600 °C.[16] This oxidation behavior in air, and the decomposition in Ar are shown in Figure 2.6a. The first oxidation regime is largely auto-oxidative since the same trend can be observed under an inert atmosphere.[17] Complete removal of PES can thus be achieved by thermal oxidation in air above 600 °C, but not in Ar. However, titanium is a material that readily oxidizes in conditions which are suitable for complete PES removal. Therefore thermal processing of Ti+PES has to be done with great care.

By keeping a relatively low temperature of only 475 °C it is possible to remove most of the ether and sulfone groups from the polymer, while slightly oxidizing Ti into semi-stable TiO_x (Figure 2.6b). The mass loss at the beginning of the measurement is attributed to the removal of water and NMP. Ti oxidation causes a slight increase in mass, prior to decay in weight loss related to the oxidation of PES. The weight loss due to PES oxidation in the sample is compensated by the growth of an oxide layer. A self-limiting growth of the TiO_x layer is clear from the TGA measurement as the curve can be seen to flatten near the end of the treatment. This layer can be considered a sub-stoichiometric oxide of Ti, thus stable TiO_2 layer is not formed. Therefore this layer may be used to oxidize the remaining carbon species under the right conditions in the next step of the thermal treatment sequence. Mass-spectrometry data from the TGA measurements further clarify that the thermal decomposition of PES under an Ar or air atmosphere (Figure S2.5) is in line with reports in the literature.[16,17]

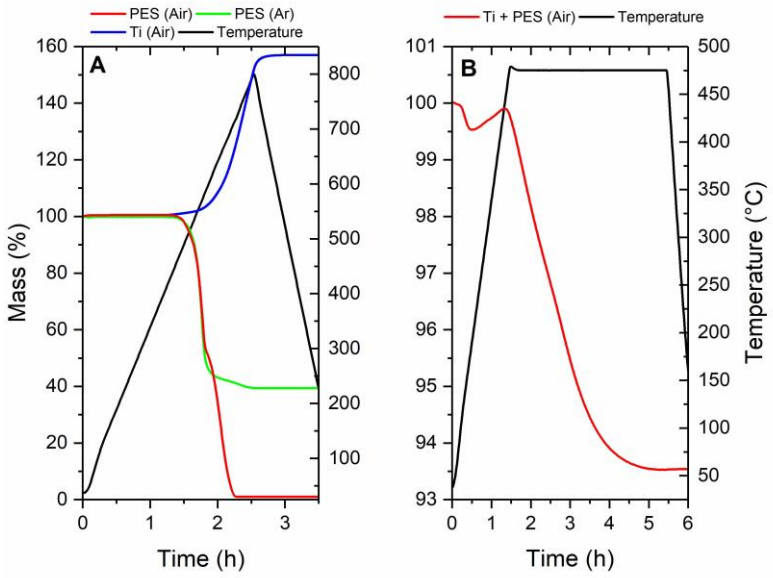

Figure 2.6. TGA of (a) PES in air and Ar atmospheres and Ti powder in an air atmosphere and (b) Ti+PES fiber in air (Ti-1).

MS analysis of the furnace exhaust (Figure 2.7) during thermal treatment of the samples allows further insight into the chemical processes that occurs during the PES decomposition and Ti oxidation. The three major decomposition products are tracked over time, being m/z 44, 64 and 78 which is assigned to CO_2, SO_2 and benzene respectively (with consideration of the fragmentation peaks).

During low temperature oxidation in air atmosphere at 475 °C (Ti-1) mostly oxidized decomposition products, such as CO_2 and SO_2, are released (with the presence of a small amount of benzene), which is in agreement with PES decomposition measured by TGA in air. From this MS result and TGA data, it can be judged that the initial oxidation of PES has been completed after treatment step Ti-1.

Following thermal treatment step in Ar (Ti-2) was performed at 800 °C to facilitate at least a minimum level of particle sintering, while preventing reaction of Ti with the substrate. During the heating stage, relatively small signals for both CO_2 and SO_2 are observed, while a more significant change is observed for the benzene-type fragment (Figure 2.7b). The formation of CO_2 and SO_2 is attributed to the reaction of the sub-stoichiometric Ti-oxide formed at 475 °C with residuals of the decomposed PES. The elegance of this two-step PES removal is that it allows for the formation of metallic Ti fibers without significant quantities of Ti-oxide or TiC.

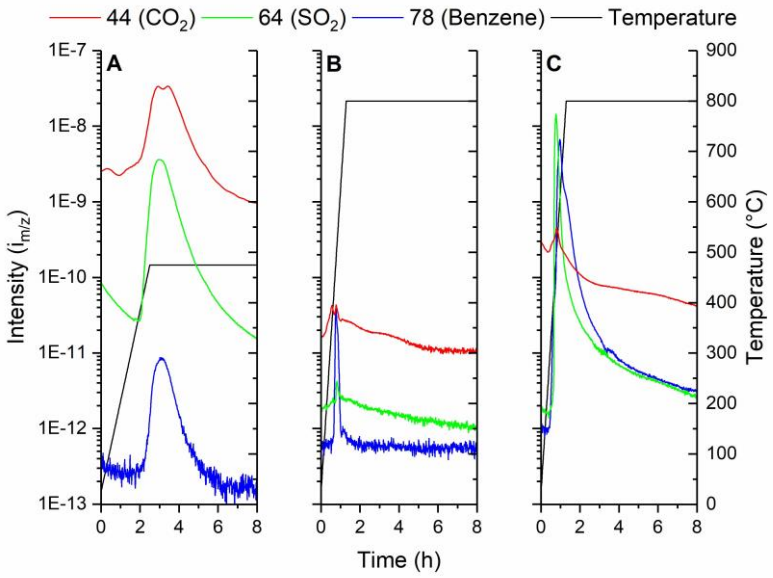

Figure 2.7. MS data from the furnace exhaust for (A) step Ti-1, (B) step Ti-2 and (C) step TiC-1.

In conditions required for Ti/TiC fibers preparation (TiC-1), CO_2 and SO_2 are still formed due to auto-oxidation. A significant increase in the signal for benzene compounds is observed due to the thermal decomposition of PES. The auto-oxidation of the sulfone and ether bonds appears to drive the polymer break-up since the CO_2 and SO_2 signal maximum appears before the one attributed to benzene compounds. The carbon residues which remain from decomposing the PES eventually lead to the formation of TiC at higher temperatures.

Physical properties of the fibers

Certain characteristic properties for the obtained porous tube electrodes are reported in Table 2.3 (see Figure S2.6, S2.7, and S2.8 for porosity, resistivity, and bending strength data respectively). First, a limited influence of sintering (800 °C vs 1100 °C) on the structural parameters can be observed. When sintering the Ti-based materials at 1100 °C the reversible phase transition from Ti-α to Ti-β (around 890 °C) occurs, resulting in the known densification of the material due to the increased sintering rate.[9] Consequently, a slight decrease in the outer diameter (OD), wall thickness, and pore size of the fibers can be noted. Furthermore, sintering leads to a relatively equal decrease in pore size for the Ti and Ti/TiN fibers, which shows that nitrogen incorporation has a minimal effect on the general geometry of the samples. The initial smaller pore size of the Ti/TiC samples indicates the presence of a rather thick TiC shell, which can increase the average particle size. The

decrease in pore size is less significant after sintering treatment which can be explained by the melting point of TiC which is ~1000 °C higher compared to Ti.

Bending strength measurements also indicate improved contact between particles after sintering. For Ti and Ti/TiN samples, the bending strength doubled after sintering at 1100 °C. Although Ti/TiC samples have the highest bending strength (TiC is known to have superior hardness to Ti), the increase after additional sintering is less prominent, again due to the higher melting point of TiC. Incorporation of nitrogen should also have resulted in enhanced bending strength, given the properties of TiN in comparison to Ti. Interestingly, it appears to have weakened the structure which can be related to the limited penetration of nitrogen into the individual Ti particles, due to the relatively mild conditions for TiN preparation.[19,20] The presence of two TiN phases (TiN and Ti_2N) further implies a disruptive boundary is present, resulting in a rather brittle shell around the Ti core. It can be improved through optimization of the nitridation procedure by increasing the temperature and time of the treatment. However, this is beyond the scope of this study.

The most striking results of Table 2.3 are resistivity values. Although numerous approximations exist for the expression of conductivity in porous materials,[21–23] it was found that these equations are not readily applicable to the pore systems which are obtained for the hollow fibers, since it is not possible for the shape parameter to be expressed or approximated with the data available.[24] Therefore the measured resistivity is presented and no adjustments have been made for the porous structure. The resistivity values found in the literature are; Ti: 0.42 μΩ·m, TiC: $8 \cdot 10^3$ μΩ·m, and TiN: $1.3 \cdot 10^{12}$ μΩ·m,[25] while those reported in Table 2.3 for the TiC and TiN containing composites are all within the range of 4-10 μΩ·m. This suggests that in all cases electrical conduction is predominantly established through Ti-Ti contacts, thus metallic Ti dominates the electrical conductivity. As previously mentioned, for the TiN samples the Ti-Ti contacts are established in the sintering procedure before conversion to TiN. For the TiC containing samples, the low resistivity suggests that during thermal treatment the formation of Ti-Ti contacts, followed by conversion of the outer Ti layer to TiC occurs. If the inter-particle contacts would be composed of TiN or TiC with high intrinsic resistivity, the apparent resistivity should increase. On the contrary, the presence of TiC or TiN, likely in an outer, but crystalline shell, results in lower resistivity, which can be attributed to the insulating layer of TiC or TiN preventing capacitive effects at the Ti/air interface.[26] The densification of the materials after additional sintering treatment results in an expected lower resistivity.

Significant improvement in resistivity was obtained in this study compared to the Ti-based porous tubes reported in the literature.[4] A resistivity value of approximately $33 \cdot 10^3$ μΩ·m was recalculated from the available data, compared to about 5 μΩ·m found in this work. It

is reasoned that the difference originates from the preparation procedure. The method reported in the literature uses 600 °C in air for oxidation of the polymer from the as-spun fiber. At this temperature, significant oxidation of titanium occurs thus high quantities of TiO_2 can be expected in such material, which can significantly increase the resistivity of the porous tube. In this work, by polymer oxidation at 475 °C, the formation of titanium dioxide can be significantly prevented, in particular when oxidation is followed by the treatment in Ar at 800 °C, resulting in a much lower resistivity.

Table 2.3. Comparison of different properties of all prepared porous tubes (95% confidence interval is given between brackets).

Sample	OD (mm)	Wall (mm)	Porosity (%)	Max pore size (µm)	MFP size (µm)	Min pore size (µm)	Bend. strength (MPa)	Resistivity (µΩ·m)
Ti	1.70 [0.04]	0.50 [0.02]	59 [2]	2.92 [0.05]	1.62 [0.02]	1.30 [0.06]	63 [5]	9.58 [0.70]
Ti/TiC	1.71 [0.02]	0.49 [0.04]	58 [2]	2.64 [0.03]	1.57 [0.02]	1.23 [0.04]	126 [4]	5.72 [0.30]
Ti/TiN	1.74 [0.04]	0.49 [0.02]	61 [2]	2.98 [0.08]	1.63 [0.03]	1.35 [0.08]	51 [3]	5.50 [0.22]
Ti-s	1.58 [0.07]	0.44 [0.03]	49 [5]	2.34 [0.08]	1.28 [0.06]	0.96 [0.06]	131 [6]	5.38 [0.58]
Ti/TiC-s	1.67 [0.04]	0.43 [0.03]	53 [4]	2.56 [0.04]	1.34 [0.04]	1.00 [0.03]	195 [7]	4.73 [0.47]
Ti/TiN-s	1.62 [0.03]	0.48 [0.03]	55 [2]	2.35 [0.05]	1.32 [0.04]	1.05 [0.04]	102 [5]	4.12 [0.29]

Conclusion

We have developed a systematic approach for the production of Ti hollow fibers of variable composition. In order to obtain a purely metallic Ti porous electrode after dry-wet spinning using PES and NMP, decomposition of PES in the presence of oxygen should be performed at mild temperatures (475 °C). Then, treatment in Ar at 800 °C is applied to decompose the oxide, concurrently removing residual PES fragments. If the formation of Ti/TiC is desired, treatment in Ar at 800 °C suffices, without the prior oxidation step. Ti-fibres can be converted to Ti/TiN at 800 °C in a nitrogen atmosphere. Generally, the produced fibers show high bending strength and remarkably low electrical resistance, which is further improved by sintering at 1100 °C. These properties make them suitable for various applications in the field of electrochemistry.

References

[1] M. W. J. Luiten-Olieman, L. Winnubst, A. Nijmeijer, M. Wessling, N. E. Benes, *J. Memb. Sci.* **2011**, *370*, 124–130.

[2] M. W. J. Luiten-Olieman, M. J. T. Raaijmakers, L. Winnubst, T. C. Bor, M. Wessling, A. Nijmeijer, N. E. Benes, *J. Memb. Sci.* **2012**, *407–408*, 155–163.

[3] R. Kas, K. K. Hummadi, R. Kortlever, P. De Wit, A. Milbrat, M. W. J. Luiten-Olieman, N. E. Benes, M. T. M. Koper, G. Mul, *Nat. Commun.* **2016**, *7*, 1–7.

[4] O. David, Y. Gendel, M. Wessling, *J. Memb. Sci.* **2014**, *461*, 139–145.

[5] I. Merino-Garcia, J. Albo, P. Krzywda, G. Mul, A. Irabien, *Catal. Today* **2020**, *346*, 34–39.

[6] D. Bell, D. Rall, M. Großeheide, L. Marx, L. Hülsdünker, M. Wessling, *Electrochem. commun.* **2020**, *111*, 106645.

[7] M. Nunez, ed., *Trends in Electrochemistry Research*, Nova Science Publishers, Inc. New York, **2007**.

[8] D. R. Lide, ed., *CRC Handbook OfChemistry and Physics, Internet Version 2005*, CRC Press, Boca Raton, FL, 2005, **2005**.

[9] M. Qian, G. B. Schaffer, C. J. Bettles, in *Sinter. Adv. Mater. - Fundam. Process.*, **2010**, pp. 324–355.

[10] E. Tal-Gutelmacher, D. Eliezer, *Jom* **2005**, *57*, 46–49.

[11] T. Smith, *Surf. Sci.* **1973**, *38*, 292–312.

[12] W. D. Sylwestrowicz, *J. Electrochem. Soc.* **1975**, *122*, 1504.

[13] I. Vaquila, L. I. Vergara, M. C. G. Passeggi, R. A. Vidal, J. Ferrón, *Surf. Coatings Technol.* **1999**, *122*, 67–71.

[14] Y. Mizuno, F. K. King, Y. Yamauchi, T. Homma, A. Tanaka, Y. Takakuwa, T. Momose, *J. Vac. Sci. Technol. A Vacuum, Surfaces, Film.* **2002**, *20*, 1716–1721.

[15] E. Gemelli, N. H. a. Camargo, *Matéria (Rio Janeiro)* **2007**, *12*, 525–531.

[16] X. G. Li, H. T. Shao, H. Bai, M. R. Huang, W. Zhang, *J. Appl. Polym. Sci.* **2003**, *90*, 3631–3637.

[17] P. Tranchard, S. Duquesne, F. Samyn, B. Estèbe, S. Bourbigot, *J. Anal. Appl. Pyrolysis* **2017**, *126*, 14–21.

[18] H. Rode, V. Hlavacek, *Combust. Sci. Technol.* **1994**, *99*, 143–160.

[19] H. Rode, V. Hlavacek, *AIChE J.* **1995**, *41*, 377–388.

[20] C. Li, X. Lv, J. Chen, X. Liu, C. Bai, *Int. J. Refract. Met. Hard Mater.* **2015**, *52*, 165–170.

[21] T. Mori, K. Tanaka, *Acta Metall.* **1973**, *21*, 571–574.

[22] I. Sevostianov, V. Kushch, *Int. J. Solids Struct.* **2009**, *46*, 4419–4429.

[23] B. Q. Li, X. Lu, *Transp. Porous Media* **2011**, *87*, 179–189.

[24] I. Sevostianov, J. Kováčik, F. Simančík, *Mater. Sci. Eng. A* **2006**, *420*, 87–99.

[25] J. F. Shackelford, W. Alexander, *CRC Materials Science and Engineering Handbook*, Boca Raton: CRC Press LLC, **2001**.

[26] R. J. D. Tilley, *Understanding Solids: The Science of Materials*, John Wiley & Sons, Ltd., United Kingdom, Chichester, **2013**.

Supplementary information 2

Materials

Titanium powder (ASTM, grade 2), particle size average 6 μm, was obtained from TLS Technick GmbH & Co. Polyethersulfone (PES, Ultrason E 6020P, BASF) was used as binder, and N-methylpyrrolidone (NMP, Sigma Aldrich) as solvent.

Characterization

Prepared porous tubes were characterized by X-Ray Diffraction (XRD, Bruker Phaser D2) and Scanning Electron Microscopy (SEM) coupled with Energy-dispersive X-ray spectroscopy (EDS) (JSM-6010LA, JEOL system). X-ray photoelectron spectroscopy (XPS) spectra were recorded on a Quantera SXM (scanning XPS microprobe) spectrometer from Physical Electronics, in which X-rays were generated from an Al Kα source, emitting at 1486.6 eV. Thermogravimetric analysis (TGA) was performed on an STA 449 F3 Jupiter, Netzch, TGA-system, using a 5 °C/min heating rate, unless otherwise indicated. TGA-MS was performed by combining the TGA-system with a mass spectrometer (1 to 100 m/z, QMS 403 D Aëolos, Netzch). The furnace exhaust was monitored using a mass-spectrometer (1 to 100 m/z, OMNISTAR, THERMOSTAR, GSD 320 Gas Analysis System, Pfeifer vacuum). Porosity was calculated from the measured apparent density of samples with known volume and weight. The pore size distribution was measured by capillary flow porometry based on the liquid extrusion technique, using a Porolux 500 Porometer. The bending strength was determined using the four-point method with a 20 mm span size, on the mechanical strength testing system INSTRON 5942. The resistivity was determined by a four-probe method using a BioLogic potentiostat. Current was initiated between the two outer probes across 88.5 mm and the voltage was measured between the two inner probes across 72.5 mm of the tube. For the porosity, conductivity, and pore size distribution, an average of 10 samples was reported. For the bending strength, every specimen in a sample group of ten had three segments tested, making a total of 30 points for any sample type.

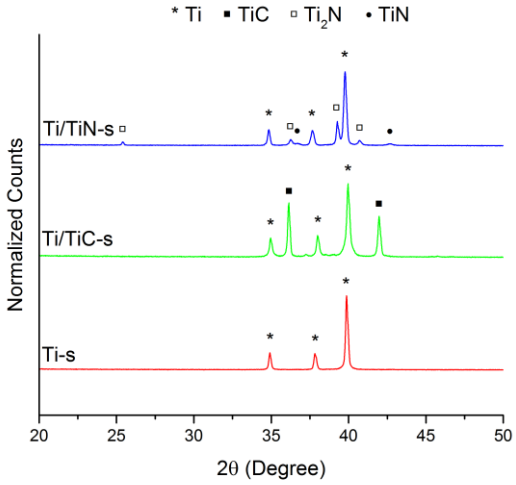

Figure S2.1. XRD of Ti-s, Ti/TiC-s and Ti/TiN-s

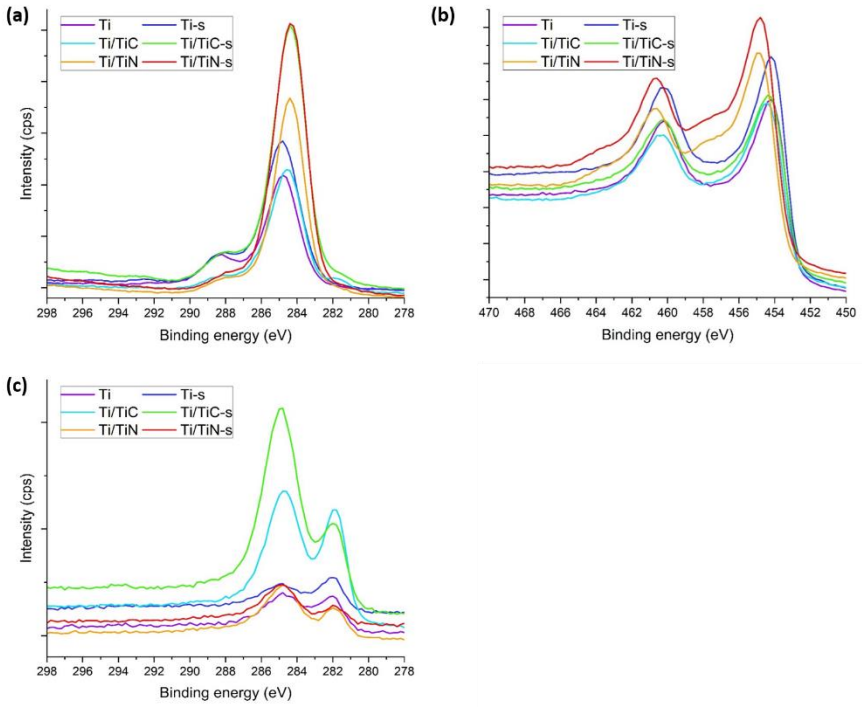

Figure S2.2. XPS spectra of prepared hollow fibers. (a) C 1s spectra, (b) Ti 2p spectra of sputtered samples and (c) C 1s spectra of sputtered samples.

In Figure S.2.2a C1s spectra of prepared hollow fibers are shown. The peak at 284.5 eV till 285.5 eV is typically assigned to adventitious carbon. TiC can be identified by the peak at ~282 eV. The peak at 288 eV is due to the presence of some surface carbonate.[S1]

Figure S.2.2b and c show Ti2p and C1s spectra of sputtered samples. The acquisition areas for the core spectra were sputtered for 2 minutes with a 3kV 3x3mm² Ar ion source. On flat titanium, this would remove approximately 10 nm of material. Since the hollow fibers are composed of sphere-like particles, sputtering is likely less effective and does not remove surface contaminations entirely. General references that have been used for interpretation of the spectra [S2],[S3].

Sputtering has reduced the amount of oxide present on top of the layer although as mentioned before this, due to the sample structure, this only has a limited effect. Ar ion sputtering removes the metal-oxide layer which would allow for better interpretation of the metallic state, however, due to the oxygen scavenging nature of Ti this remains in a lower valence oxide state (likely the majority is Ti^{3+}). However, the Ar ion sputtering of a metallic compound in the vicinity of a carbon source results in conversion to a metal carbide. Hence TiC is dominant in the spectra of Ti and Ti/TiC, and the thickness of the TiC layer cannot be estimated.[S1],[S4] It can also be seen in C1s spectra where TiC is observed in each sample. The TiN samples are less prone to carbide formation. The spectra of the Ti/TiN composites are significantly shifted towards higher binding energy, indicating TiN is still a dominant species at the surface after sputtering.[S5]

[S1] J. Luthin, Ch. Linsmeier, *Physica Scripta*, **2001**, T91, 134-137

[S2] J. F. Moulder, W. F. Stickle, P. E. Sobol, K. D. Bomben, Handbook of X-ray Photoelectron Spectroscopy, **1992**, Perkin-Elmer Corporation, Eden Prairie

[S3] A. V. Naumkin, A. Kraut-Vass, S. W. Gaarenstroom, and C. J. Powell, NIST X-ray Photoelectron Spectroscopy Database 20, Version 4.1 (Web Version), http://srdata.nist.gov/xps

[S4] M.C. Biesinger, L.W.M. Lau, A. Gerson and R.St.C. Smart, *Applied Surface Science*, **2010**, 257, 887-898

[S5] D. Jaeger, J. Patscheider, *J. Electron Spectrosc. Relat. Phenom.* **2012**, 185, 523-534

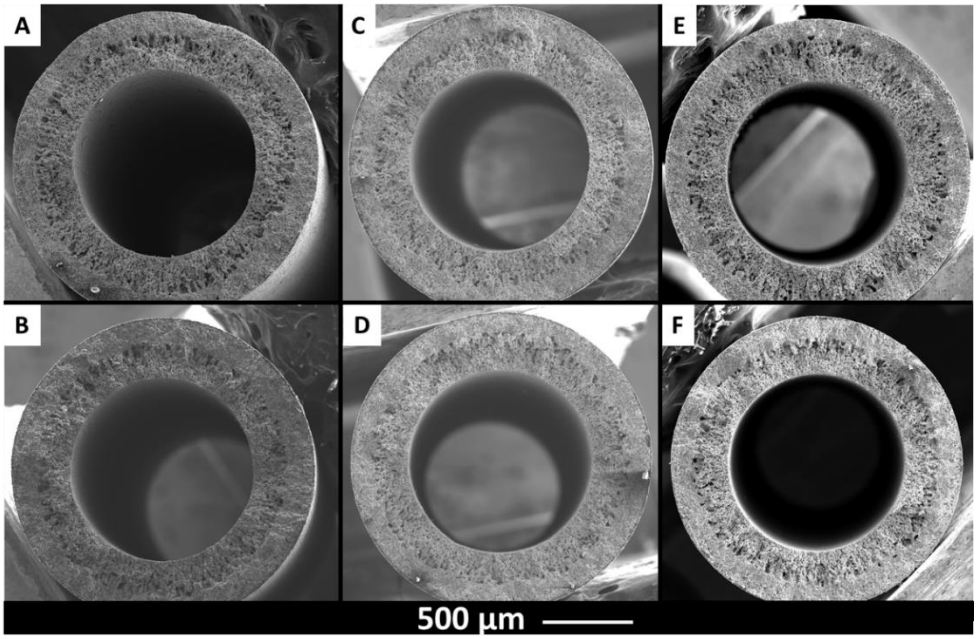

Figure S2.3. Cross-sectional SEM images of (A) Ti, (B) Ti-s, (C) Ti/TiC, (D) Ti/TiC-s, (E) Ti/TiN, (F)Ti/TiN-s.

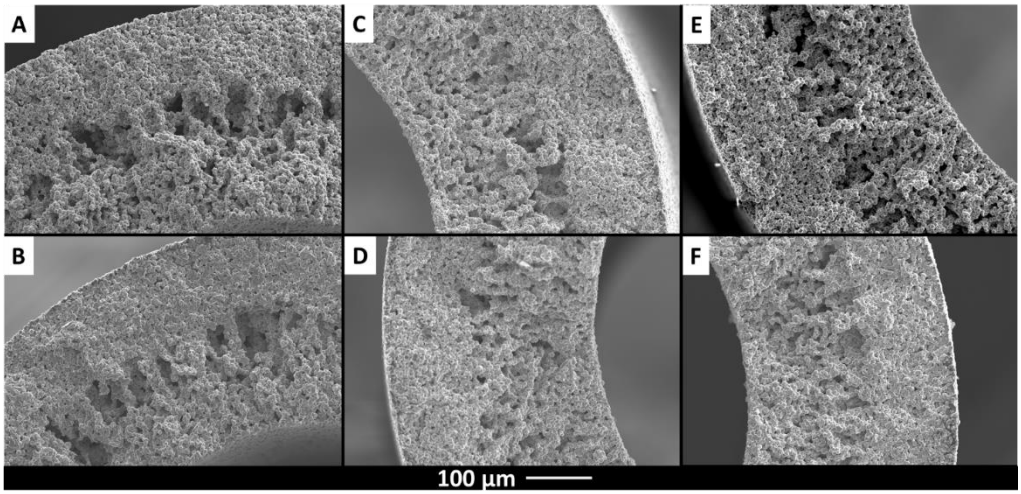

Figure S2.4. Cross-sectional SEM images of (A) Ti, (B) Ti-s, (C) Ti/TiC, (D) Ti/TiC-s, (E) Ti/TiN, (F)Ti/TiN-s at higher magnification.

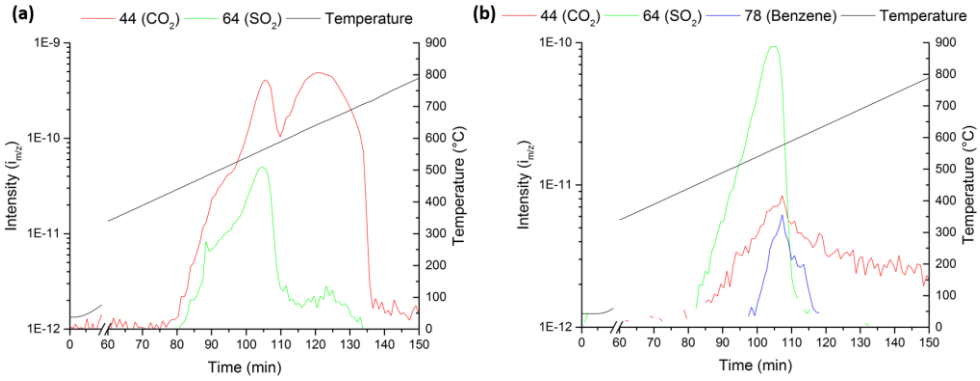

Figure S2.5. TGA-MS of PES in (a) air and (b) Ar.

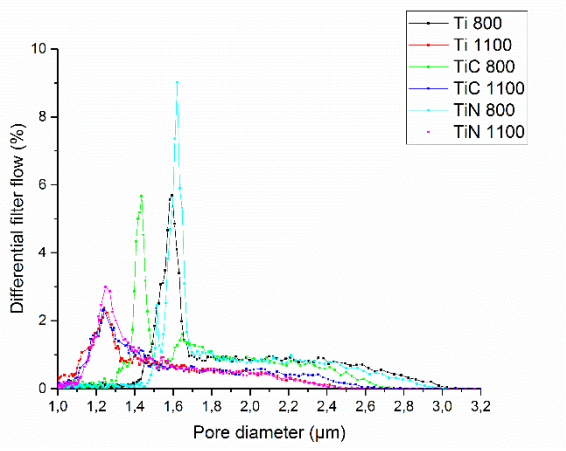

Figure S2.6. Pore size distribution obtained by capillary flow porometry.

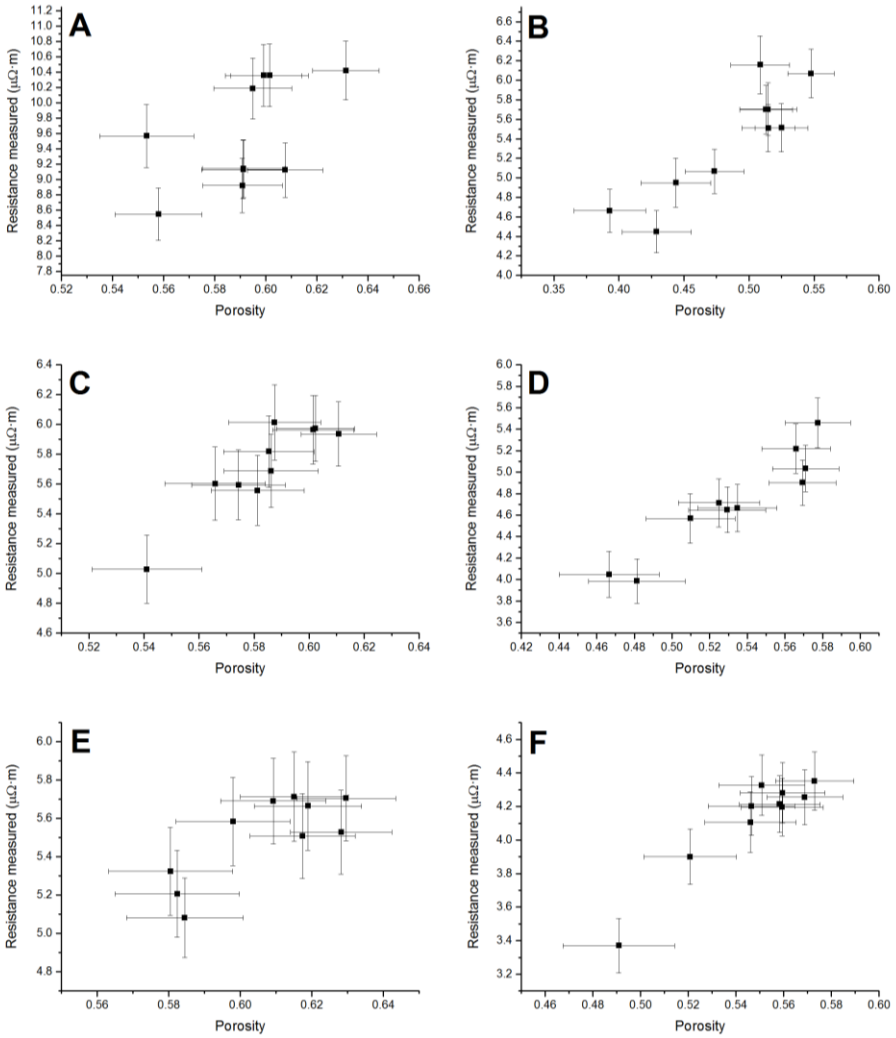

Figure S2.7. Resistance of (A) Ti, (B) Ti-s, (C) Ti/TiC, (D) Ti/TiC-s, (E) Ti/TiN, (F)Ti/TiN-s versus porosity.

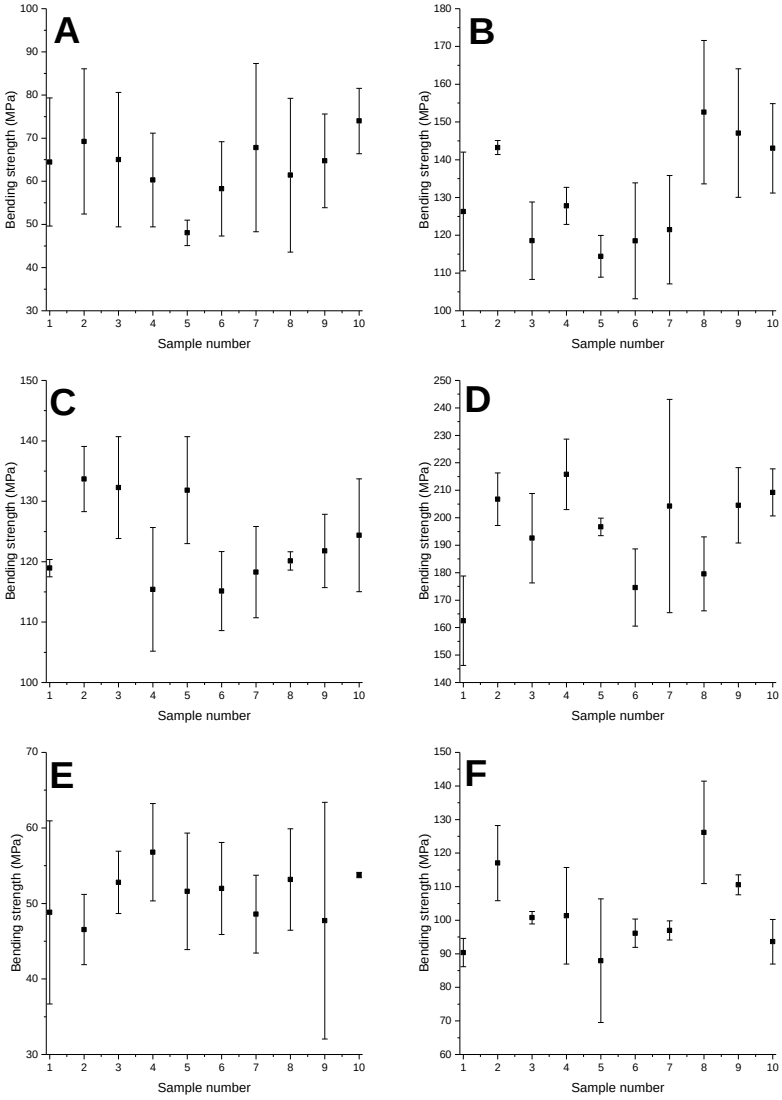

Figure S2.8. Bending strength of (A) Ti, (B) Ti-s, (C) Ti/TiC, (D) Ti/TiC-s, (E) Ti/TiN, (F)Ti/TiN-s measured on 10 different samples. Error bar indicate spread over 3 repetitions.

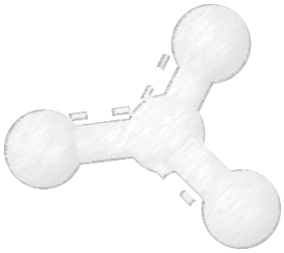

Chapter 3

Electroreduction of NO_3^- on tubular porous Ti electrodes

This chapter is based on:

P. M. Krzywda, A. Paradelo Rodriguez, L. Cino, N. E. Benes, B. T. Mei, G. Mul, "Electroreduction of NO_3^- on tubular porous Ti electrodes", *Catalysis Science* & *Technology*, **2022**, DOI:10.1039/D2CY00289B.

Abstract

Non-efficient fertilizer use in agriculture causes nitrate runoff, polluting rivers and streams. This pollution can be mitigated by partially converting nitrate into ammonia – rebalancing the composition to ammonium nitrate, and allowing recycling of fertilizer. Here, we present efficient electrochemical conversion of nitrate (50 mM) to ammonia in acidic electrolyte using tubular porous Ti electrodes. A high faradaic efficiency (FE) of 58 % and partial current density to ammonia of -33 mA/cm² at - 1 V vs RHE were achieved in the absence of inert gas purge. Additionally, we reveal the formation of hydroxylamine, as well as NO and N_2O by spontaneous decomposition of nitrite, as has been determined by EC-MS analysis. The effective increase in local mass transport by introducing a flow of inert gas exiting the wall of the hollow fiber electrode, results in an unprecedently high partial current density to ammonia of ~-75 mA/cm² while maintaining a faradaic efficiency of up to 45 %. This concept facilitates nitrate conversion at high FE even at low concentrations, and holds promise for development to practical scale if potential and exiting gas flow rate are well controlled.

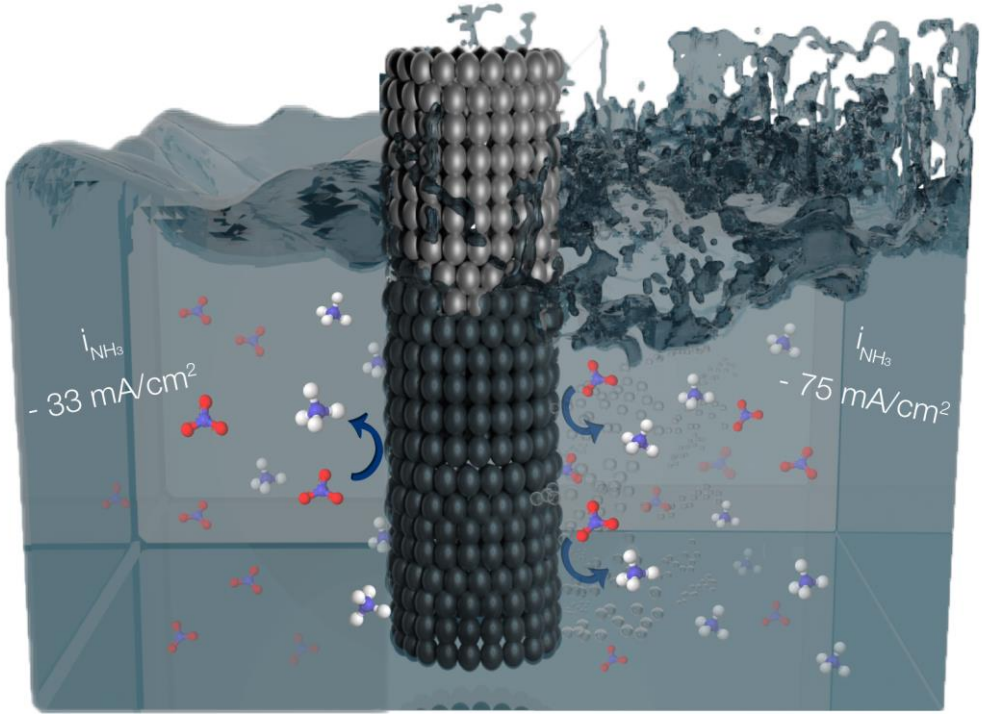

Introduction

The efficiency of food production in the agricultural sector depends on the efficient utilization of nitrogen-based fertilizers.[1] The production of fertilizer includes the industrial synthesis of NH_3 by the Haber-Bosch process, which largely contributes to the global carbon footprint.[2] Alternative approaches which allow for a more environmentally friendly, green ammonia synthesis are explored,[3] and electrochemical routes appear to be of particular interest for small-scale, renewable energy-based production facilities. Although N_2 is the most attractive resource for electrochemical ammonia production due to its abundancy,[4] the stability of the N_2 molecule limits the electrochemical conversion rates currently achieved, if any.[5] Waste streams containing NO_x have recently been considered as an alternative feedstock for green NH_3 synthesis, such as nitric oxide[6,7] and nitrate.[8–10]

Focusing on nitrate, various sources are available[11,12] and among others utilization of agricultural runoff might be of interest. Over-fertilization combined with low nitrogen utilization efficiencies in agriculture[13] result in fertilizer release into the groundwater, mostly in the form of nitrates. Ammonium nitrate produced from collected (possibly concentrated) and partially reduced nitrate can thus be considered as recycled fertilizer.[14] Alternatively, NO_3^- obtained from direct oxidation of nitrogen by an electrochemical[15–18] or plasma (catalytic)[19–23] approach might be available as a resource for ammonia production. It has been proven that plasma is potentially viable for electricity-based HNO_3 production,[24] which can be consecutively converted to ammonia in one process.[25,26] A decentralized, small-scale ammonium nitrate production unit for the production of carbon-free, green fertilizer also appears feasible. Still, nitrate electroreduction is complex,[27] and suitable electrode materials and configurations for efficient electrochemical production of ammonia still need to be developed. Moreover, research on the electroreduction of nitrate has been primarily performed for purification of drinking water, targeting selective reduction to nitrogen in neutral electrolyte conditions,[28] even though the kinetics of the reaction are more favorable in acidic or basic pH conditions.[29]

In general, Cu has been identified as a suitable electrode for nitrate reduction to ammonia,[30] yet in acidic electrolyte electrode stability is insufficient (e. g. by dissolution of Cu in (diluted) nitric acid solution[31]). Titanium, which is available at a low cost,[32] has been reported as one of the elements offering high stability in various process conditions, and allows operation in an extended electrochemical window due to poor activity for hydrogen evolution. Efficient removal of nitrate was reported in acidic conditions using a Ti cathode and a Pt anode,[33] and preferential ammonia formation rather than N_2 formation was reported.[32] Recently, metallic Ti plates were extensively studied, and the best NH_3

selectivity was observed at high nitrate concentration and in strongly acidic pH conditions, which result in both, high abundance of NO_3^- and H^+ at the Ti surface.[29] DFT calculations suggest that a combination of Ti and graphitic carbon nitride is potentially interesting for the efficient formation of ammonia.[34] Finally, TiO_2 nanotubes with a high concentration of oxygen vacancies (TiO_{2-x}) were reported to produce NH_3 with 85 % faradaic efficiency in neutral pH,[35] further improved to 92 % by additional functionalization with Pd.[36] Still high faradaic efficiencies are only observed at low to moderate current densities.

Low current densities are most likely caused by mass transport limitations of the reactant, especially when nitrate is present in low concentrations.[37,38] A low concentration of nitrate close to the electrode surface results in preferential hydrogen production, and clearly high mass transport rates are required to improve process efficiency. Specific catalyst design,[39] reactor design,[40] increasing the NO_3^- concentration,[29] or inducing efficient convection in the cell have been investigated to mitigate mass transfer limitations. Hollow fiber-based electrode geometries were shown to enable efficient reactant gas supply to the electro-active surface thus minimizing mass transport problems caused by the low solubility of reactants in aqueous solutions.[6,41–43] Similarly, hollow fiber electrodes might circumvent mass transport problems observed for reactions where reactants are exclusively supplied from the electrolyte.

Herein, we report the use of Ti based hollow fiber electrodes for electrochemical nitrate reduction in acidic electrolyte. We will compare a case of conventional mixing by gas introduction through a separate sparger, with conditions of efficient mixing near the solid-liquid interface by introducing an inert gas flow through the porous wall of the electrode. We will demonstrate that low concentrations of nitrate (50 mM KNO_3) can be converted to ammonia at high partial current densities and that the concept of flow-induced mixing significantly improves nitrate conversion. We suggest that this concept might be generally applicable for systems limited by mass transport.

Experimental section

Electrode preparation and characterization

Ti hollow fibers were prepared by dry-wet spinning according to a previously reported method.[44] In brief, Ti powder was mixed with polyethersulfone (PES) and N-methylpyrrolidone (NMP) to form a homogeneous suspension. The spinning mixture was pressed through a spinneret with water as a bore liquid. Fibers were thermally treated at 800 °C in order to remove the polymer and form the metallic hollow fiber. Ti fibers sintered at 800 °C were used in this work.

Hollow fiber electrode assemblies were prepared using silver epoxy glue to ensure electrical contact to a Swagelok stainless steel tube (Figure S3.1). The assembly was covered with two-compartment adhesive glue to prevent contact of silver or the stainless steel tube with the electrolyte. To ensure homogeneous distribution of gas through the fibers, the open-end of the fiber was also covered with adhesive. Electrodes were characterized using Scanning Electron Microscopy (SEM) (JSM-6010LA, JEOL system) and X-ray diffraction (XRD, Bruker Phaser D2). For EC-MS experiments a Ti disc (⌀ 5 mm) was polished following the routine of cleaning provided by Pine Research.

Electrochemical measurements

All electrochemical measurements were carried out at room temperature using a BioLogic VSP potentiostat. A gas-tight, H-type cell (a Nafion 117 membrane was used for compartment separation) was used for linear scan voltammetry and chronoamperometry experiments. A Pt mesh and Ag/AgCl (3 M NaCl, BASi) were used as counter and reference electrode, respectively. Measured potentials were corrected for the solution resistance (iR drop) and converted to potentials vs RHE using:

$$E_{RHE} = E_{Ag/AgCl} + 0.059\,pH + E^{0}_{Ag/AgCl}$$

Nitrate concentrations between 1 and 50 mM KNO_3 were tested. To minimize differences in solution resistance the total amount of ions was adjusted by using potassium perchlorate. The cell was purged with Ar for 30 min prior to the experiments, to remove dissolved oxygen. Electrochemical measurements were performed using gas flow rates as specified, using either flow-through (Ar flow through the hollow fiber electrode) or no-flow (Ar was introduced through an external sparging line next to hollow fiber electrode) conditions. A schematic representation of the gas supply is shown in Figure S3.2. Linear scan voltammetry measurements were performed with a scan rate of 50 mV/s and stable LSVs are shown. Generally, chronoamperometry experiments were performed for 30 min in an acidic electrolyte (80% iR drop corrected- see Table S3.2).

Stability measurements were performed for 4 h. The electrolyte was refreshed after 3 h if no flow was used, and every 1 h for experiments performed in flow-through mode using an Ar flow of 20 ml/min. The electrochemical surface area (ECSA) of the hollow fiber electrodes was measured before and after the stability test by the capacitance method. Cyclic voltammograms in the purely capacitive potential were measured at variable scan rates from 20 to 100 mV/s in Ar saturated 0.1 M $KClO_4$. Product detection and quantification (calibration curves see Figure S3.3 – S3.5) are described in detail in the supporting information.

To further analyze the product composition EC-MS measurements were performed using a SpectroInlets (Copenhagen, Denmark) system, with He as carrier gas at a flow rate of 1 ml/min. Chronoamperometry was performed at different potentials. Potentials were applied for 30s. Afterwards the system was allowed to rest at OCV conditions in between potential pulses. An Ag/AgCl (sat. KCl, CH Instrument) and a Pt mesh were used as reference and counter electrode respectively. Counter and working compartments are separated by a borosilicate filter, which in combination with the long distance between the electrodes prevents product diffusion from one to the other electrode. The schematic representation of the cell design is shown in Figure S3.2. Decomposition experiments using the EC-MS set-up were performed without the electrode assembled. Here, the chip was covered with the electrolyte and a solution of interest was dropped into the electrolyte to determine the decomposition products.

Results and discussion

Ti electrode characterization

Compared to widely employed flat electrodes, hollow fiber electrodes allow for gas supply through the porous structure of the wall into the electrolyte. The gas distribution is largely dependent on the porosity of the wall. SEM images (Figure 3.1) of a representative Ti hollow fiber reveal the uniform pore distribution over the entire length of the fiber, which should lead to homogeneous gas distribution. The XRD pattern shows that the hollow fiber is composed solely of metallic Ti.[44]

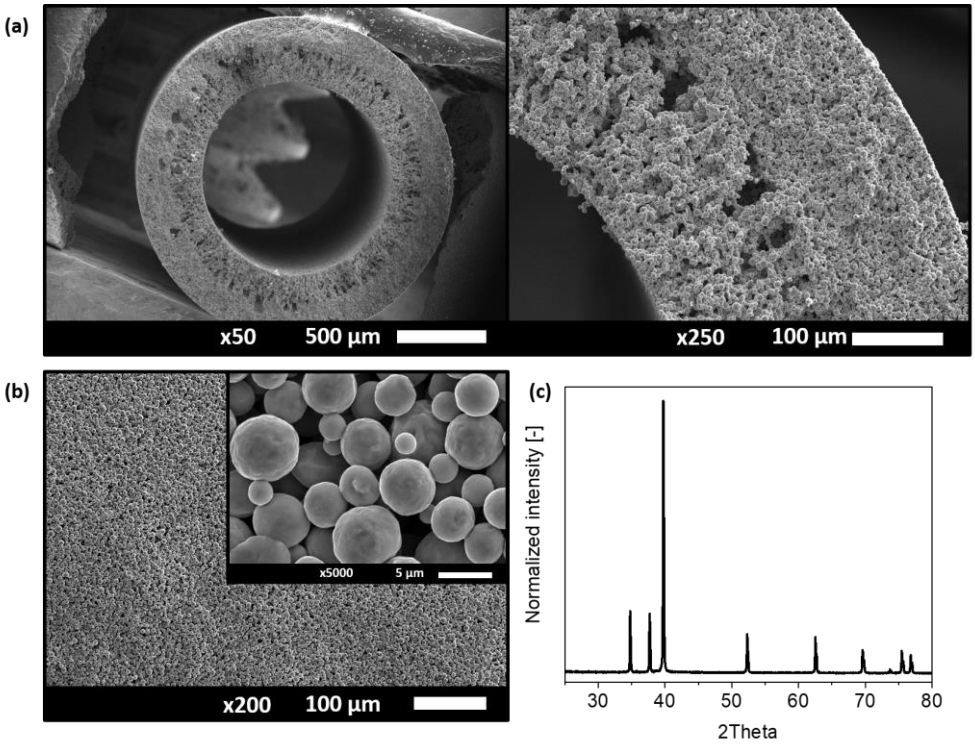

Figure 3.1. Characterization of Ti hollow fiber electrode. SEM images of (a) the cross section at different magnifications and (b) the surface of the fiber. (c) XRD pattern obtained from the Ti hollow fiber electrode.

NO_3^- electroreduction on a Ti electrode

Voltammetry

The activity of the Ti hollow fibers was tested for NO_3^- electroreduction in 0.1 M $HClO_4$ (pH 1) and 0.1 M $KClO_4$ (pH 7) using KNO_3 as nitrate source in different concentrations. For experiments performed in the neutral electrolyte (Figure S3.6) a relatively high onset potential of ~-0.6 V vs RHE is observed. Increasing concentrations of KNO_3, as well as mixing induced by gas flow through the electrode, have only a minor effect on the current density, suggesting an overall low activity for NO_3^- electroreduction. This is likely due to the sluggish kinetics of the H_2O reduction, caused by the additional dissociation step.[45,46]

Linear scan voltammetry performed in 0.1 M $HClO_4$ at different NO_3^- concentrations are shown in Figure 3.2a. In contrast to the onset potential in neutral conditions, here it is already observed at -0.05 V vs RHE, and significantly higher current densities can be achieved (Figure S3.7), indicating faster kinetics of NO_3^- reduction in acidic conditions.[29]

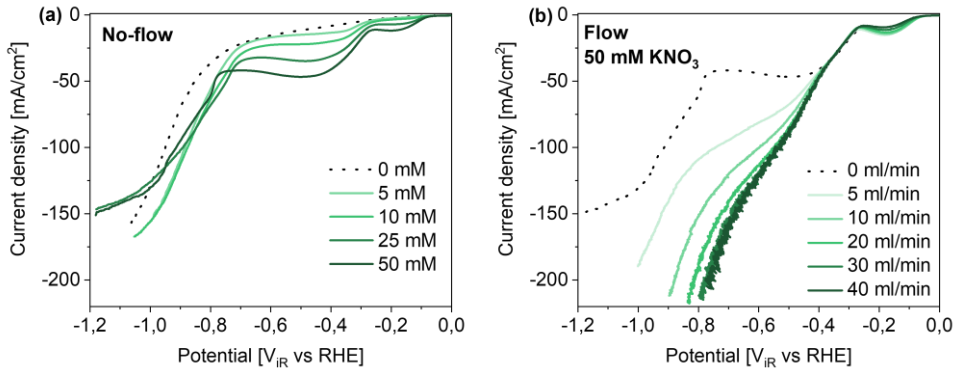

Figure 3.2. Linear scan voltammetry using Ti hollow fiber electrodes in 0.1 M $HClO_4$. (a) The influence of nitrate concentration (KNO_3) in "no-flow" conditions and (b) the influence of Ar flow rate on current density at 50 mM KNO_3.

With increasing KNO_3 concentration, two plateau-like regions are observed before the hydrogen evolution occurs at potentials < -0.8 V vs RHE (Figure 3.2a). The first plateau region starting at ~ -0.1 V vs RHE has previously been assigned to the reduction of NO_2[6], formed in a 1 e^- transfer reaction form NO_3^- (see Table S3.1). Afterwards in the potential range between -0.3 V and ~ -0.8 V vs RHE, a second mass-transport limited region is observed, which becomes more obvious at increasing nitrate concentrations. Besides nitrate, we also suggest that proton transport becomes limiting at relatively high nitrate concentrations, considering that the reduction of NO_3^- to ammonia requires 9 H^+ (see Table S3.1). In fact, it was previously reported that H^+ transport limitations in NO_3^- electroreduction on a flat Ti electrode in acidic electrolyte can occur already at ~ -25 mA/cm², in nitrate concentrations of 0.1 M.[29] Presumably, hydrogen evolution (HER) starts to compete at potentials < -0.8 V vs RHE, as indicated by the current increase also observed in the absence of NO_3^-. Finally, linear sweep voltammetry also reveals the diffusion limitation of proton reduction at potentials below approx. -1 V vs RHE.

Flow-through experiments using Ar as an inert sparging gas were subsequently performed at various flow rates and a constant concentration of nitrate (50 mM) (Figure 3.2b). At moderate flow rates of 5 mL.min^{-1}, a significant increase in diffusion-limited current is obtained in the potential range between -0.3 V and ~ -0.8 V vs RHE as shown in Figure 3.2b, while increasing the flow to 20 mL.min^{-1} further enhances the current density, to unprecedented values for Ti hollow fibers, as high as 200 mA.cm^{-2}. Likely, higher flow rates cause additional (smaller) pores between the sintered Ti particles to open,[6] inducing more efficient, homogeneous mixing at the solid-liquid interface. It should be mentioned that the extent of enhancement of current density by gas flow, is a function of the nitrate

concentration. Specifically, at lower NO_3^- concentrations, gas flow affects the system to a lower extent (see Figure S3.8). In blank experiments and at the lowest nitrate concentrations (1 mM KNO_3) only the HER seems to be affected by the introduction of a gas flow, as a result of the mitigation of proton transport limitations and likely improved hydrogen bubble release. Thus, the observed impact of gas flow through the porous wall of the hollow fiber confirms that transport of both, NO_3^- and H^+ to the electrode surface is significantly improved by local mixing (see Figure S3.9 for a schematic representation).

Selectivity towards ammonia

The selectivity of the Ti hollow fiber electrodes towards ammonia was further studied using electrolytes containing 50 mM of KNO_3. The reported faradaic efficiency was determined using chronoamperometric measurements with a duration of 30 min.

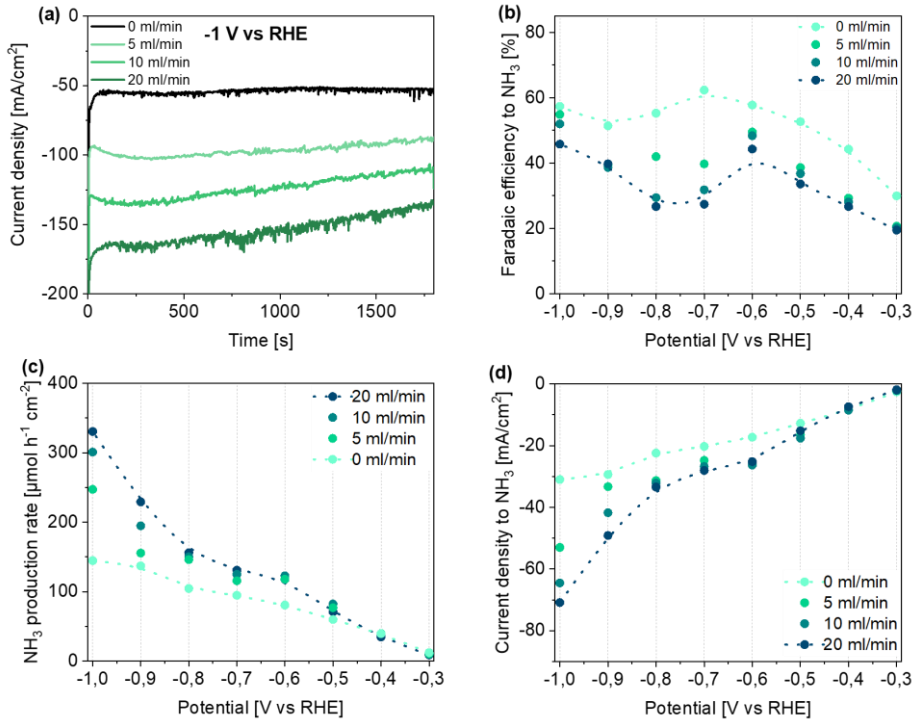

Figure 3.3. Performance of Ti hollow fiber electrodes for the electrochemical reduction of NO_3^- to NH_3 in 0.1 M $HClO_4$ using 50 mM KNO_3. (a) Obtained current density profiles during chronoamperometry at -1 V vs RHE at different Ar flow rates. Potential- and Ar flow rate-dependent (b) faradaic efficiency, (c) production rate, and (d) partial current density to ammonia. Note that only ammonia in the catholyte was quantified here (see Figure S3.14 and S3.16 for measurements including ammonia quantified in anolyte). Dotted lines are used for guidance only.

Generally, a stable current density was obtained throughout the measurement, independent of the applied potential (see Figure 3.3a and Figure S3.10). An increase in current density was observed by increasing the Ar flow rate, which is in agreement with the LSV study. Only for measurements performed at a high flow rate, a slight decrease in current density with time was noticed, which can be assigned to the depletion of the nitrate in the electrolyte. Reactant depletion is confirmed by NO_3^- conversion calculations reported in Figure S3.11. Moreover, to support the hypothesis that flow-through conditions facilitate effective mixing, chronoamperometry at -0.6 V vs RHE was performed using vigorous magnetic stirring. The similarity in current density with "no-flow" and stirred conditions, and the significantly higher current densities obtained in purged conditions, are evidence for the highly effective mixing at the electrode-electrolyte interface by gas flow exiting the pores of the hollow fiber structure (Figure S3.12).

Quantification of the ammonia concentrations in the catholyte compartment revealed that the current efficiency to NH_3 is generally increasing with more negative potential. Yet, we like to emphasize two observations revealed in Figure 3b. First, a decrease in faradaic efficiency is observed after maximizing in the potential range of ~ -0.6 to -0.7 V vs RHE, in particular in flow-through conditions. Second, in the absence of flow, the highest FE of ~ 65 % was reached (at -0.7 V vs RHE), while in flow-through conditions a lower FE of ~ 50 % was obtained (at -0.6 V vs RHE), decreasing by approx. 20 % in the range of -0.6 to ~-0.75 V, to again increase at potentials < -0.8 V vs RHE. The drop in FE is also associated with the shoulder in the current potential profile observed during LSV measurements in no-flow conditions (see Figure 3.2b dotted line). We will explain these observations in the following paragraph, providing information on trends in other products. Now we like to state that even though the FE in flow-through conditions is lower than in the absence of flow, the NH_3 production rate, as well as partial current density to ammonia, are significantly larger, especially at more negative potentials, reaching production rates of 330 $\mu mol\ h^{-1}\ cm^{-2}$ and partial current densities of -70 mA/cm^{-2} respectively (Figure 3.3c and 3.3d). To the best of our knowledge, these obtained faradaic efficiencies, as well as partial current densities to ammonia (based on geometrical surface area) are the highest reported for Ti electrodes used for the electroreduction of nitrate to ammonia in similar conditions. Moreover, in our study low nitrate concentrations (50 mM) are used, which generally result in even lower conversion efficiency.[29]

Potential-dependent product distribution

To further discuss the change in selectivity with applied potential and flow rate, detailed analysis and quantification of liquid-phase products were performed (please also see Figure S3.13). In the absence of flow (Figure 3.4, left) the total FE to liquid products is rather

independent on potential and amounts to ~60-75%. Interestingly, in the potential range between -0.3 and -0.6 V vs RHE, the FE of hydroxylamine decreases, compensated by an increase in NH_3. In flow conditions, the total FE of liquid-phase products is dependent on potential (Figure 3.4, right). In the potential range between -0.3 and -0.6 V vs RHE the ammonia FE increases, and the hydroxylamine FE is rather constant. The strongest attenuation of the FE is observed at -0.7 V and -0.8 V, and a significant reduction in FE for both hydroxylamine and NH_3 is obtained. At -0.9 V and -1.0 V, the FE towards NH_3 increases again, accompanied by a slight increase in FE for hydroxylamine which will be discussed further.

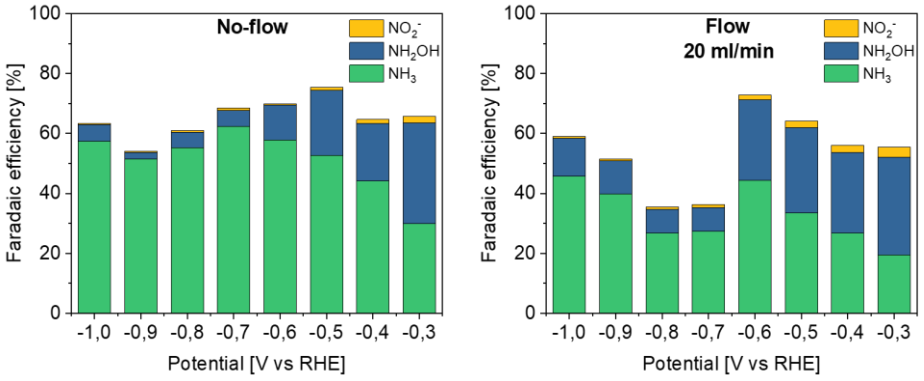

Figure 3.4. Total faradaic efficiency of liquid products. In no-flow (left) and flow (20 ml/min, right) configuration after chronoamperometry in 0.1 M $HClO_4$ with 50 mM KNO_3. See Figure S3.15 for measurements at 5 and 10 ml/min which fit a trend in product composition from no-flow to a flow of 20 ml/min.

Moreover, in contrast to the outlined trend in the FE towards ammonia, in flow-through conditions, we observe that the faradaic efficiencies for nitrite (NO_2^-) and hydroxylamine (NH_2OH) are generally higher (Figure S3.13). We propose that the changes in selectivity in flow-through conditions are caused by local pH changes. As a general rule, although it might be catalyst dependent, selectivity to NO_2^- [33,47,48] and NH_2OH [49,50] in nitrate electroreduction is more favorable at higher pH, while ammonia formation is more favorable in an acidic environment. Thus, at the higher current density in flow-through conditions, the pH will locally increase, thereby influencing the reaction selectivity.[37,51] It so seems that a locally acidic pH cannot be sustained by flow-induced proton transport, as a consequence of the enhancement in current density by the favorable transport of nitrate. This is likely related to the previously mentioned reaction stoichiometry (9 moles of protons and 1 mole of nitrate are needed for production of 1 mole of NH_3 and 3 moles of H_2O).

Considering that closing the electron balance is not feasible when only liquid phase products are considered, an attempt was made to detect gaseous products using online electrochemical mass-spectrometry (EC-MS).[52] Here, considering the specifications of the EC-MS, a Ti disc electrode instead of an electrode in hollow fiber geometry was used. Mass spectra of the selected signals recorded during chronoamperometry at different potentials are shown in Figure 3.5. After recording the background signal, potential pulses were applied (starting from -0.3 V vs RHE) for 30 s, which is sufficient to observe the formation of products with low vapor pressure without favoring their excessive accumulation in the small volume electrochemical cell. Ammonia and hydroxylamine were not followed in EC-MS experiments due to their non-volatile nature at low pH.

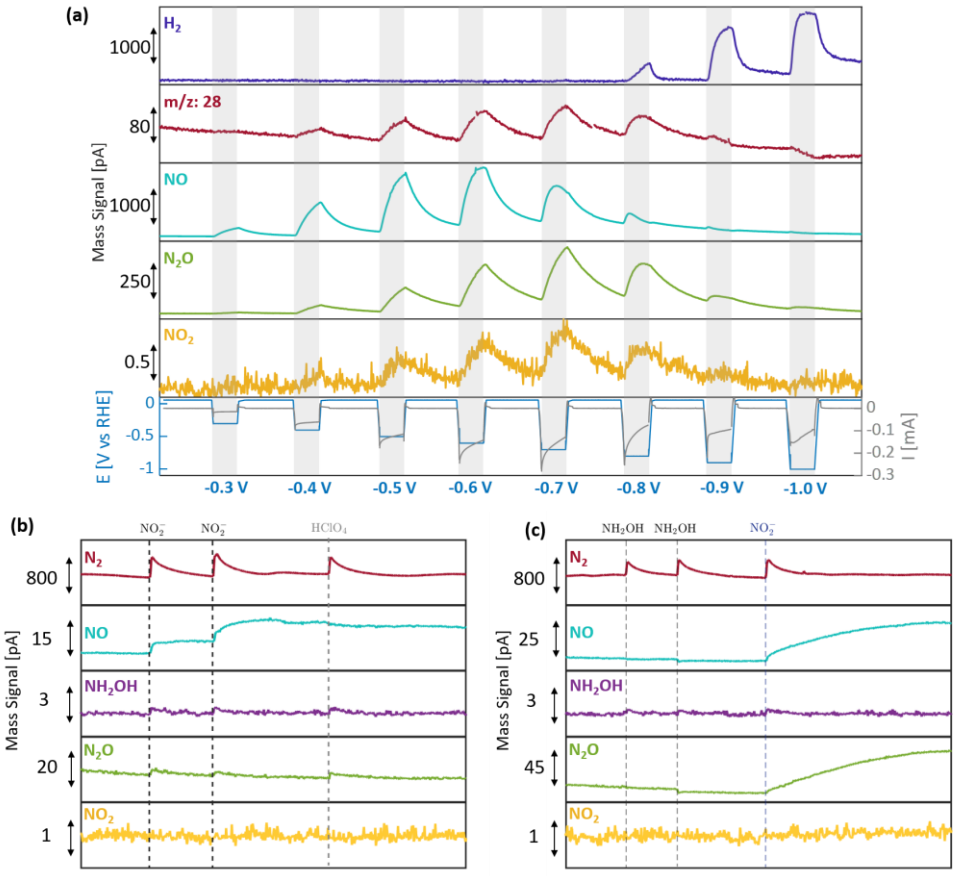

Figure 3.5. In situ EC-MS on Ti disc (a) during chronoamperometry in 0.1 M $HClO_4$ with 50 mM KNO_3 at different potentials. (b, c) Product distribution obtained for decomposition reactions using NO_2^- and NH_2OH solutions. Note that the increase of signals at m/z: 28, 33, and 44 is due to the addition of a non-deaerated solution as evidenced by the addition of 0.1 M $HClO_4$ (b) where NO signal does not increase.

Nitric oxide (m/z: 30) is observed almost throughout the entire potential range, peaking at -0.6 V vs RHE, similar to the potential in which the FE towards ammonia shows a minimum in the flow-through experiments shown in Figure 3.3b. Please note that the mass signal for NO is significantly larger than the signal of any other volatile nitrogen products. NO is not observed at the highest applied potentials (> -0.9 V), at which hydrogen evolution is dominant, in line with the reported LSV measurements performed with Ti hollow fiber electrodes (Figure 3.2), and the generally expected high overpotential for H_2 evolution on Ti. Similarly, m/z: 28 and m/z: 44 (N_2O) were observed with the highest peak intensity at -0.7 V vs RHE. Considering that during bulk electrolysis nitrogen is not detected (in preliminary experiments), and the signal intensity ratio between m/z: 44 and 28 matches the ratio expected for N_2O (according to the NIST database), the appearance of the signal at m/z: 28 originates from the fragmentation of N_2O in the mass spectrometer. Thus N_2, frequently reported in the literature as a product of nitrate reduction, is not observed here.[33,53] Surprisingly, a potential-dependent increase in the signal at m/z: 46 was also detected, which can be assigned to traces of NO_2 formation.

The detected gas-phase products might originate from a proton-coupled electron transfer reaction, i.e. the direct electrochemical reduction of NO_3^- (see Table S3.1), or homogeneous reactions of formed products in the electrolyte. Nitrite has rich homogeneous chemistry in the electrolyte, which can be summarized by Reactions 3.1-3.5.[51,54] Reactions 3.1-3.3 show that NO_2^- (HNO_2 in acid) decomposes, thereby releasing NO and NO_2 via disproportionation reactions. Since an increase in FE to NO_2^- was observed using the hollow fiber electrode as a function of increasing flow rate, it is expected that disproportion is increased in flow-through conditions, partially explaining the 'missing electrons' in the balance reported above.

$$H^+ + NO_2^- \leftrightarrow HNO_2 \quad (3.1)$$

$$2HNO_{2\,(aq)} \leftrightarrow NO_{(aq)} + NO_{2(aq)} + H_2O \quad (3.2)$$

$$3HNO_{2\,(aq)} \leftrightarrow HNO_3 + 2NO + H_2O \quad (3.3)$$

$$2NO_2 + H_2O \rightarrow HNO_2 + H^+ + NO_3^- \quad (3.4)$$

$$NH_3OH^+ + NO_2^- \rightarrow N_2O + 2H_2O \quad (3.5)$$

In fact, the spontaneous formation of NO was confirmed by MS measurement (Figure 3.5b). The addition of a NO_2^- solution (pH 7) to 0.1 M $HClO_4$ in the absence of the Ti electrode, resulted in an immediate increase in the signal of the mass fragment associated with the formation of NO (m/z: 30). NO_2 was not detected due to the relatively small concentration of NO_2^- added to the electrolyte and the fast dissociation of NO_2 in water (Reaction 3.4). In addition to the disproportion reaction of nitrite, the reaction between nitrite and hydroxylamine (which was also detected in electrolysis experiments) will result

in N_2O formation in an acid environment (Reaction 3.5).[55,56] In Figure 3.5c MS signals do not change when NH_2OH solution is added, but after the addition of NO_2^- both, the NO and N_2O signals rise, the former again in agreement with reaction 3.2, and the latter confirming the occurrence of reaction 3.5. Note that the increase in the m/z: 28 is not observed, due to the high background signal arising from air, exposed to the solution by the open-cell configuration used in these experiments.

Although the electrochemical formation of any gaseous products cannot be excluded (see Table S3.1), it is evident by the performed analysis that homogeneous reactions of electrochemically formed nitrite likely explain the 'missing electrons' in the electron balance. Most importantly, the formation of gaseous products might explain the significant drop in faradaic efficiency observed at ~ -0.7 V and -0.8 V vs RHE in flow-through conditions (Figure 3.4b). We again note that this drop is in agreement with the (peak) formation rates of NO and N_2O as observed by EC-MS analysis (Figure 3.5). Therefore, not only formation but also decomposition of NO_2^- (and NH_2OH) is expected to be enhanced in this potential window by introducing flow. We suggest that flow-through configurations not only promote the transport of protons and nitrate towards the electrode, but also of nitrite and NH_2OH away from the electrode. Rather than consecutive electrochemistry towards ammonia, homogeneous chemistry in solution is promoted. As such the decrease in hydroxylamine FE at -0.7 and -0.8 V vs. RHE (see Figure 3.4) is observed because of its reaction with nitrite forming N_2O. At more negative potentials (-0.9 and -1 V vs RHE) formation of NO_2^- is less dominant, and thus the observed faradaic efficiency to NH_2OH increases again, additionally causing an overall increase in total faradaic efficiency to liquid products.

Finally, it appears to be important to address the increase in faradaic efficiency to ammonia for potentials more negative than -0.6 V vs RHE. Similar behavior was observed on Ti plate electrodes at -0.75 V vs RHE at high nitrate concentrations (0.4 M NO_3^-) but was not discussed in detail.[29] We suggest that the interaction of nitrate with electrochemically formed H_2 might be responsible for the increase in FE observed in the H_2 evolution regime. It is known that the reduction of nitrate in aqueous solutions can occur in the presence of hydrogen over a variety of catalysts[57,58] and can lead to the formation of ammonia.[59] It is possible that a drop in FE is due to the onset of HER and at more negative potentials, where production of H_2 increases, non-electrochemical hydrogenation of NO_3^- to NH_4^+ can take place also obscuring the faradaic efficiency determination.

Electrode stability

In order to evaluate the durability of the electrode, stability tests were performed at -0.6 V (Figure S3.17) and -1 V vs RHE (Figure 3.6) in flow-by and flow-through configurations.

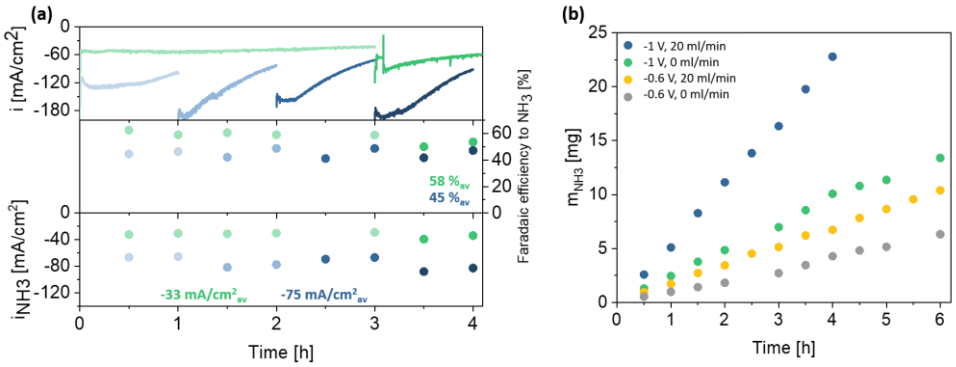

Figure 3.6. Stability test in 0.1 M $HClO_4$ with 50 mM KNO_3. (a) Overall current density as well as faradaic efficiency and partial current density to NH_3 at -1 V vs RHE with 0 ml/min (green) and 20 ml/min (blue) flow rate. (b) NH_3 mass increase during stability test at different conditions.

Independent on the applied potential, a decrease in current density over time is observed in flow-through conditions due to depletion of nitrate (see also Figure 3.3 and Figure S3.11). Therefore, the electrolyte was refreshed periodically. Despite small variations in current density after introduction of fresh nitrate, the faradaic efficiency to ammonia was stable over the period tested, reaching ~ 58 % and 45 % at no-flow and flow-through conditions (20 ml/min Ar) respectively (on average during 4h). Moreover, a linear increase in m_{NH3} was observed for all conditions tested (Figure 3.6b) and the electrochemically active surface area (ESCA) remained the same before and after the stability test (Figure S3.18). Also, SEM and XRD characterization do not reveal any significant deterioration of the electrode structure and composition (see Figures S3.19 and S3.20). Most importantly, a remarkable partial current density to ammonia of ~-75 mA/cm² was maintained over 4 h of electrolysis used with 50 mM KNO_3 in acidic electrolyte and polarized at -1 V vs RHE (Table S3.4). We assign the improvement in comparison to previous studies to efficient mass transport of NO_3^- to the electrode surface. However, we note that the geometrical surface area was used to calculate current density, which is standard practice nowadays. For comparison, partial current densities to ammonia based on the actual electrochemically active surface area are shown in Figure S3.21. Still, the faradaic efficiency reported here (58 % at -1V vs RHE in no-flow conditions) exceeds values reported earlier obtained for similar electrolyte compositions and reactor configurations where FEs to ammonia of < 20 % are

reported (Table S3.4). Given this significant increase, we speculate that electrode preparation is of importance. Here, Ti hollow fibers were used that undergo a thermal treatment likely having a positive influence on catalytic activity. Moreover, phase pure Ti is used in this study while contaminations likely in form of TiC and/or TiN can be observed in other reports.[29] We emphasize that the phase purity of Ti electrodes will be of interest for further investigation. Finally, we like to highlight that in this work nitrate waste streams of low nitrate concentration were targeted, yet higher nitrate concentrations will potentially further increase selectivity towards ammonia.

Conclusions

Using Ti hollow fiber electrodes for electroreduction of nitrate in 50 mM KNO_3 at -1 V vs RHE, a faradaic efficiency of 58 % towards ammonia is achieved in acidic conditions, with performance stability of over 4 h. Other products formed are hydroxylamine, NO, and N_2O, the latter formed by homogeneous disproportionation chemistry of nitrite. Optimizing mass transport by the introduction of an exiting flow of inert gas enhances the partial current density to ~ -75 mA/cm^2 with a FE of ~45%. We have revealed the overall, potential and gas flow dependent trends in product formation can be explained by 1) local pH changes affecting proton-coupled electron reactions to ammonia, nitrite, and hydroxylamine, 2) homogenous reactions of nitrite and hydroxylamine to NO and N_2O, promoted by gas flow induced favorable liquid mixing, and finally 3) catalytic hydrogenation of nitrate resulting in an overall increase in liquid product formation at the most negative potentials investigated. The reported current densities for electrochemical formation of ammonia are among the highest ever reported for Ti-based electrodes.

References

[1] J. Lim, C. A. Fernández, S. W. Lee, M. C. Hatzell, *ACS Energy Lett.* **2021**, 3676–3685.

[2] K. H. R. Rouwenhorst, P. M. Krzywda, N. E. Benes, G. Mul, L. Lefferts, *Ullmann's Encycl. Ind. Chem.* **2020**, 1–20.

[3] K. H. R. Rouwenhorst, P. M. Krzywda, N. E. Benes, G. Mul, L. Lefferts, in *Techno-Economic Challenges Green Ammon. as an Energy Vector*, **2020**, pp. 41–83.

[4] G. Qing, R. Ghazfar, S. T. Jackowski, F. Habibzadeh, M. M. Ashtiani, C. P. Chen, M. R. Smith, T. W. Hamann, *Chem. Rev.* **2020**, *120*, 5437–5516.

[5] S. Z. Andersen, V. Čolić, S. Yang, J. A. Schwalbe, A. C. Nielander, J. M. McEnaney, K. Enemark-Rasmussen, J. G. Baker, A. R. Singh, B. A. Rohr, M. J. Statt, S. J. Blair,

S. Mezzavilla, J. Kibsgaard, P. C. K. Vesborg, M. Cargnello, S. F. Bent, T. F. Jaramillo, I. E. L. Stephens, J. K. Nørskov, I. Chorkendorff, *Nature* **2019**, *570*, 504–508.

[6] P. M. Krzywda, A. Paradelo, B. T. Mei, N. E. Benes, G. Mul, *ChemElectroChem* **2022**, DOI doi.org/10.1002/celc.202101273.

[7] J. Long, S. Chen, Y. Zhang, C. Guo, X. Fu, D. Deng, J. Xiao, *Angew. Chemie Int. Ed.* **2020**, *59*, 9711–9718.

[8] G. F. Chen, Y. Yuan, H. Jiang, S. Y. Ren, L. X. Ding, L. Ma, T. Wu, J. Lu, H. Wang, *Nat. Energy* **2020**, DOI 10.1038/s41560-020-0654-1.

[9] R. Daiyan, T. Tran-Phu, P. Kumar, K. Iputera, Z. Tong, J. Leverett, M. H. A. Khan, A. A. Esmailpour, A. Jalili, M. Lim, A. Tricoli, R.-S. Liu, X. Lu, E. Lovell, R. Amal, *Energy Environ. Sci.* **2021**, *14*, 3588–3598.

[10] P. Li, Z. Jin, Z. Fang, G. Yu, *Energy Environ. Sci.* **2021**, DOI 10.1039/d1ee00545f.

[11] Y. Zhang, F. Li, Q. Zhang, J. Li, Q. Liu, *Sci. Total Environ.* **2014**, *490*, 213–222.

[12] S. Roy, M. S. Hegde, G. Madras, *Appl. Energy* **2009**, *86*, 2283–2297.

[13] J. W. Erisman, M. A. Sutton, J. Galloway, Z. Klimont, W. Winiwarter, *Nat. Geosci.* **2008**, *1*, 636–639.

[14] L. F. Greenlee, *Nat. Energy* **2020**, 1–2.

[15] M. Kuang, Y. Wang, W. Fang, H. Tan, M. Chen, J. Yao, C. Liu, J. Xu, K. Zhou, Q. Yan, *Adv. Mater.* **2020**, *32*, 1–7.

[16] S. Han, C. Wang, Y. Wang, Y. Yu, B. Zhang, *Angew. Chemie* **2021**, *133*, 4524–4528.

[17] C. Dai, Y. Sun, G. Chen, A. C. Fisher, Z. J. Xu, *Angew. Chemie - Int. Ed.* **2020**, *59*, 9418–9422.

[18] M. Anand, C. S. Abraham, J. K. Nørskov, *Chem. Sci.* **2021**, *12*, 6442–6448.

[19] B. S. Patil, N. Cherkasov, J. Lang, A. O. Ibhadon, V. Hessel, Q. Wang, *Appl. Catal. B Environ.* **2016**, *194*, 123–133.

[20] F. Jardali, S. Van Alphen, J. Creel, H. Ahmadi Eshtehardi, M. Axelsson, R. Ingels, R. Snyders, A. Bogaerts, *Green Chem.* **2021**, *23*, 1748–1757.

[21] Y. Yu, C. Wang, Y. Yu, Y. Huang, C. Liu, S. Lu, B. Zhang, *J. Mater. Chem. A* **2020**, *8*, 19623–19630.

[22] E. Vervloessem, M. Aghaei, F. Jardali, N. Hafezkhiabani, A. Bogaerts, *ACS Sustain. Chem. Eng.* **2020**, *8*, 9711–9720.

[23] H. Patel, R. K. Sharma, V. Kyriakou, A. Pandiyan, S. Welzel, M. C. M. Van De Sanden, M. N. Tsampas, *ACS Energy Lett.* **2019**, *4*, 2091–2095.

[24] K. H. R. Rouwenhorst, F. Jardali, A. Bogaerts, L. Lefferts, *Energy Environ. Sci.* **2021**, *14*, 2520–2534.

[25] L. Li, C. Tang, X. Cui, Y. Zheng, X. Wang, H. Xu, S. Zhang, T. Shao, K. Davey, S. Z. Qiao, *Angew. Chemie - Int. Ed.* **2021**, *60*, 14131–14137.

[26] L. Hollevoet, F. Jardali, Y. Gorbanev, J. Creel, A. Bogaerts, J. A. Martens, *Angew. Chemie - Int. Ed.* **2020**, *59*, 23825–23829.

[27] Y. Wang, C. Wang, M. Li, Y. Yu, B. Zhang, *Chem. Soc. Rev.* **2021**, *50*, 6720–6733.

[28] M. Duca, M. T. M. Koper, *Energy Environ. Sci.* **2012**, *5*, 9726–9742.

[29] J. M. McEnaney, S. J. Blair, A. C. Nielander, J. A. Schwalbe, D. M. Koshy, M. Cargnello, T. F. Jaramillo, *ACS Sustain. Chem. Eng.* **2020**, *8*, 2672–2681.

[30] Q. Hu, Y. Qin, X. Wang, Z. Wang, X. Huang, H. Zheng, K. Gao, H. Yang, P. Zhang, M. Shao, C. He, *Energy Environ. Sci.* **2021**, *14*, 4989–4997.

[31] M. N. Desai, S. S. Rana, *Anti-Corrosion Methods Mater.* **1973**, *20*, 8–10.

[32] A. S. Fajardo, P. Westerhoff, C. M. Sanchez-Sanchez, S. Garcia-Segura, *Appl. Catal. B Environ.* **2021**, *281*, 119465.

[33] J. Yao, Y. Mei, T. Yuan, J. Chen, H. Pan, J. Wang, *J. Electroanal. Chem.* **2021**, *882*, 115019.

[34] H. Niu, Z. Zhang, X. Wang, X. Wan, C. Shao, Y. Guo, *Adv. Funct. Mater.* **2020**, *2008533*, 1–8.

[35] R. Jia, Y. Wang, C. Wang, Y. Ling, Y. Yu, B. Zhang, *ACS Catal.* **2020**, *10*, 3533–3540.

[36] Y. Guo, R. Zhang, S. Zhang, Y. Zhao, Q. Yang, Z. Huang, B. Dong, C. Zhi, *Energy Environ. Sci.* **2021**, *14*, 3938–3944.

[37] S. Garcia-Segura, M. Lanzarini-Lopes, K. Hristovski, P. Westerhoff, *Appl. Catal. B Environ.* **2018**, *236*, 546–568.

[38] P. H. van Langevelde, I. Katsounaros, M. T. M. Koper, *Joule* **2021**, *5*, 290–294.

[39] W. Sun, H. Ji, L. Li, H. Zhang, Z.-K. Wang, J.-H. He, J.-M. Lu, *Angew. Chem. Int. Ed. Engl.* **2021**, *60*, 22933–22939.

[40] C. Yan, S. Kakuturu, A. H. Butzlaff, D. M. Cwiertny, S. Mubeen, C. J. Werth, *ACS ES&T Eng.* **2021**, *1*, 204–215.

[41] I. Merino-Garcia, J. Albo, P. Krzywda, G. Mul, A. Irabien, *Catal. Today* **2020**, *346*, 34–39.

[42] R. Kas, K. K. Hummadi, R. Kortlever, P. De Wit, A. Milbrat, M. W. J. Luiten-Olieman, N. E. Benes, M. T. M. Koper, G. Mul, *Nat. Commun.* **2016**, *7*, 1–7.

[43] X. Wei, D. Vogel, L. Keller, S. Kriescher, M. Wessling, *ChemElectroChem* **2020**, *7*, 4679–4684.

[44] R. P. H. Jong, P. M. Krzywda, N. E. Benes, G. Mul, *RSC Adv.* **2020**, *10*, 31901–31908.

[45] X. Zou, X. Huang, A. Goswami, R. Silva, B. R. Sathe, E. Mikmeková, T. Asefa, *Angew. Chemie - Int. Ed.* **2014**, *53*, 4372–4376.

[46] C. T. Dinh, A. Jain, F. P. G. de Arquer, P. De Luna, J. Li, N. Wang, X. Zheng, J. Cai, B. Z. Gregory, O. Voznyy, B. Zhang, M. Liu, D. Sinton, E. J. Crumlin, E. H. Sargent, *Nat. Energy* **2019**, *4*, 107–114.

[47] X. Xing, D. A. Scherson, C. Mak, *J. Electrochem. Soc.* **1990**, *137*, 2166–2175.

[48] S. Taguchi, J. M. Feliu, *Electrochim. Acta* **2008**, *53*, 3626–3634.

[49] Z. Wang, D. Richards, N. Singh, *Catal. Sci. Technol.* **2021**, 705–725.

[50] E. Pérez-Gallent, M. C. Figueiredo, I. Katsounaros, M. T. M. Koper, *Electrochim. Acta* **2017**, *227*, 77–84.

[51] I. Katsounaros, *Curr. Opin. Electrochem.* **2021**, *28*, 100721.

[52] D. B. Trimarco, S. B. Scott, A. H. Thilsted, J. Y. Pan, T. Pedersen, O. Hansen, I. Chorkendorff, P. C. K. Vesborg, *Electrochim. Acta* **2018**, *268*, 520–530.

[53] B. P. Dash, S. Chaudhari, *Water Res.* **2005**, *39*, 4065–4072.

[54] V. Rosca, M. Duca, M. T. DeGroot, M. T. M. Koper, *Chem. Rev.* **2009**, *109*, 2209–2244.

[55] F. T. Bonner, J. Kada, K. G. Phelan, *Inorg. Chem.* **1983**, *22*, 1389–1391.

[56] A. A. Bothner-By, L. Friedman, *J. Chem. Phys.* **1952**, *20*, 5473–5475.

[57] O. S. G. P. Soares, J. J. M. Órfão, M. F. R. Pereira, *Catal. Letters* **2008**, *126*, 253–260.

[58] C. J. Werth, C. Yan, J. P. Troutman, *ACS ES&T Eng.* **2021**, *1*, 6–20.

[59] L. Wei, D. J. Liu, B. A. Rosales, J. W. Evans, J. Vela, *ACS Catal.* **2020**, *10*, 3618–3628.

Supplementary information 3

Materials

Titanium powder (TLS Technik GmbH & Co., ASTM, grade 2) with an average particle size of 6 μm, polyethersulfone (PES, BASF, Ultrason E 6020P), and N-methylpyrrolidone (NMP, Sigma Aldrich, ≥99 %) were used for Ti hollow fiber preparation. $HClO_4$ (Sigma Aldrich, 70 %) and $KClO_4$ (Sigma Aldrich, ≥99 %) were used for preparation of the supporting electrolyte. KNO_3 (Sigma Aldrich, ≥99.0 %) was used as NO_3^- source. Ammonium chloride (Alfa Aesar, 99.999 %), maleic acid (Sigma Aldrich, ≥99 %), DMSO-d6 (Sigma Aldrich, 99.5 atom % D), hydroxylamine hydrochloride (Sigma Aldrich, 99.995%), acetone (Sigma Aldrich, 99.5%) and methanol (Sigma Aldrich, ≥99.9 %) were used for product detection and calibration. Silver epoxy glue (Chemtronics, CW2400) and two-component adhesive glue (Weicon, 10550024) were used to prepare the electrode assembly.

Figure S3.1. Photograph of Ti hollow fiber electrode assembly.

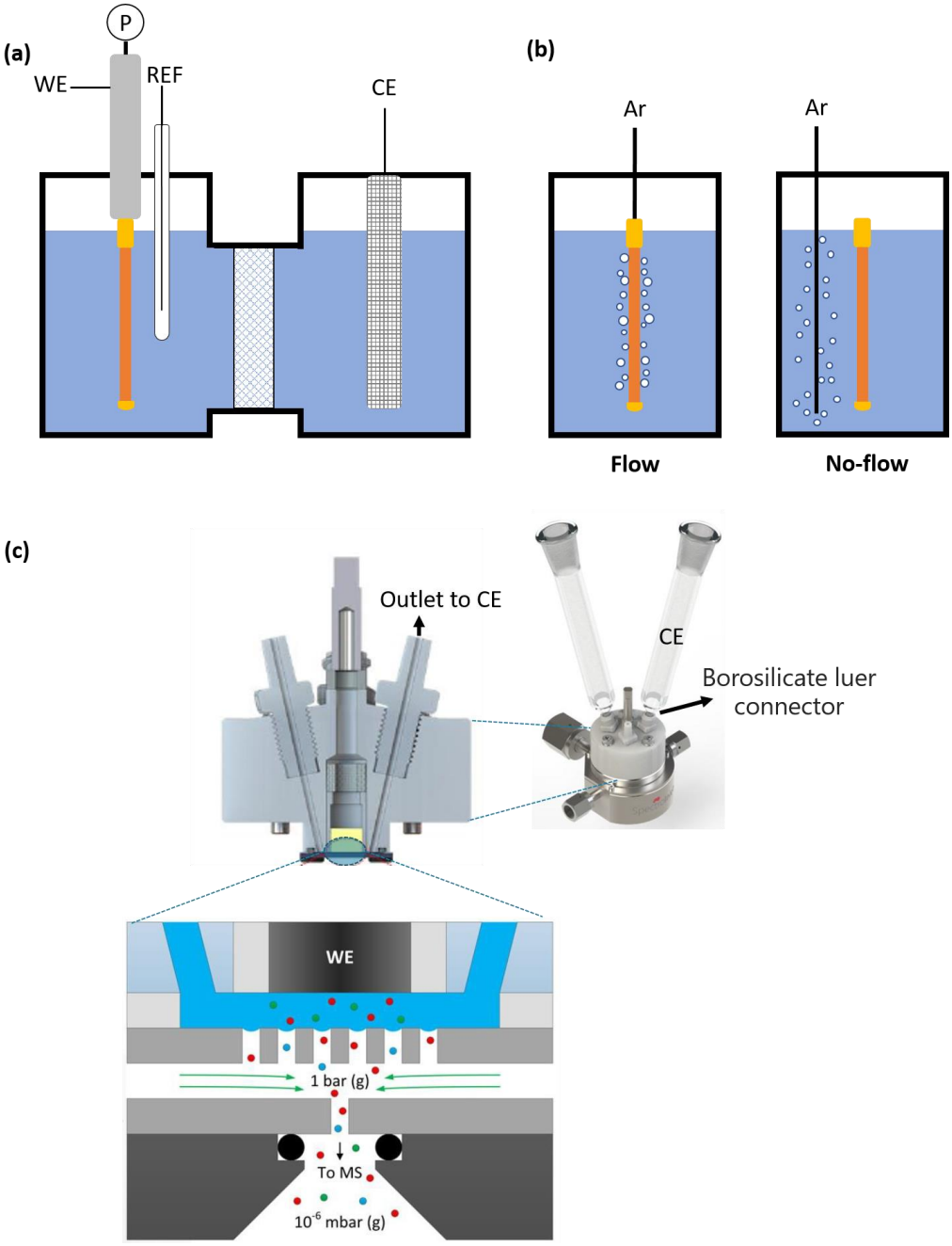

Figure S3.2. Schematic representation of (a) the applied electrochemical cell; (b) gas flow configurations of the working electrode compartment, and (c) the EC-MS set-up, and principle of the chip technology provided by SpectroInlets.

Ammonia quantification

The concentration of ammonia was determined by ^{1}H NMR spectroscopy based on methods described elsewhere.[S1,S2] Calibration was performed using standard NH_4Cl solutions with known concentration. Generally, 0.5 ml of the (standard) solution was mixed with 50 µl of 0.5 M H_2SO_4 containing 10 mM maleic acid (internal standard) and 25 µl of DMSO-d6 as locking solvent. ^{1}H NMR spectra were recorded on a Bruker 400MHz spectrometer with 1000 scans (Figure S3.3). The area ratio of the NH_4^+ peak at 6.79 ppm and the maleic acid peak at 6.22 ppm were plotted versus NH_3 concentration (Figure S3.3).

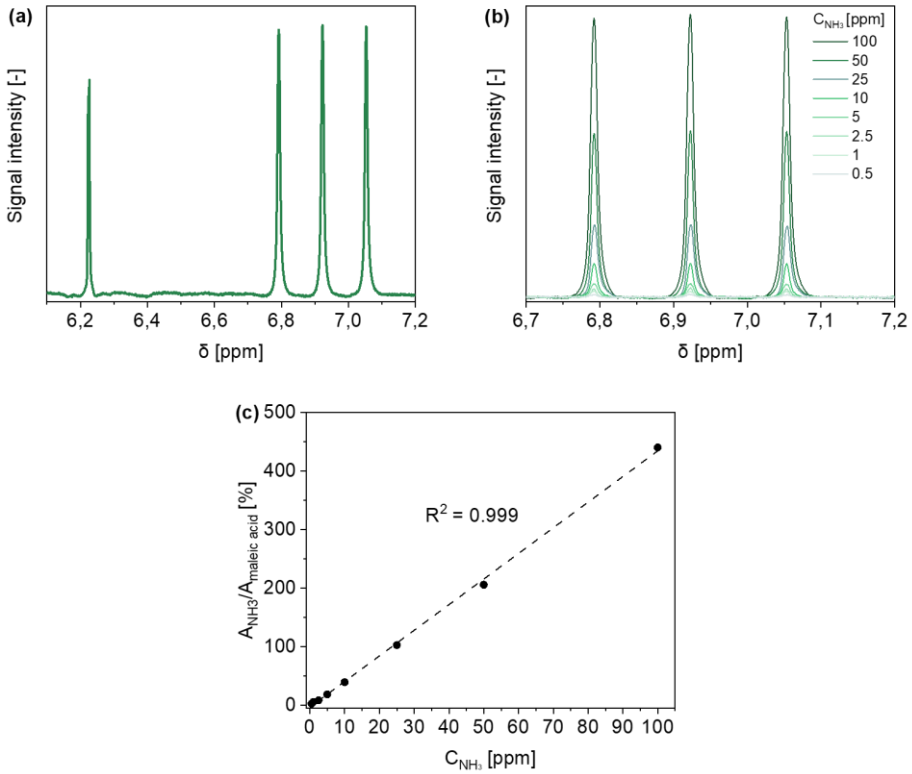

Figure S3.3. ^{1}H NMR spectrum of (a) 50 ppm NH_4^+ with 10 mM maleic acid and (b) different concentration of NH_4^+. (c) Calibration curve for NH_4^+ quantification.

Hydroxylamine quantification

The hydroxylamine content was determined by gas chromatography according to a method published elsewhere.[S3] In short, samples obtained after electrolysis were neutralized by the addition of a NaOH solution. To allow for quantification, hydroxylamine was reacted with acetone to form acetone oxime by the addition of 2 µl of methanol/acetone (1:1 v/v) to 4 ml of neutralized sample solution. Acetone oxime was quantitatively detected by gas chromatography (GC-FID, Figure S3.4). Following the procedures described above, the calibration curve was prepared using standard solutions of hydroxylamine hydrochloride (Figure S3.4).

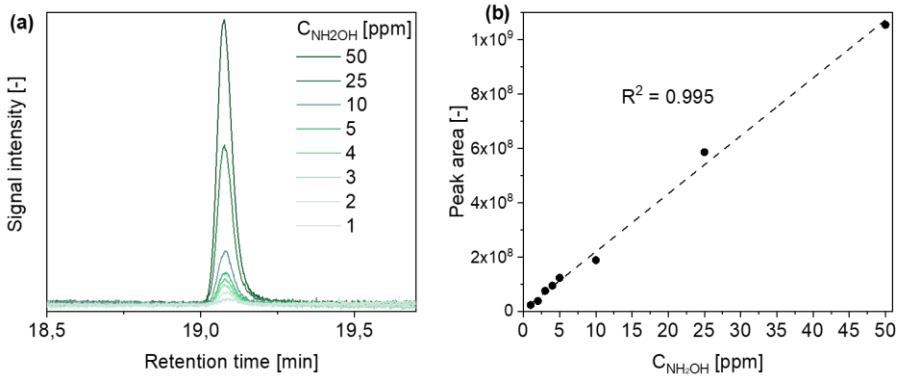

Figure S3.4. (a) Chromatogram (GC-FID) of NH_2OH with different concentration. (b) Calibration curve for NH_2OH quantification.

Nitrite quantification

The concentration of NO_2^- was determined using the commercial Spectroquant® Nitrite test (Supelco), where nitrite ions react with sulfanilic acid to form a diazonium salt, which then reacts with N-(1-naphthyl)ethylenediamine dihydrochloride to form a red-violet azo dye. Generally, electrolyte solution was mixed with 0.1 M NaOH (to achieve the required pH range) and 1 microspoon of reagent. After the reagent was dissolved, the reaction mixture was left for 10 min and absorption at 520 nm was measured by UV-Vis spectrometer. Following the procedure described above, the calibration curve was prepared using standard solutions of KNO_2 (Figure S3.5).

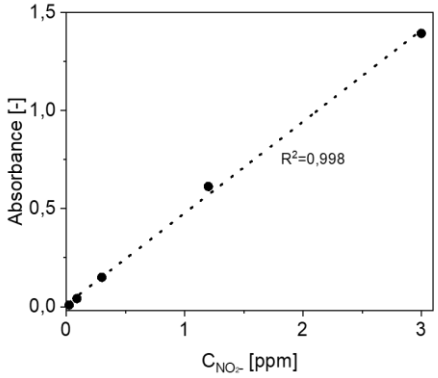

Figure S3.5. Calibration curve for NO_2^- quantification by UV-Vis spectroscopy.

Table S3.1. Standard reduction potentials of NO_3^- electroreduction reactions.

Reaction	E^0 [V vs RHE]
$NO_3^- + 2H^+ + e^- \rightarrow NO_2 + H_2O$	0.77
$NO_3^- + 2H^+ + 2e^- \rightarrow NO_2^- + H_2O$	0.94
$NO_3^- + 4H^+ + 3e^- \rightarrow NO + 2H_2O$	0.96
$2NO_3^- + 10H^+ + 8e^- \rightarrow N_2O + 5H_2O$	1.12
$2NO_3^- + 12H^+ + 10e^- \rightarrow N_2 + 6H_2O$	1.25
$NO_3^- + 7H^+ + 6e^- \rightarrow NH_2OH + 2H_2O$	0.73
$2NO_3^- + 16H^+ + 14e^- \rightarrow N_2H_4 + 6H_2O$	0.82
$NO_3^- + 9H^+ + 8e^- \rightarrow NH_3 + 3H_2O$	0.88

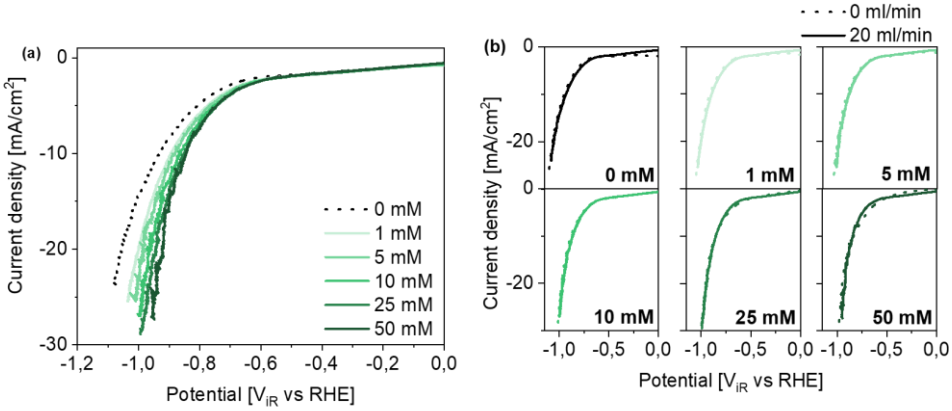

Figure S3.6. Linear scan voltammetry of Ti hollow fiber in neutral pH electrolyte with (a) increasing KNO_3 concentration in the no-flow configuration and (b) Ar flow rate through the electrode.

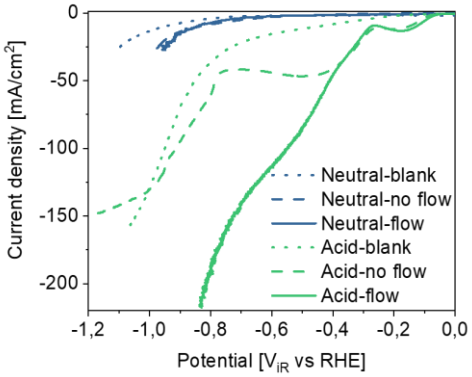

Figure S3.7. Comparison of Ti hollow fiber electrode activity for NO_3^- electroreduction in acidic and neutral pH electrolyte based on linear scan voltammetry.

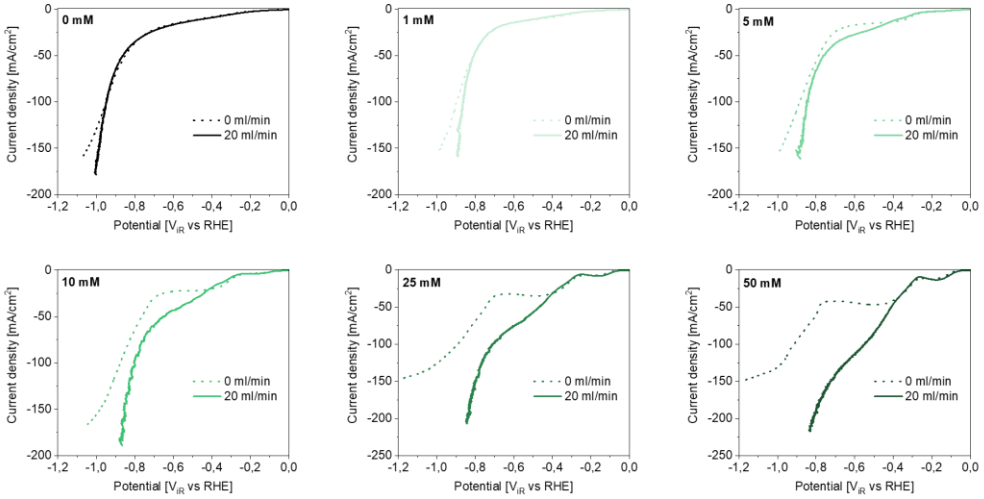

Figure S3.8. No-flow vs flow at different nitrate concentrations, showing flow has a significant effect at concentrations larger than ~5 mM.

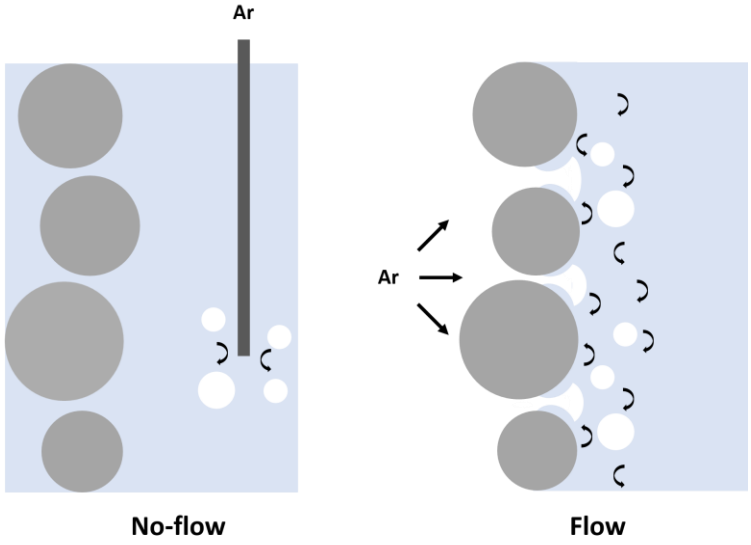

Figure S3.9. Schematic representation of mixing effect induced by gas bubbles exiting the pores of the hollow fiber electrode (right), compared to a traditional configuration sparging the Ar gas in the vicinity of the fiber (left).

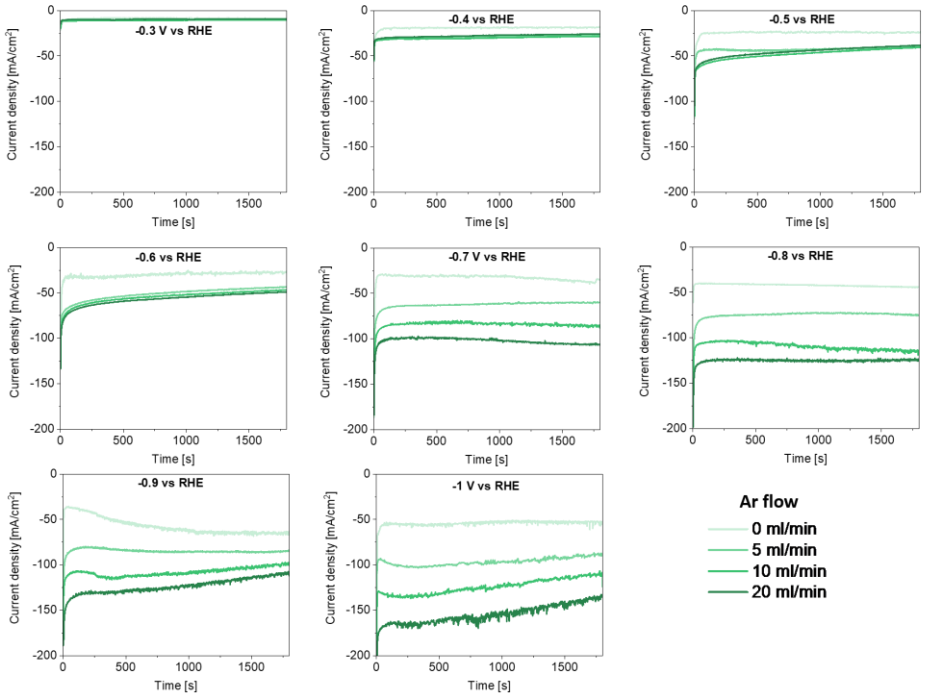

Figure S3.10. Current density during chronoamperometry at different potentials and Ar flow rate.

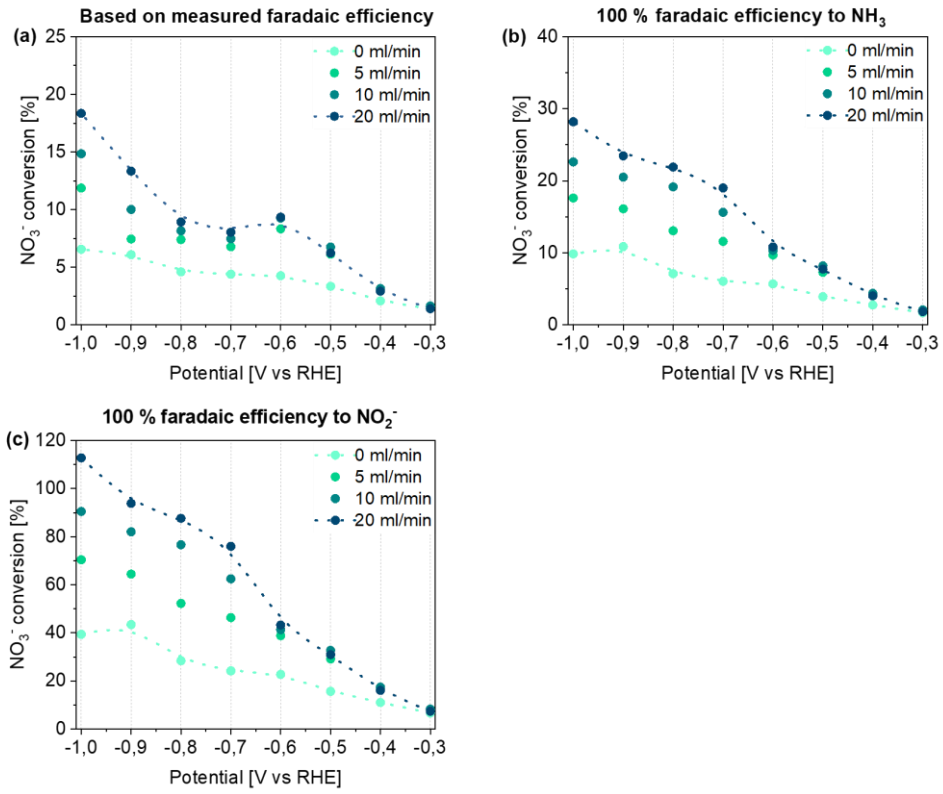

Figure S3.11. NO_3^- conversion depending on applied potential and Ar flow rate, calculated based on (a) the measured faradaic efficiency, (b) the assumption of 100 % faradaic efficiency to NH_3 and (c) assumption of 100 % faradaic efficiency to NO_2^-.

The total charge passed during electrolysis was used in NO_3^- conversion calculations. In Figure S3.11a, the measured faradaic efficiency to each product detected was used for calculation. Note that in addition to the considered proton-coupled electrochemical reactions also decomposition of formed products might occur (as discussed in the main article). Thus, the real NO_3^- conversion is likely higher than presented by the estimations used. Nevertheless, in order to visualize the influence of products formed on nitrate conversion, here we assume 100 % faradaic efficiency to either ammonia (Figure S3.11b) or nitrite (Figure S3.11c). As evident, especially in the case of NO_2^- formation, nitrate conversion close to 100 % be obtained. Most importantly NO_3^- conversion values calculated here are convincingly showing that depletion of the reactant in the electrolyte can influence the current density, especially at more negative potentials/higher current densities and flow rates.

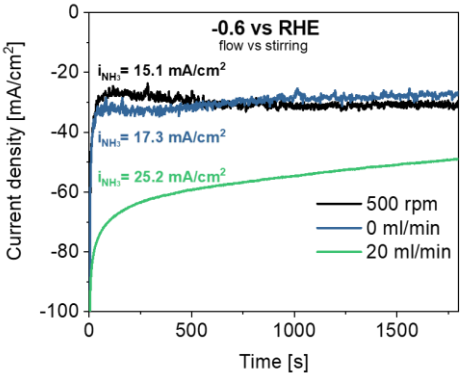

Figure S3.12. Current density during chronoamperometry at -0.6 V vs RHE in no flow (0 ml/min) and flow (20 ml/min) configuration compared to electrolyte stirred with 500 rpm.

An experiment with magnetic stirring was performed to reveal the improvement of bubble-induced mixing compared to the traditional way of convective mixing. As shown, a similar current density and partial current density to ammonium were observed in chronoamperometry at -0.6 V vs RHE in 50 mM KNO_3 acidic electrolyte using no-flow configuration and additional stirring at 500 rpm. It proves that even in a no-flow configuration, gas bubbles (supplied next to the electrode rather than through) provide similar convection in the system like stirring with 500 rpm. Most importantly, the result shows a big improvement when gas is supplied through the electrode which creates more efficient mixing closer to the electrode surface.

Table S3.2. Measured iR drop before each chronoamperometry experiment.

iR drop [Ω] – 80% compensation				
Potential	**Flow [ml/min]**			
[V vs RHE]	**0**	**5**	**10**	**20**
-0.3	3.433	3.664	3.735	5.291
-0.4	5.087	5.515	5.521	5.953
-0.5	4.161	3.903	3.910	4.167
-0.6	5.856	5.270	4.961	5.203
-0.7	3.447	3.832	3.420	3.528
-0.8	3.400	3.425	3.520	4.024
-0.9	5.070	5.403	5.841	5.999
-1.0	4.055	3.869	3.476	3.573

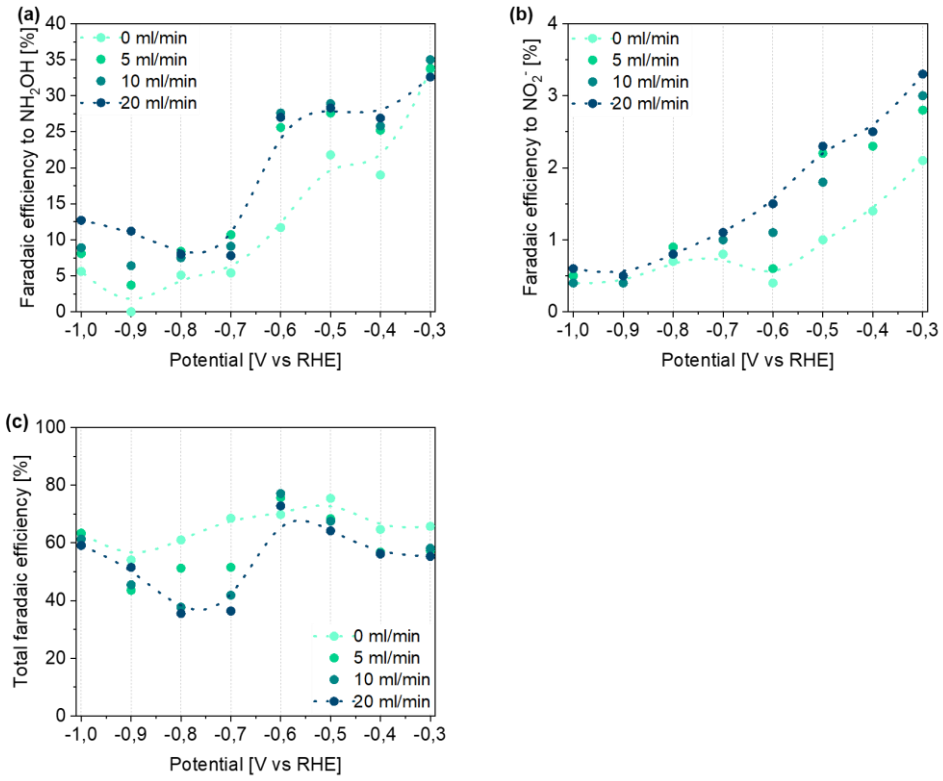

Figure S3.13. Faradaic efficiency to (a) NH_2OH, (b) NO_2^- and (c) total faradaic efficiency including NH_3 depending on applied potential and Ar flow rate.

Faradaic efficiency to NH_3 – error estimation

Since it is very difficult to prepare hollow fiber electrodes with high reproducibility, error in faradaic efficiency to ammonia was estimated based on 3 different measurements (different electrodes) in chronoamperometry at -0.6 V vs RHE at 0 ml/min and 20 ml/min.

Table S3.3. Estimation of error in faradaic efficiency to NH_3.

Flow rate [ml/min]	Faradaic efficiency to NH_3 [%]				
	Run 1	**Run 2**	**Run 3**	**average**	**Standard dev.**
0	60.4	50.2	64.9	58.8	6.1
20	45.6	34.9	37.1	39.2	4.6
				Average	**5.4**

Therefore, on average, an error bar of ±5.5 % was estimated for faradaic efficiency to ammonia

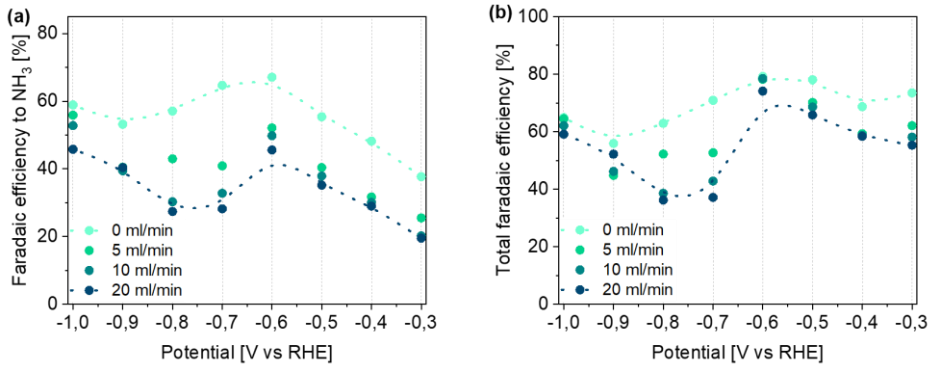

Figure S3.14. Faradaic efficiency to (a) NH_3 and (b) total faradaic efficiency including ammonia measured in a counter compartment.

Since ammonia (NH_4^+ in acid) can cross the Nafion membrane, its concentration was also measured in the counter compartment of the electrolytic cell. However, due to the low concentration measured in the CE compartment, the accuracy of the measurement can be questionable due to possible contaminations with ambient ammonia (common in the nitrogen electroreduction field). Therefore, faradaic efficiency including NH_3 from a counter compartment is only shown in the supplementary information. The data presented in the main text of the manuscript only include ammonia detected in the working electrode compartment.

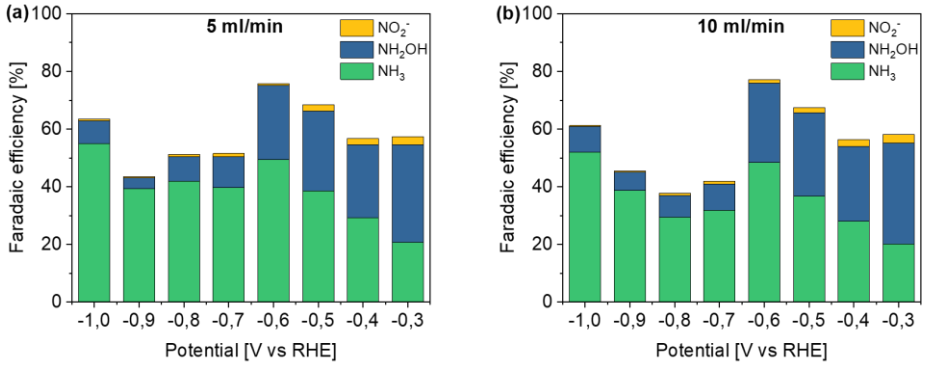

Figure S3.15. Total faradaic efficiency in flow configuration at (a) 5 ml/min and (b) 10 ml/min Ar flow.

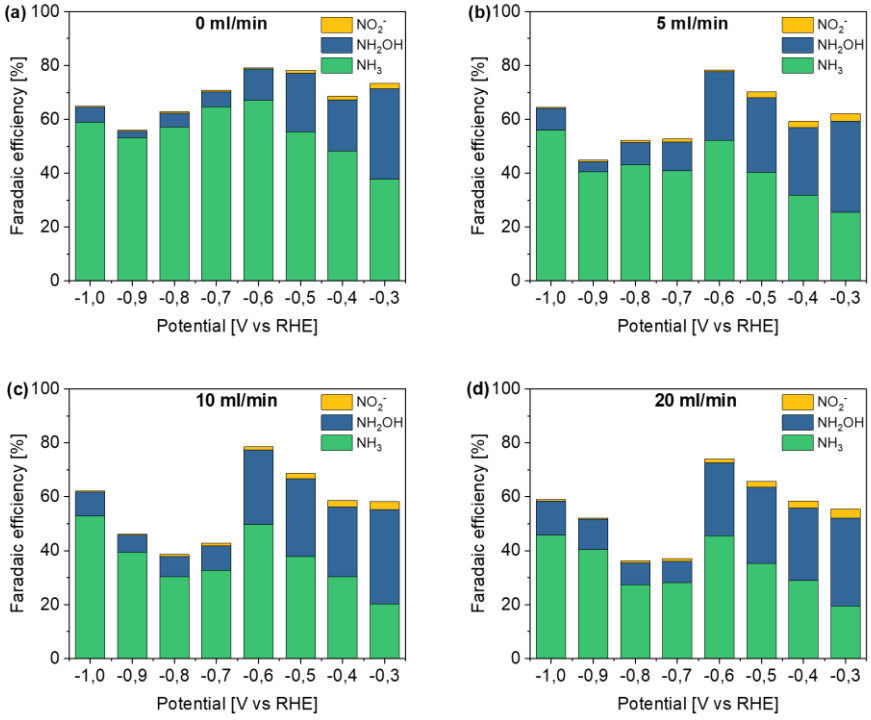

Figure S3.16. Total faradaic efficiency at different Ar flow rate including ammonia measured in a counter compartment.

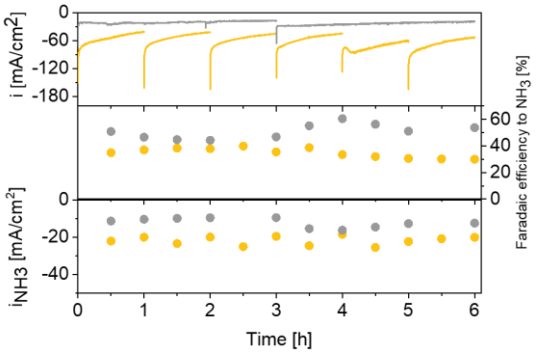

Figure S3.17. Stability test at -0.6 V vs RHE with 0 (gray) and 20 ml/min (yellow) flow rate showing overall current density as well as faradaic efficiency and partial current density to NH_3.

The partial current density to ammonia shown in Figure 3.6a in the main text was calculated as an average of all points measured (every 30 min). Each point was calculated using the

faradaic efficiency to ammonia and the total charge passed over the period measured, thus resulting in the partial current density to ammonia reported in the main text.

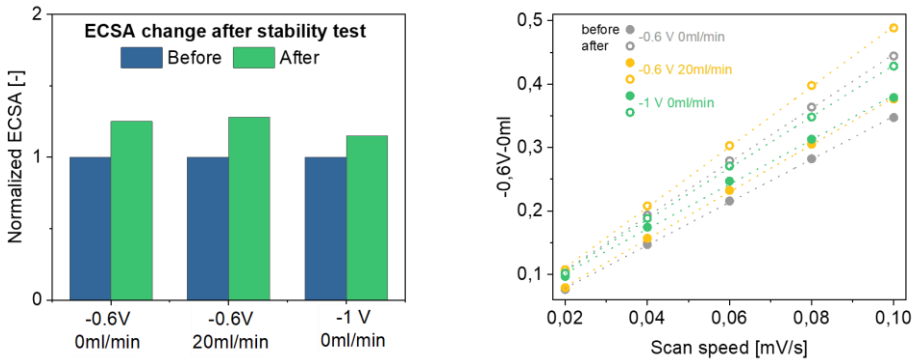

Figure S3.18. ECSA of Ti hollow fiber electrode before and after stability test at different conditions.

A slight increase in surface area can be related to surface reoxidation of the Ti electrode before chronoamperometry tests. TiO_x could be reduced increasing the surface area of Ti or the formation of TiH_x could also possibly influence the ECSA.

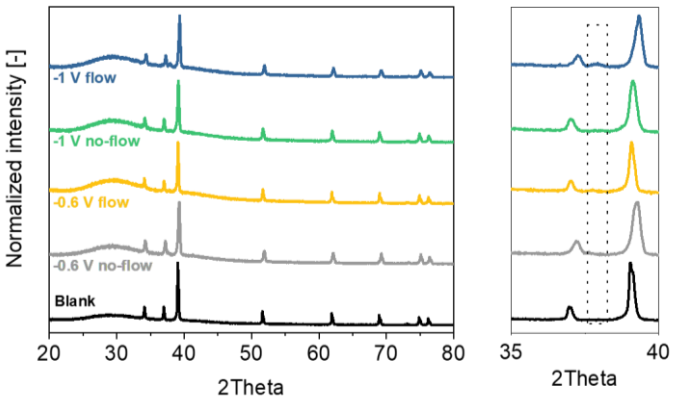

Figure S3.19. XRD of Ti hollow fiber electrode before and after stability test at different conditions.

Minor XRD peak was observed after the stability test at -0.6 V flow, -1V no-flow, and -1 V flow which could be assigned to TiH_x formation, however, the effect is significantly lower than presented before on Ti electrodes in the literature.[S4] A broad peak in the range of 25-35 degrees is assigned to residues of the carbon tape which was used for SEM analysis prior to XRD analysis (compare XRD of Ti fiber in Figure 3.1d in the main text where no carbon tape was used prior to XRD).

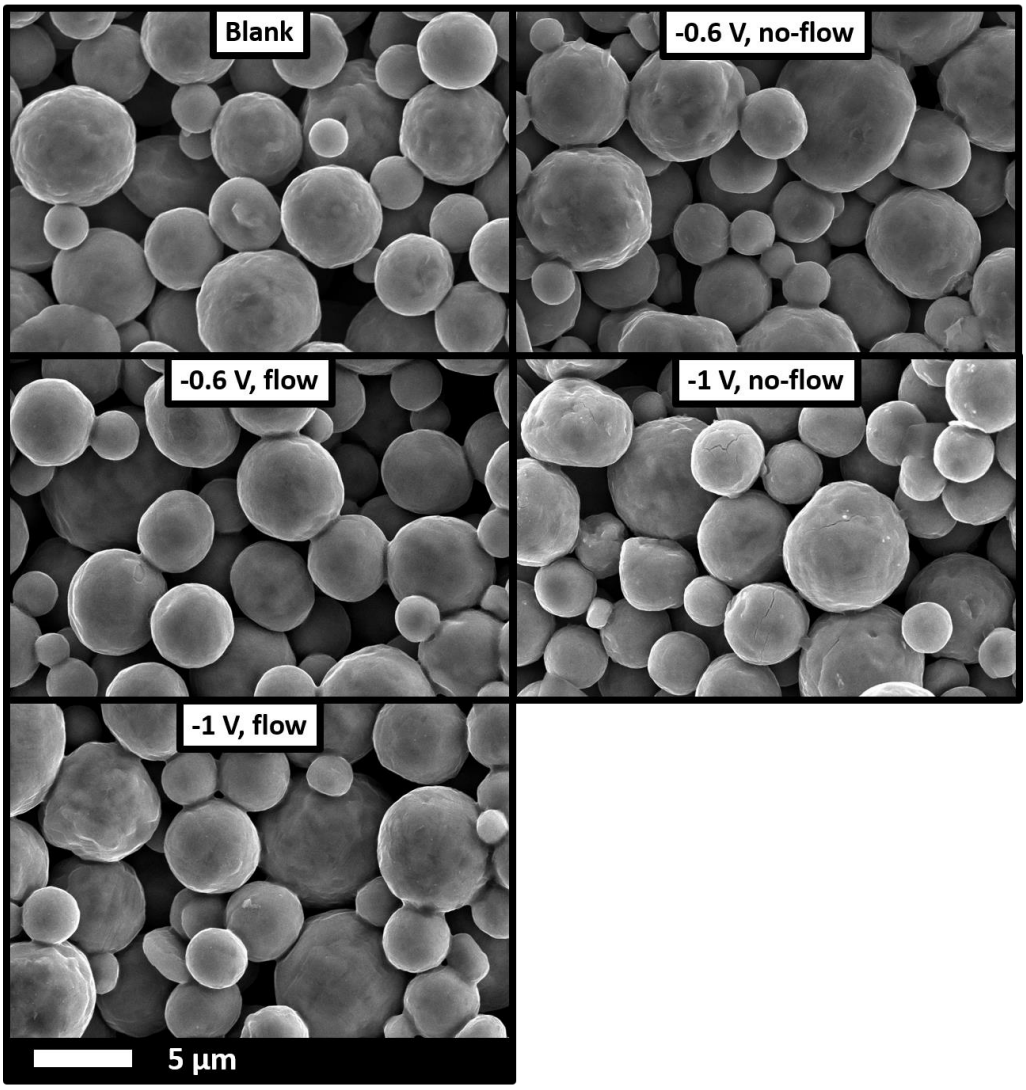

Figure S3.20. SEM of Ti hollow fiber electrode before and after stability test at different conditions.

(a)

Flow [ml/min]	Capacitance [mF/cm²]
0	3,47
5	3,26
10	3,22
20	3,20
Ti disc	**0,0452**

(b)

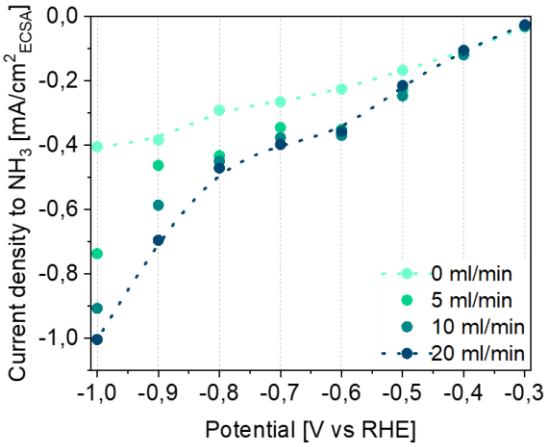

Figure S3.21. (a) Capacitance value for Ti hollow fiber electrode depending on the Ar flow rate. (b) Partial current density to ammonia based on ECSA depending on applied potential and Ar flow rate.

As shown in our previous study, ECSA of Ti hollow fiber electrode can slightly change depending on the flow rate.[S5] Therefore ECSA at a specific flow rate was used for calculating partial current density to NH_3. Capacitance values measured at different flow rates are compared to the capacitance of flat Ti disc for ESCA estimation.

Table S3.4. Comparison of Ti-based electrodes performance for NO_3^- electroreduction.

Catalyst	Electrolyte pH	[NO_3^-]	E/i applied	i to NH_3 [mA/cm²]	FE [%]	ref
Ti	Neutral	100 mg/L	-20 mA/cm2	-0.5	2.5 %	[S6]
Ti	Neutral	50 mg/L	-38 mA/cm2	-2.1	5.6	[S7]
Ti	pH 3	100mg-N/L	-1.26 V vs SCE	-	~30% N-efficiency	[S8]
TiO_{2-x}	Neutral	3.6 mM	-1.6V vs SCE	-	85	[S9]
Ti	Acidic	0.4 M	-1 V vs RHE	-22	82	[S4]
		50 mM	-1 V vs RHE	-4.6	<20	
Ti hollow fiber No-flow	Acidic	50 mM KNO3	-1 V vs RHE	~-33	58	This work*
Ti hollow fiber Flow	Acidic		-1 V vs RHE	~-75	45	This work*

*based on 4 h stability measurement

It is important to mention that not all literature reports presented in Table S3.4 were focused on NH_3 as a reaction product which can reflect on the data presented. Denitrification to N_2 has been the main topic so far in the nitrate electrolysis field and N_2 was the target product. Only recently ammonia is of interest which opens up the possibility for decentralized, small-scale green ammonia production plants for fertilizer applications where NO_x produced via N_2 oxidation or from waste streams can be used as feedstock.

SI References

[S1] A. C. Nielander, J. M. McEnaney, J. A. Schwalbe, J. G. Baker, S. J. Blair, L. Wang, J. G. Pelton, S. Z. Andersen, K. Enemark-Rasmussen, V. Čolić, S. Yang, S. F. Bent, M. Cargnello, J. Kibsgaard, P. C. K. Vesborg, I. Chorkendorff and T. F. Jaramillo, ACS Catal., 2019, 9, 5797–5802.

[S2] R. Y. Hodgetts, A. S. Kiryutin, P. Nichols, H.-L. Du, J. M. Bakker, D. R. Macfarlane and A. N. Simonov, ACS Energy Lett., 2020, 5, 736–741.

[S3] D. J. Darke, J. Chromatogr. B, 1980, 181, 449–452.

[S4] J. M. McEnaney, S. J. Blair, A. C. Nielander, J. A. Schwalbe, D. M. Koshy, M. Cargnello and T. F. Jaramillo, ACS Sustain. Chem. Eng., 2020, 8, 2672–2681.

[S5] P. M. Krzywda, A. Paradelo, B. T. Mei, N. E. Benes and G. Mul, ChemElectroChem, 2022, DOI:doi.org/10.1002/celc.202101273.

[S6] M. Li, C. Feng, Z. Zhang and N. Sugiura, Electrochim. Acta, 2009, 54, 4600–4606.

[S7] X. Ma, M. Li, C. Feng, W. Hu, L. Wang and X. Liu, J. Electroanal. Chem., 2016, 782, 270–277.

[S8] J. Yao, Y. Mei, T. Yuan, J. Chen, H. Pan and J. Wang, J. Electroanal. Chem., 2021, 882, 115019.

[S9] R. Jia, Y. Wang, C. Wang, Y. Ling, Y. Yu and B. Zhang, ACS Catal., 2020, 10, 3533–3540.

Chapter 4

Effect of electrolyte and electrode configuration on Cu-catalyzed nitric oxide reduction to ammonia

This chapter is based on:

P. M. Krzywda, A. Paradelo Rodríguez, N. E. Benes, B. T. Mei, G. Mul "Effect of electrolyte and electrode configuration on Cu-catalyzed nitric oxide reduction to ammonia", *ChemElectroChem*, 9, e202101273, **2022**.

Abstract

Reduction of nitric oxide was investigated using Cu electrodes in acid and neutral pH conditions. Analysis of Cu discs in stagnant electrolyte by Electrochemical Mass Spectrometry (EC-MS), revealed the favorable formation of ammonia in an acidic electrolyte, while N_2O and N_2 are formed in significant quantities in neutral conditions. Additional evaluation of Cu electrodes in hollow fiber geometry was performed using 10 vol% NO in Ar supplied through the porous electrode structure and off-line determination of ammonia by ^1H NMR spectroscopy. The pH-dependent performance of the Cu hollow fiber is in agreement with EC-MS data at low gas flow rates, showing the highest ammonia selectivity in acidic conditions. However, at relatively high gas flow rates, almost 90 % faradaic efficiency and an NH_3 production rate of 400 μmol h^{-2} cm^{-2} were obtained in neutral electrolyte at -0.6 V vs RHE, likely due to enhanced availability of NO at the electrode surface, suppressing the hydrogen evolution reaction. This approach shows conversion of waste NO gas to valuable green fertilizer components is possible.

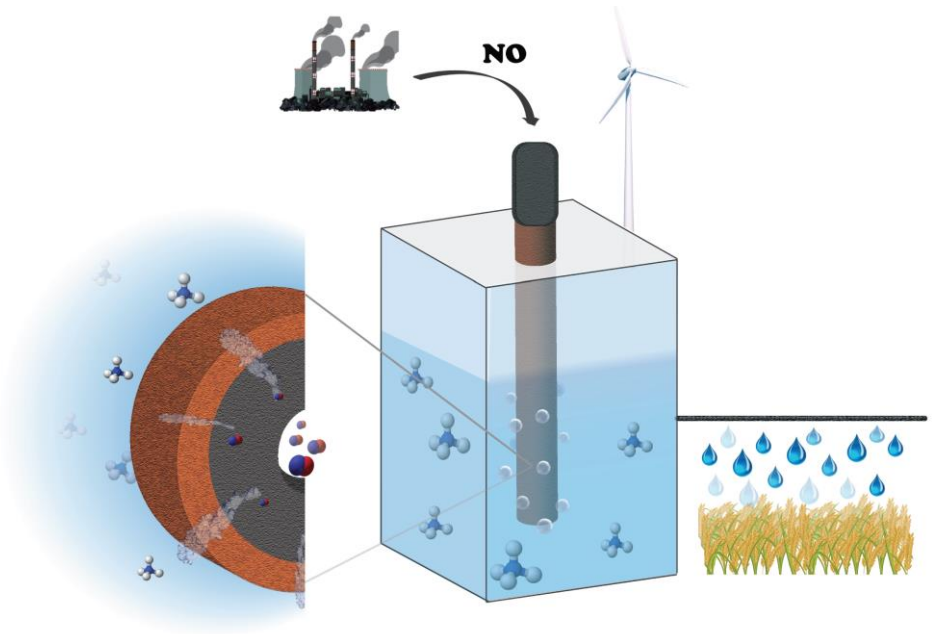

Introduction

Ammonia is an essential chemical for production of fertilizers, and thus crucial for the global food supply. Currently, ammonia is predominantly produced by the energy-intensive Haber-Bosch process,[1] leading to significant carbon dioxide emissions. Thus, non-conventional, potentially green ammonia synthesis routes are presently explored.[1,2] Compared to the traditional centralized production, emerging routes are of particular interest for small-scale, localized fertilizer production[2] and might additionally provide potential as an energy storage technology.[3] Among other approaches, the electrochemical one appears to be of interest allowing for ammonia synthesis from abundant sources, i.e. nitrogen and water, at ambient conditions.[4] Yet, electrochemical ammonia synthesis from nitrogen is hampered by the stability of molecular N_2 and thus a low selectivity towards the desired product. In fact, it appears to be difficult to produce ammonia at concentrations above adventitious NH_3 levels and false-positive results can easily be obtained.[5–8]

Alternative feedstocks for ammonia synthesis are nitrogen oxides (NO_x), which are usually considered as pollutants.[9] Most studies concerning the electrochemical conversion of NO_x focus on selective reduction to N_2.[10] Only recently NO_x utilization for ammonia production was reported.[11–15] Nitric oxide, one of the major air pollutants, is formed in various combustion processes.[16] Reduction of NO is thermodynamically favored over N_2 reduction, see eq. 4.1 to 4.4.[8]

$$2NO + 2H^+ + 2e^- \rightleftharpoons N_2O + H_2O \qquad E^0 = 1.59 \text{ V vs RHE} \quad (4.1)$$
$$2NO + 4H^+ + 4e^- \rightleftharpoons N_2 + 2H_2O \qquad E^0 = 1.68 \text{ V vs RHE} \quad (4.2)$$
$$2NO + 6H^+ + 6e^- \rightleftharpoons 2NH_2OH \qquad E^0 = 0.38 \text{ V vs RHE} \quad (4.3)$$
$$2NO + 10H^+ + 10e^- \rightleftharpoons 2NH_3 + 2H_2O \qquad E^0 = 0.71 \text{ V vs RHE} \quad (4.4)$$

So far only a few catalysts have been proposed for electrochemical formation of ammonia from NO. Besides Bi, Au/C[11], Ag[17] and Fe[18] electrodes, copper was demonstrated to be a promising material for NH_3 formation by both theoretical and experimental investigations in neutral and alkaline conditions.[12,19–21] Using Cu foam electrode, ammonia production rate of 517 μmol h^{-1} cm^{-2} (faradaic efficiency of 93.5 %) was achieved in neutral pH electrolyte at -0.9 V vs RHE using a pure NO (100 %) stream provided by sparging into the solution close to the electrode surface.[12] It is worth noting that NO feeds are usually not purified and thus higher nitrogen oxides[22] might be present in the feed, complicating a precise performance evaluation.

One of the big challenges associated with electrochemical conversion of NO to NH_3 is the low solubility of NO in aqueous electrolytes resulting in mass transport limitations and unfavorable conversion. Moreover, when considering NO utilization from combustion

processes, any feasible process should be able to operate at a relatively low NO concentration.[23] Electrolyte engineering was proposed to overcome those limitations by using a Fe-based complex able to capture NO, thus increasing its concentration in the electrochemical cell.[17] However, the presence of metal complexes in the electrolyte can be detrimental to the direct application of the produced ammonia as green fertilizer.

Herein, we further explore the influence of the electrolyte composition on the performance of Cu electrodes using acid and neutral electrolytes and propose a non-conventional type of electrode geometry in the form of hollow fiber electrodes[24] to minimize mass transport limitations in NO electroreduction to ammonia. While acidic conditions appear favorable to prevent the formation of partially reduced products in mass transfer limited conditions, Cu-decorated Ti hollow fibers are shown to enable ammonia production with rates of 400 μmol h^{-1} cm^{-2} (at -0.6 V vs RHE with almost 90 % faradaic efficiency) using diluted nitric oxide streams (10 % NO) in a flow-through configuration, and sodium sulfate as pH neutral electrolyte.

Experimental section

Electrode preparation

Ti hollow fibers (Figure S4.1a) were prepared by dry-wet spinning according to the previously reported method.[25] In brief, Ti powder was mixed with PES and NMP to form a homogeneous suspension. The spinning mixture was pressed through a spinneret with water as bore liquid. Fibers were thermally treated in order to remove the polymer and form the metallic hollow fiber.

Cu-Ti fibers were prepared by air spraying of Cu-particle suspensions on as-prepared Ti hollow fibers. 40 mg of 1 μm Cu particles were dispersed in 2 ml of isopropanol and sprayed in three sequential steps using an air gun. During spraying a 5 cm long Ti fiber was rotated horizontally. Modified fibers were dried at 80 °C in-between every spraying step. A final layer using 25 nm Cu particles was included in the procedure to achieve a homogeneous surface coating. Finally, Cu-Ti fibers were thermally treated at 600 °C for 2 h in Ar atmosphere with a 10 °C/min heating rate (see Figure S4.1b). Prepared electrodes were characterized using X-ray diffraction (XRD, Bruker Phaser D2) and Scanning Electron Microscopy (SEM) coupled with Energy-Dispersive Xray Spectroscopy (EDS) (using a JSM-6010LA, JEOL system). The pore size distribution was measured by capillary flow porometry based on the liquid extrusion technique, using a Porolux 500 Porometer.

Hollow fiber electrode assemblies were prepared using silver epoxy glue to ensure electrical contact to Swagelok stainless steel tube (Figure S4.1c). The assembly was covered with two-compartment adhesive glue to prevent either silver or the stainless steel tube to get in contact with the electrolyte. To ensure homogeneous distribution of NO through the fibers, the open-end of the fiber was also covered with adhesive.

Electrochemical measurements

All electrochemical measurements were carried out at room temperature using a BioLogic VSP potentiostat. A gas-tight, H-type cell (Nafion 117 membrane was used for compartment separation) was used for linear scan voltammetry and chronoamperometry experiments. In addition to experiments with hollow fibers, rotating disc electrode measurements using Cu disc (Pine research, polished) were performed in 0.05 M H_2SO_4 (pH 1). A graphite rod and an Ag/AgCl (3 M NaCl, BASi) were used as counter and reference electrode, respectively. Measured potentials were corrected for solution resistance (iR drop) and converted to potentials vs RHE using:

$$E_{RHE} = E_{Ag/AgCl} + 0.059\,pH + E^0_{Ag/AgCl}$$

10 % (vol) nitric oxide in Ar was used in all experiments (unless otherwise indicated). Higher nitrogen oxides[26] were removed by passing nitric oxide subsequently through 1 M NaOH and the respective electrolyte used, prior to entering the electrochemical cell (Schematic representation of the electrochemical cell is shown in Figure S4.2b).

The cell was purged with Ar for 30 min to remove oxygen while cleaning the electrode (cyclic voltammetry, 50 cycles in the potential range of 0.35 to -0.75 V vs RHE). Afterwards the cell was purged with 10 % NO in Ar for 30 min to achieve saturation of the electrolyte with NO. Electrochemical measurements were performed using gas flow rates as specified using either flow-through (gas flow through the hollow fiber electrode) or flow-by (gas was introduced through an external sparging line next to the hollow fiber electrode) conditions. A schematic representation of the reactant feed gas supply is shown in Figure S4.2c. Chronoamperometry experiments were performed for 1h in an acidic electrolyte and 30 min in a neutral electrolyte to allow for sufficient accumulation of ammonia in the electrolyte and reliable product detection. The electrochemical surface area of the hollow fiber electrodes for both gas feed configurations was estimated from capacitance measurements. To determine the capacitance, cyclic voltammetry in the capacitive potential region was performed at variable scan rates from 20 to 100 mV/s in Ar saturated 0.1 M $HClO_4$.

Additionally, EC-MS measurements (SpectroInlets, Copenhagen, Denmark, Figure S4.2a) were employed to further elucidate the reduction of NO at Cu surfaces. He or NO (pure, unpurified) were used as carrier gas (1 ml/min). Ag/AgCl (sat. KCl, CH Instrument) and a Pt mesh were used as reference and counter electrode, respectively.

Results and discussion

EC-MS analysis of NO electroreduction on Cu

As outlined, copper is one of the most promising electrode materials for ammonia synthesis from nitric oxide.[12] To investigate the potential-dependent product formation during NO reduction in acidic and neutral electrolyte, EC-MS analysis was performed. CVs in the absence and presence of NO along with the corresponding MS analysis are shown in Figure 4.1 (reference measurements are provided in Figure S4.5).

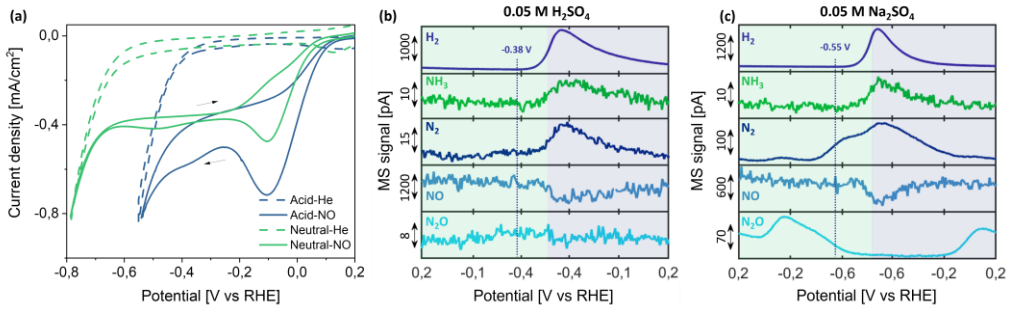

Figure 4.1. EC-MS measurements of NO electroreduction on a Cu disc. (a) Cyclic voltammetry curves (10 mV/s) and desorbed products in (b) 0.05 M H_2SO_4 and (c) 0.05 M Na_2SO_4. The green domains represent reductive scans, while the violet domains represent oxidative scans in the CV.

In acid (blue trace), hydrogen evolution was observed at ~-0.38 V, while in neutral conditions ~-0.55 V was required. This is in agreement with the sluggish kinetics of the HER in the neutral electrolyte, caused by the required water dissociation step[27,28]. In the presence of NO two reductive current maxima are clearly present, of which the first, depending on the electrolyte, has an onset potential of ~0.1 V vs RHE in acidic, and at ~0 V vs RHE in neutral conditions, respectively, maximizing at ~-0.1 V vs RHE independent of the electrolyte used. We assume this current response can be assigned to the reduction of NO_2, which is present in the feed due to the lack of purification of the NO used for the EC-MS experiments. A smaller, second minimum can be observed at -0.4 and -0.5 V, respectively in acid and neutral conditions. In addition, a limiting current plateau, likely associated with the transport limited reduction of NO, is revealed before hydrogen

evolution occurs. The transport limitation of NO was additionally confirmed by rotating disc electrode measurements (Figure S4.6). With increasing rotation rate an increase in current density in the potential range of interest is observed, confirming that NO diffusion limitations must be minimized to achieve efficient ammonia formation by bulk electrolysis.

When scanning in the negative potential direction (light green domain in Figure 4.1b), mass spectrometry does not show any product formation in acidic conditions up to -0.4 V. This suggests that the current measured at -0.1 V should be assigned to the formation of surface adsorbed or liquid-dissolved products, such as NH_4^+ (see also control experiments performed without NO in solution, Figure S4.5, where no products are detected besides H_2 at the most negative potentials). Scanning in the negative potential direction in neutral conditions (Figure 4.1c) shows N_2O formation initiating at ~0 V vs RHE, (m/z: 44 alongside with its m/z: 28 fragment of much lower intensity, referred to as the N_2 signal in Figure 4.1c) is observed. This is in agreement with literature, showing FeNC catalysts to be more active for N_2O formation from NO at higher pH conditions.[18] Despite this agreement with literature, it should be mentioned that the reduction of NO_2, usually a contaminant in NO,[26] might also contribute to the formation of N_2O. At more negative potentials a decrease in N_2O signal is associated with an increase in N_2 (m/z: 28), maximizing at ~-0.6 V vs. RHE. The formation of N_2 is initially in majority associated with the secondary reduction of N_2O, rather than the primary reduction of NO.[29] In fact, the sharp decrease in N_2O signal initiating at -0.4 V vs RHE in neutral electrolyte matches the onset of N_2 formation. Moreover, we observe a drop in N_2O signal below the baseline level (see also Figure S4.7) at potentials where peak formation of N_2 is observed, which suggests NO is likely contaminated with N_2O. Finally, in the last stages of the negative scan, close to the lower limit of the applied potential, a secondary increase in N_2 signal suggests a minor contribution of direct NO reduction to N_2.

Interestingly, in the positive scan direction (gray domains in Figures 4.1b and c), significantly more gaseous products are detected. In acid conditions a decrease of the signal associated with m/z: 30 is observed, which corresponds to the consumption of NO, agreeing with positive MS responses in N_2 (m/z: 28) and possibly NH_3 (m/z: 17)[29]. To the best of our knowledge NH_3 formation from NO in acidic electrolyte in bulk electrolysis experiments has not yet been previously reported. The NH_3 MS signal shows a similar response in shape to the response of H_2, which is of much higher intensity. Due to the small EC-MS cell volume and relatively high reduction currents for H_2 evolution, a pH change induced by proton reduction might allow for the partial transformation of NH_4^+ to NH_3 and thus allows for the detection of ammonia. Note that m/z: 17 is only detected at highly negative potentials while NH_4^+ formation at more positive potentials should not be excluded, as shown by theory as well as experimental work.[12,21] Further work is required

to rule out any contribution to m/z: 17 of water, potentially changing in concentration during NO reduction (see eq. 4.1-4.4). Although shifted by -0.2 V, the product evolution in neutral conditions is quite similar to that observed in acid conditions. However, due to the higher current densities observed, acidic conditions seem to be more favorable for NO electroreduction to ammonia, in particular in conditions when NO supply is limited.

The results obtained by cyclic voltammetry are in good agreement with chronoamperometric data (Figure S4.8), where the onset of gaseous product formation is clearly observed, confirming that H_2 is being produced at -0.3 V and -0.5 V vs RHE in acidic and neutral electrolyte, respectively.

NO electroreduction on Cu-Ti hollow fiber

Cu-Ti electrode characterization

As shown above by EC-MS and RDE experiments ammonia formation occurs on Cu electrodes, likely with the highest FE in acid conditions. Still mass transport limitations in NO likely influence the selectivity in conversion of NO. Hollow fiber electrodes allow for an efficient supply of gaseous NO to the electrode surface, similar to widely-applied gas diffusion electrodes. Transport of liquid-dissolved species toward hollow fiber electrodes is, however, based on convection rather than diffusion. Cu-based hollow fiber electrodes were prepared to evaluate the effect of enhanced transport of NO on the faradaic efficiency towards ammonia production.

In the hollow fiber electrode geometry gas is supplied from the inside of the tube. Due to the porous structure (Figure 4.2) and pore-filling with electrolyte, a pressure buildup in the electrode is observed. It is expected that only the outer part of the electrode is forming an electroactive three-phase boundary and thus only the outer surface of a Ti hollow fiber was modified with Cu. XRD patterns, as well as SEM images of the prepared electrodes, confirm the successful decoration of Ti hollow fibers with metallic Cu (Figure 4.2). Moreover, SEM images of Cu-Ti electrodes reveal a uniform distribution of Cu on the Ti surface (Figure 4.2c and Figure S4.9). After modification with Cu, a narrowing of the pores of the electrode is noticeable (compare SEM of Ti electrode in Figure S4.10) due to the presence of smaller Cu particles. Additional confirmation of smaller pores is obtained by pore size distribution measurements (Figure 4.2d).

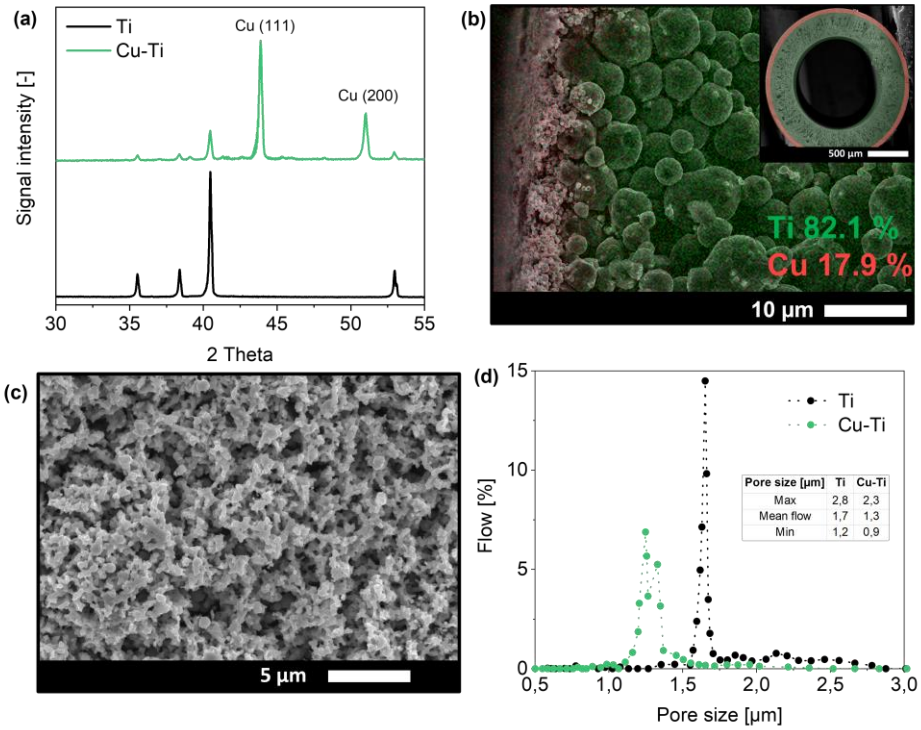

Figure 4.2. (a) XRD patterns of the Ti and Cu-Ti hollow fibers[24,25]. (b) SEM images of the Cu-Ti hollow fiber displaying a cross section including EDS analysis (c) and a view perpendicular to the surface. (d) Pore size distribution of Ti and Cu-Ti hollow fibers.

The effect of NO supply methodology on current density

Linear scan voltammetry was performed (Figure 4.3) in acidic and neutral pH electrolyte to investigate the influence of flow configurations and flow rates on the potential-current behavior of as-prepared Cu-Ti hollow fiber electrodes. In both electrolytes, only a minor increase in current was observed when NO was supplied in flow-by configuration (dotted lines – for magnification in the active region see Figures S4.11 and S4.12), when compared to reference measurements performed in pure Ar flow. In agreement with the EC-MS data, the presence of NO results in a larger current enhancement in acidic environment, than in neutral conditions. When NO was supplied through the hollow fiber electrode (solid lines in Figure 4.3) at 5 mL.min^{-1} in acidic conditions (Figure 4.3a), a significant current enhancement associated with the presence of NO is observed, prior to the onset of hydrogen evolution, indicating that the NO concentration at the electrode-electrolyte interface is significantly increased and a limiting current density of ~-8 mA.cm^{-2} is obtained.

For feed gas compositions with higher NO concentration (Figure S4.13), even higher current densities were observed. Therefore, efficient transport of NO to the electrode surface in hollow fiber electrode configuration is demonstrated. It is interesting to note that also unmodified Ti hollow fibers appear to be active for NO reduction (Figures S4.11 and S4.13). Still, compared to Cu-Ti electrodes, the significant cathodic shift in onset potential renders the use of bare Ti electrodes less useful for NO electroreduction. Moreover, based on previous reports, the selectivity for ammonia formation is expected to be higher for Cu-based electrodes.[12]

In neutral conditions, the effect of applying 5 ml min^{-1} of gas flow through the fiber is more dramatic (note the difference in scales of Figures 4.5a and b), leading to high current densities in NO reduction.

Since supplying NO through the electrode increases the current densities, the influence of gas flow rate was evaluated in both electrolyte compositions (Figure 4.3). A diffusion-limited current of -20 mA/cm^2 at the highest flow rates obtained at ~-0.35 V for measurements in acidic electrolyte whereas the current plateau is only apparent for low flow rates of max. 5 mL.min^{-1} in neutral conditions and already exceeds -50 mA/cm^2 at ~- 0.55 V.

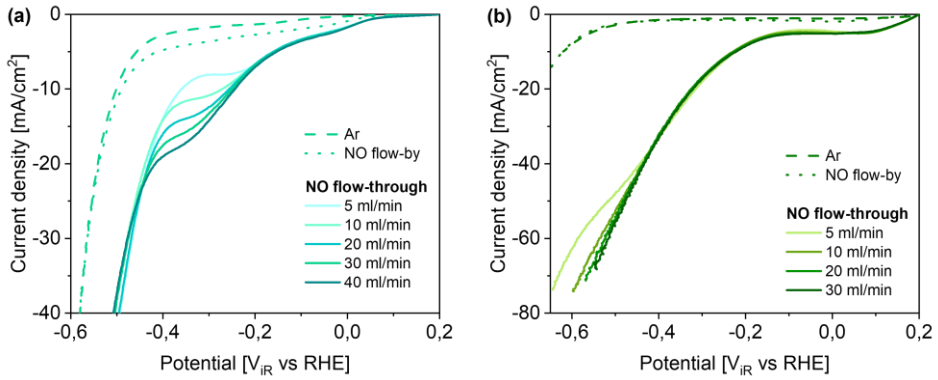

Figure 4.3. LSVs of Cu-Ti electrodes in flow-by and flow-through operation, at different NO flow rates in (a) 0.05 M H_2SO_4 and (b) 0.05 M Na_2SO_4. Note that the reductive current in pure Ar flow in 0.05 M H_2SO_4 (Figure 4.3a) is assigned to SO_4^{2-} adsorption on the Cu electrode (see also Figure S4.14). Also, note the difference in scale of current density in Figures 4.3a and b.

In agreement with the measurements obtained by EC-MS two distinct potential regimes are identified in both electrolytes. The first regime in the potential window from 0 to -0.2 V vs RHE appears to be almost flow rate independent (see Figure S4.12 and S4.15 for

magnification in acidic and neutral electrolytes respectively). Considering the similarities with the EC-MS measurements, the current is assigned to NO_2 reduction still being present in low quantities despite careful NO purification[26] (see Figures S4.6 and S4.16 for additional information, also discussing the possible role of contamination of NO with NO_2).[30] A second flow rate and electrolyte-dependent current regime is observed in the potential range between -0.2 V and -0.5 V vs RHE, i.e. before hydrogen evolution occurs for measurements performed in acidic electrolyte. With increasing NO flow rate, as expected the limiting current increases. Considering that at flow rates above 30 ml/min the influence of flow rate becomes less relevant as shown in Figure S4.17, measurements at higher flow rates were not performed.

In neutral electrolyte, the onset of the potential window associated with flow-induced NO reduction occurs at a significantly more negative potential (below -0.4 V vs RHE). Also, the hydrogen evolution is again showing a shift in onset potential, in agreement with CVs measured using Cu discs (Figure 4.1a). Moreover, the observed current increase is predominantly related to enhanced NO availability at the electrode interface as also revealed by RDE experiments and measurements performed at high NO concentrations. Particularly due to an inhomogeneous pore size distribution (Figure 4.2d), pore-opening depends on the actual flow rate, as a higher pressure (thus higher flow rate) is required to remove liquid from smaller pores. Thus, only at high flow rates, an efficient formation of a three-phase boundary layer occurs (for a schematic representation of this phenomena see Figure S4.18). This is supported by capacitance measurements revealing a decrease in electrochemical surface area at higher flow rates (Figure S4.19) as well as decreasing intensity of the SO_4^{2-} adsorption peak in Ar saturated electrolyte (Figure S4.20).

The significant difference in current density between the electrolytes could be related to a change in the hydrogen surface coverage of the Cu surface, the general suppression of the hydrogen evolution in electrolytes of higher pH, or possibly a change in reaction mechanism caused by a surface pH increase in a neutral electrolyte, which can cause interaction of NO with OH^- forming NO_2^-/NO_3^-.[20] However, additional studies into the NO electroreduction mechanism on Cu surfaces are needed to fully resolve this behavior.

Selectivity of NO electroreduction on the Cu-Ti hollow fiber

Based on the obtained results the applicability of Cu-Ti hollow fiber electrodes for ammonia electrosynthesis from nitric oxide was studied using chronoamperometry in the relevant potential range of NO reduction, i.e. -0.1 to -0.4 V vs RHE in acidic and -0.1 to -0.6 V vs RHE in the neutral electrolyte at varying gas flow rate. Faradaic efficiency and

NH_3 production rate were determined over 60 min and 30 min of constant potential electrolysis for acidic and neutral electrolyte, respectively (Figure 4.4).

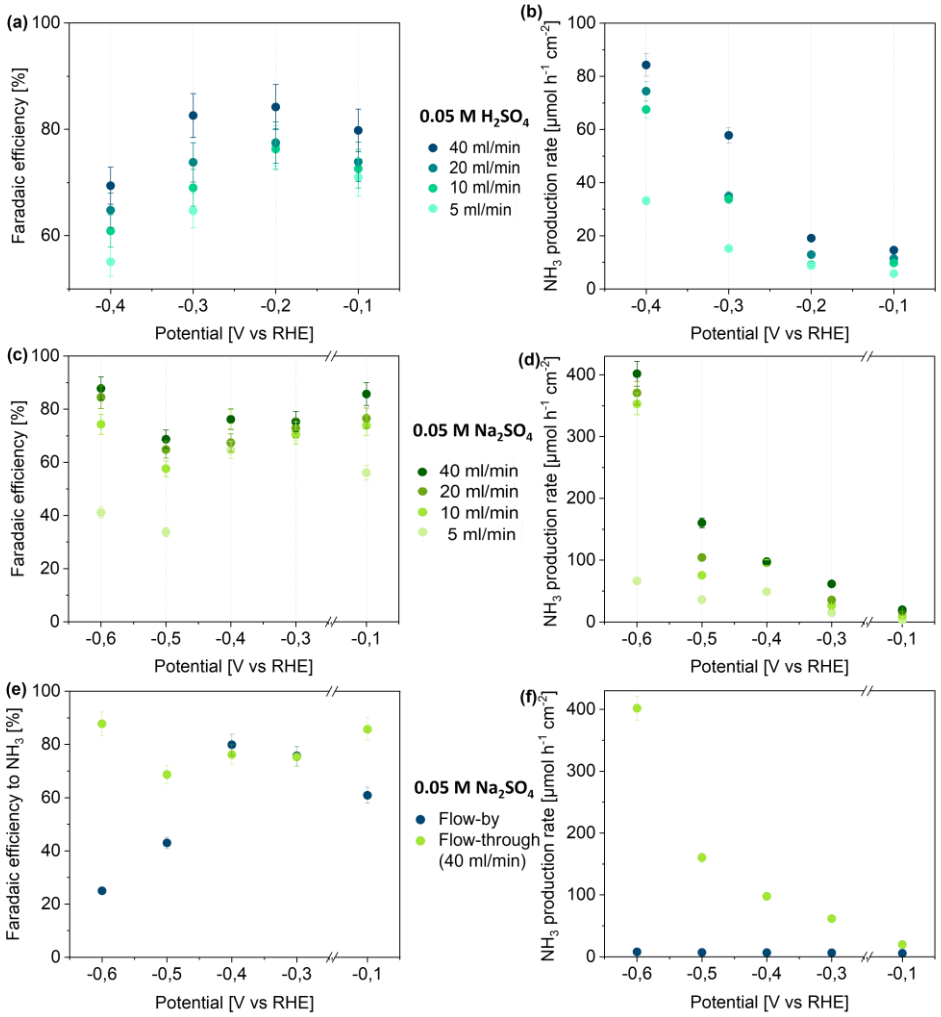

Figure 4.4. Selectivity in NO electroreduction to NH_3 using the Cu-Ti hollow fiber electrode. Faradaic efficiency and NH_3 production rate are shown in (a, b) for 0.05 M H_2SO_4 and in (c, d) for 0.05 M Na_2SO_4 electrolyte in flow-through electrode configuration. (e, f) Comparison of faradaic efficiency and NH_3 production rate in flow-through (at 40 ml/min) and flow-by configuration in 0.05 M Na_2SO_4 electrolyte.

First, the data in Figure 4.4 can be compared to the EC-MS data. If one compares the FE in the absence of flow at the potentials applied in the EC-MS measurements, and for the hollow fiber electrode, the effect of the electrolyte appears consistent. In Figure 4.4e only

25%-40% FE is achieved in neutral conditions in flow-by mode or at low NO velocity (Figure 4.4c), while in acid conditions the FE is 60-80 % in the potential range also investigated in the EC-MS (the remainder being the formation of H_2).

Higher flow rates resulted in an overall increase in FE to ammonia as well as its production rate. This is assigned to the opening of pores and the resulting favorable interaction of NO with the Cu surface. It is worth noting that similar behavior was observed on Ti electrodes (Figure S4.21 and S4.22) but due to generally larger pores the effect is less pronounced. Considering the relatively low current densities in a flow-through mode in acid conditions, the obtained production rates are relatively low and maximize at ~80 μmol h^{-1} cm^{-2}.

The remaining FE in neutral conditions is assigned to the formation of either N_2O and N_2 (at more positive potentials) and H_2 (at more negative potentials) in agreement with EC-MS data. The general trend observed here for the product-potential dependency matches well with the literature[31] where N_2O is expected to be produced at more positive potentials and NH_3 at potentials < -0.1 V vs RHE. It is worth noting that minor quantities of hydroxylamine were detected (Figures S4.24 and S4.25).

Overall an averaged faradaic efficiency of 85 % was obtained in acid conditions, nevertheless, the measurements suffered from the stability of the electrode, and a stable current was not maintained for extended periods of time (Figure S4.26a). In fact, roughening of the electrode surface was observed by SEM (Figure S4.26b and c) and pressure changes in the hollow fiber throughout the measurement indicated copper corrosion/detachment (Figure S4.27) in acid conditions.

The most striking result of Figure 4.4, is the significant effect of flow rate on the performance of the Cu-Ti electrodes in neutral conditions (see also Figure S4.23). The faradaic efficiency for NO reduction to ammonia reached almost 90 % at -0.6 V vs RHE in flow-through mode (40 ml/min flow rate), with very little competing hydrogen evolution (compare to Figure S4.25b and c where combined faradaic efficiency of NH_3 and NH_2OH is shown). This translates in an ammonia production rate of ~400 μmol h^{-1} cm^{-2} (see Figure 4.4f). As previously stated, applying the increased flow rate suppresses the formation of hydrogen due to enhanced availability of NO which is the main reason for increased FE to NH_3 compared to fiber operation in flow-by conditions. In addition, the formation of N_2O and N_2 is also suppressed which could be related to a secondary effect of the increasing gas velocity, i.e. minimizing changes in pH due to convective mixing induced by the exiting gas bubbles. Moreover, the Cu-Ti hollow fiber electrode stability was verified over the period tested, i.e. 30 min electrolysis (Figure S4.27, S4.28, S4.29 and associated description in the supplementary information).

The optimized results obtained here are in fact comparable to recent reports using Cu foam electrodes.[12] Importantly it has to be noted, that significantly lower concentrations of NO have been utilized in this study, i.e. 10 % NO, being of relevance when considering NO utilization from combustion processes.

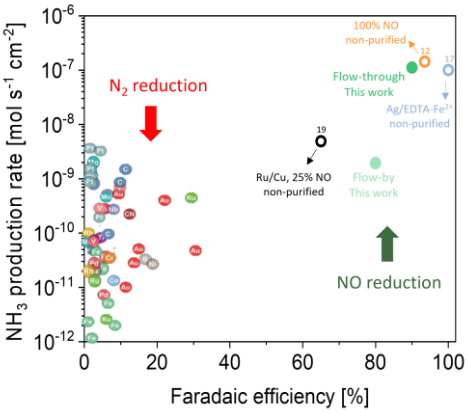

Figure 4.5. NH_3 production rate vs faradaic efficiency on different catalysts in N_2 electroreduction compared to NO electroreduction in neutral electrolyte in this study. NO reduction data from [12,17,19]. N_2 reduction data reproduced with modification from [32].

A detailed comparison of faradaic efficiency and production rate of NH_3 obtained by electrochemical reduction of NO and N_2 obtained in recent studies is shown in Figure 4.5. Although N_2 seems to be the most relevant feed for ammonia synthesis due to its abundancy, electrochemical NO reduction appears to be promising considering that the amount of produced ammonia significantly overcomes adventitious contamination. Using NO as a feed for electrochemical green ammonia synthesis is more facile than N_2 as long as decentralized production of ammonia at sites with NO_x waste streams is targeted. Despite the high faradaic efficiencies for ammonia formation from NO, the overall energy demand is still high. The well-established Haber-Bosch process requires approx. 10 kWh/kg of NH_3 [33,34] which compared to results in this study is ~2 times lower (Figure S4.30). However, it is worth noting that further improvements can be achieved. The benefit of ammonia formation in our system compared to the present literature is due to the beneficial properties of our flow-through hollow fiber electrode compared to widely used flow-by systems. Moreover, lower NO concentrations were utilized while maintaining a high conversion rate. For practical application, the electrochemical conversion of nitrogen oxides holds promise, as ammonia separation is not needed since the electrolyte has the potential to be used as green fertilizer directly after electrolysis.

Conclusions

The effect of electrolyte and electrode geometry for the reduction of nitric oxide to ammonia at low NO concentrations has been investigated using Cu electrodes. In mass transfer limited conditions, acid conditions favor the formation of ammonia, minimizing partial reduction of NO to N_2O and/or N_2. It is shown however that hollow fiber electrodes are very efficient to achieve a high reactant concentration at the electrode surface which significantly increases current density for conversion of NO to NH_3, in particular at neutral pH. Faradaic efficiencies of almost 90 % with NH_3 production rates of 400 μmol h^{-2} cm^{-2} were obtained in neutral electrolyte at -0.6 V vs RHE in a flow-through system configuration. Importantly feed gas containing only 10 % NO was used. It is expected that further improvements in NO conversion will be obtained by adjusting the surface distribution and morphology of Cu as well as the general pore size distribution.

References

[1] K. H. R. Rouwenhorst, P. M. Krzywda, N. E. Benes, G. Mul, L. Lefferts, *Ullmann's Encycl. Ind. Chem.* **2020**, 1–20.

[2] K. H. R. Rouwenhorst, P. M. Krzywda, N. E. Benes, G. Mul, L. Lefferts, in *Techno-Economic Challenges Green Ammon. as an Energy Vector*, **2020**, pp. 41–83.

[3] N. Salmon, R. Bañares-Alcántara, *Sustain. Energy Fuels* **2021**, *5*, 2814–2839.

[4] G. Hochman, A. S. Goldman, F. A. Felder, J. M. Mayer, A. J. M. Miller, P. L. Holland, L. A. Goldman, P. Manocha, Z. Song, S. Aleti, *ACS Sustain. Chem. Eng.* **2020**, *8*, 8938–8948.

[5] S. Z. Andersen, V. Čolić, S. Yang, J. A. Schwalbe, A. C. Nielander, J. M. McEnaney, K. Enemark-Rasmussen, J. G. Baker, A. R. Singh, B. A. Rohr, M. J. Statt, S. J. Blair, S. Mezzavilla, J. Kibsgaard, P. C. K. Vesborg, M. Cargnello, S. F. Bent, T. F. Jaramillo, I. E. L. Stephens, J. K. Nørskov, I. Chorkendorff, *Nature* **2019**, *570*, 504–508.

[6] L. F. Greenlee, J. N. Renner, S. L. Foster, *ACS Catal.* **2018**, *8*, 7820–7827.

[7] G. Y. Duan, Y. Ren, Y. Tang, Y. Z. Sun, Y. M. Chen, P. Y. Wan, X. J. Yang, *ChemSusChem* **2020**, *13*, 88–96.

[8] J. Choi, B. H. R. Suryanto, D. Wang, H. Du, R. Y. Hodgetts, F. M. F. Vallana, D. R. Macfarlane, A. N. Simonov, *Nat. Commun.* **2020**, *11*, 1–10.

[9] R. Daiyan, T. Tran-Phu, P. Kumar, K. Iputera, Z. Tong, J. Leverett, M. H. A. Khan, A. A. Esmailpour, A. Jalili, M. Lim, A. Tricoli, R.-S. Liu, X. Lu, E. Lovell, R. Amal, *Energy Environ. Sci.* **2021**, *14*, 3588–3598.

[10] M. Duca, M. T. M. Koper, *Energy Environ. Sci.* **2012**, *5*, 9726–9742.

[11] J. Choi, J. Choi, H. L. Du, H. L. Du, C. K. Nguyen, C. K. Nguyen, B. H. R. Suryanto, A. N. Simonov, A. N. Simonov, D. R. MacFarlane, D. R. MacFarlane, *ACS Energy Lett.* **2020**, *5*, 2095–2097.

[12] J. Long, S. Chen, Y. Zhang, C. Guo, X. Fu, D. Deng, J. Xiao, *Angew. Chemie Int. Ed.* **2020**, *59*, 9711–9718.

[13] P.-F. Sun, W.-L. Wang, X. Zhao, J.-S. Dang, *Phys. Chem. Chem. Phys.* **2020**, *22*, 22627–22634.

[14] J. M. McEnaney, S. J. Blair, A. C. Nielander, J. A. Schwalbe, D. M. Koshy, M. Cargnello, T. F. Jaramillo, *ACS Sustain. Chem. Eng.* **2020**, *8*, 2672–2681.

[15] N. C. Kani, J. A. Gauthier, A. Prajapati, J. Edgington, I. Bordawekar, W. Shields, M. Shields, L. C. Seitz, A. R. Singh, M. R. Singh, *Energy Environ. Sci.* **2021**, DOI 10.1039/d1ee01879e.

[16] S. Roy, M. S. Hegde, G. Madras, *Appl. Energy* **2009**, *86*, 2283–2297.

[17] D. Y. Kim, D. Shin, J. Heo, H. Lim, J. A. Lim, H. M. Jeong, B. S. Kim, I. Heo, I. Oh, B. Lee, M. Sharma, H. Lim, H. Kim, Y. Kwon, *ACS Energy Lett.* **2020**, *5*, 3647–3656.

[18] D. H. Kim, S. Ringe, H. Kim, S. Kim, B. Kim, G. Bae, H. S. Oh, F. Jaouen, W. Kim, H. Kim, C. H. Choi, *Nat. Commun.* **2021**, *12*, 1–11.

[19] J. Shi, C. Wang, R. Yang, F. Chen, N. Meng, Y. Yu, B. Zhang, *Sci. China Chem.* **2021**, *64*, 1493–1497.

[20] J. Soto-Hernández, C. R. Santiago-Ramirez, E. Ramirez-Meneses, M. Luna-Trujillo, J.-A. Wang, L. Lartundo-Rojas, A. Manzo-Robledo, *Appl. Catal. B Environ.* **2019**, *259*, 118048.

[21] H. Wan, A. Bagger, J. Rossmeisl, *Angew. Chemie Int. Ed.* **2021**, *60*, 21966–21972.

[22] M. T. De Groot, M. Merkx, A. H. Wonders, M. T. M. Koper, *J. Am. Chem. Soc.* **2005**, *127*, 7579–7586.

[23] I. Aouini, A. Ledoux, L. Estel, S. Mary, *Oil Gas Sci. Technol.* **2014**, *69*, 1091–1104.

[24] R. Kas, K. K. Hummadi, R. Kortlever, P. De Wit, A. Milbrat, M. W. J. Luiten-Olieman, N. E. Benes, M. T. M. Koper, G. Mul, *Nat. Commun.* **2016**, *7*, 1–7.

[25] R. P. H. Jong, P. M. Krzywda, N. E. Benes, G. Mul, *RSC Adv.* **2020**, *10*, 31901–31908.

[26] J. A. Colucci, M. J. Foral, S. H. Langer, *Electrochim. Acta* **1985**, *30*, 521–528.

[27] X. Zou, X. Huang, A. Goswami, R. Silva, B. R. Sathe, E. Mikmeková, T. Asefa,

Angew. Chemie - Int. Ed. **2014**, *53*, 4372–4376.

[28] C. T. Dinh, A. Jain, F. P. G. de Arquer, P. De Luna, J. Li, N. Wang, X. Zheng, J. Cai, B. Z. Gregory, O. Voznyy, B. Zhang, M. Liu, D. Sinton, E. J. Crumlin, E. H. Sargent, *Nat. Energy* **2019**, *4*, 107–114.

[29] B. H. Ko, B. Hasa, H. Shin, E. Jeng, S. Overa, W. Chen, F. Jiao, *Nat. Commun.* **2020**, *11*, 1–9.

[30] B. J. Finlayson-Pitts, L. M. Wingen, A. L. Sumner, D. Syomin, K. A. Ramazan, *Phys. Chem. Chem. Phys.* **2003**, *5*, 223–242.

[31] J. Long, C. Guo, X. Fu, H. Jing, G. Qin, H. Li, J. Xiao, *J. Phys. Chem. Lett.* **2021**, *12*, 6988–6995.

[32] I. J. McPherson, T. Sudmeier, J. Fellowes, S. C. E. Tsang, *Dalt. Trans.* **2019**, *48*, 1562–1568.

[33] K. H. R. Rouwenhorst, A. G. J. Van der Ham, G. Mul, S. R. A. Kersten, *Renew. Sustain. Energy Rev.* **2019**, *114*, DOI 10.1016/j.rser.2019.109339.

[34] S. Ghavam, M. Vahdati, I. A. G. Wilson, P. Styring, *Front. Energy Res.* **2021**, *9*, 1–19.

[35] A. C. Nielander, J. M. McEnaney, J. A. Schwalbe, J. G. Baker, S. J. Blair, L. Wang, J. G. Pelton, S. Z. Andersen, K. Enemark-Rasmussen, V. Čolić, S. Yang, S. F. Bent, M. Cargnello, J. Kibsgaard, P. C. K. Vesborg, I. Chorkendorff, T. F. Jaramillo, *ACS Catal.* **2019**, *9*, 5797–5802.

[36] R. Y. Hodgetts, A. S. Kiryutin, P. Nichols, H.-L. Du, J. M. Bakker, D. R. Macfarlane, A. N. Simonov, *ACS Energy Lett.* **2020**, *5*, 736–741.

[37] D. J. Darke, *J. Chromatogr. B* **1980**, *181*, 449–452.

Supplementary information 4

Materials

Titanium powder (TLS Technik GmbH & Co., ASTM, grade 2) with an average particle size of 6 μm, polyethersulfone (PES, BASF, Ultrason E 6020P) and N-methylpyrrolidone (NMP, Sigma Aldrich, ≥99 %) were used for Ti hollow fiber preparation. For surface modification of Ti hollow fibers 1 μm Cu powder (SkySpring nanoparticles, 99.8 %) and 25 nm Cu powder (Sigma Aldrich, TEM) were used. In the following, Cu-modified Ti hollow fibers are referred to as Cu-Ti hollow fiber. Nitric oxide (Linde, 2.5 N purity grade) diluted with Ar was used as feed. Ammonium chloride (Alfa Aesar, 99.999 %), maleic acid (Sigma Aldrich, ≥99 %), DMSO-d6 (Sigma Aldrich, 99.5 atom % D), hydroxylamine hydrochloride (Sigma Aldrich, 99.995%), acetone (Sigma Aldrich, 99.5%) and methanol (Sigma Aldrich, ≥99.9 %) were used for product detection and calibration. H2SO4 (Sigma Aldrich, ≥97.5 %), HClO4 (Sigma Aldrich, 70 %), and Na2SO4 (Sigma Aldrich, ≥99.0 %) were used for electrolyte preparation. Silver epoxy glue (Chemtronics, CW2400) and two-component adhesive glue (Weicon, 10550024) were used to prepare the electrode assembly.

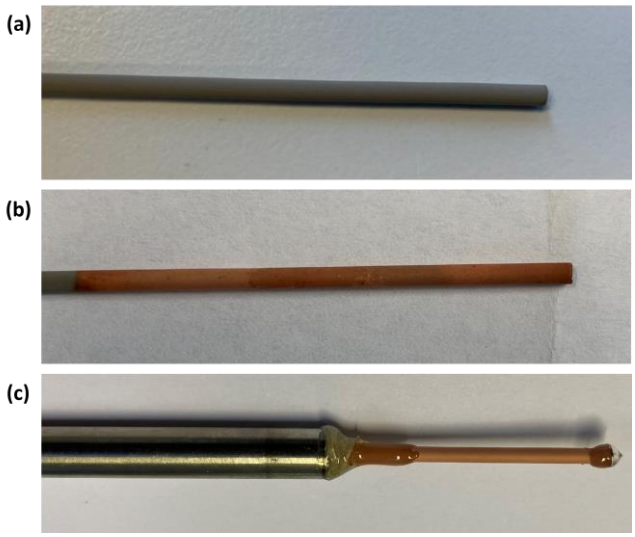

Figure S4.1. Photograph of (a) Ti hollow fiber, (b) Cu-Ti hollow fiber and (c) Cu-Ti electrode assembly.

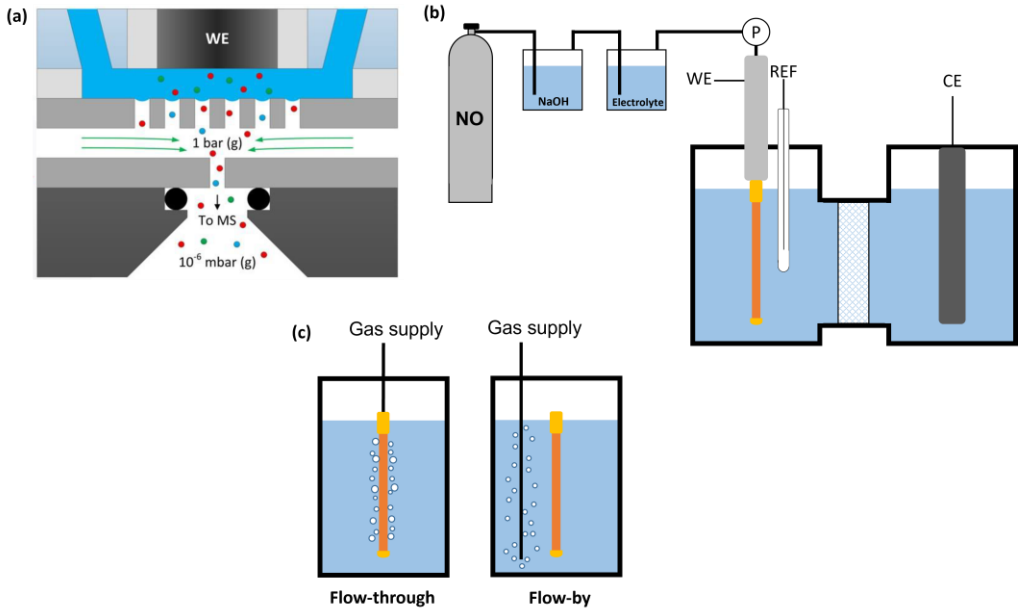

Figure S4.2. Schematic representation of (a) EC-MS set-up and (b) electrolytic cell with gas purification. (c) Working electrode compartment with flow-through and flow-by gas supply.

Ammonia quantification

The concentration of ammonia was determined by ^{1}H NMR spectroscopy based on methods described elsewhere [35,36]. Calibration was performed using standard NH_4Cl solutions with known concentration. Generally 0.5 ml of the (standard) solution was mixed with 50 µl of 0.5 M H_2SO_4 containing 10 mM maleic acid (internal standard) and 25 µl of DMSO-d6 as locking solvent. ^{1}H NMR spectra were recorded on a Bruker 400MHz spectrometer with 1000 scans (Figure S4.3). The area ratio of the NH_4^+ peak at 6.79 ppm and the maleic acid peak at 6.22 ppm were plotted versus NH_3 concentration (see Figure S4.3c).

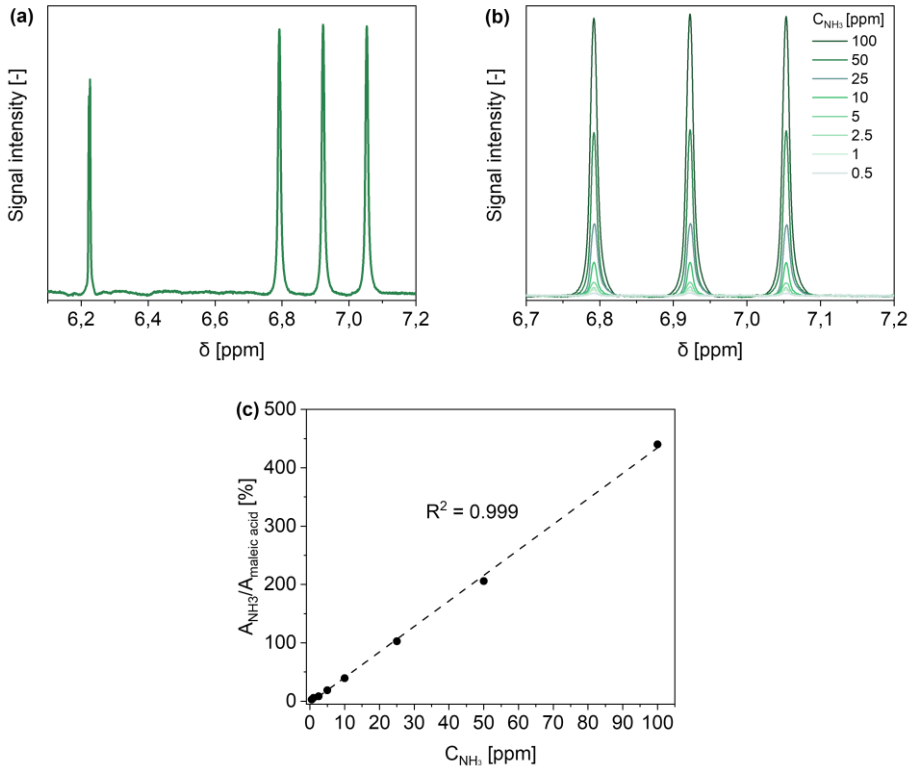

Figure S4.3. ^{1}H NMR spectrum of (a) 50 ppm NH_4^+ with 10 mM maleic acid and (b) different concentration of NH_4^+. (c) Calibration curve for NH_4^+ quantification.

Hydroxylamine quantification

The hydroxylamine content was determined by gas chromatography according to a method published elsewhere [37]. In short, samples obtained after electrolysis were neutralized by the addition of NaOH or H_2SO_4 solution. To allow for quantification, hydroxylamine was reacted with acetone to form acetone oxime by addition of 2 µl of methanol/acetone (1:1 v/v) to 4 ml of neutralized sample solution. Acetone oxime was quantitatively detected by gas chromatography (GC-FID, see Figure S4.4a). Following the procedures described above, the calibration curve was prepared using standard solutions of hydroxylamine hydrochloride (Figure S4.4b). A quantification error of 5 % was estimated based on the analytical techniques used.

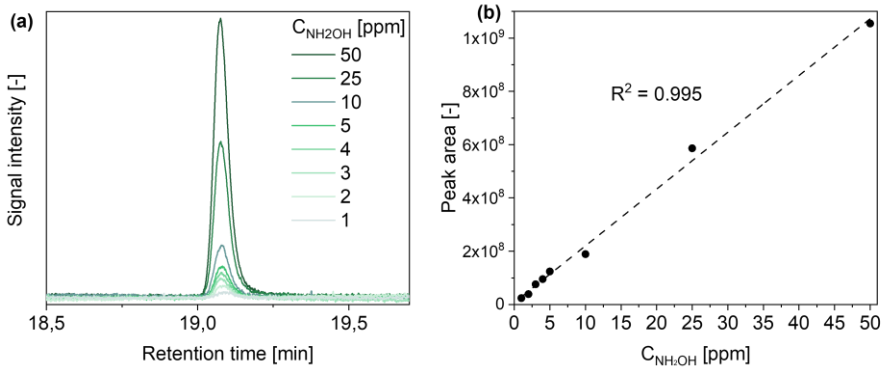

Figure S4.4. (a) Chromatogram (GC-FID) of NH_2OH with different concentration. (b) Calibration curve for NH_2OH quantification.

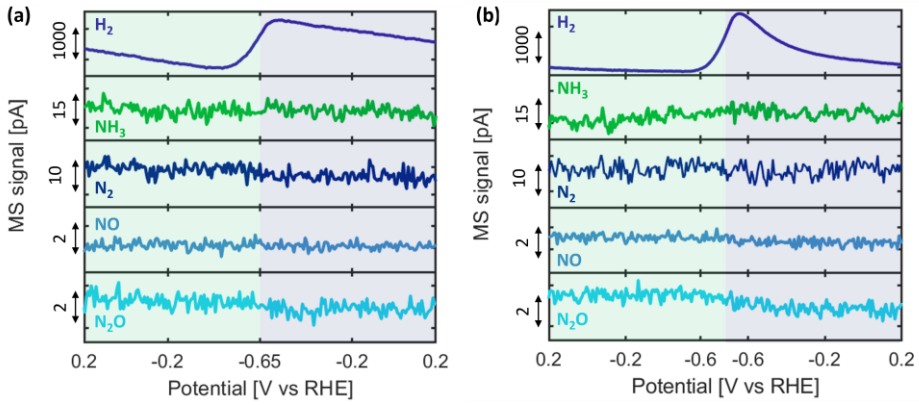

Figure S4.5. EC-MS analysis of desorbed products from Cu surface during cyclic voltammetry in Ar saturated (a) 0.05 M H_2SO_4 and (b) 0.05 M Na_2SO_4.

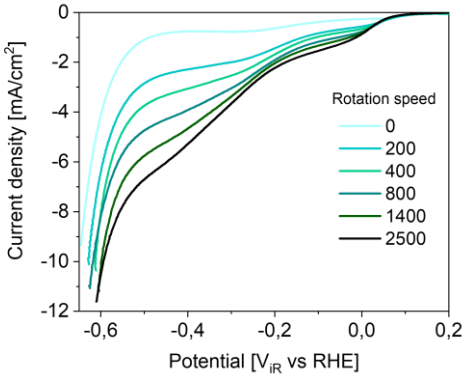

Figure S4.6. LSV of Cu disc in NO saturated 0.05 M H_2SO_4 at different rotation rates.

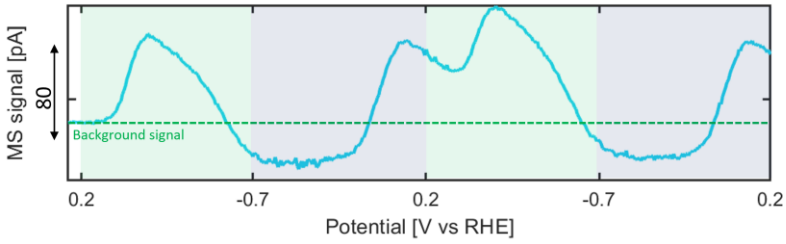

Figure S4.7. EC-MS analysis of m/z: 44 desorbed from Cu surface during first and second cyclic voltammetry cycle in NO saturated 0.05 M Na_2SO_4. (reductive scan – green domains and oxidative scan – purple domains)

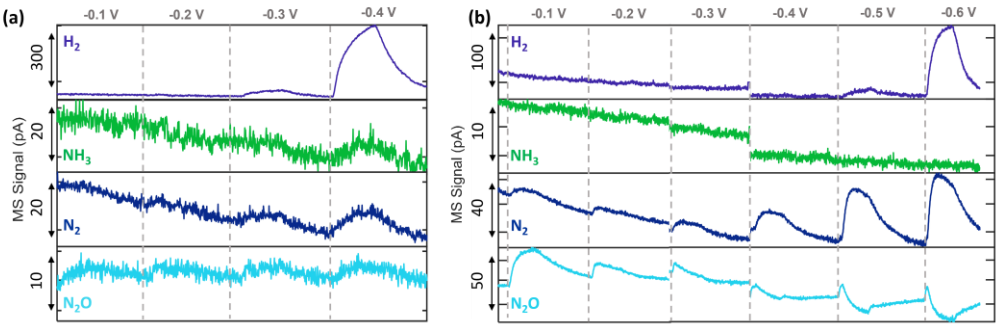

Figure S4.8. EC-MS analysis of desorbed products from Cu surface during chronoamperometry in NO saturated (a) 0.05 M H_2SO_4 and (b) 0.05 M Na_2SO_4.

Lack of m/z: 17 in neutral electrolyte can be explained based on potential which is not high enough. Lower current densities during chronoamperometry than during CV are observed as can be also seen in H_2 peak which indicates a significantly smaller amount of H_2 being formed compared to CV experiments thus pH change will be less significant in this case.

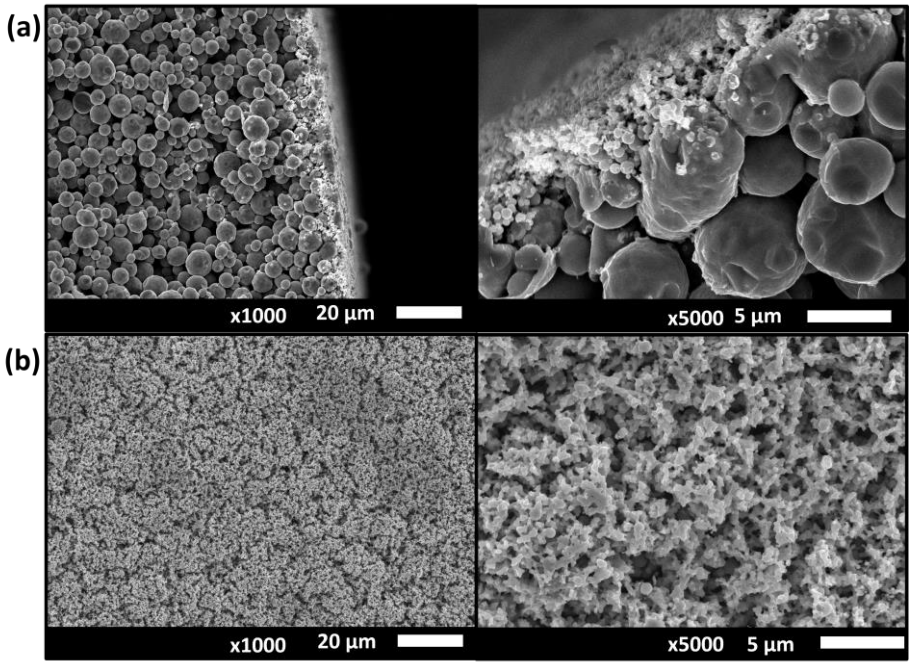

Figure S4.9. SEM images of (a) cross section and (b) surface of Cu-Ti hollow fiber.

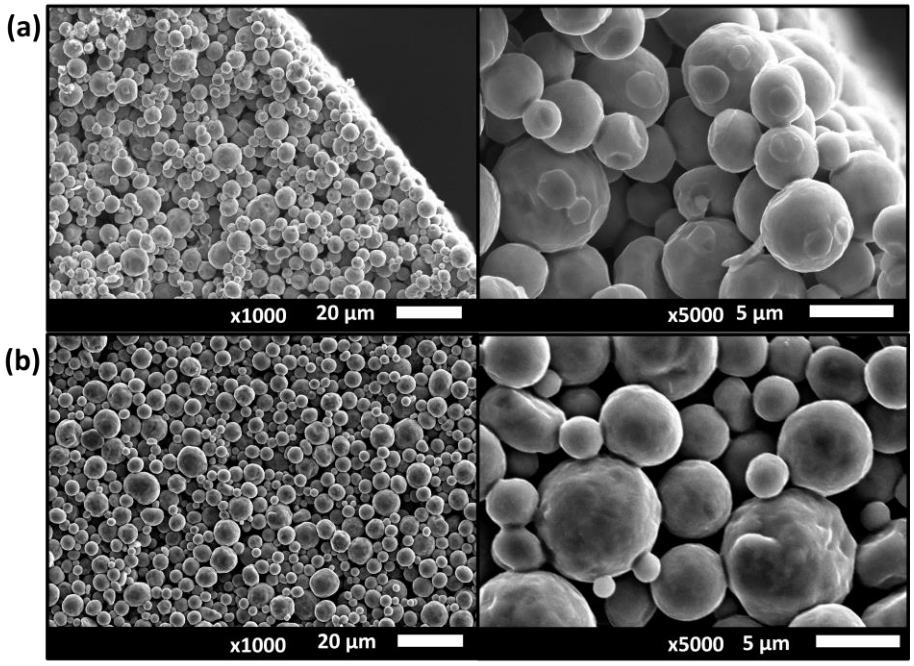

Figure S4.10. SEM images of (a) cross section and (b) surface of Ti hollow fiber.

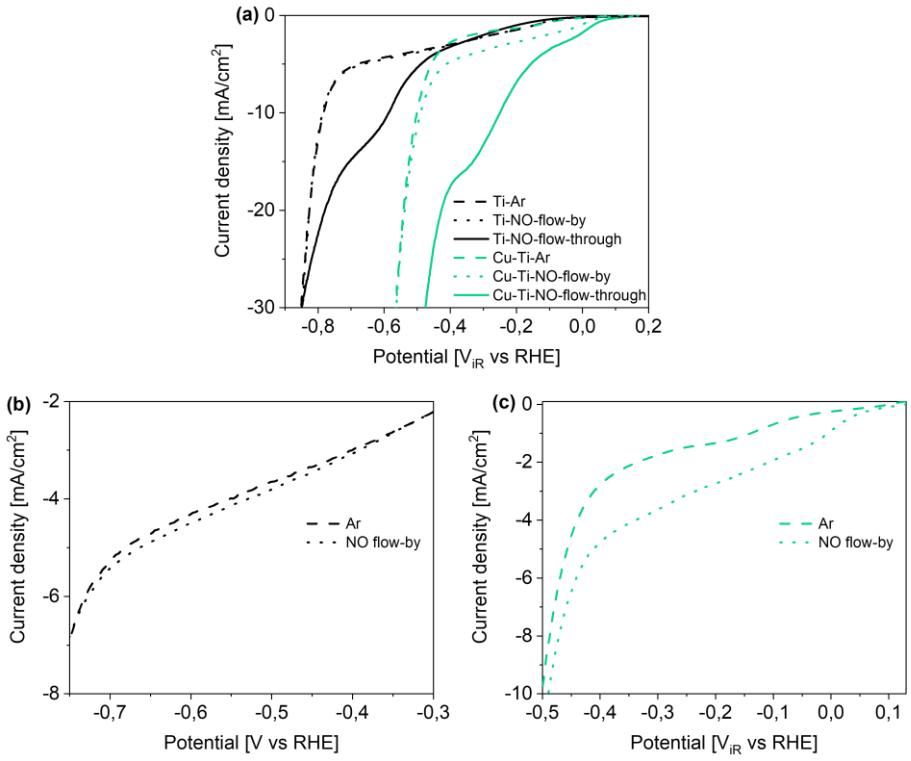

Figure S4.11. (a) LSV of NO reduction in flow-by and flow-through configuration on Ti and Cu-Ti hollow fiber electrode. Magnification into the active region in flow-by configuration on (b) Ti and (c) Cu-Ti electrode.

In flow-by configuration (dotted lines) very low activity was observed on Ti catalyst (Figure S4.12a for magnification) which is in agreement with available literature and explains limited number of studies of NO reduction on Ti. Cu coated hollow fiber shows a clear response in presence of NO indicating better activity of Cu compared to Ti for NO electroreduction however reduction rate is relatively low.

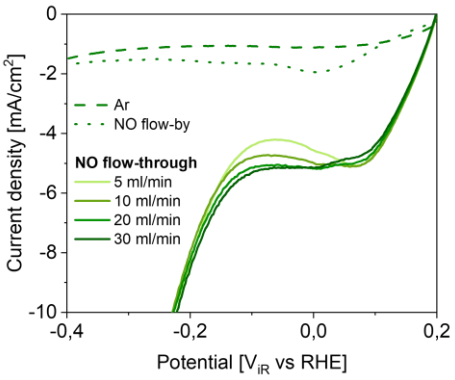

Figure S4.12. LSV of flow-by and flow-through Cu-Ti electrode at different NO flow rates in neutral electrolyte – magnification into first flow-dependent potential regime.

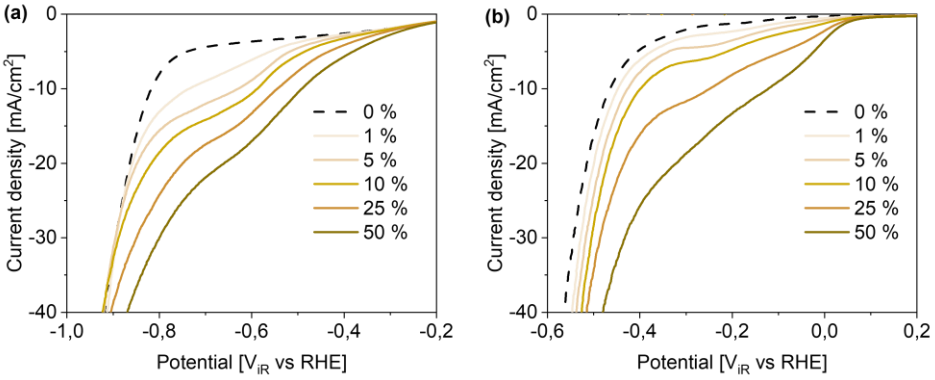

Figure S4.13. LSV of (a) Ti and (b) Ti-Cu hollow fiber in acidic electrolyte with different concentration of NO (flow-through at 20 ml/min).

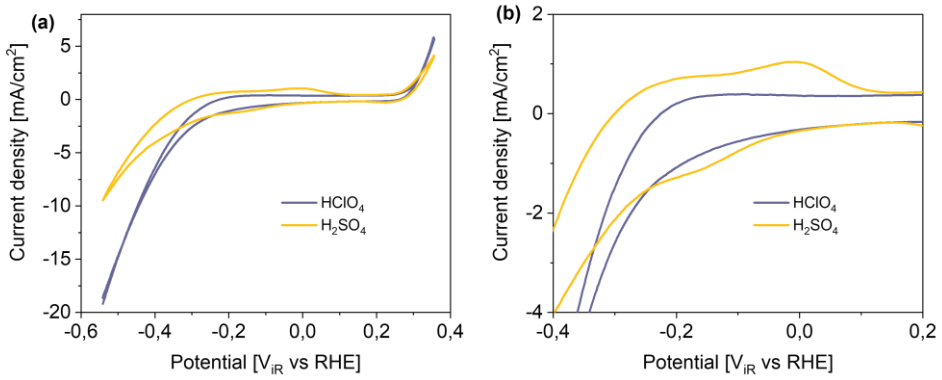

Figure S4.14. CV of Cu-Ti electrode in Ar saturated 0.05 M H_2SO_4 and 0.1 M $HClO_4$ in (a) whole potential range measured and (b) with zoom into SO_4^{2-} adsorption and desorption peaks.

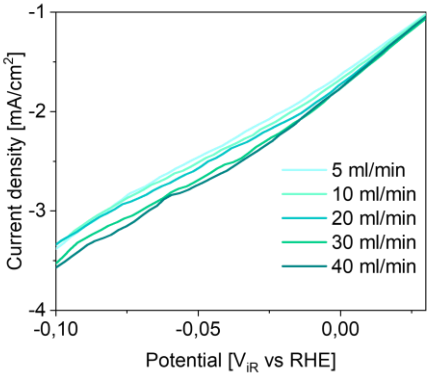

Figure S4.15. LSV of flow-through Cu-Ti electrode at different NO flow rates in acidic electrolyte – magnification into first distinct potential regime.

NO_2^-/NO_3^- reduction is expected in this potential region. The peak at the same position but with higher intensity was observed on Cu disc in EC-MS experiments where NO gas was not purified which confirms peak assignment. This peak is barely affected by changing flow rate in contrast to RDE measurements where mass transport limitations in that region were observed (Figure S4.6). However, no membrane was used in RDE measurements which caused interaction of NO with formed oxygen on counter electrode as well as oxidation of NO to NO_2^-/NO_3^- which results in higher concentration of contaminants what can be affected by rotation rate. Similar behavior was observed on the hollow fiber electrode when NO was not purified (Figure S4.16).

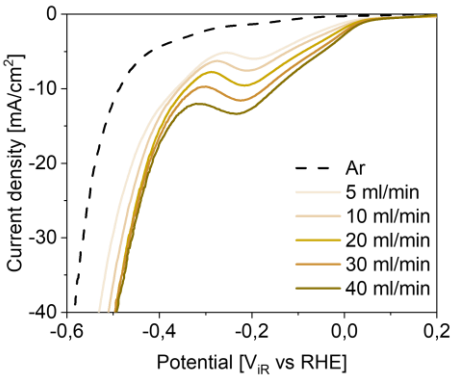

Figure S4.16. LSV of flow-through Cu-Ti electrode at different NO flow rates in acidic electrolyte without NO purification.

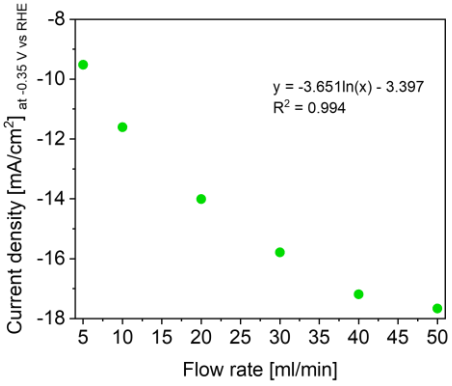

Figure S4.17. Current density on Cu-Ti hollow fiber electrode at -0.35 V vs RHE plotted against flow rate.

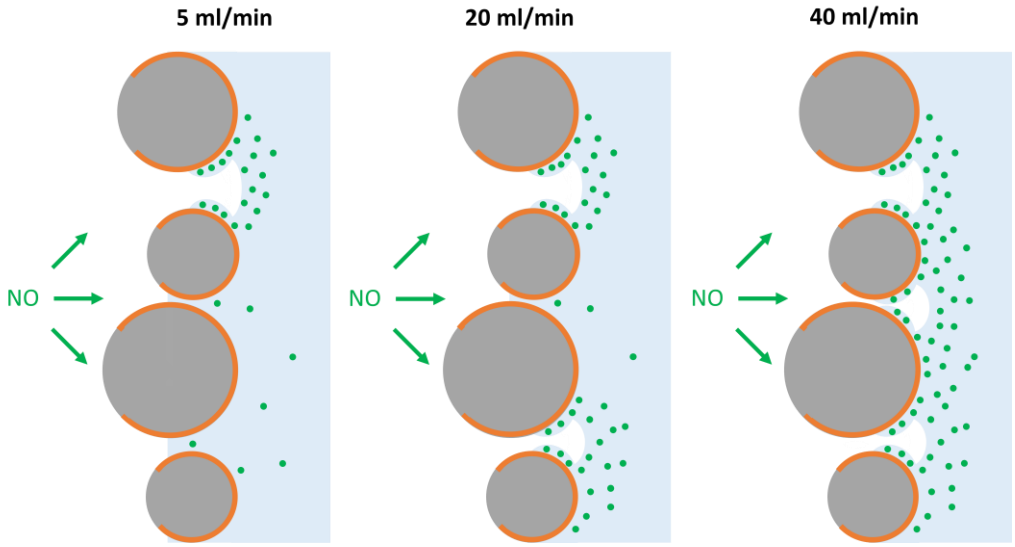

Figure S4.18. Schematic representation of pore opening depending on gas flow rate through Cu-Ti hollow fiber electrode.

At a higher flow rate, more pores will be open thus NO will be supplied to the electrode surface through more channels resulting in more area of electrode with closer contact with NO thus more efficient transport.

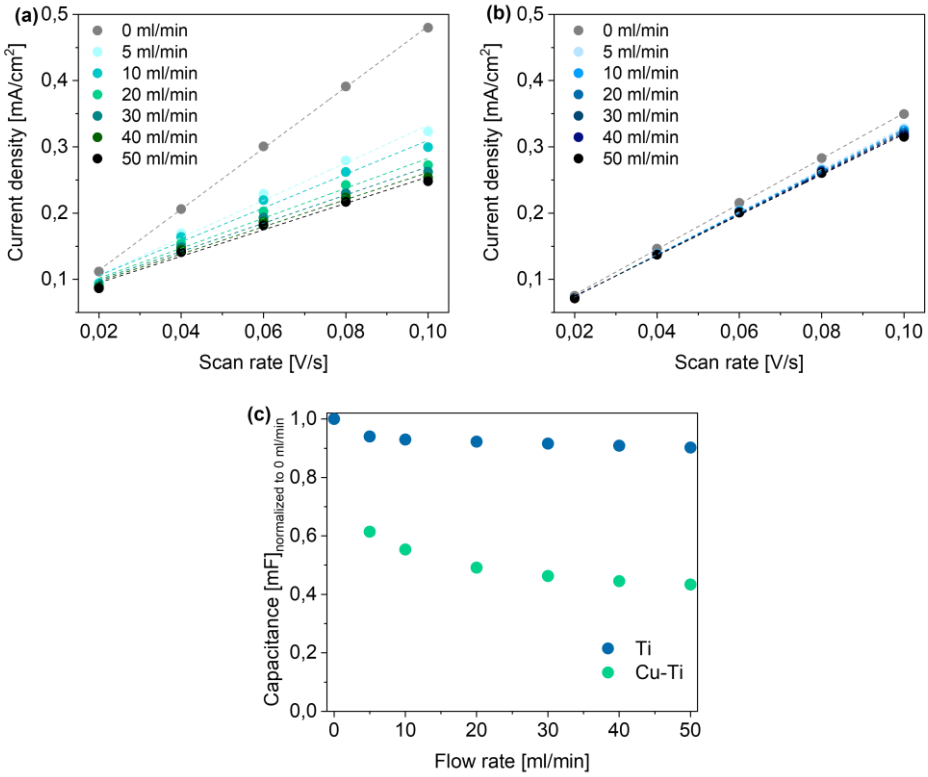

Figure S4.19. Capacitance value change depending on the flow rate on (a) Cu-Ti and (b) Ti hollow fiber electrode. (c) Normalized capacitance to 0 ml/min on both, Cu-Ti and Ti hollow fiber electrode.

At higher flow rates, smaller surface area of the electrode is observed. Higher flow rate results in increased pressure inside the electrode, pushing the liquid boundary slightly towards the outside which causes the opening of smaller pores. At no flow situation, electrolyte goes deeper into fiber wall thus surface area is higher (see also schematic in Figure S4.18). This can support the hypothesis about current density increase with flow rate being more pronounced on Cu-Ti than Ti. The decrease in ESCA on Cu-Ti electrode at higher flow rates is significantly higher compared to Ti electrode confirming the presence of smaller pores in Cu-Ti.

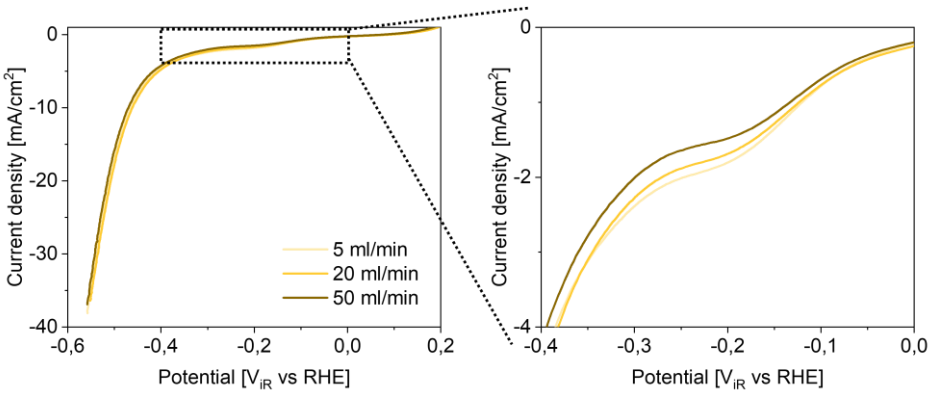

Figure S4.20. LSV of Ar flow-through Cu-Ti hollow fiber in 0.05 M H_2SO_4. The peak of SO_4^{2-} adsorption is decreasing with an increasing flow rate which is in line with decreasing surface area at higher flow rates.

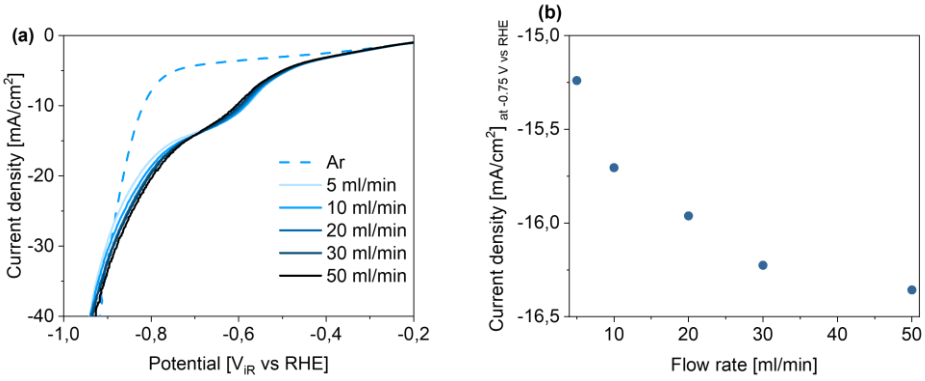

Figure S4.21. (a) LSV of flow-through Ti hollow fiber electrode at different NO flow rates in 0.05 M H_2SO_4 with (b) corresponding current density on Ti hollow fiber electrode at -0.75 V vs RHE plotted against flow rate.

A similar trend of current density increase with changing flow rate was observed on Ti electrode however till significantly lower extend compared to Cu-Ti. This difference could be related to the bigger pore size of Ti fiber compared to Cu-Ti which means that increasing flow rate from 5 to 50 ml/min does not open a lot of new pores. Most of them will be already open at 5 ml thus small influence of flow rate.

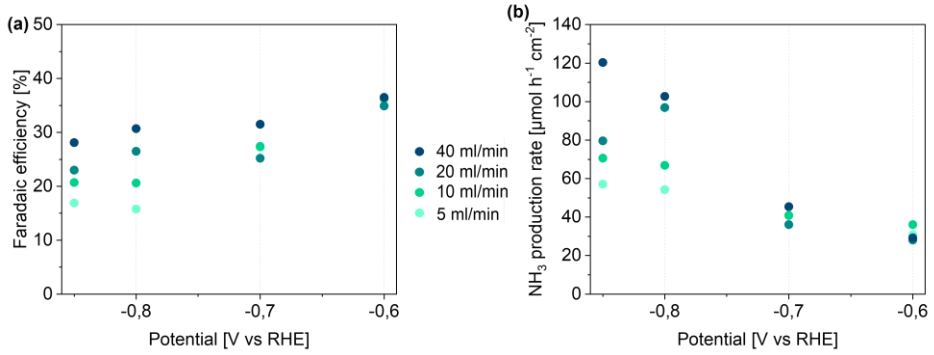

Figure S4.22. (a) Faradaic efficiency and (b) production rate of NO electroreduction to NH_3 in acidic electrolyte on Ti hollow fiber electrode.

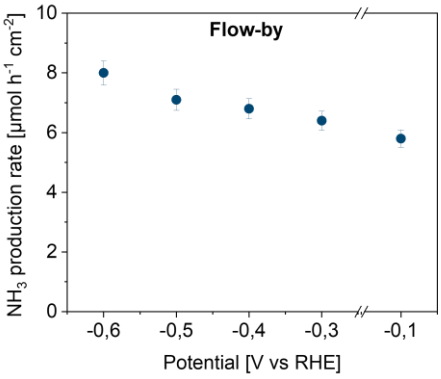

Figure S4.23. NH_3 production rate on Cu-Ti hollow fiber in flow-by configuration in 0.05 M Na_2SO_4 electrolyte. Magnification of Figure 4.4f in the main text.

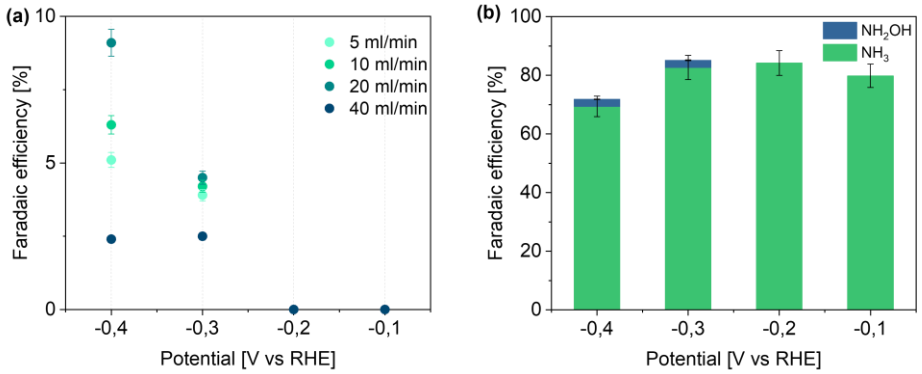

Figure S4.24. (a) Faradaic efficiency of NO electroreduction to NH_2OH in acidic electrolyte. (b) Total faradaic efficiency of products in liquid phase after electrolysis in flow-through mode at 40 ml/min flow rate.

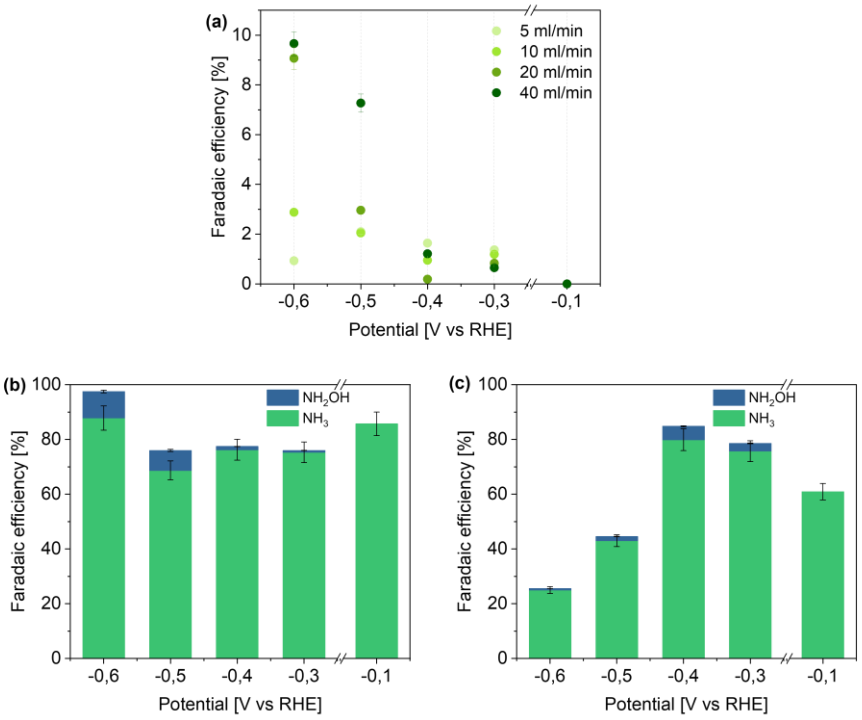

Figure S4.25. (a) Faradaic efficiency of NO electroreduction to NH_2OH in neutral electrolyte. Total faradaic efficiency of products in liquid phase after electrolysis in (b) flow-through mode at 40 ml/min flow rate and (c) flow-by mode.

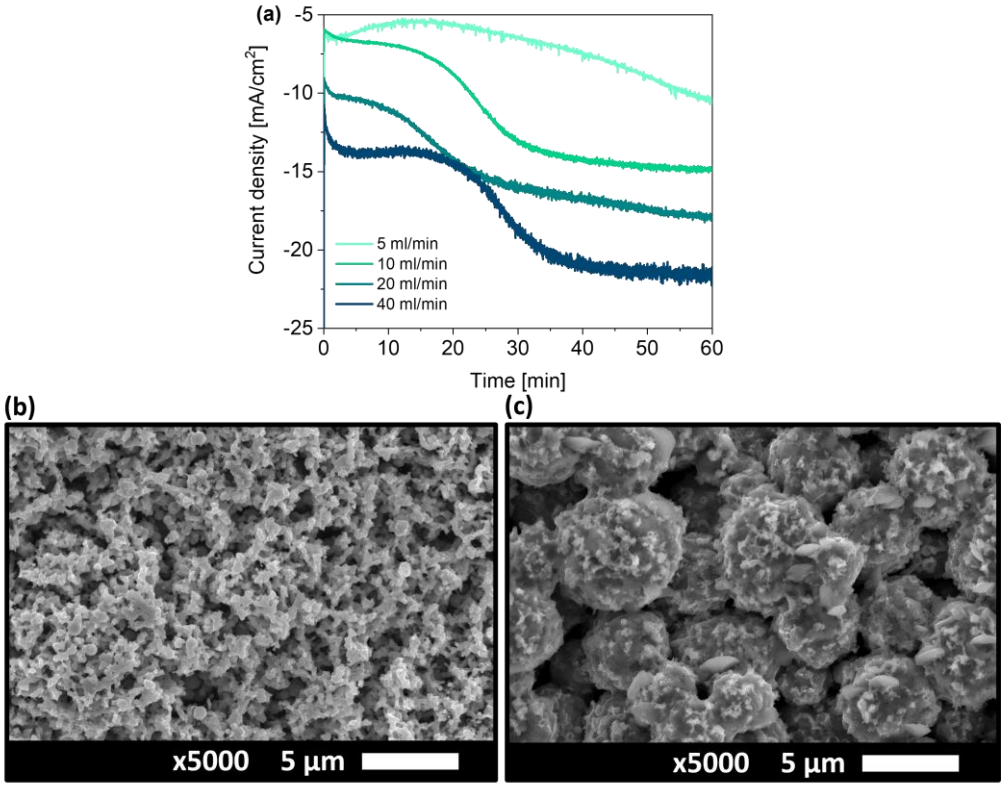

Figure S4.26. Instability of Cu surface during NO electroreduction in acidic electrolyte. (a) Current during chronoamperometry at -0.4 V vs RHE at different gas flow rates, (b) SEM images of Ti-Cu electrode before and (c) after chronoamperometry at -0.4 V.

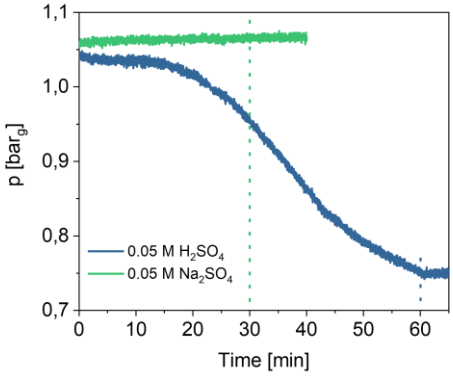

Figure S4.27. Pressure on Cu-Ti hollow fiber electrode during NO electrolysis in acidic and neutral pH electrolyte.

In Figure S4.27, pressure on Cu-Ti hollow fiber with 20 ml/min flow rate during chronoamperometry at -0.5 V vs RHE in neutral electrolyte and -0.4 V vs RHE in acidic electrolyte are shown. In neutral electrolyte pressure is stable over the entire measurement indicating electrode stability while in acidic electrolyte pressure is gradually decreasing. It indicates that pores are becoming larger while reaction is progressing which very likely happens due to corrosion which is in line with current instability and SEM images of electrode after reaction. Surprisingly, pressure stabilizes after electrolysis (after 60 min – OCV) suggesting that corrosion stopped happening which shows that it is only an issue while running the reaction thus products/intermediates must be responsible for the observed behavior. Metal ion-ammonia complex formation might explain the observed changes in electrode morphology. However, ammonia is only present in low quantities (ppm level) and thus severe corrosion as observed here seems less likely. Thus, besides the reported formation of metal ion-ammonia complexes, another possible explanation for the severe changes in electrode morphology might be the formation of NO_2^- and NO_3^- by reaction between NO and locally formed OH^- (due to the increased pH on the electrode surface). The formed NO_2^-/NO_3^- might be considered as dissociated HNO_2 and HNO_3 in acidic electrolyte, likely inducing spontaneous dissolution of metallic copper. Given the negative potential, dissolved Cu can re-deposit on the cathode surface causing surface morphology changes.

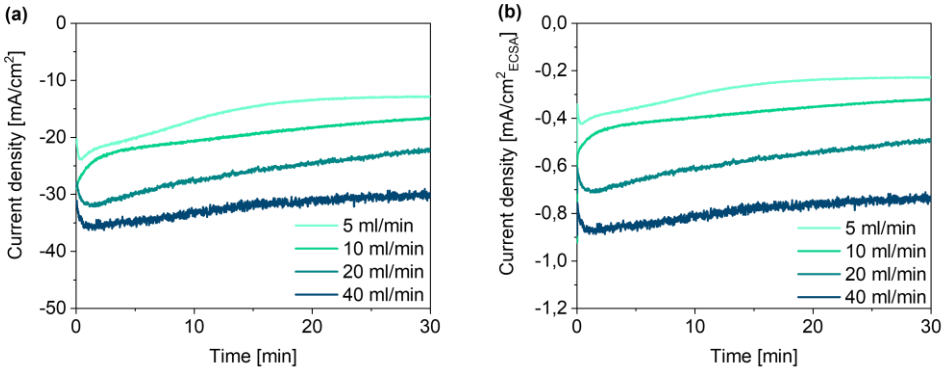

Figure S4.28. Current density during chronoamperometry at -0.5 V vs RHE in neutral electrolyte using Cu-Ti hollow fiber electrode at different gas flow rate calculated based on (a) geometrical surface area and (b) electrochemical active surface area (ECSA).

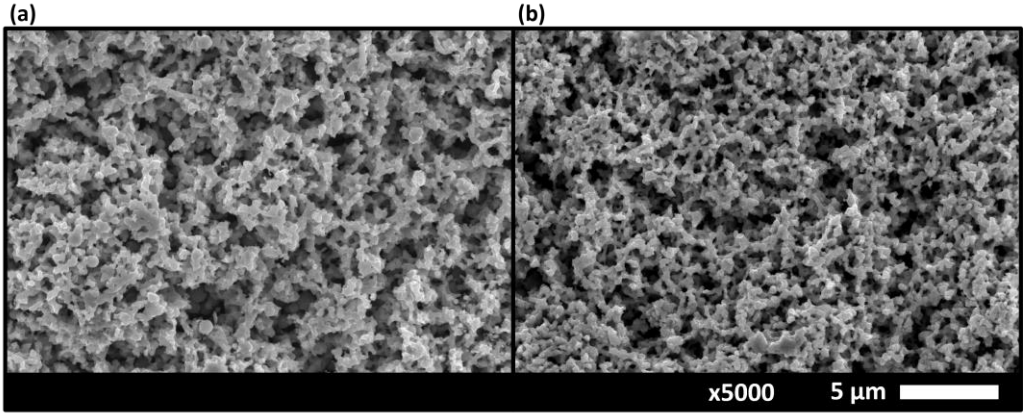

Figure S4.29. SEM images of Ti-Cu electrode (a) before and (b) after chronoamperometry at -0.5 V in neutral electrolyte.

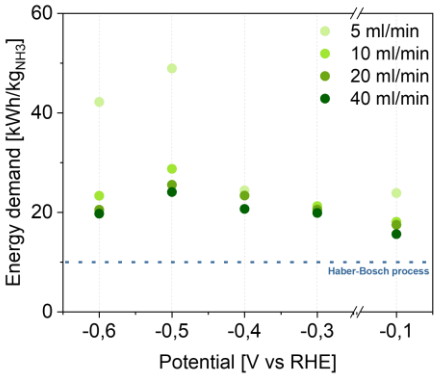

Figure S4.30. Energy demand for ammonia formation depending on potential.

In this calculations, the potential on the counter electrode was assumed to be 1.6 V which should be enough for an oxygen evolution reaction to occur.

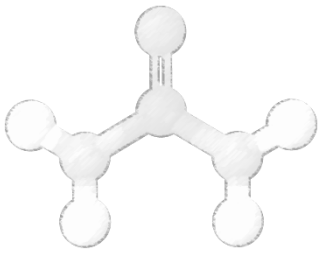

Chapter 5

Carbon-Nitrogen bond formation on Cu electrodes during CO_2 reduction in NO_3^- solution

This chapter is based on:

P. M. Krzywda, A. Paradelo Rodriguez, N. E. Benes, B. T. Mei, G. Mul, "Carbon-Nitrogen bond formation on Cu electrodes during CO_2 reduction in NO_3^- solution", **2022** - submitted to *Applied Catalysis B: Environmental*.

Abstract

Simultaneous electrochemical reduction of NO_3^- and CO_2 over rough Cu electrodes is demonstrated to yield urea in chronoamperometry experiments. Furthermore, we demonstrate by use of Surface-Enhanced Raman Spectroscopy and Electrochemical Mass Spectrometry that simultaneous reduction of NO_3^- and CO_2 on Cu surfaces additionally leads to an alternative C-N coupling reaction, forming cyanide. The assignment of the Raman bands at 2080 and 2150 cm^{-1} to Cu-C≡N–like species on reduced and oxidized Cu surfaces, respectively, was confirmed by reference experiments using KCN solutions. The formation of cyanide species only occurs when simultaneous reduction of NO_3^- and CO_2 is performed, while do not form in electrolytes containing NH_4^+ and CO_2, or NO_3^- and $HCOO^-$. Several Cu-C≡N–like species of variable complexity are soluble, causing restructuring of the Cu surface. The soluble species can redeposit at positive potentials and be oxidized to form NO. The implications of these observations for development of electrodes and processes for electrochemical formation of urea, and the potential practical utilization of the formed cyanide species, are briefly discussed.

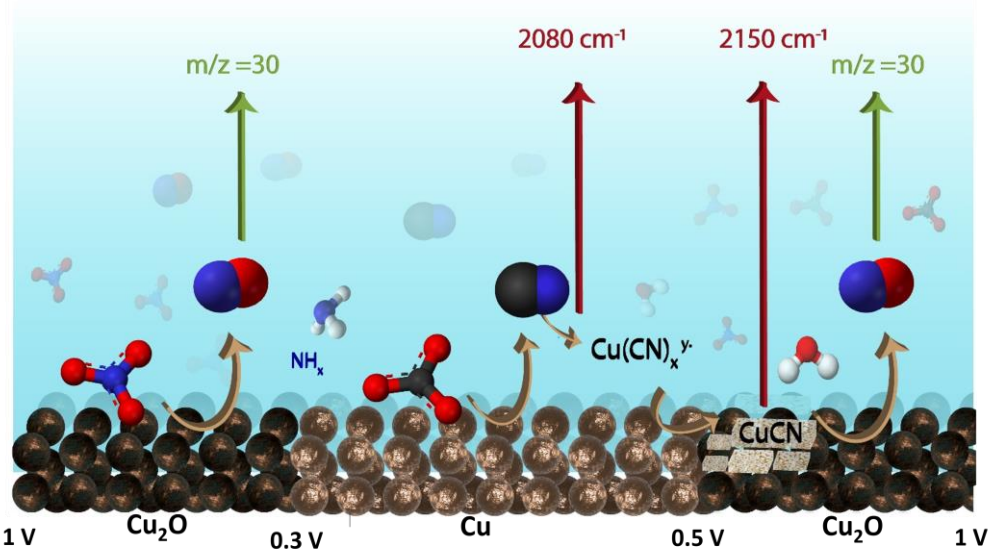

Introduction

Urea is one of the most important nitrogen-based fertilizers playing a very important role in securing the worldwide food supply.[1] The chemical is industrially produced from CO_2 and NH_3 in an energy-intensive process consuming 173 kWh per ton of urea,[2] with an annual production capacity of 155 Mt.[3] Ammonia needed for urea production is mainly produced by the Haber-Bosch process. However, small-scale production by non-conventional renewable technologies for ammonia synthesis, based on electrochemistry, are also of interest.[4,5] While electrochemical N_2 reduction to NH_3 suffers from very low activity,[6] NO_3^- can be considered an alternative feedstock, which requires a lower overpotential and shows more favorable reaction kinetics.[7–9] Green ammonia produced from nitrate could be coupled to urea production in decentralized fertilizer production plants, at locations where waste NO_3^- streams are available.[10]

Rather than the synthesis of urea by electrochemical nitrate reduction and (thermo)catalytic conversion of CO_2 and NH_3 in series, particularly interesting is the simultaneous electrochemical conversion of CO_2 and nitrogen-containing substrates,[11–14] such as NO_3^-,[15–17] NO_2^-,[18–20] or N_2 [21–23]. Since copper is a good catalyst for CO_2 activation[24] as well as for NH_3 formation from NO_x,[25] copper has been mostly investigated for electrochemical synthesis of urea. Only low faradaic efficiencies and urea formation rates were achieved, due to competing reactions of CO_2, and in particular the dominant, more favorable reduction of NO_3^-. Furthermore, the mechanism of urea formation on Cu surfaces is not very well understood. Although it has been suggested that CO- and NH_x-surface intermediates are required for the synthesis of urea, little is known about the C-N coupling mechanism on Cu surfaces, nor about the formation of alternative products during the reaction.

In the present study, we confirm urea formation on rough polycrystalline Cu surfaces and show results of Surface-Enhanced Raman Spectroscopy (SERS) to identify adsorbed species during simultaneous reduction of CO_2 and NO_3^-. SERS is a suitable technique to detect reaction intermediates and it was already successfully used to monitor electrochemical reduction of CO_2 on Cu surfaces.[26,27] Moreover, we demonstrate by Electrochemical Mass Spectrometry (EC-MS) potential dependent formation of gaseous products from the electrode surface. On the basis of experiments presented in this study, and additional electrochemical carbon-nitrogen coupling reaction yielding Cu-C≡N–like species is presented to occur on rough, polycrystalline Cu electrodes, besides the formation of urea.[28] This finding contributes to the further understanding of electrochemical C-N coupling reactions on Cu surfaces,[29–32] and likely explains the vast restructuring of the electrode surface during the synthesis of urea.

Experimental section

Electrode preparation and characterization

For bulk electrolysis measurements, polycrystalline rough Cu coated on Ti hollow fiber electrodes were used. Ti support was prepared according to the previously reported method [33]. Modification of Ti with Cu was performed by spray-coating using Cu particles and appropriate thermal treatment according to our previous work.[34] Moreover, in order to achieve higher roughness of the prepared Cu surface, electrodeposition of Cu was performed on previously spray-coated Cu-Ti electrodes. 0.1 M $CuSO_4$ (pH 2) was used as an electroplating bath, graphite rod, and Ag/AgCl (3 M NaCl, BASi) were used as counter and reference electrode respectively. A potential of -0.4 V vs RHE was applied for 160 s after which the electrode was rinsed with MiliQ water and dried in a flow of Ar. SEM of prepared Cu-Ti electrode is shown in Figure S5.1.

For SERS experiments, polycrystalline rough Cu electrodes were prepared according to the procedure described elsewhere.[27] In brief, Cu discs were mechanically polished followed by anodic treatment in 85% phosphoric acid (3 V for 2.5 min), sonication in MiliQ water, and drying in an Ar stream. A photograph of the prepared electrode is shown in Figure S5.2. For EC-MS experiments a polycrystalline rough Cu disc (⌀ 5 mm) was polished following the routine of cleaning provided by Pine Research.

Electrodes were characterized using X-ray diffraction (XRD, Bruker Phaser D2) and Scanning Electron Microscopy (SEM) (JSM-6010LA, JEOL system).

Electrochemical measurements

H-type cell with Nafion 117 membrane was used in chronoamperometry experiments for urea electrosynthesis. 0.1 M $KHCO_3$ with 50 mM KNO_3, platinized Ti mesh and Ag/AgCl (3 M NaCl, BASi) were used as electrolyte, counter and reference electrode respectively. The electrolyte was purged with 20 ml/min of CO_2 30 min before and during the electrolysis (1 h) to ensure full saturation of the electrolyte.

Raman spectra were recorded using an Avantes AvaRaman spectrometer equipped with an Intertec λ = 785 nm laser. The distance between the Raman probe with a focal length of 10mm and the Cu surface was adjusted to obtain the largest intensity of Raman signals. Electrolyte flow was adjusted to 1.8 ml/min. Ag/AgCl (3 M NaCl, BASi) and platinized Ti mesh were used as reference and counter electrode respectively. The schematic representation of the cell design is shown in Figure S5.3. Each electrode was electrochemically activated *in situ* in 0.1 M $KClO_4$ by 5 oxidation-reduction cycles in the

range between 2 and -1.4 V vs RHE in order to achieve enhanced Raman signals due to an increase in roughness of the electrode (SEM of Cu electrode before and after activation is shown in Figure S5.4). Next, the electrolyte was changed for compositions reflecting the process conditions of urea formation or respective blanks. The electrolyte was continuously purged with CO_2 or Ar. Raman spectra were recorded during cyclic voltammetry (unless indicated otherwise) between +0.9 and -1.1 V vs RHE starting at the oxidative potential with a scan speed of 10 mV/s and spectral integration time of 5 s. The potential interval between spectra in the presented graphs is 0.2 V unless otherwise indicated.

Chronoamperometry measurements were performed in a one-compartment cell, with Ag/AgCl (3 M NaCl, BASi) and platinized Ti mesh used as reference and counter electrode respectively. The electrolyte was continuously purged with CO_2 or Ar. A potential of -0.3 V vs RHE was applied for 30 min, after which the electrode was removed from the electrolyte, rinsed with MiliQ water and dried in a flow of Ar. The electrochemical surface area (ECSA) was measured before and after chronoamperometry by the capacitance method. Cyclic voltammograms in the potential region where no faradaic current is observed were measured at variable scan rates from 20 to 100 mV/s in Ar saturated 0.1 M $KClO_4$.

EC-MS measurements were performed using a SpectroInlets (Copenhagen, Denmark) system, with He or CO_2 as carrier gas at 1 ml/min flow rate. Cu disc was pre-treated by cyclic voltammetry cycles in order to get a stable CV signal. Different m/z signals were recorded during cyclic voltammetry (unless otherwise indicated). Ag/AgCl (sat. KCl, CH Instrument) and Pt mesh were used as reference and counter electrode respectively. The schematic representation of the cell design is shown in Figure S5.3.

All electrochemical measurements were carried out at room temperature using a BioLogic VSP potentiostat. Recorded potentials were recalculated to Reversible Hydrogen Electrode scale according to the following equation:

$$E_{RHE} = E_{Ag/AgCl} + 0.059\,pH + E^0_{Ag/AgCl}$$

Results and discussion

Urea electrosynthesis

In order to verify the possibility of electrochemical urea formation on rough, polycrystalline Cu electrodes, bulk electrolysis experiments were performed in CO_2 saturated 0.1 M $KHCO_3$ with 50 mM KNO_3. The faradaic efficiency and urea production rate at different potentials are shown in Figure S5.6. The faradaic efficiency towards urea is low (~3% at

- 0.4 V vs RHE) likely due to the highly competing NO_3^-, CO_2, and H^+ reduction reactions. Moreover, surface instability was obvious by comparison of SEM images of the as-prepared and used electrodes (Figure S5.7). Despite these observed adversities, urea formation on rough polycrystalline Cu electrodes was verified, and we will now proceed by analyzing surface chemistry and providing an explanation for surface instability.

In situ SERS analysis of the Cu electrode in the presence of CO_2 and NO_3^-

To determine the surface chemical processes at variable potential, SERS spectra of the Cu surface in CO_2 saturated 0.1 M $KHCO_3$ with 50 mM KNO_3 were performed during cyclic voltammetry (Figure 5.1) and are shown separately for reductive and oxidative scans (Figure 5.1b and 5.1c), respectively.

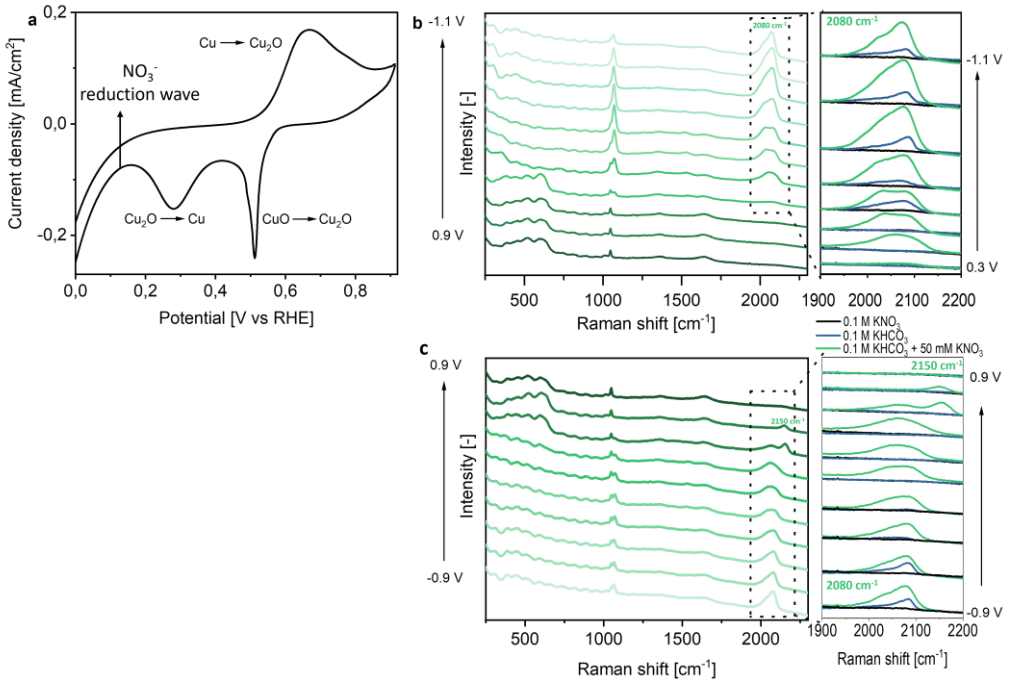

Figure 5.1. CO_2 saturated 0.1 M $KHCO_3$ with 50 mM KNO_3 electrolyte. (a) Cyclic voltammetry of Cu electrode; (b) *In situ* SERS of a Cu surface during a reductive scan and (c) during an oxidative scan, with magnification into the high wavelength region with respective measurements in blank electrolytes. The potential interval between spectra is 0.2 V.

The expected characteristic signals for Cu-oxides were observed. In the reductive scan at 0.5 V reduction of CuO to Cu_2O is observed, followed by reduction of Cu_2O to metallic Cu (Figure 5.1a) after which catalytic wave for NO_3^- electroreduction is observed. Those surface chemical changes are in agreement with characteristic peaks at 610 and 520 cm^{-1} in the SER spectra, which have been assigned to Cu_2O[35] (Figure 5.1b). At more negative potentials those Raman signals disappear, only to re-appear again in the oxidative scan at 0.5 V (Figure 5.1c), in agreement with the oxidative current in Figure 5.1a assigned to oxidation of Cu to Cu_2O. Importantly these spectral observations confirm that the Raman intensities primarily originate from the electrode surface. Raman peaks at ~1050 and 1070 cm^{-1} in Figures 5.1b and 5.1c can be assigned to nitrate in solution, and surface adsorbed carbonate, respectively, based on reference spectra recorded in KNO_3 and $KHCO_3$ solutions (see Figures S5.9, S5.10 and S5.11).

In the reductive sweep (Figure 5.1b) up to 0.3 V, little changes are observed in the Raman spectra. When reduction of Cu-oxides is completed, a signal at ~2080 cm^{-1} appears and grows in intensity at more negative potential. Although the band position is similar to that assigned to Cu-adsorbed C≡O (~2070 cm^{-1}), the potential at which the band is observed (0.3 V vs RHE), is quite different from previous observations in the absence of nitrate [27,36] (see Figure S5.9 and the comparative analysis in the magnification of the high wavenumber region in Figure 5.1b). Moreover, the standard reduction potential of CO_2 to CO is -0.106 V vs RHE [37] and residual CO from previous scans can be excluded since the spectra of a first scan are shown. At more negative potentials (-0.7 V vs RHE), the signal at 360 cm^{-1} from Cu-CO should appear in case CO is actually formed (See Figures S5.9 and S5.11). However, such signal is not observed at any condition in the presence of NO_3^-, suggesting CO is not formed, and/or kinetically more rapidly converted in the presence of NO_3^-. The presence of nitrate also affects the dynamics of adsorbed CO_3^{2-}, visible at ~1070 cm^{-1}. It appears more stable in the presence, than in the absence of nitrate (compare the measurement in the absence of nitrate in Figure S5.11). This could also be related to an explanation in the literature for the effect of the presence of small amounts of NO_x in CO_2, which can significantly reduce the selectivity of CO_2RR because of the more positive onset potential for reduction of NO_x compared to CO_2.[37,38]

During the oxidative scan (Figure 5.1c), the 2080 cm^{-1} peak does not disappear at -0.4 V vs RHE like in the case of CO formed by CO_2 reduction[27] (see also Figure S5.4). This is additional proof that the observed Raman band originates from a product formed only in the presence of NO_3^- and CO_3^{2-}. Finally, when Cu_2O is formed (0.5 V vs RHE), the ~2080 cm^{-1} peak disappears while a new band at 2150 cm^{-1} appears. The variation of the ~2080 cm^{-1} and ~2150 cm^{-1} peak area as a function of potential is shown in Figure S5.12.

Both Raman bands, at ~2080 cm^{-1} and ~2150 cm^{-1}, clearly show a Stark effect (see Figure S5.13), proving that surface-adsorbed species are formed. Besides CO, carbon-nitrogen triple bonds show significant intensity at these wavenumbers, out of which cyanide is the most simple compound.[39,40] Although it was also reported that Cu-H (adsorbed hydrogen) can appear at the same position in SEIRAS,[41] in a control experiment in Ar saturated 0.1 M $KClO_4$ no signal was observed (Figure S5.14). A summary of the observed Raman bands can be found in Table 5.1.

Table 5.1. Summary of SERS signals observed in this work. *Signals related to cyanide observed in this work.

Position [cm^{-1}]	Assignment	Ref.
275 360	Cu-CO	[27,42]
350 1540	CO_3^{2-} $(C\text{-}O)_{asym}$	[27]
520 610	Cu_2O	[35]
1048	NO_3^-	[43,44]
1072	CO_3^{2-} $(C\text{-}O)_{sym}$	[27,36]
1360	bicarbonate	[27]
1640	H_2O	[27]
2070	C≡O	[27,36]
~2080*	$Cu(C{\equiv}N)_n^{(n-1)}$	[45,46]
~2150*	CuC≡N	[45]
300*	Cu-CN	[47]

In order to prove that the formation of CN is electrochemically driven, SERS of a Cu surface in CO_2 saturated 0.1 M $KHCO_3$ with 50 mM KNO_3 was recorded at OCV (Figure 5.2a). No signals in the 2000-2500 cm^{-1} region were observed after prolonged periods of time. At -0.3 V vs RHE, a broad peak at ~2080 cm^{-1} appears and remains visible throughout the measurement. Subsequently, at OCV when Cu_2O signals appear due to surface oxidation of metallic Cu, the band at ~2150 cm^{-1} appears and subsequently slightly decreases in intensity over time, while shifting position from 2154 cm^{-1} to 2149 cm^{-1}. This suggests that the product formed under reductive potential changes frequency when oxidation of Cu occurs to form a Cu_2O containing surface. Moreover, in order to exclude any homogeneous reactions induced by Cu ions possibly present in the solution, cyclic voltammetry in blank electrolytes were performed, and SERS at OCV was measured afterwards, while adding $KHCO_3$ or KNO_3 (Figure 5.2b). The signal at ~2150 cm^{-1} was not observed in any such experiment, proving that the reaction is exclusively driven electrochemically.

The influence of anodic processes on the observed Raman signals was excluded by performing experiments in the presence of a Nafion membrane separating the anodic and cathodic compartment of the electrochemical cell (see Figure S5.15). The same Raman spectra were observed (also during cyclic voltammetry), and therefore anodic processes likely do not interfere with the observed phenomena.

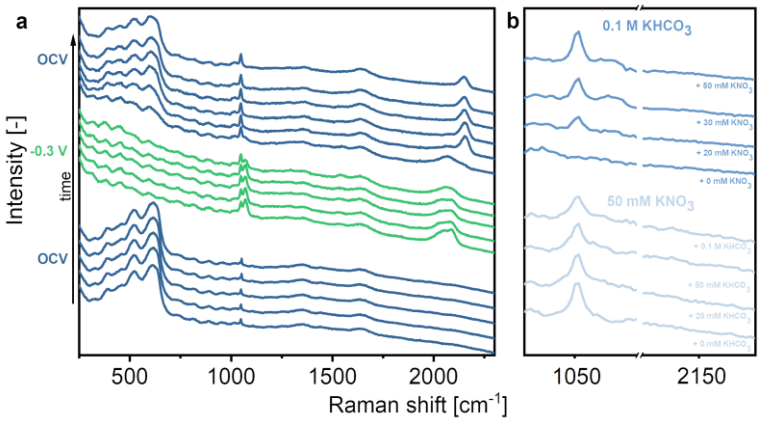

Figure 5.2. In situ SERS of a Cu surface at open circuit voltage. (a) CO_2 saturated 0.1 M $KHCO_3$ with 50 mM KNO_3 electrolyte recorded at OCV, at -0.3 V vs RHE and again at OCV (the time interval between spectra is 1 min). (b) SERS spectra recorded at OCV after cyclic voltammetry in CO_2 saturated 0.1 M $KHCO_3$ (dark blue) or Ar/CO_2 saturated 50 mM KNO_3 (light blue) with addition of different amounts of $KHCO_3$ or KNO_3 at OCV.

Is Cyanide a decomposition product of urea?

While Cu-C≡N like species are clearly formed in similar conditions (potential, electrolyte composition) to urea, Raman spectroscopy does not provide indications of urea formation, likely due to the limited time applied in the cyclic voltammetry experiment. To verify if cyanide is a product of decomposition of urea, potential dependent SERS analysis of 50 mM urea in CO_2 saturated 0.1 M $KHCO_3$ is shown in Figure S5.16. Urea in aqueous solution can undergo multiple reactions.[48,49] Most importantly it can hydrolyze to cyanate and ammonium, which is a reversible reaction.[50] In neutral solution, cyanate may decompose further to produce ammonium ions and carbonate.[51,52] Potential dependent SERS analysis shows several Raman peaks of urea appearing at 0 V vs RHE, of which the potential dependent wavenumber of a peak in the range of 703 to 713 cm^{-1} is most indicative of urea adsorption, although the vibrational assignment of this peak remains elusive. In cyclic voltammetry, the spectra are additionally dominated by the conversion of CO_2 to CO (compare Figures S5.16 and S5.9), while the formation of Cu-C≡N – like

species is not observed. Cu-C≡N – like species therefore do not appear to be a consecutive product of urea decomposition.

Is Cyanide an intermediate toward other products?

In order to further confirm the presence of cyanide, SERS of the Cu surface in CO_2 saturated $KHCO_3$ in the presence of KCN was measured, and the results are shown in Figure 5.3.

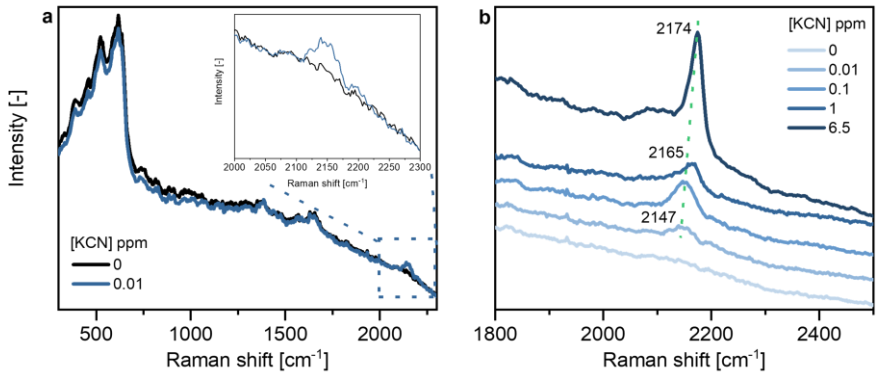

Figure 5.3. In situ SERS of a Cu surface in CO_2 saturated 0.1 M $KHCO_3$ at OCV with addition of KCN. (a) With 0 and 0.01 ppm of KCN; (b) with increasing concentration of KCN.

In the presence of only 10 ppb of KCN, a signal at 2147 cm^{-1} appears (Figure 5.3a) which matches the peak observed during in-situ SERS analysis. It was proven that SERS can be successfully used for the detection of trace amounts of cyanides as demonstrated for Au in the gas phase[47] as well as in solution for Ag[53] and Cu, where Cu(I) surfaces can be very effective in detection due to the formation of CuCN[54]. The position of the peak is similar to the C≡N stretching frequency of solid CuCN[45] and is concentration dependent (Figure 5.3b). In excess of CN^- in aqueous solution, CuCN can form several soluble complexes, generalized as $Cu(CN)_n^{(n-1)}$ (n = 2, 3, 4), which structure depends on the CN^-/Cu ratio.[55] At higher CN^- concentration, Raman signals of Cu_2O decrease in intensity (Figure S5.17) which proves a chemical reaction of CN^- with (surface) copper oxide is likely, forming higher CuCN-complexes.[56]

In order to verify the behavior of the Cu-C≡N Raman bands during a potential sweep, cyclic voltammetry in 0.1 M $KHCO_3$ with addition of 0.1 ppm of KCN was performed (Figure 5.4). The obtained results, i.e. the observation of strong signals at ~2080 cm^{-1}, are in excellent agreement with the experimental results obtained in CO_2 and NO_3^- containing

electrolyte. Note that NO_3^- was not added in this measurement. Thus, the observed Cu-CN complexes originate from the dissolved KCN added to the solution. $Cu(CN)_n^{(n-1)}$ can result in different Raman signals, depending on the type of complex, which is determined by the concentration of CN^- as well as the pH of the solution.[45,46] It is common knowledge in the field that the pH near the electrode surface is changing during electrochemical reactions. A low pH might favor the decomposition of cyanide complexes to HCN,[46] while a higher pH will stabilize cyanide complexes. That the pH near the surface of our electrode is rather basic, is thus confirmed by the observation of $Cu(CN)_n^{(n-1)}$ complexes.

When higher KCN concentrations were used (Figure S5.18), Cu_2O bands were hardly visible during a CV, which again confirms the chemical attack of CN^- towards Cu(I)-oxide, forming $Cu(CN)_n^{(n-1)}$ complexes. This likely explains the broad peak observed even at positive potentials, and the very small signal at 2170 cm^{-1} attributed to solid Cu-C≡N.

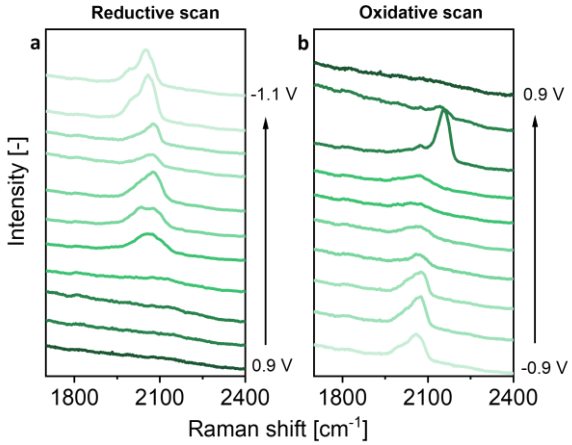

Figure 5.4. In situ SERS of a Cu surface in CO_2 saturated 0.1 M $KHCO_3$ with 0.1 ppm KCN. Recorded during (a) reductive scan and (b) oxidative scan of cyclic voltammetry.

Moreover, in order to prove the formation of cyanide, isotopic labeling experiments with $KH^{13}CO_3$ and $K^{15}NO_3$ were performed (Figure S5.19). The results show peak shifts with both, ^{13}C and ^{15}N, proving the involvement of carbon and nitrogen in the species responsible for the observed vibrations at ~2080 and ~2150 cm^{-1}. More importantly, these experiments did not reveal the formation of other surface intermediates or products, other than the previously discussed $Cu(CN)_n^{(n-1)}$ complexes.

Furthermore, the electrode surface was analyzed after chronoamperometry at -0.3 V vs RHE. The electrochemical surface area was significantly increased indicating surface roughening, and the XRD pattern shows a specific increase of the Cu (220) facet (Figure

S5.20). Moreover, the SEM images clearly show changes (Figure S5.21), which appear very similar to the ones observed after bulk electrolysis (See Figure S5.2). Results indicate surface reorganization and thus surface instability during electrolysis in the presence of CO_2 and NO_3^-, which we correlate to cyanide formation and subsequent interaction with the Cu surfaces on both types of electrodes tested (by chronoamperometry and Raman analysis, respectively).

Can cyanide be formed in other electrolytes?

In order to reveal what species are responsible for reaction towards cyanide, cyclic voltammetry with i) formate ($HCOO^-$) instead of bicarbonate, and ii) ammonium salt instead of nitrate were performed (Figures S5.22 and S5.23). Since at 0.3 V no CO_2 reduction products are expected (see standard reduction potentials of CO_2 in Table S5.1), formate was chosen as one of the most simple products from CO_2 reduction in a $2e^-$ transfer reaction.[57] On the other hand, NH_4^+ was chosen as N-source, since this is the most likely product of NO_3^- reduction on Cu surfaces.[58] In both cases, no signals related to cyanide were observed.

Since cyanide formation requires the removal of oxygen from NO_3^-, it is very likely that NH_x intermediates on the electrode surface are involved in the reaction (it was reported that stable NH_x adsorbed on the cathode surface can exist[59]). Therefore, we conclude that adsorbed NH_x on Cu surfaces reacts with adsorbed CO_3^{2-} (possibly through CO), forming Cu-C≡N – like species and water, as shown in the schematic overview in Figure 5.6. These intermediates are very similar to those proposed for the formation of urea, and therefore cyanide and urea formation are likely to form in parallel through common intermediates.

In situ EC-MS analysis

To complement the results obtained by SERS, electrochemical mass spectrometry was used, which allows to track gaseous products desorbed from the electrode surface with high sensitivity.[60] Mass spectra of selected signals recorded during CV scans on rough, polycrystalline Cu discs are shown in Figures S5.24, S5.25, and S5.26. Comparison of the m/z: 30 signal in different electrolytes is shown in Figure 5.5a (no other differences were observed). Since no products with carbon-nitrogen triple bond with m/z: 30 are expected, the signal is assigned to nitric oxide, which was confirmed by isotopically labeling experiments. The intensity development of the m/z: 31 signal is clearly visible when $K^{15}NO_3$ is used (Figure S5.27).

In CO_2 saturated $KHCO_3$ with 50 mM KNO_3 as well as in Ar saturated 0.1 M KNO_3, NO is observed in the reductive scan as a product of NO_3^- electroreduction (obviously NO was not found in CO_2 saturated $KHCO_3$). The difference in onset potential for NO formation can be explained by different concentrations of NO_3^- as well as pH changes near the surface of the electrode. Although the starting pH is the same (6.8), in the case of CO_2 saturated $KHCO_3$, the buffering capacity of the electrolyte likely prevents large pH changes as compared to electrolytes containing KNO_3 only. It could also very well be that residual C≡N species and adsorbed carbonate inhibit the reduction of NO_3^- somewhat (the second potential sweep is shown), further explaining the different trends in NO production as a function of potential. In the oxidative scan (blue line), NO is not formed in the case of 0.1 KNO_3. This suggests that surface oxides of Cu are required to induce the formation of NO from nitrate. More importantly, NO is observed in an oxidative scan if CO_2 and NO_3^- are present in the electrolyte. It starts to appear at ~0.4 V, which matches the potential of the occurrence of the peak at 2150 cm^{-1} in the in-situ SERS experiments. In addition, nitric oxide formation was monitored during chronoamperometry at -0.3 V vs RHE, and could not be detected as shown in Figure 5.5b. However, when approaching OCV conditions, the NO signal appears and slowly decreases over time, again in agreement with the SERS spectra recorded at OCV (see Figure 5.2; a blank measurement with 0.1 M KNO_3 can be found in Figure S5.28).

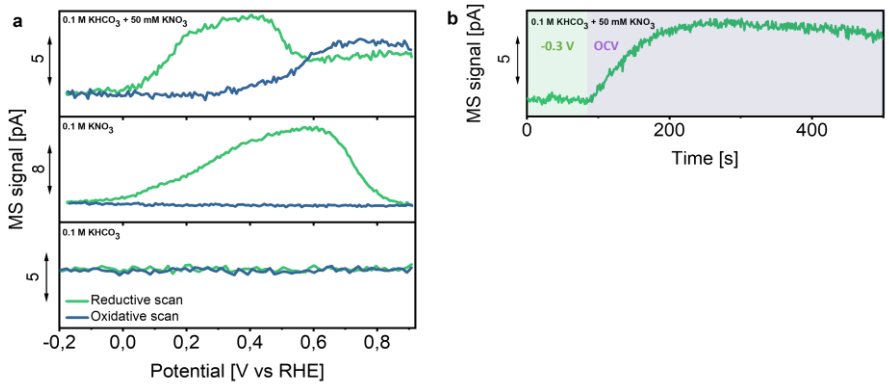

Figure 5.5. MS analysis of nitric oxide (m/z: 30) desorbed from the Cu surface. (a) During cyclic voltammetry (second cycle) in different electrolytes (the green line represents the reductive scan, and the blue line the oxidative scan). (b) During chronoamperometry at -0.3 V vs RHE (green domain) and subsequent OCV (violet domain) in CO_2 saturated 0.1 M $KHCO_3$ + 50 mM KNO_3.

The formation of NO during an oxidative scan suggests oxidation of a (surface adsorbed) product, formed in the reductive scan, which based on SERS data is a Cu-C≡N – like species. Formed cyanide in the solution can be decomposed by direct electrooxidation.[61] Cu is effective in this reaction by forming complexes that can oxidize at less positive potentials than free cyanide.[62] In fact, it has been previously shown that those complexes can be oxidized at potentials slightly more positive than 0 V vs RHE.[62] Moreover, oxidation to NO_3^- was found to be catalyzed by copper oxide[63] which very likely involves NO as an intermediate which can desorb from the electrode surface. In our system, NO starts to appear at 0.4 V where oxidation of cyanide complexes is possible on Cu electrodes and the peak of this signal is observed at potentials where copper is oxidized, both in good agreement with the literature.

The overall mechanism of cyanide formation and consecutive chemistry deduced from SERS and EC-MS experiments is schematically shown in Figure 5.6, representing one cyclic voltammetry cycle.

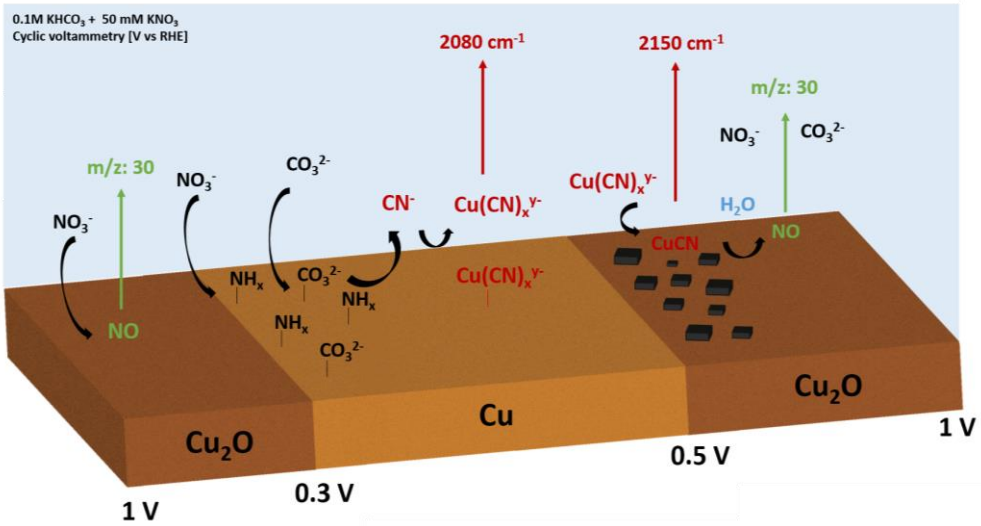

Figure 5.6. Scheme summarizing observed phenomena during CO_2 electroreduction in the presence of NO_3^- evaluated by SERS and EC-MS. One cyclic voltammetry cycle is illustrated.

A perspective

On the basis of experiments presented in this study, an additional carbon-nitrogen electrochemical coupling reaction is presented to occur on rough, polycrystalline Cu electrodes, besides the formation of urea. We have confirmed that cyanide is not a consecutive product of urea decomposition, nor is formed in formate-nitrate, or carbonate-

ammonia solutions. We speculate that cyanide formation competes with urea electrosynthesis, and is formed from similar intermediates.

The data presented here, do not allow identification of a specific active Cu site, but only demonstrate that the oxidation state of Cu influences the C≡N vibration frequency in the spectrum, and oxidation to form NO from C≡N likely takes place once the surface is oxidized. Studies with single Cu crystals would help to identify the nature of the active sites of Cu electrodes for both, C≡N and urea formation, although preventing surface reorganization will be a challenge. Distribution of all possible reaction products across the potential range could give an estimation of competitive reactions, and could reveal the formation of other carbon-nitrogen products.

We demonstrate that the development of a functional system for urea electrosynthesis (as reported in literature) should consider cyanide formation and subsequent electrode dissolution and instability. Additionally, we speculate that the in-situ formation of cyanide might introduce the possibility of electrochemical synthesis of industrially relevant chemicals from waste CO_2 and NO_3^-. For example, hydrogen cyanide, nitriles, or it might be utilized to generate cyano groups commonly used in organic synthesis.

Conclusions

Concluding, simultaneous electroreduction of CO_2 and NO_3^- on Cu electrodes was investigated using Surface-Enhanced Raman Spectroscopy and Mass Spectrometry. Although urea was detected in bulk electrolysis experiments on rough, polycrystalline Cu surfaces, spectroscopic evidence for the formation of urea was not found. However, cyanide could be detected, which we propose is formed in a parallel pathway to the production of urea. Partially reduced NO_3^- (NH_x) likely reacts with adsorbed CO_3^{2-} on the Cu surface forming C≡N, which then converts to cyanide complexes with copper. At positive potentials, likely solid CuCN is observed, and at the same time oxidation of cyanide complexes was detected to produce NO. These results show the complexity of carbon-nitrogen bond formation on Cu surfaces. Cu instability due to chemical attack of CN^- as well as the formation of toxic cyanides, should be considered as potential difficulties in interpretation of bulk electrolysis experiments using Cu.

References

[1] J. H. Meessen, *Ullman's Encycl. Ind. Chem.* **2012**, 657–695.

[2] L. Fiamelda, Suprihatin, Purwoko, *IOP Conf. Ser. Earth Environ. Sci.* **2020**, *472*, DOI 10.1088/1755-1315/472/1/012034.

[3] M. Aresta, A. Dibenedetto, A. Angelini, *Chem. Rev.* **2014**, *114*, 1709–1742.

[4] K. H. R. Rouwenhorst, P. M. Krzywda, N. E. Benes, G. Mul, L. Lefferts, *Ullmann's Encycl. Ind. Chem.* **2020**, 1–20.

[5] K. H. R. Rouwenhorst, P. M. Krzywda, N. E. Benes, G. Mul, L. Lefferts, in *Techno-Economic Challenges Green Ammon. as an Energy Vector*, **2020**, pp. 41–83.

[6] S. Z. Andersen, V. Čolić, S. Yang, J. A. Schwalbe, A. C. Nielander, J. M. McEnaney, K. Enemark-Rasmussen, J. G. Baker, A. R. Singh, B. A. Rohr, M. J. Statt, S. J. Blair, S. Mezzavilla, J. Kibsgaard, P. C. K. Vesborg, M. Cargnello, S. F. Bent, T. F. Jaramillo, I. E. L. Stephens, J. K. Nørskov, I. Chorkendorff, *Nature* **2019**, *570*, 504–508.

[7] D. Hao, Z. gang Chen, M. Figiela, I. Stepniak, W. Wei, B. J. Ni, *J. Mater. Sci. Technol.* **2021**, *77*, 163–168.

[8] I. Katsounaros, *Curr. Opin. Electrochem.* **2021**, *28*, 100721.

[9] J. M. McEnaney, S. J. Blair, A. C. Nielander, J. A. Schwalbe, D. M. Koshy, M. Cargnello, T. F. Jaramillo, *ACS Sustain. Chem. Eng.* **2020**, *8*, 2672–2681.

[10] L. F. Greenlee, *Nat. Energy* **2020**, *5*, 557–558.

[11] M. Shibata, K. Yoshida, N. Furuya, *J. Electroanal. Chem.* **1995**, *387*, 143–145.

[12] M. Shibata, K. Yoshida, N. Furuya, *J. Electroanal. Chem.* **1998**, *442*, 67–72.

[13] M. Shibata, K. Yoshida, N. Furuya, *J. Electrochem. Soc.* **1998**, *145*, 595.

[14] M. Shibata, K. Yoshida, N. Furuya, *Denki Kagaku* **1998**, *6*, 584.

[15] D. Saravanakumar, J. Song, S. Lee, N. H. Hur, W. Shin, *ChemSusChem* **2017**, *10*, 3999–4003.

[16] P. Siva, P. Prabu, M. Selvam, S. Karthik, V. Rajendran, *Ionics (Kiel).* **2017**, *23*, 1871–1878.

[17] C. Lv, L. Zhong, H. Liu, Z. Fang, C. Yan, M. Chen, Y. Kong, C. Lee, D. Liu, S. Li, J. Liu, L. Song, G. Chen, Q. Yan, G. Yu, *Nat. Sustain.* **2021**, DOI 10.1038/s41893-021-00741-3.

[18] N. Meng, Y. Huang, N. Meng, Y. Huang, Y. Liu, Y. Yu, B. Zhang, *Cell Reports Phys. Sci.* **2021**, *2*, 100378.

[19] Y. Feng, H. Yang, Y. Zhang, X. Huang, L. Li, T. Cheng, Q. Shao, *Nano Lett.* **2020**, *20*, 8282–8289.

[20] N. Cao, Y. Quan, A. Guan, C. Yang, Y. Ji, L. Zhang, G. Zheng, *J. Colloid Interface Sci.* **2020**, *577*, 109–114.

[21] C. Chen, X. Zhu, X. Wen, Y. Zhou, L. Zhou, H. Li, L. Tao, Q. Li, S. Du, T. Liu, D. Yan, C. Xie, Y. Zou, Y. Wang, R. Chen, J. Huo, Y. Li, J. Cheng, H. Su, X. Zhao, W. Cheng, Q. Liu, H. Lin, J. Luo, J. Chen, M. Dong, K. Cheng, C. Li, S. Wang, *Nat. Chem.* **2020**, *12*, DOI 10.1038/s41557-020-0481-9.

[22] Menglei Yuan, J. Chen, Y. Bai, Z. Liu, J. Zhang, T. Zhao, Q. Wang, S. Li, H. He, G. Zhang, *Angew. Chemie - Int. Ed.* **2021**, *60*, 10910–10918.

[23] M. Yuan, J. Chen, Y. Bai, Z. Liu, J. Zhang, T. Zhao, Q. Shi, S. Li, X. Wang, G. Zhang, *Chem. Sci.* **2021**, *12*, 6048–6058.

[24] A. H. Shah, Y. Wang, A. R. Woldu, L. Lin, M. Iqbal, D. Cahen, T. He, *J. Phys. Chem. C* **2018**, *122*, 18528–18536.

[25] V. Rosca, M. Duca, M. T. DeGroot, M. T. M. Koper, *Chem. Rev.* **2009**, *109*, 2209–2244.

[26] A. V. Markin, N. E. Markina, J. Popp, D. Cialla-May, *rends Anal. Chem.* **2018**, *108*, 247–259.

[27] M. Moradzaman, G. Mul, *ChemElectroChem* **2021**, *8*, 1478–1485.

[28] C. Tang, Y. Zheng, M. Jaroniec, S. Z. Qiao, *Angew. Chemie - Int. Ed.* **2021**, 2–21.

[29] Y. Wu, Z. Jiang, Z. Lin, Y. Liang, H. Wang, *Nat. Sustain.* **2021**, DOI 10.1038/s41893-021-00705-7.

[30] M. Jouny, J. J. Lv, T. Cheng, B. H. Ko, J. J. Zhu, W. A. Goddard, F. Jiao, *Nat. Chem.* **2019**, *11*, 846–851.

[31] Z. Tao, Y. Wu, Z. Wu, B. Shang, C. Rooney, H. Wang, *J. Energy Chem.* **2022**, *65*, 367–370.

[32] J. E. Kim, J. H. Jang, K. M. Lee, M. Balamurugan, Y. I. Jo, M. Y. Lee, S. Choi, S. W. Im, K. T. Nam, *Angew. Chemie Int. Ed.* **2021**, DOI 10.1002/anie.202108352.

[33] R. P. H. Jong, P. M. Krzywda, N. E. Benes, G. Mul, *RSC Adv.* **2020**, *10*, 31901–31908.

[34] P. M. Krzywda, A. Paradelo, B. T. Mei, N. E. Benes, G. Mul, *ChemElectroChem* **2021**.

[35] H. Y. H. Chan, C. G. Takoudis, M. J. Weaver, *J. Phys. Chem. B* **1999**, *103*, 357–365.

[36] I. V. Chernyshova, P. Somasundaran, S. Ponnurangam, *Proc. Natl. Acad. Sci. U. S. A.* **2018**, *115*, E9261–E9270.

[37] B. H. Ko, B. Hasa, H. Shin, E. Jeng, S. Overa, W. Chen, F. Jiao, *Nat. Commun.* **2020**, *11*, 1–9.

[38] B. U. Choi, Y. C. Tan, H. Song, K. B. Lee, J. Oh, *ACS Sustain. Chem. Eng.* **2021**, *9*, 2348–2357.

[39] D. Martín-Yerga, A. Pérez-Junquera, M. B. González-García, J. V. Perales-Rondon, A. Heras, A. Colina, D. Hernández-Santos, P. Fanjul-Bolado, *Electrochim. Acta* **2018**, *264*, 183–190.

[40] J. Han, N. J. Blackburn, T. M. Loehr, *Inorg. Chem.* **1992**, *31*, 3223–3229.

[41] J. Heyes, M. Dunwell, B. Xu, *J. Phys. Chem. C* **2016**, *120*, 17334–17341.

[42] C. M. Gunathunge, X. Li, J. Li, R. P. Hicks, V. J. Ovalle, M. M. Waegele, *J. Phys. Chem. C* **2017**, *121*, 12337–12344.

[43] Z. Zhou, G. G. Huang, T. Kato, Y. Ozaki, *J. Raman Spectrosc.* **2011**, *42*, 1713–1721.

[44] P. A. Mosier-Boss, S. H. Lieberman, *Appl. Spectrosc.* **2000**, *54*, 1126–1135.

[45] G. C. Lukey, J. S. J. Van Deventer, S. T. Huntington, R. L. Chowdhury, D. C. Shallcross, *Hydrometallurgy* **1999**, *53*, 233–244.

[46] C. Souza, D. Majuste, V. S. T. Ciminelli, *Hydrometallurgy* **2014**, *142*, 1–11.

[47] R. K. Lauridsen, T. Rindzevicius, S. Molin, H. K. Johansen, R. W. Berg, T. S. Alstrøm, K. Almdal, F. Larsen, M. S. Schmidt, A. Boisen, *Sens. Bio-Sensing Res.* **2015**, *5*, 84–89.

[48] J. Y. Hwang, Y. Y. Wang, C. C. Wan, *J. Appl. Electrochem.* **1987**, *17*, 684–694.

[49] A. M. Woods, The Adsorption of Urea on Polycrystalline Gold Electrodes, University of Saskatchewan, **2016**.

[50] A. N. Alexandrova, W. L. Jorgensen, *J. Phys. Chem. B* **2007**, *111*, 720–730.

[51] M. W. Lister, *Can. J. Chem.* **1955**, *33*, 426–440.

[52] N. Wen, M. H. Brooker, *J. Phys. Chem.* **1995**, *99*, 359–368.

[53] T. C. Dao, N. M. Kieu, T. Q. N. Luong, T. A. Cao, N. H. Nguyen, V. V. Le, *Adv. Nat. Sci. Nanosci. Nanotechnol.* **2018**, *9*, DOI 10.1088/2043-6254/aabef8.

[54] C. V. Gopal Reddy, F. Yan, Y. Zhang, T. Vo-Dinh, *Anal. Methods* **2010**, *2*, 458–460.

[55] A. Valiuniene, V. Antanavičius, Ž. Margarian, I. Matulaitiene, G. Valinčius, *Medziagotyra* **2013**, *19*, 385–389.

[56] B. Wels, D. C. Johnson, *J. Electrochem. Soc.* **1990**, *137*, 2785–2791.

[57] Z. Sun, T. Ma, H. Tao, Q. Fan, B. Han, *Chem* **2017**, *3*, 560–587.

[58] R. Daiyan, T. Tran-Phu, P. Kumar, K. Iputera, Z. Tong, J. Leverett, M. H. A. Khan, A. A. Esmailpour, A. Jalili, M. Lim, A. Tricoli, R.-S. Liu, X. Lu, E. Lovell, R. Amal, *Energy Environ. Sci.* **2021**, *14*, 3588–3598.

[59] M. Duca, M. O. Cucarella, P. Rodriguez, M. T. M. Koper, *J. Am. Chem. Soc.* **2010**, *132*, 18042–18044.

[60] D. B. Trimarco, S. B. Scott, A. H. Thilsted, J. Y. Pan, T. Pedersen, O. Hansen, I. Chorkendorff, P. C. K. Vesborg, *Electrochim. Acta* **2018**, *268*, 520–530.

[61] I. Dobrosz-Gómez, M. Á. Gómez García, G. H. Gaviria, E. GilPavas, *J. Appl. Electrochem.* **2020**, *50*, 217–230.

[62] A. Socha, E. Kuśmierek, in *Chem. Prot. Environ. 2*, Plenum Press, New York, **1996**, pp. 283–293.

[63] S. C. Cheng, M. Gattrell, T. Guena, B. MacDougall, *Electrochim. Acta* **2002**, *47*, 3245–3256.

Supplementary information 5

Materials

Titanium powder (TLS Technik GmbH & Co., ASTM, grade 2) with an average particle size of 6 μm, polyethersulfone (PES, BASF, Ultrason E 6020P) and N-methylpyrrolidone (NMP, Sigma Aldrich, ≥99 %) were used for Ti hollow fiber preparation. For surface modification of Ti hollow fibers 1 μm Cu powder (SkySpring nanoparticles, 99.8 %), 25 nm Cu powder (Sigma Aldrich, TEM) and $CuSO_4$ (Sigma Aldrich, ≥99 %) were used. Sulfuric acid (Sigma Aldrich, 95.0-98.0 %), H_3PO_4 (Sigma Aldrich, 85 wt. % in H_2O), 2,3-Butanedione monoxime (Sigma Aldrich, ≥99.0 %) and Thiosemicarbazide (Sigma Aldrich, 99 %) were used for urea detection. Cu foil (Alpha Aesar, 99.99%) and Cu disc (Pine research)) were used for electrode preparation for SERS and EC-MS respectively. Electrolyte solutions were prepared using MiliQ water and $KClO_4$ (Sigma Aldrich, 99.99 %), $KHCO_3$ (Sigma Aldrich, 99.7 %), KNO_3 (Sigma Aldrich, ≥99.0 %), $(NH_4)_2CO_3$ (Sigma Aldrich, ≥99.5 %), HCOOK (Sigma Aldrich, ≥99.0 %), KCN (Sigma Aldrich, ≥98.0 %), $K^{15}NO_3$ (Sigma Aldrich, 98 atom % ^{15}N), $KH^{13}CO_3$ (Sigma Aldrich, 99 atom% ^{13}C), $^{13}CO_2$ (Campro Scientific, min. 99.9 atom % ^{13}C).

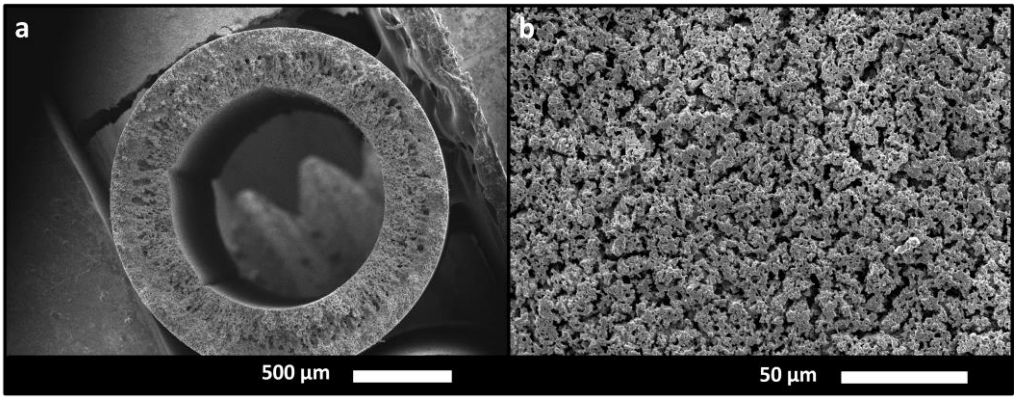

Figure S5.1. SEM images of the Cu coated Ti hollow fiber electrode for urea electrosynthesis experiments. (a) Cross section and (b) surface of the electrode.

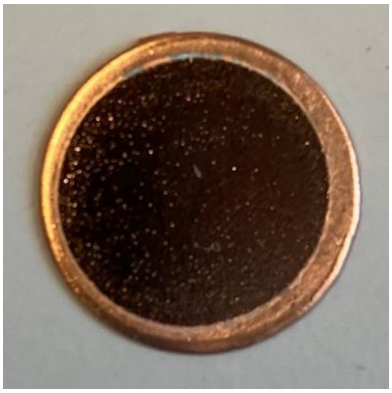

Figure S5.2. Photograph of the Cu electrode used in SERS experiments.

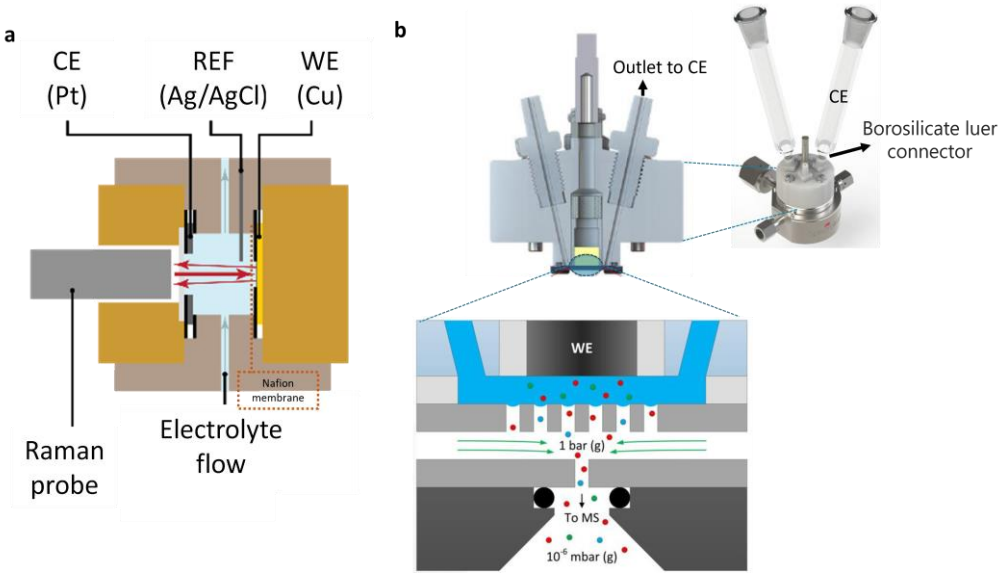

Figure S5.3. Schematic representation of the techniques used in this study. (a) The SERS set-up and (b) the EC-MS principles, showing that the CE is separated from the WE at quite far distance, in a separate compartment connected to the WE compartment, through a borosilicate filter and a Luer-lock.

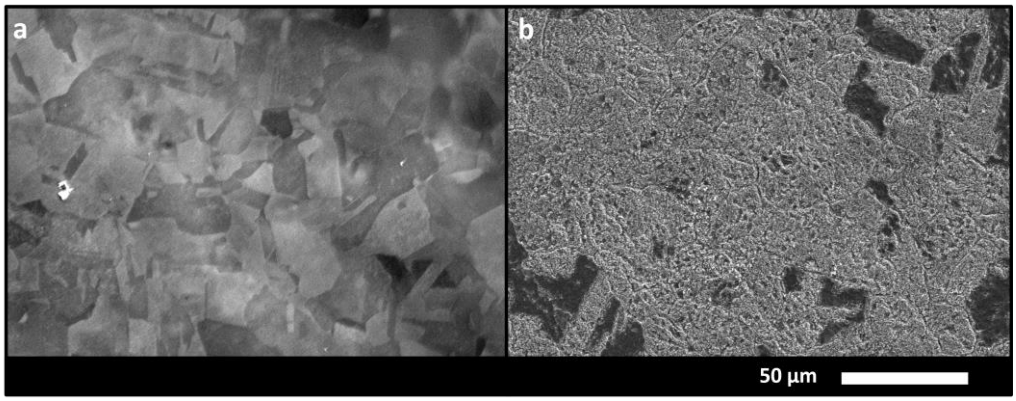

Figure S5.4. SEM images of the Cu electrode used in SERS experiments. (a) Before and (b) after electrochemical activation.

Urea quantification

The amount of produced urea was quantified spectrophotometrically using the diacetylmonoxime method. [S1] First, 0.1 ml of electrolyte was mixed with 2 ml acid solution (7.5 ml concentrated H_2SO_4, 2.5 ml concentrated H_3PO_4 and 15 ml of H_2O) and 1 ml of diacetylmonoxime (DAMO)-thiosemicarbazide (TSC) solution (2.5 mg of TSC and 125 mg of DAMO in 25 ml of H_2O). Next, the solution was mixed vigorously and heated for 20 min at 80 °C. After cooling to room temperature, absorbance at 525 nm was measured in UV-Vis spectrometer. Calibration was performed using standard urea solutions with a known concentration (Figure S5.5).

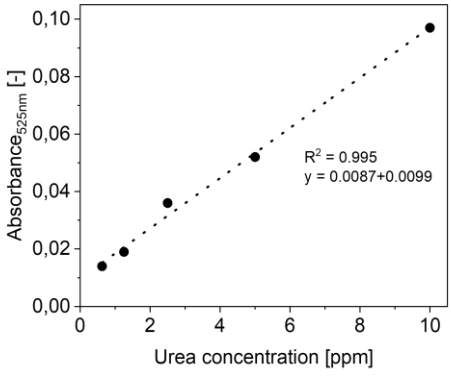

Figure S5.5. Calibration curve for urea quantification. Absorbance at 525 nm.

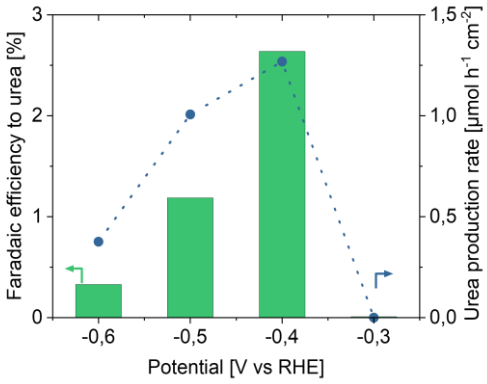

Figure S5.6. Urea selectivity in simultaneous reduction of CO_2 and NO_3^- on a polycrystalline, rough Cu-Ti electrode in 0.1 M $KHCO_3$ and 50 mM KNO_3. Measured after 1 h of electrolysis at each potential.

The remaining FE is mostly due to the formation of H_2 and NH_3, which are readily formed over Cu surfaces at the applied potentials. Gas-phase products of CO_2 reduction, such as CO, CH_4 or C_2H_4 were not observed, probably due to the thermodynamically more favorable reduction potentials of nitrate reduction.

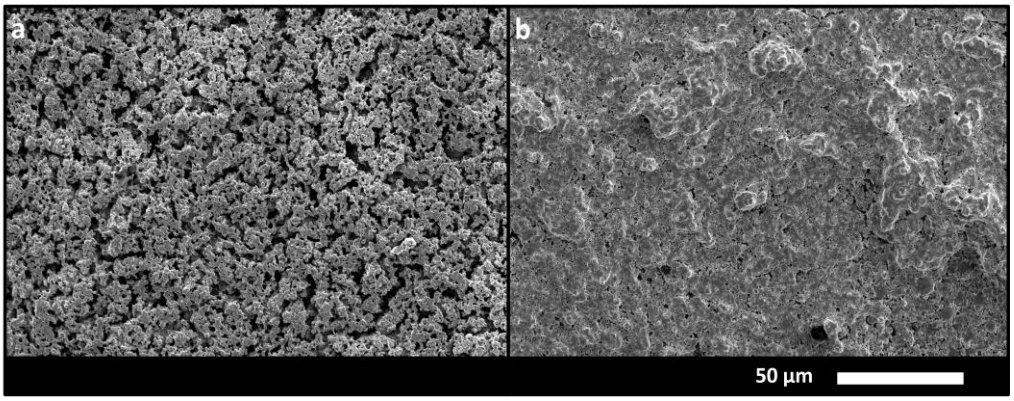

Figure S5.7. SEM images showing a top view of the Cu coated Ti hollow fiber electrode. (a) before and (b) after chronoamperometry for 30 minutes at -0.6 V vs RHE in 0.1 M $KHCO_3$ and 50 mM KNO_3. Significant surface reconstruction has occurred, indicating dissolution and re-deposition of Cu species.

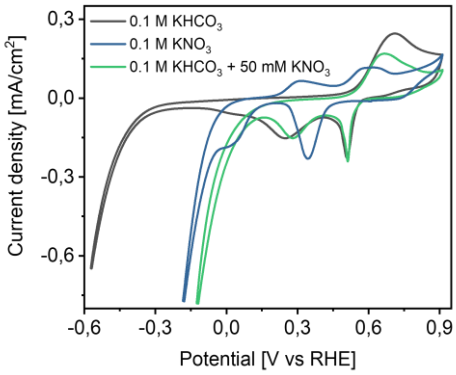

Figure S5.8. Cyclic voltammetry of the applied Cu electrode in different electrolytes. CVs were recorded using the EC-MS cell.

The addition of 50 mM KNO_3 to $KHCO_3$ does not significantly affect the reduction and re-oxidation potentials of Cu oxide and metallic Cu respectively. The shift in potential required for the reduction of Cu oxide in 0.1 M KNO_3 (blue line) is attributed to local pH changes, more pronounced in unbuffered KNO_3 electrolyte, than in CO_2 saturated $KHCO_3$ solution, which acts as a buffer. Please also note that reduction of CO_2 initiates at much more negative potentials than reduction of nitrate, i.e. at ~ -0.35 V (see also Table S5.1).

Table S5.1. Standard reduction potentials of several CO_2 and NO_3^- electroreduction reactions.

Reaction	E^o vs RHE
Standard reduction potentials of NO_3^- [S2]	
$NO_3^- + 2H^+ + e^- \rightleftharpoons NO_2 + H_2O$	0.77
$NO_3^- + 2H^+ + 2e^- \rightleftharpoons NO_2^- + H_2O$	0.94
$NO_3^- + 4H^+ + 3e^- \rightleftharpoons NO + 2H_2O$	0.96
$2NO_3^- + 10H^+ + 8e^- \rightleftharpoons N_2O + 5H_2O$	1.12
$2NO_3^- + 12H^+ + 10e^- \rightleftharpoons N_2 + 6H_2O$	1.25
$NO_3^- + 7H^+ + 6e^- \rightleftharpoons NH_2OH + 2H_2O$	0.73
$2NO_3^- + 16H^+ + 14e^- \rightleftharpoons N_2H_4 + 6H_2O$	0.82
$NO_3^- + 9H^+ + 8e^- \rightleftharpoons NH_3 + 3H_2O$	0.88
Standard reduction potentials of CO_2 [S3]	
$CO_2 + 2H^+ + 2e^- \rightleftharpoons HCOOH$	-0.25
$CO_2 + 2H^+ + 2e^- \rightleftharpoons CO + H_2O$	-0.11
$2CO_2 + 12H^+ + 12e^- \rightleftharpoons C_2H_4 + 4H_2O$	0.06
$CO_2 + 8H^+ + 8e^- \rightleftharpoons CH_4 + H_2O$	0.17

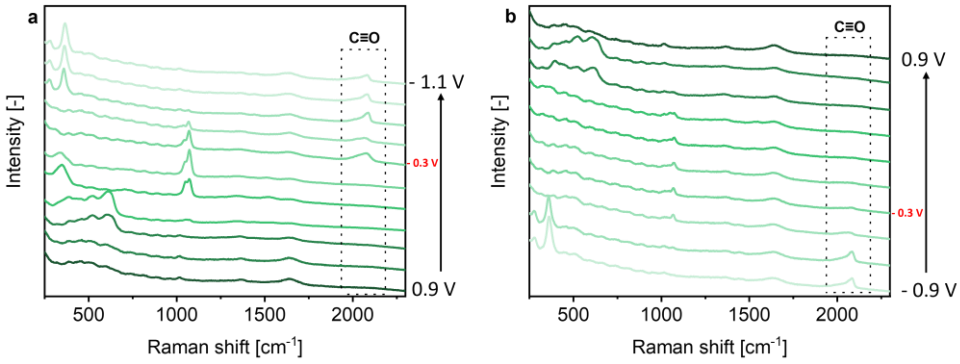

Figure S5.9. In situ SERS of a Cu surface in CO2 saturated 0.1 M $KHCO_3$. Recorded during (a) a reductive scan and (b) an oxidative scan in cyclic voltammetry. The potential interval between spectra amounts to ~0.2 V.

SERS experiments performed with Cu electrodes in CO_2 saturated 0.1 M $KHCO_3$ (Figure S5.9), showing typical signals related to CO_2 reduction on rough Cu surfaces, in agreement with literature.[S4-S8] The bands related to Cu_2O are discussed in the main article. The bands at 350 and 1540 cm^{-1} indicate adsorbed carbonate and can be assigned to the asymmetric C-O stretching mode of strongly adsorbed bidentate carbonate.[S4-S6] Below 0.3 V vs RHE, the C-O symmetric stretching modes of chemisorbed CO_3^{2-} can be observed at 1072 cm^{-1} .[S7] This (shouldered) signal is growing with potential, disappears at -0.7 V and shows up again (at lower intensity) in an oxidative scan. At negative potentials, starting from -0.3 V, a broad, weak signal at ~2070 cm^{-1} appears, which corresponds to the C≡O stretching mode of adsorbed CO on Cu.[S4,S7] The band at 360 cm^{-1} appearing at -0.7 V in the reductive scan can also be assigned to CO adsorbed on Cu (Cu-CO), and in agreement with other studies.[S4,S8] In the oxidative scan at around -0.4 V, all CO signals disappear.

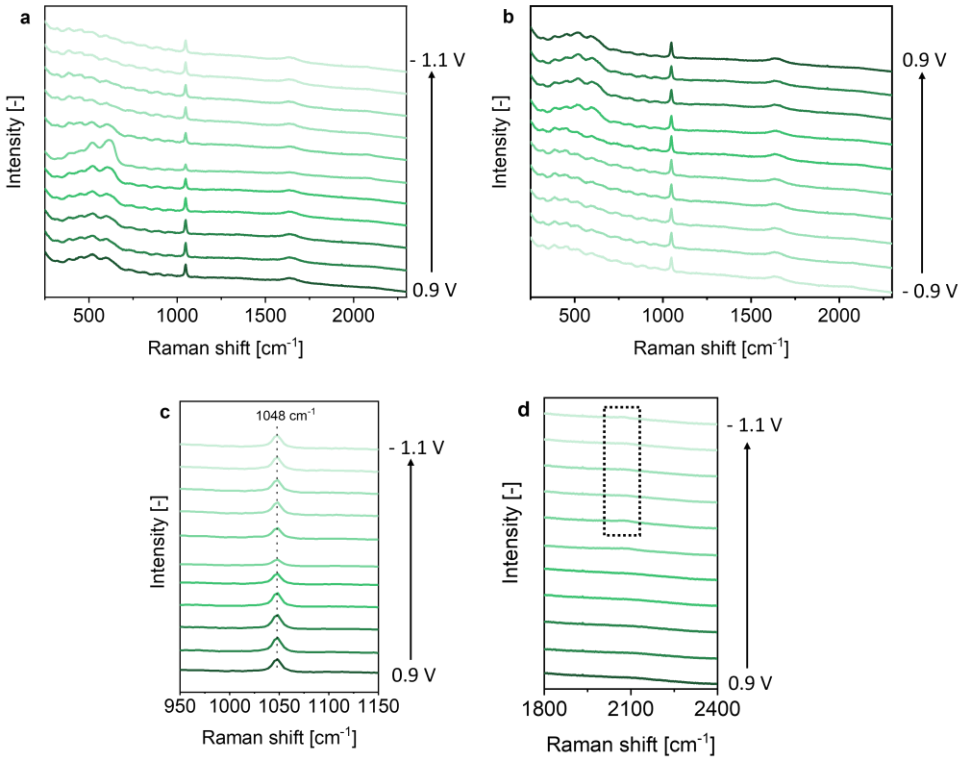

Figure S5.10. In situ SERS of a Cu surface in Ar saturated 0.1 M KNO_3. Recorded during (a) a reductive scan and (b) an oxidative scan of cyclic voltammetry. Magnification of (c) the 1048 cm^{-1} peak and (d) the ~2070 cm^{-1} peak, which is now absent in the reductive scan due to the absence of bicarbonate and CO_2.

SERS experiments performed with Cu electrodes in Ar saturated 0.1 M KNO_3 show the spectral fingerprint of copper oxidation and reduction and the H_2O signal at 1640 cm^{-1} (Figure S5.10a and b), in agreement with previous experiments. In addition, a signal at 1048 cm^{-1} is present which is assigned to the symmetric NO_3^- stretch vibration.[S9–S11] Considering that a stark shift was not observed (Figure S5.10c) the signal likely originates from NO_3^- in solution rather than from any adsorbed form on the Cu surface.[S12] Interestingly, spectral intensities in the high wavenumber range are very minor, not only showing these are related to the presence of carbonate in Figure S5.9, but also excluding the formation of N_2O.[S13]

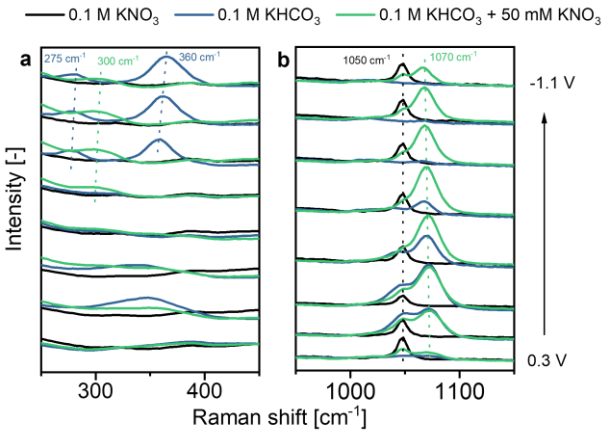

Figure S5.11. Comparison of selected Raman signals in different electrolytes. In the region of (a) 250 – 450 cm^{-1} and (b) 950 – 1150 cm^{-1}.

In Figure S5.11a Cu-CO signals in 0.1 M $KHCO_3$ can be observed at negative potentials starting at ~ -0.7 V, which are absent in the presence of NO_3^-. Interestingly, a signal at ~300 cm^{-1} is observed in 0.1 M $KHCO_3$ with 50 mM KNO_3 electrolyte. Based on similar signals detected at 290 cm^{-1} on Au electrode when exposed to CN^-,[S14] the ~300 cm^{-1} band position can be assigned to a Cu-CN bending mode. In Figure S5.11b comparison of the peaks in the 1100 to 1000 cm^{-1} is shown, demonstrating the contribution of nitrate vibrations to the 1050 cm^{-1} peak at reductive potentials below ~-0.3 V, while overlap of nitrate and carbonate bands occurs at potentials more positive than -0.3 V.

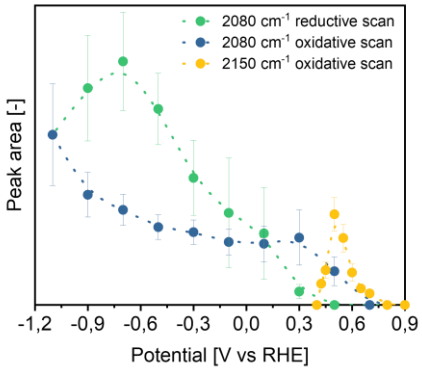

Figure S5.12. Peak area versus potential for the 2080 cm^{-1} and 2150 cm^{-1} peaks. Clearly, the 2150 cm^{-1} band is present at a limited potential window (0.45 to 0.75 V), and only appears in oxidative scans.

Standard deviation was determined from 3 different measurements, and indicated by the error bars. Signal intensity will depend on surface roughness, which can be slightly different between the samples and also between different spots on the sample.

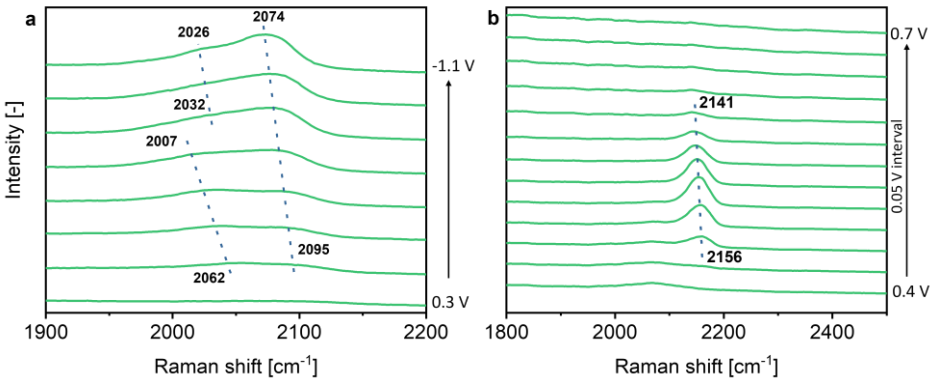

Figure S5.13. Stark effect of ~2080cm^{-1} and 2150cm^{-1} peaks. Recorded during (a) reductive and (b) oxidative scan of cyclic voltammetry (magnification in the relevant potential region).

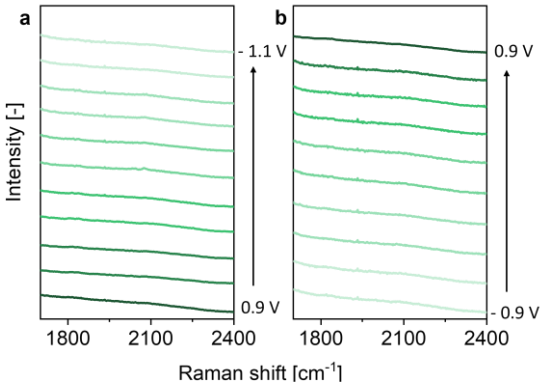

Figure S5.14. In situ SERS of a Cu surface in Ar saturated 0.1 M $KClO_4$. Recorded during (a) reductive scan and (b) an oxidative scan of cyclic voltammetry.

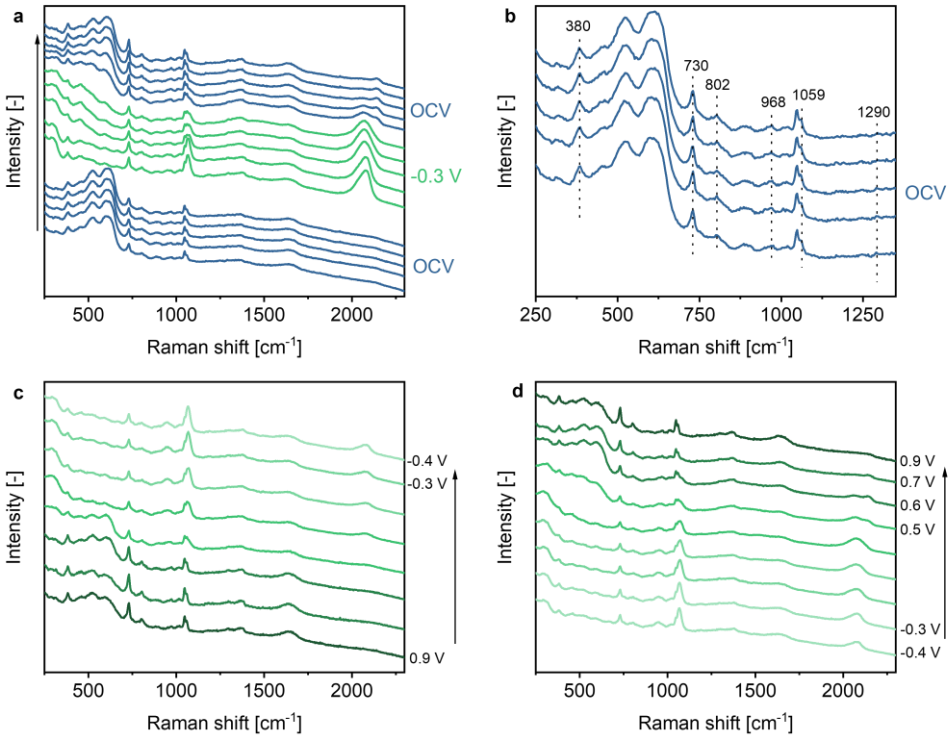

Figure S5.15. In situ SERS of Cu surface in presence of Nafion membrane. (a) CO_2 saturated 0.1 M $KHCO_3$ with 50 mM KNO_3 electrolyte recorded at OCV, at -0.3 V vs RHE and again at OCV (the time interval between spectra is 1 min). (b) zoom into the spectra at OCV with Nafion-related signals indicated. Cyclic voltammetry of the Cu electrode during (c) a reductive and (d) an oxidative scan.

In order to exclude the influence of anodic processes on the observed Raman signals, studies at OCV (Figure S5.15a and S5.15b) and cyclic voltammetry (Figure S5.15c and S5.15d) were repeated after insertion of a Nafion membrane in between the anode and the cathode. Clearly, the Raman signals at ~2080 cm^{-1} and ~2150 cm^{-1} are again obvious, proving that anodic processes do not interfere with the measurements. The additional Raman signals observed in measurements with membranes at 380, 730, 802, 968, 1059 and 1290 cm^{-1} are assigned to Nafion.[S15] Note that the potential range is affected by the presence of the Nafion membrane. In this cell configuration bubbles created on the electrode do not release very easily, interfering with the measurement, thus assessment of relatively highly negative potentials in this cell configuration is not possible.

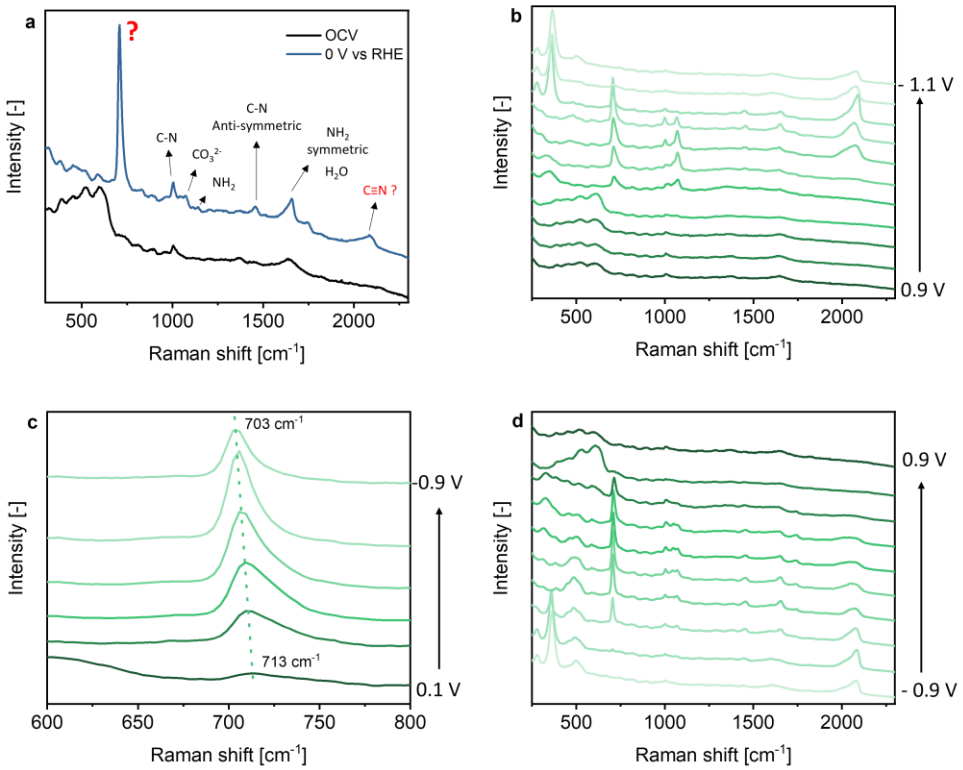

Figure S5.16. In situ SERS of a Cu surface in CO_2 saturated 0.1 M $KHCO_3$ with 50 mM urea. (a) at OCV and 0 V vs RHE; (b) during a reductive scan with (c) magnification into ~710 cm^{-1} signal; (d) during an oxidative scan.

At OCV there is only one signal which could be assigned to urea which is the symmetric stretching vibration of C-N at 1005 cm^{-1} (Figure S5.16a).[S16] Surprisingly, at 0 V vs RHE additional Raman signals appear which can be related to the adsorption of urea on the Cu surface. It is known that urea can adsorb on metallic electrodes such as Pt,[S17] Au,[S18] Ag [S19] or Cu [S20] under reductive potentials and is therefore frequently studied as a potential inhibitor of Cu corrosion in neutral and alkaline media.[S21] Most of the signals can be assigned to urea and bicarbonate.[S4,S16] The most intense band at ~709 cm^{-1} cannot be easily assigned according to existing literature. As a Stark effect in the CV cycle is evident (Figure S5.16c) the species responsible for the Raman intensity must be surface adsorbed. When the system goes back to OCV, all signals disappear and only urea in solution is observed, which is explained by reversible adsorption of urea on metallic electrodes.

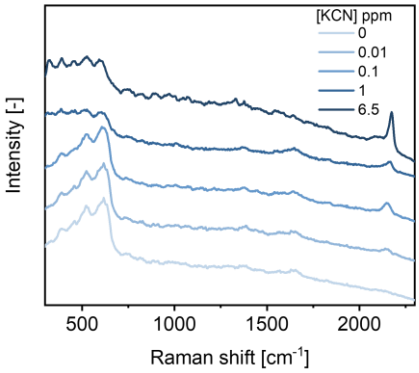

Figure S5.17. In situ SERS of a Cu surface in CO_2 saturated 0.1 M $KHCO_3$ with increasing concentration of KCN. Spectra were recorded at open circuit potential.

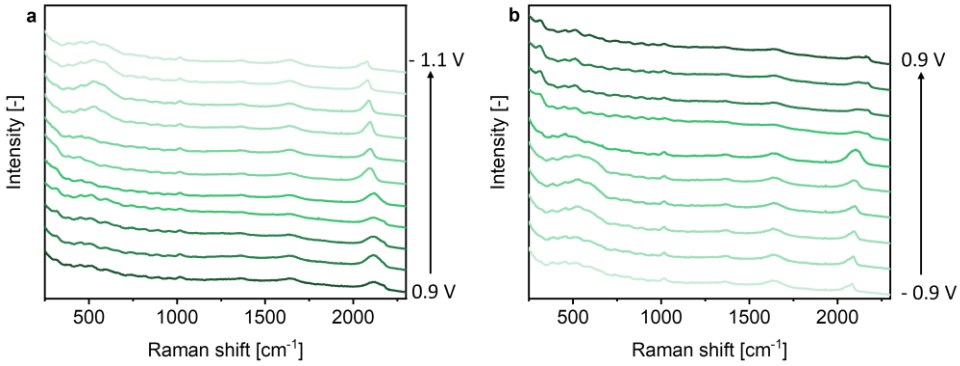

Figure S5.18. In situ SERS of a Cu surface in CO_2 saturated 0.1 M $KHCO_3$ with 10mM KCN. Recorded during (a) a reductive scan and (b) an oxidative scan in cyclic voltammetry.

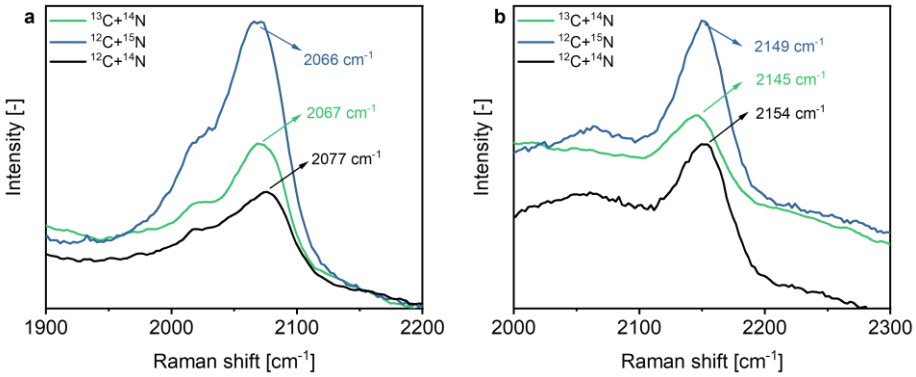

Figure S5.19. In situ SERS of a Cu surface in CO_2 saturated 0.1 M $KHCO_3$ with 50 mM KNO_3 with isotopically labeled carbon (^{13}C) and nitrogen (^{15}N). Recorded during (a) reductive scan at -1 V vs RHE and (b) oxidative scan at 0.5 V vs RHE.

With both ^{13}C and ^{15}N-labeled compounds in solution, the Raman signal observed in the reductive scan shifts by approx. 10 cm^{-1} to lower wavenumbers. According to literature, the expected peak shift for CN^- in aqueous solution for ^{13}C or ^{15}N-labeled compounds is 43 cm^{-1} and 32 cm^{-1}, respectively.[S22] Here, the observed peak is rather broad and likely consists of 2 or 3 overlapping signals which makes it difficult to determine the exact peak position. Moreover, the calculated theoretical shift likely deviates from experimental observations considering the simplifications used in the harmonic oscillator model.

In the oxidative scan, the peak at ~2150 cm^{-1} also seems to shift. However, it is difficult to claim the exact value of the peak shift due to the fact that the position of this peak can depend on the concentration of CN^- in the solution. In the case of experiments with ^{12}C + ^{15}N, the peak appears to have a slightly higher intensity. Considering that it is still shifted to lower wavelengths, this observation confirms the response of the peak to a $^{14}N/^{15}N$ exchange. In the case of ^{13}C + ^{14}N experiments, the peak intensity is lower than observed during blank experiments thus it is difficult to claim a shift in peak position.

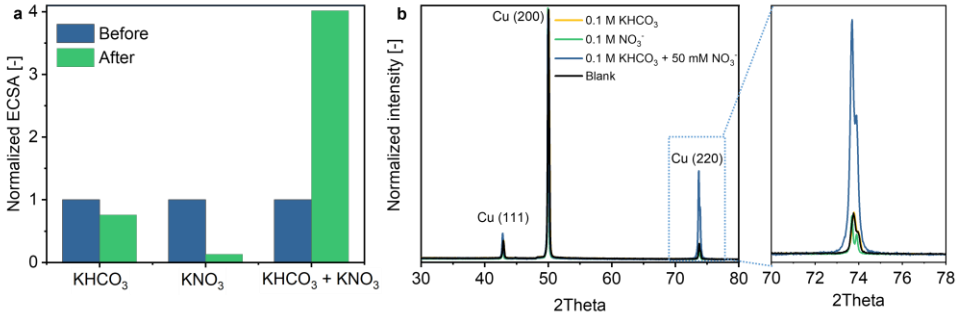

Figure S5.20. Surface change after 30 min of chronoamperometry at -0.3 V vs RHE. (a) ECSA before and after as well as (b) XRD patterns of the Cu surface.

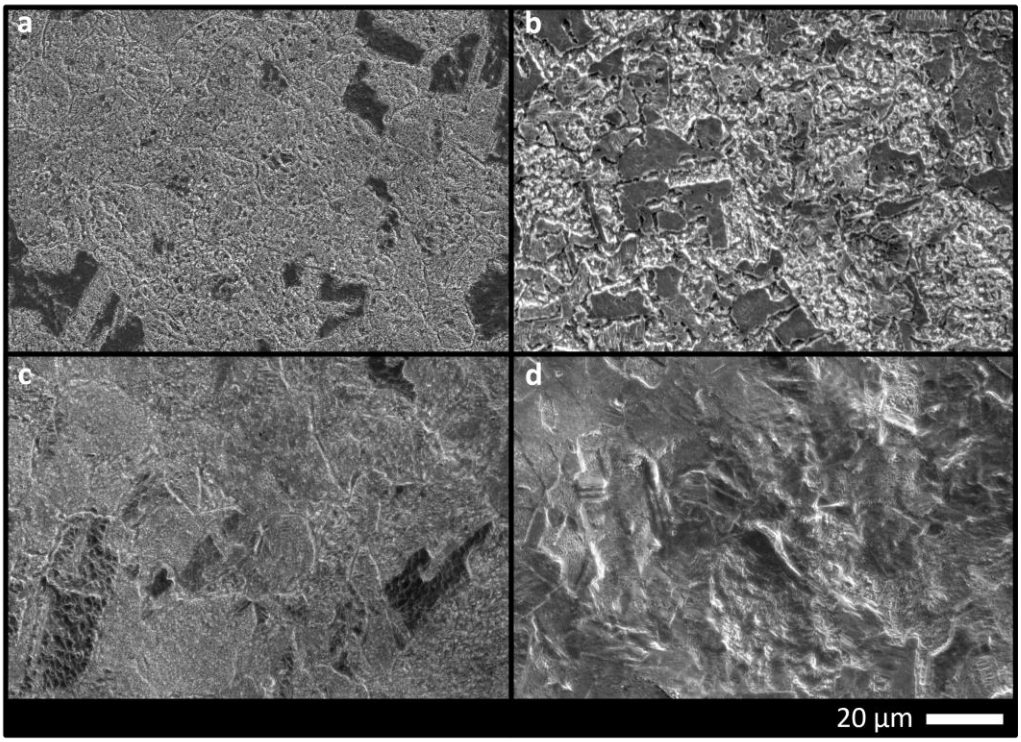

Figure S5.21. SEM images of Cu surface after 30 min chronoamperometry at -0.3 V vs RHE. (a) blank electrode; after chronoamperometry in (b) 0.1 M $KHCO_3$, (c) 0.1 M KNO_3, (d) 0.1 M $KHCO_3$ + 50 mM KNO_3.

The formation of cyanide complexes can be furthermore confirmed by a change of the Cu surface upon attack of CN^-. Chronoamperometry at -0.3 V vs RHE was performed in all electrolytes tested. ECSA before and after each experiment was measured and in fact, a significant increase in surface area was observed after electrolysis in 0.1 M $KHCO_3$ with 50 mM KNO_3 (Figure S5.20a) which could be related to surface roughening in the presence of cyanide. Moreover, the corresponding XRD pattern shows an increase of the Cu (220) facet which also indicates a surface change (Figure S5.20b). In addition, SEM images (Figure S5.21) reveal a change in morphology of the Cu surface after chronoamperometry.

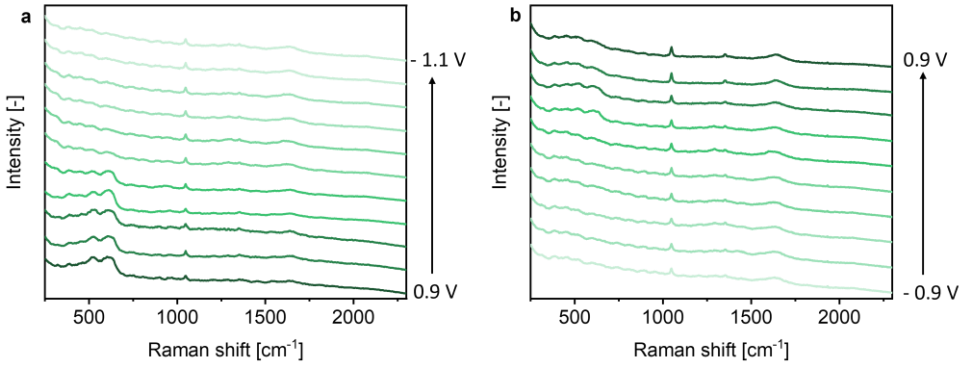

Figure S5.22. In situ SERS of a Cu surface in Ar saturated 50 mM HCOOK with 50 mM KNO_3. Recorded during (a) reductive scan and (b) oxidative scan of cyclic voltammetry.

SERS of a Cu surface in Ar saturated 0.1 M HCOOK with 50 mM KNO_3 during CV (Figure S5.22) shows no signals associated with cyanide. The only signals observed are the ones from Cu_2O, NO_3^-, H_2O and $HCOO^-$ at 1353 cm^{-1}.[S4] This result suggests that CO_3^{2-} adsorbed on the surface is necessary for cyanide formation.

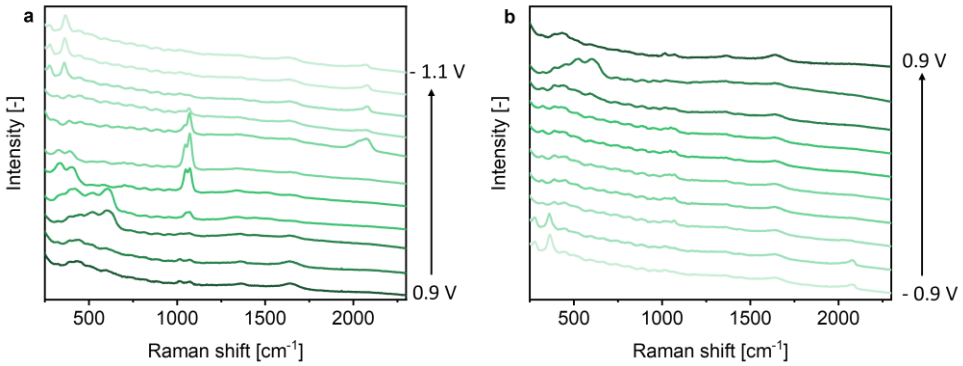

Figure S5.23. In situ SERS of a Cu surface in CO_2 saturated 0.1 M $KHCO_3$ with 20 mM $(NH_4)HCO_3$. Recorded during (a) reductive scan and (b) oxidative scan of cyclic voltammetry.

SERS of a Cu surface in CO_2 saturated 0.1 M $KHCO_3$ with 20 mM $(NH_4)HCO_3$ (Figure S5.23) shows no signals associated with cyanide. A weak signal at 410 to 383 cm^{-1} can be observed when metallic Cu is formed which could be assigned to Cu-N from adsorbed ammonia however further experiments would be necessary to convincingly prove this hypothesis. On Ag electrode, Ag-N formation was reported at 325 cm^{-1} but only at high concentrations.[S23] Relatively strong signals of NH_3 can be found above 3000 cm^{-1} [S24] being out of the range of wavenumbers detectable with our system.

In-situ EC-MS

All measured m/z signals are shown in Figure S5.24, Figure S5.25 and Figure S5.26. The potential range for the CV experiments conducted with the EC-MS does not match the one made in SERS experiments due to the intrinsic limitations of the small-volume cell used. However, SERS signals are observed already at 0.3 V vs RHE in the reductive scan thus the selected potential range is sufficient to observe the difference between measurements. 2 cyclic voltammetry cycles are shown in each case.

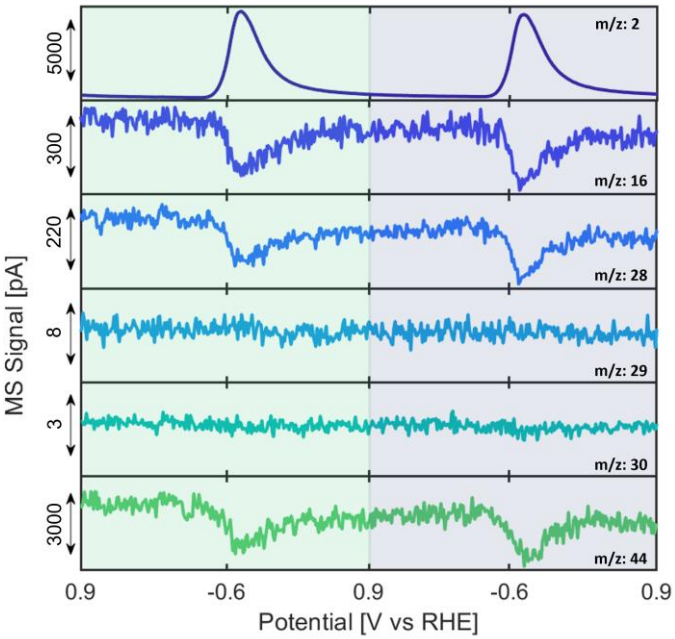

Figure S5.24. EC-MS analysis of desorbed products from Cu surface during cyclic voltammetry in CO_2 saturated 0.1 M $KHCO_3$.

The only gas product detected in CO_2 saturated 0.1M $KHCO_3$ (Figure S5.24) was H_2 at potentials below -0.4 V. MS fragments from CO_2 itself overlap with most common CO_2 reduction products therefore it is difficult to detect them using MS. However, a dip in m/z signals related to CO_2 confirms its conversion.

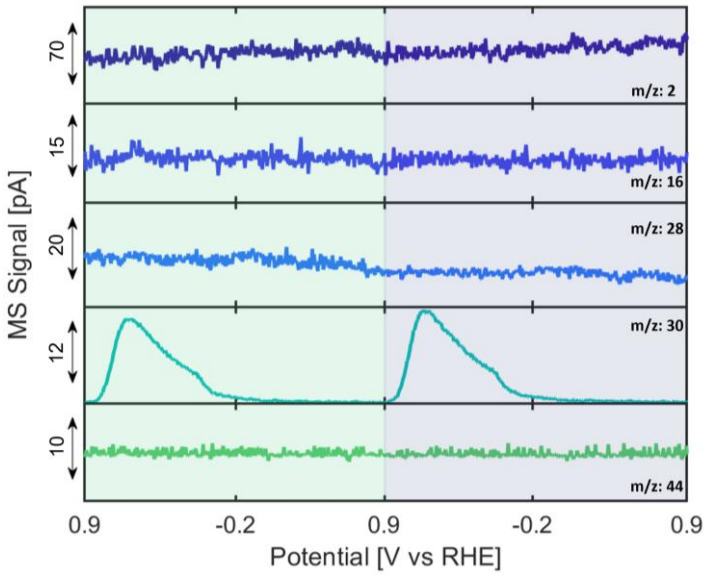

Figure S5.25. EC-MS analysis of desorbed products form Cu surface during cyclic voltammetry in Ar saturated 0.1 M KNO_3.

In Ar saturated 0.1 M KNO_3 electrolyte electroreduction of nitrate is detected in reductive scan starting at 0.8 V (Figure S5.25) by an increase in the m/z: 30 signal (nitric oxide). Since no signals are observed in the first cycle, the 2nd and 3rd cycle are shown. Other gas products are not detected which suggests the formation of non-volatile compounds at more negative potentials, likely NH_4^+. NO formation was not observed in the oxidative scan which suggests that copper oxide is necessary to reduce NO_3^- to NO. The previous report showed no gas products on Cu electrodes in NO_3^- electroreduction however in the studied potential range (0.25 V to -1 V) no copper oxide is expected.[S25]

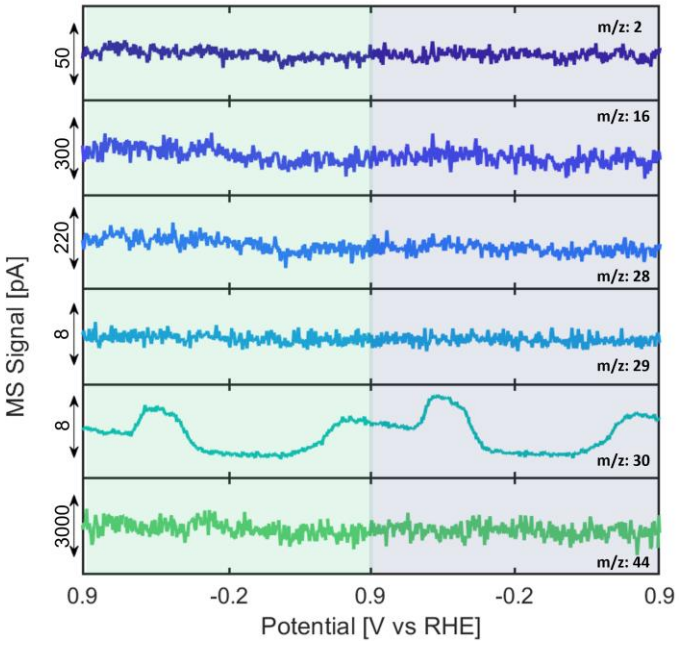

Figure S5.26. EC-MS analysis of desorbed products form Cu surface during cyclic voltammetry in CO_2 saturated 0.1 M $KHCO_3$ with 50 mM KNO_3.

In CO_2 saturated $KHCO_3$ with 50 mM KNO_3 (Figure S5.26), no other gas products than NO were detected. Since no signals are observed in a reductive scan of the first CV cycle, 2nd and 3rd cycles are shown which results in increased signal of NO at the beginning of 2nd CV cycle (NO formed in an oxidative scan of 1st cycle).

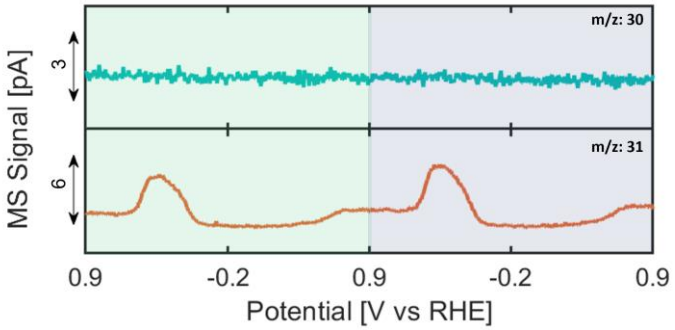

Figure S5.27. EC-MS analysis of m/z: 30 and m/z: 31 desorbed from Cu surface during cyclic voltammetry in CO_2 saturated 0.1 M $KHCO_3$ with 50 mM $K^{15}NO_3$.

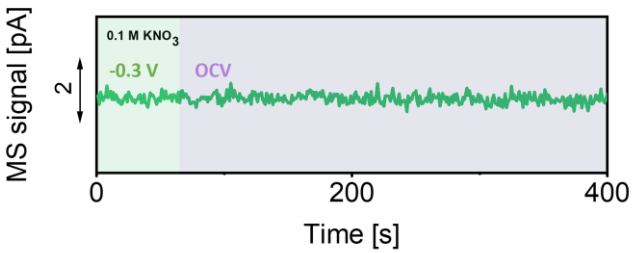

Figure S5.28. MS analysis of nitric oxide (m/z: 30) desorbed from the Cu surface during chronoamperometry at -0.3 V vs RHE and subsequent OCV in Ar saturated 0.1 M KNO_3.

SI References

[S1] S. C. Cheng, M. Gattrell, T. Guena, B. MacDougall, *Electrochem. Acta* **2002**, 47, 3245–3256.

[S2] J. M. McEnaney, S. J. Blair, A. C. Nielander, J. A. Schwalbe, D. M. Koshy, M. Cargnello, T. F. Jaramillo, *ACS Sustain. Chem. Eng.* **2020**, *8*, 2672–2681.

[S3] J. W. Vickers, D. Alfonso, D. R. Kauffman, *Energy Technol.* **2017**, *5*, 775–795.

[S4] M. Moradzaman, G. Mul, *ChemElectroChem* **2021**, *8*, 1478–1485.

[S5] V. Chernyshova, S. Ponnurangam, P. Somasundaran, *Phys. Chem. Chem. Phys.* **2013**, *15*, 6953–6964.

[S6] M. Moradzaman, G. Mul, *ACS Catal.* **2020**, *10*, 8049–8057.

[S7] I. V. Chernyshova, P. Somasundaran, S. Ponnurangam, *Proc. Natl. Acad. Sci. U. S. A.* **2018**, *115*, E9261–E9270.

[S8] C. M. Gunathunge, X. Li, J. Li, R. P. Hicks, V. J. Ovalle, M. M. Waegele, *J. Phys. Chem. C* **2017**, *121*, 12337–12344.

[S9] Z. Zhou, G. G. Huang, T. Kato, Y. Ozaki, *J. Raman Spectrosc.* **2011**, *42*, 1713–1721.

[S10] P. A. Mosier-Boss, S. H. Lieberman, *Appl. Spectrosc.* **2000**, *54*, 1126–1135.

[S11] Z. Zhou, G. G. Huang, Y. Ozaki, *Chem. Lett.* **2010**, *39*, 1203–1205.

[S12] D. P. Butcher, A. A. Gewirth, *Nano Energy* **2016**, *29*, 457–465.

[S13] M. Lust, A. Pucci, A. Otto, *J. Raman Spectrosc.* **2006**, *37*, 166–174.

[S14] R. K. Lauridsen, T. Rindzevicius, S. Molin, H. K. Johansen, R. W. Berg, T. S. Alstrøm, K. Almdal, F. Larsen, M. S. Schmidt, A. Boisen, *Sens. Bio-Sensing Res.* **2015**, *5*, 84–89.

[S15] L. Zhang, C. Pan, J. Zhu, C. Wang, *Nanotechnology* **2005**, *16*, 2242–2244.

[S16] I. Durickovic, L. Thiebaud, P. Bourson, T. Kauffmann, M. Marchetti, *Appl. Spectrosc.* **2013**, *67*, 1205–1209.

[S17] V. Climent, A. Rodes, R. Albalat, J. Claret, J. M. Feliu, A. Aldaz, *Langmuir* **2001**, *17*, 8260–8269.

[S18] R. Holze, S. Schomaker, *Electrochim. Acta* **1990**, *35*, 613–620.

[S19] A. Lukomska, J. Sobkowski, *J. Solid State Electrochem.* **2005**, *9*, 277–283.

[S20] A. Łukomska, J. Sobkowski, *J. Solid State Electrochem.* **2007**, *11*, 253–258.

[S21] F. Altaf, R. Qureshi, S. Ahmed, A. Y. Khan, A. Naseer, *J. Electroanal. Chem.* **2010**, *642*, 98–101.

[S22] S. Yoshikawa, D. H. O'Keeffe, W. S. Caughey, *J. Biol. Chem.* **1985**, *260*, 3518–3528.

[S23] L. A. Sanchez, J. R. Lombardi, R. L. Birke, *Chem. Phys. Lett.* **1984**, *108*, 45–50.

[S24] Y. Liu, T. Asset, Y. Chen, E. Murphy, E. O. Potma, I. Matanovic, D. A. Fishman, P. Atanassov, *iScience* **2020**, *23*, 101757.

[S25] E. Pérez-Gallent, M. C. Figueiredo, I. Katsounaros, M. T. M. Koper, *Electrochim. Acta* **2017**, *227*, 77–84.

Chapter 6

Summary and Perspective

Summary

Continuously increasing CO_2 levels caused by the industrial revolution, drive the need for the development of new, more environmentally friendly processes for the chemical industry. In this thesis, the formation of green ammonia for fertilizer applications was studied, using a novel, hollow fiber electrode geometry.

In **Chapter 1**, an introduction to the topics discussed in this thesis is given. The importance of ammonia for prosperity in the present and future world is discussed. Traditional as well as non-conventional ammonia synthesis routes are introduced, with an emphasis on electrochemical approaches. Special attention is given to nitrogen conversion in an aqueous electrolyte in ambient conditions where the current literature status is described. Due to the difficulties with N_2 reduction, NO_x resources are proposed as an alternative feedstock for ammonia electrosynthesis. Various electrode configurations are described which should help to overcome mass transport limitations in NO_x conversion to NH_3, and the hollow fiber electrode design is introduced. Moreover, the concept of decentralized, small-scale green fertilizer production plants is presented, where waste NO_x together with electrochemically-, or plasma generated NO_x from N_2 are used as feed for ammonium-based fertilizer formation. Additionally, attempts of electrochemical reduction of N_2 to NH_3 are presented. Ru-Ti and TiN hollow fibers were used as electrocatalysts for nitrogen activation, however, no success was achieved. Adventitious ammonia contaminations are shown to be the reason for false-positive and irreproducible results. For systems containing N-components, such as TiN, it is especially difficult to describe reliable performance due to the spontaneous release of NH_4^+ from TiN in acidic conditions. This corrosion behavior is dependent on the quantity of surface defects and likely on the crystal structure of the TiN-based electrode.

Preparation of inorganic hollow fibers is described in **Chapter 2**. Titanium was chosen as the main base material due to its high corrosion resistance and the high overpotential required for the hydrogen and oxygen evolution reactions, providing a large window of operation for electrochemical purposes. Fibers were prepared via a dry-wet spinning technique using Ti particles, PES as binder, and NMP as solvent. A 2-step thermal decomposition of PES in air at 475 °C and Ar at 800 °C allows for efficient polymer removal, and thus a metallic Ti hollow fiber could be obtained. Moreover, Ti-based composites were prepared by variations in thermal treatment. Ti/TiN hollow fibers were prepared by heating Ti tubes at 800 °C in N_2 atmosphere. On the other hand, omitting the first treatment step in air leads to the formation of a Ti/TiC hollow fiber. Detailed characterization of the prepared hollow fibers reveals their porous structure, elemental

composition as well as low resistivity, what makes them very promising for electrochemical applications.

The applicability of as-prepared hollow fiber tubes for electrochemical applications is described in **Chapter 3**. Metallic Ti hollow fibers sintered at 800 ^{0}C were used as a cathode for electrochemical reduction of nitrate to ammonia. In low NO_3^- concentrations, the hydrogen evolution reaction (HER) can be dominant, due to the low availability of nitrate close to the electrode surface. Therefore, efficient mass transport is crucial for efficient nitrate conversion. High activity for nitrate removal in acidic conditions was found, with mass transport limited currents at ~-50 mA/cm^2 in 50 mM KNO_3. When inert gas was flown through the hollow fiber, diffusion limitations were greatly minimized, and the current density reached values of even ~-200 mA/cm^2 during linear scan voltammetry (LSV) when a flow rate of 40 ml/min was applied. Bubbles generated by inert gas flow through the electrode wall, apparently induce efficient electrolyte mixing close to the electrode surface. During electrolysis at a stable potential of -1 V vs RHE, a faradaic efficiency of 58 % and a partial current density to NH_3 of -33 mA/cm^2 were achieved in the absence of gas flow, while flow-induced mixing increased the partial current density up to ~-75 mA/cm^2 with 45 % faradaic efficiency over 4 h measurement. Most importantly, the mixing behavior induced by hollow fibers was not comparable to traditional magnetic stirring, proving that local mass transport is greatly improved in the developed system. The presented approach can be applied for fertilizer production in the form of ammonium nitrate.

In **Chapter 4**, inert gas was replaced by nitric oxide in order to test the performance of the developed hollow fibers in the conversion of reactive gases, rather than supply of reactant from the solution. NO has a very low solubility in an aqueous electrolyte, which results in a low NO concentration in the electrolyte and induces diffusion limitations. In order to increase selectivity to ammonia, copper was chosen as electrocatalyst. Initially, EC-MS studies on Cu discs revealed acidic pH as favorable conditions for efficient ammonia synthesis, avoiding the formation of partially reduced NO, while in neutral pH, formation of N_2O was observed. For bulk electrolysis studies, Ti hollow fibers were decorated with a porous copper layer and 10 % NO was supplied through the hollow fibers which resulted in a significantly higher current density compared to the traditionally used "flow-by" concept. Although good activity for ammonia was observed, low electrode stability due to corrosion in acidic pH was observed. On the other hand, stable electrode performance in neutral pH allowed for almost 90 % faradaic efficiency and an NH_3 production rate of 400 μmol/h/cm^2 at -0.6 V vs RHE. Most importantly, supplying NO through the hollow fiber electrode resulted in suppression of the hydrogen evolution reaction due to increased availability of the reactant close to the electrode surface. Thus, a new approach for efficient

conversion of gases with low solubility was presented, while nitric oxide conversion is of significance for the production of ammonia and green fertilizer applications.

Next, simultaneous electroreduction of NO_3^- and CO_2 was investigated in order to produce urea, the most common N-based fertilizer (**Chapter 5**). The proof of concept for urea formation on a rough, polycrystalline copper electrode in CO_2 saturated 0.1 M $KHCO_3$ with 50 mM KNO_3 electrolyte was shown. Due to the high complexity of the chemistry involved, *in-situ* Surface-Enhanced Raman Spectroscopy was used to monitor adsorbed species on the Cu surface during cyclic voltammetry. In the presence of NO_3^- in $KHCO_3$, a lack of CO formation was observed, likely due to the preferential reduction of nitrate over CO_2. Most importantly, a compound with a carbon-nitrogen triple bond was identified in the range of 2080-2150 cm^{-1}, depending on the applied potential. It is proposed that partially reduced NO_3^- likely in forms NH_x intermediates, which react with adsorbed CO_3^{2-} on the Cu surface forming the C≡N bond. Formed cyanide creates complexes with copper which results in electrode dissolution and thus instability. The formation of cyanides was additionally confirmed by electrochemical mass spectrometry where the release of nitric oxide was observed as a product of (solid) CuCN oxidation. Although no characteristic urea signals were observed, a parallel pathway for alternative C-N coupling reactions was found. Results presented in this chapter give bigger insight into the complexity of simultaneous reduction of CO_2 and NO_3^- and show difficulties with the development of a functional system for urea electrosynthesis.

In the last chapter (**Chapter 6**), the main findings are summarized and a perspective on the topics raised in this thesis is given.

Perspective

The novel type of electrode configuration presented in this thesis can be considered as an attractive competitive technology to commonly known gas diffusion electrodes. Convection rather than diffusion provides additional advantages in the form of bubbles exiting the electrode wall causing intensive mixing. Therefore this electrode geometry is attractive not only for gases but also for liquid-phase reactants where mass transport limitations exist. Although this is an excellent tool for lab-scale research, not much is known about the electrode behavior on a bigger scale where bundles of fibers are used rather than a single electrode. The length of the electrode as well as the distance between the fibers in a stack can influence the mass transport and overall activity. One of the biggest challenges to overcome might be the rather low mechanical stability, which can cause fibers to frequently break. Nevertheless, if industrial applications will become of interest, the

infrastructure for large-scale production of hollow fibers via dry-wet spinning already exists in the membrane field, and thus can be used as an easy starting point.

Electrochemical reduction of N_2 in ambient conditions is the most interesting approach for ammonia synthesis from all electrochemical variations. However, in the current state this method is not feasible due to the lack of catalyst able to active the highly stable N_2 molecule. Most importantly, a huge problem with reliable data in the literature exists, which makes it difficult to choose the path to follow due to a lack of trust in published results. The reliability needs to be improved in order to make progress in the field. Once that is achieved, this topic can continue with a strong focus on catalyst development. Although very challenging, with new developments in the field of materials science and with the help of theoretical guidance it might be possible. However, even if strong evidence of nitrogen reduction reaction will be presented, a lot of further work on understanding and optimization will be required if a practical application will be targeted. Look at a similar technology - CO_2 electroreduction: although widely studied already since the 19th century, its industrial applications are very limited mostly due to low conversion rates and electrodes stability. Therefore, there is a very long way for electrochemical N_2 reduction in ambient conditions to become significant from a practical point of view, if any.

Alternatively, NO_x electroreduction to ammonia is proposed which is more feasible than the reduction of N_2, at least from a thermodynamics point of view. However, many products can be formed in this reaction, and the discovery of selective catalysts is crucial for practical applications. The catalyst also needs to be robust. If nitrate is recycled, contaminants might accumulate in the feed to the electrode, which can have a significant effect on performance and stability. Similar problems exist with gaseous NO_x formed in combustion processes, where contaminants such as CO, CO_2 and SO_2 are present. Therefore, further research, besides selective catalyst development, should address the effect of various contaminations possibly present in the system to determine which of them should be removed prior the recycling. Purification and a potential NO_x stream concentration process should also be investigated from the economic point of view, to determine the potential investment interest. Likely, additional sources of NO_x will be required to make this system more attractive. Electrochemical N_2 oxidation might suffer from similar difficulties like N_2 reduction unless oxidation at high temperatures will be considered. However, plasma technology known for NOx production since 19th century holds promise and should be intensively investigated to reduce the energy consumption.

Addition of CO_2 to above mentioned system with NO_x can be a very attractive way of simultaneous utilization of both. CO_2 is commonly present in industrial off gas, so it will very likely be available in the same industrial exhaust as NO_x. A mixture of CO_2 and NO

could be supplied in the gas phase through the wall of the hollow fiber structure, and NO_3^- would be available in the electrolyte. If efficient urea formation with low cost can be achieved, the system can be promising. However, urea is the most important nitrogen fertilizer mainly due to the relatively low cost of production. As a consequence, any new approach for urea synthesis must be revolutionary in order to compete with existing processes. Moreover, note that eventually carbon used for urea synthesis will be released into the atmosphere due to urea decomposition to CO_2 and NH_4^+ in the soil. If carbon capture is not possible (which seems very difficult on farms), CO_2, even though reused, will end up in the atmosphere. For this reason, ammonium nitrate rather than urea is considered as the future of nitrogen fertilizers, with no carbon footprint. However, that should not diminish the importance of research on this topic. This system is very interesting from the academic point of view. 2 complex reactions occurring together on the same electrode can cause additional interactions not known to the scientific world. It can bring knowledge about other, more attractive carbon-nitrogen coupling reactions as discovered in this thesis. Other conditions, electrocatalysts or measurement techniques can reveal even more, unexpected carbon-nitrogen compounds. Therefore further studies into this direction are strongly recommended.

Although the overall research presented in this thesis is far away from practical, "industrial" applications, a lot of knowledge about electrochemical conversions was gained, which can be used to guide future research and one thus could say that a small, but important contribution to the energy transition was achieved.

Samenvatting

Door constant toenemende CO_2 waardes, veroorzaakt door de industriële revolutie, is er behoefte aan veranderingen door middel van de ontwikkeling van nieuwe, milieuvriendelijkere oplossingen voor de chemische industrie. In dit proefschrift is de vorming van groene ammoniak voor bemestingsdoeleinden bestudeerd met behulp van nieuwe holle-vezelelektrodegeometrie.

In **Hoofdstuk 1** wordt een inleiding gegeven op de onderwerpen die in dit proefschrift worden besproken. Het belang van ammoniak in de huidige en toekomstige wereld wordt behandeld. Zowel traditionele als niet-conventionele routes voor de synthese van ammoniak worden geïntroduceerd met de nadruk op elektrochemische benaderingen. In het bijzonder wordt aandacht besteed aan stikstofconversie in waterige elektrolyt in omgevingsomstandigheden, zoals die in de huidige literatuur wordt beschreven. Vanwege de moeilijkheden met N_2-reductie wordt NO_x voorgesteld als een alternatieve grondstof voor de elektrosynthese van ammoniak. Er worden verschillende elektrodeconfiguraties beschreven die zouden moeten helpen om de massatransportlimiteringen bij NO_x-conversie naar NH_3 te overwinnen. Dit gebeurt met een introductie tot het ontwerp van holle-vezelelektroden. Verder wordt het concept gepresenteerd van gedecentraliseerde, kleinschalige productie-installaties voor groene meststoffen. Hier wordt NO_x-afval samen met elektrochemisch of plasma gegenereerde NO_x uit N_2 gebruikt als voeding voor de vorming van meststoffen op basis van ammonium. Daarnaast worden pogingen tot elektrochemische reductie van N_2 tot NH_3 gepresenteerd. Ru-Ti en TiN holle vezels werden gebruikt als elektrokatalysatoren voor stikstofactivering, maar er werd geen succes behaald. Onvoorziene ammoniakverontreinigingen blijken de reden te zijn voor vals positieve en niet-reproduceerbare resultaten. Voor een systeem dat N-componenten in de vorm van TiN bevat blijkt het bijzonder moeilijk te zijn om betrouwbare prestaties te zien vanwege de spontane afgifte van NH_4^+ uit TiN in zure omstandigheden. Dit corrosiegedrag is afhankelijk van de oppervlaktedefecten en waarschijnlijk ook van de kristalstructuur van de op TiN gebaseerde elektrode.

De bereiding van anorganische holle vezels wordt beschreven in **Hoofdstuk 2**. Titanium is gekozen als hoofdmateriaal vanwege de hoge corrosieweerstand en hoge overpotentiaal voor waterstof- en zuurstofontwikkelingsreacties, wat een groot werkvenster voor elektrochemische doeleinden oplevert. Vezels zijn bereid via een droog-nat-spintechniek met behulp van Ti-deeltjes, PES als een bindmiddel en NMP als een oplosmiddel. Thermische ontleding van PES in twee stappen, namelijk in lucht bij 475 °C en in Ar bij 800 °C, zorgt voor een efficiënte polymeerverwijdering, waardoor metalen Ti holle vezels kunnen worden gemaakt. Daarnaast zijn Ti-gebaseerde composieten bereid door variaties

in thermische behandeling toe te passen. Ti/TiN holle vezels zijn verkregen door Ti-buizen te verhitten tot 800 ºC in een N_2-atmosfeer. Anderzijds heeft het weglaten van de eerste behandelingsstap in lucht tot de vorming van Ti/TiC holle vezels geleid. Gedetailleerde karakterisering van de geprepareerde holle vezels laat hun poreuze structuur, elementaire samenstelling en lage weerstand zien, wat ze veelbelovend maakt voor elektrochemische toepassingen.

De toepasbaarheid van de bereide holle vezelbuizen voor elektrochemische doeleinden is getest in **Hoofdstuk 3**. Metallische Ti holle vezels gesinterd bij 800 ºC zijn gebruikt als kathode voor elektrochemische reductie van nitraat tot ammoniak. In lage NO_3^--concentraties kan HER dominant zijn vanwege de lage beschikbaarheid van nitraat dicht bij het elektrode-oppervlak. Daarom is efficiënt massatransport cruciaal voor een efficiënte nitraatomzetting. Een hoge activiteit voor nitraatverwijdering in zure omstandigheden is gevonden met massatransport-beperkte stroom bij ~-50 mA/cm² in 50 mM KNO_3. Diffusiebeperkingen zijn sterk geminimaliseerd wanneer een inert gas door de holle vezel wordt geleid, waardoor de stroomdichtheid zelfs ~-200 mA/cm² bereikt tijdens lineaire scan-voltammetrie met een stroomsnelheid van 40 ml/min. Bellen die worden gegenereerd door de inerte gasstroom door de elektrodewand induceren een efficiënte elektrolytmenging dicht bij het elektrodeoppervlak. Hierdoor wordt de toevoer van reactanten aanzienlijk verbeterd. Tijdens elektrolyse bij een stabiel potentiaal van -1 V vs RHE en in de afwezigheid van een gasstroom is een Faraday-efficiëntie van 58% en een partiële stroomdichtheid naar NH_3 van -33 mA/cm² bereikt. Door stroming geïnduceerde menging heeft de partiële stroomdichtheid tot ~75 mA/cm² met een Faraday-efficiëntie van 45% over een meting van 4 uur verhoogd. Het belangrijkste is dat het menggedrag in de holle vezels niet vergelijkbaar is met traditioneel magnetisch roeren, wat bewijst dat het lokale massatransport in een ontwikkeld systeem aanzienlijk wordt verbeterd. De gepresenteerde benadering kan worden toegepast voor de productie van kunstmest in de vorm van ammoniumnitraat.

In **Hoofdstuk 4** is inert gas vervangen door stikstofmonoxide om het prestatievermogen van de ontwikkelde holle vezels te testen voor de omzetting van reactief gas in plaats van de reactant uit de oplossing. NO heeft een zeer lage oplosbaarheid in waterige elektrolyt, wat resulteert in een lage NO-concentratie. Daarom worden diffusiebeperkingen verwacht. Om de selectiviteit naar ammoniak te verhogen is koper gekozen als elektrokatalysator. EC-MS-onderzoeken op een koperen schijf onthullen in eerste instantie dat een zure pH een gunstige conditievoorwaarde is voor efficiënte ammoniaksynthese. Hierbij wordt de vorming van gedeeltelijk gereduceerd NO vermeden in een gebied met beperkt massatransport, terwijl in een neutrale pH de vorming van N_2O wordt waargenomen. Voor bulkelektrolyse-onderzoeken is een poreuze koperlaag op de holle Ti-vezels gezet en is 10%

NO toegevoerd via de holle vezels, wat heeft geresulteerd in een aanzienlijk hogere stroomdichtheid in vergelijking met het traditioneel gebruikte doorstroomconcept. Hoewel een goede activiteit voor ammoniak is waargenomen, is tevens een lage elektrodestabiliteit als gevolg van corrosie in zure pH waargenomen. Daarentegen zorgt een stabiele elektrode in neutrale pH voor bijna 90% Faraday-efficiëntie en een NH_3-productiesnelheid van 400 μmol/h/cm² bij -0,6 V vs RHE. Het belangrijkste is dat het toevoeren van NO door de holle-vezelelektrode resulteert in onderdrukking van waterstofontwikkeling als gevolg van een verhoogde beschikbaarheid van de reactant dicht bij het elektrode-oppervlak. Een nieuwe benadering voor efficiënte omzetting van gassen met een lage oplosbaarheid wordt gepresenteerd aan de hand van het voorbeeld van de omzetting van stikstofmonoxide naar ammoniak voor toepassingen met betrekking tot groene mest.

Vervolgens is gelijktijdige elektroreductie van NO_3^- en CO_2 onderzocht om ureum te produceren, de meest voorkomende meststof op N-basis (**Hoofdstuk 5**). Een concepttest wordt getoond voor ureumformatie op een ruwe, polykristallijne koperelektrode in een met CO_2 verzadigde oplossing van 0,1 M $KHCO_3$ met 50 mM KNO_3 elektrolyt. Vanwege de hoge complexiteit van dit systeem is *in situ* 'surface enhanced' Raman spectroscopie gebruikt om geadsorbeerde soorten op het Cu-oppervlak te bestuderen tijdens cyclische voltammetrie. In aanwezigheid van NO_3^- in $KHCO_3$ is een gebrek aan CO-vorming waargenomen, waarschijnlijk als gevolg van preferentiële reductie van nitraat in plaats van CO_2. Het belangrijkste is dat een drievoudige koolstof-stikstofbinding is gevonden in het bereik van 2080-2150 cm^{-1}, afhankelijk van de toegepaste potentiaal waarvan is bevestigd dat deze tot cyanide behoort. Gedeeltelijk gereduceerd NO_3^-, waarschijnlijk in de vorm van NH_x, reageert met geadsorbeerd CO_3^{2-} op het Cu-oppervlak, waarbij C≡N wordt gevormd. Het gevormde cyanide creëert complexen met koper, wat resulteert in het oplossen van de elektrode en dus instabiliteit veroorzaakt. De vorming van cyaniden is bovendien bevestigd door elektrochemische massaspectrometrie, waarbij afgifte van stikstofmonoxide is waargenomen als product van vaste CuCN-oxidatie. Hoewel er geen karakteristieke ureumsignalen zijn waargenomen, is een parallelle route voor een alternatieve C-N-koppelingsreactie gevonden. De resultaten die in dit hoofdstuk worden gepresenteerd, geven een beter inzicht in de complexiteit van gelijktijdige reductie van CO_2 en NO_3^- en laten problemen zien bij de ontwikkeling van een functioneel systeem voor de elektrosynthese van ureum.

In het laatste hoofdstuk (**Hoofdstuk 6**) worden de belangrijkste bevindingen samengevat en wordt een perspectief gegeven op de onderwerpen die in dit proefschrift naar voren zijn gebracht.

List of publications

P. M. Krzywda, A. Paradelo Rodriguez, L. Cino, N. E. Benes, B. T. Mei, G. Mul, "Electroreduction of NO_3^- on tubular porous Ti electrodes", *Catalysis Science* & *Technology*, DOI 10.1039/D2CY00289B, **2022**.

P. M. Krzywda, A. Paradelo Rodriguez, N. E. Benes, B. T. Mei, G. Mul, "Carbon-Nitrogen bond formation on Cu electrodes during CO_2 reduction in NO_3^- solution", **2022** - *submitted to Applied Catalysis B: Environmental.*

P. M. Krzywda, A. Paradelo Rodriguez, N. E. Benes, B. T. Mei, G. Mul, "Effect of electrolyte and electrode configuration on Cu-catalyzed nitric oxide reduction to ammonia", *ChemElectroChem,* 9, e202101273, **2022**.

P. M. Krzywda, A. Paradelo Rodriguez, N. E. Benes, B. T. Mei, G. Mul, "Cover Feature: Effect of electrolyte and electrode configuration on Cu-catalyzed nitric oxide reduction to ammonia (ChemElectroChem 5/2022)", DOI 10.1002/celc.202200078, **2022**.

K. H. R. Rouwenhorst, **P. M. Krzywda**, N. E. Benes, G. Mul, L. Lefferts, "Ammonia Production Technologies" in *Techno-Economic Challenges of Green Ammonia as an Energy Vector*, 41-83, **2021**.

K. H. R. Rouwenhorst, **P. M. Krzywda**, N. E. Benes, G. Mul, L. Lefferts "Ammonia, 4. Green ammonia production", *Ullmann's Encyclopedia of Industrial Chemistry*, **2020**.

I. Merino-Garcia, J. Albo, **P. M. Krzywda**, G. Mul, A. Irabien, "Bimetallic Cu-based hollow fibre electrodes for CO_2 electroreduction", *Catalysis Today*, 346, 34-39, **2020**.

R. P. H. Jong, **P. M. Krzywda**, N. E. Benes, G. Mul, "Preparation of Ti, Ti/TiC or Ti/TiN based hollow fibres with extremely low electrical resistivity", *RSC Advances*, 10, 31901, **2020**.

W. Kasprzyk, **P. M. Krzywda**, S. Bednarz, D. Bogdał, "Fluorescent citric acid-modified silicone materials", *RSC Advances*, **2015**, 5, 90473.

Acknowledgements

At the end of this thesis and the entire PhD adventure, it is time to thank everybody who contributed to my success. It has been an inspiring and life-changing experience but also very challenging and stressful. I would not have been able to complete it all by myself.

First I would like to thank my supervisors for the opportunity to do PhD at University of Twente in PCS and FiF groups. Guido, thank you for giving me the freedom to choose my own research paths, make my own decisions and for not losing hope even at the most difficult stages of my PhD. Your enthusiasm and positive energy are very uplifting. Nieck, thank you for your contribution to the project and all opportunities I got by joining the MST cluster. Our cooking workshops are definitely a memorable experience. Bastian, although officially you were not my supervisor, I do consider you as one. Your input to my work in the last and the most difficult stage of my PhD was invaluable. I have learned a lot from you.

Thank you to everybody who supported my research activities. Robert M., thanks for building my setups and providing a helpful hand when I encountered technical difficulties. I have learned a lot of technical details from you. Frank, I enjoyed our random chats in the hallway of Meander. Bob, I really enjoyed having you around. Sorry for all filaments you had to change because they burned out on my watch. Thank you to Mieke, Cindy, Herman and Harmen for technical support. Thank you to Lidy, Dorothy and Annet for your help with all administrative matters.

Thank you to all PCS colleagues who made these 4.5 years a wonderful experience. Many thanks to my Paranymphs for support during thesis preparation and standing by my side during the defense. Ainoa, thank you for the nice collaboration, you managed to get what you could from the picky Sniffer. Your graphical abstracts make my thesis look way better! Liniker, it was always nice to complain to each other about all struggles we had, especially over a beer. I hope you will remember my guitar song forever. Nakul, Devin, Ronald, Robert B., thank you for the very nice friendship. I enjoyed all drinks and dinners we had together, especially the spontaneous ones. You were always there for serious and less serious conversations which made the PCS lab a fun place, even in the most difficult times. I had a great time with you guys. Vera, I always enjoyed our chats in the office. Thank you for introducing me to scuba diving. Kasper, your outstanding videos and very specific choice of songs always created a fantastic atmosphere. Never lose that spirit! I hope there are no hidden jokes in the Dutch summary. Mozhgan, thank you for introducing me to Persian cuisine and leaving your magic Cu electrodes which gave me a chapter. Yibin, I will never forget your distinctive voice in the Meander's hallways. Senior PCS members, Kai

and Alex, it was great to meet you and I hope we will keep seeing each other during PCS alumni activities! Anne, thanks for discussions about hollow fibers and taking charge of E-Triple-C project management tasks. Without you we would have never sent our "bi-weekly" project updates. Kaijan, hope you will get your Nature paper. Martijn, I enjoyed your jokes about me making ammonia. Guess what, I made ammonia! Margot, try to keep graduation movies tradition within the new generation of PCS members. Shri, you are the most dangerous and fearless futsal player I have ever seen. Shreyas, although we have not known each other for a long time, I will not forget the "burger me evenings". Marco, Georgios, David, Nathalia, Dalia, Talal, Tursun, Max, Lisanne, Sean, Sobhan, good luck to all of you. You will need it.

Special thanks go out to the PhotoKai team members. It was an honor to be able to score one goal. I am glad we could always beat POF and I will miss our victory juice.

Thank you to the FiF group and the MST cluster members. Although we didn't spend a lot of time together, you were always very helpful. Thanks!

Thanks to all students I could work with, Lukas, Bas, Gijs, Josefien. I enjoyed working with you and learned a lot by supervising you. Thank you for your input in this thesis.

I would like to acknowledge my committee members for the time spent on evaluating my thesis and attending my defense.

Finally, a big thank you to my partner for all support and understanding I got, especially in the most stressful parts of my PhD. You played a big role in achieving my success. Thank you so much! Wielkie podziękowania dla moich rodziców za możliwość nauki i wsparcie na każdym etapie życia. Bez Was ten doktorat nie byłby możliwy.

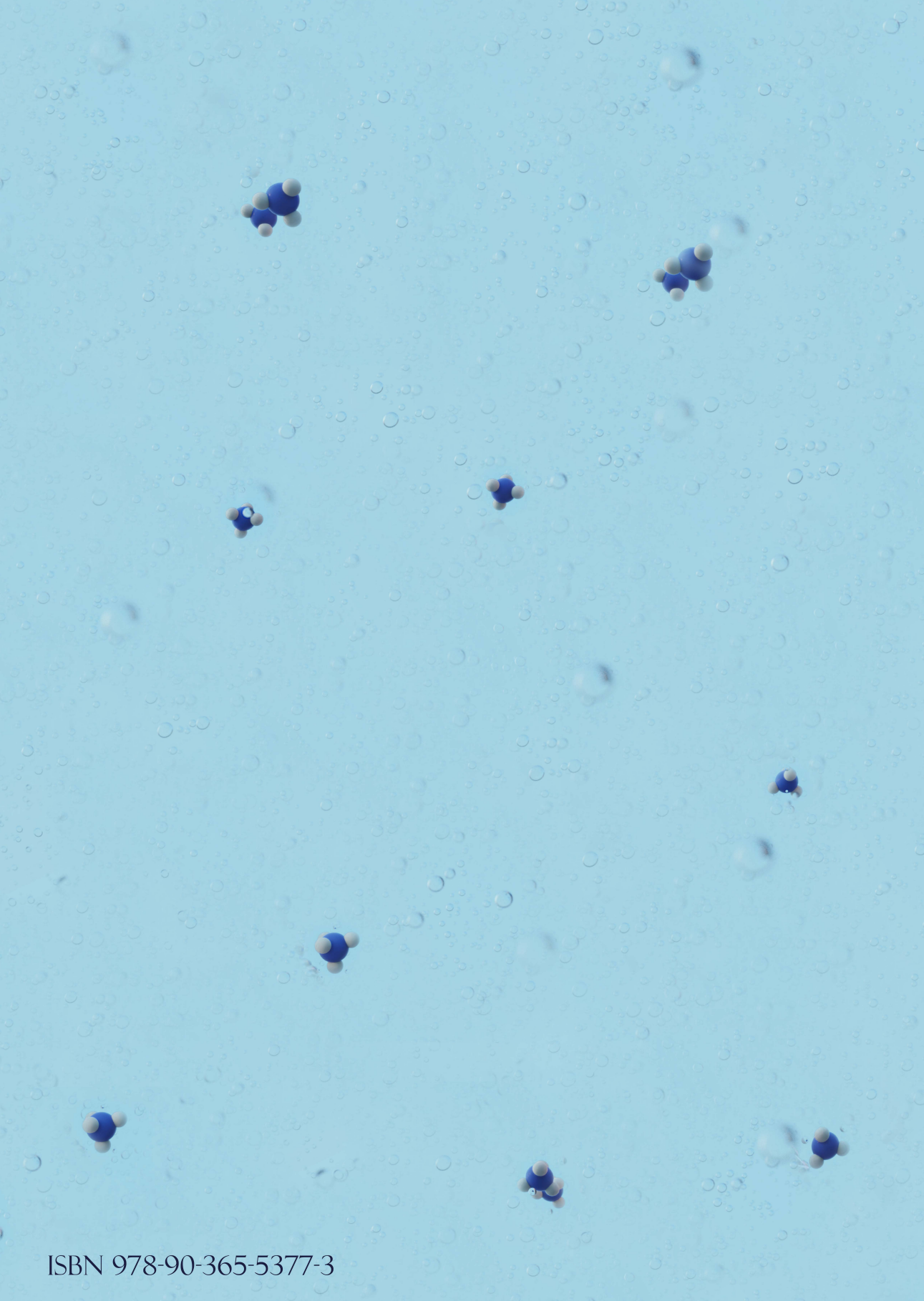

ISBN 978-90-365-5377-3